

P-162

NASA Contractor Report 174937

# Analysis of Results from Wind Tunnel Tests of Inlets for an Advanced Turboprop Nacelle Installation

J.P. Hancock, V. Lyman, and A.P. Pennock

LOCKHEED-GEORGIA COMPANY  
Marietta, Georgia

Prepared for  
National Aeronautics and Space Administration  
Lewis Research Center  
Cleveland, Ohio 44135

CONTRACT NAS3-23710  
JUNE 1986

NP0-10011

Unclass  
0237126


CSCL OIA G3/02

(NASA-CR-174937) ANALYSIS OF RESULTS FROM WIND TUNNEL TESTS OF INLETS FOR AN ADVANCED TURBOPROP NACELLE INSTALLATION REPORT, 1 NOV. 1982 - 30 Jun. 1986 (Lockheed-Georgia Co.) 162 P

Date for general release July 1989





1. Report No. NASA CR-174937		2. Government Accession No.		3. Recipient's Catalog No.	
4. Title and Subtitle ANALYSIS OF RESULTS FROM WIND TUNNEL TESTS OF INLETS FOR AN ADVANCED TURBOPROP NACELLE INSTALLATION				5. Report Date June 1986	
				6. Performing Organization Code	
7. Author(s) J. P. Hancock, V. Lyman, and A. P. Pennock				8. Performing Organization Report No. LG85ER0105	
				10. Work Unit No.	
9. Performing Organization Name and Address Lockheed Georgia Co. 86 South Cobb Drive Marietta, GA 30063				11. Contract or Grant No. NAS3-23710	
				13. Type of Report and Period Covered Contractor Report 11-01-82 to 6-30-85	
12. Sponsoring Agency Name and Address National Aeronautics and Space Administration Washington, D.C. 20546				14. Sponsoring Agency Code 505-31-3B	
				15. Supplementary Notes Project Manager, George L. Stefko, NASA Lewis Research Center, Cleveland, Ohio 44135	
16. Abstract Inlets for tractor installations of advanced turboprop propulsion systems were tested in three phases, covering a period from November, 1982 to January, 1984. Nacelle inlet configuration types included single scoop, twin scoop, and annular arrangements. Tests were performed with and without boundary layer diverters and several different diverter heights were tested for the single scoop inlet. This same inlet was also tested at two different axial positions. Test Mach Numbers ranged from Mach 0.20 to 0.80. Types of data taken were (1) internal and external pressures, including inlet throat recoveries, (2) balance forces, including thrust-minus-drag, and (3) propeller blade stresses.					
17. Key Words (Suggested by Author(s)) Inlets; Advanced Turboprops; Wind Tunnel Tests; Nacelles				18. Distribution Statement 	
19. Security Classif. (of this report)		20. Security Classif. (of this page)		21. No. of pages	22. Price*



[REDACTED]

[REDACTED]

## FOREWORD

This report was prepared by the Lockheed-Georgia Company, Marietta, Georgia, for the NASA-Lewis Research Center, Cleveland, Ohio, under Contract NAS3-23710, entitled "Turboprop Inlet Installation Technology Effort". George L. Stefko was the project manager for the NASA-Lewis Research Center. Lockheed's program manager was B. H. Little. A substantial amount of supporting work was provided by D. D. Tanner and T. A. Wynosky of Pratt and Whitney Aircraft in East Hartford, Connecticut. Propeller blade stress testing and analysis were performed by Harry Wainauski, Prem Bansal, and Bennett Brooks from the Hamilton Standard Division of United Technologies Corporation.



## TABLE OF CONTENTS

Section	Page
COVER PAGE	
TITLE PAGE	i
FOREWORD	ii
TABLE OF CONTENTS	iii
SUMMARY	1
INTRODUCTION	2
INLET DESIGN	3
Design Criteria	3
Inlet Location	3
Inlet Sizing	5
Design Methodology	5
MODEL DESCRIPTION	12
Propeller	12
Nacelle & Inlets	12
Instrumentation	26
TEST FACILITY	34
Wind Tunnel	34
Propeller Test Rig	34
TEST DESCRIPTION -- CONFIGURATIONS, PROCEDURES, AND RUN SUMMARY	36
TEST RESULTS AND DISCUSSION	43
Inlet Total Pressure Recovery	43
Effect of Peripheral Extent -	43
Effect of Boundary Layer Diverter Height -	45
Effect of Mass Flow Ratio -	45
Effect of Mach Number -	48

Inlet Pressure Distortion	51
Inlet Static Pressure Patterns -	51
Inlet Total Pressure Contours -	55
Cowl Pressure Distributions	61
Effect of Inlet Type -	61
Effect of Mach Number -	85
Effect of Mass Flow Ratio -	85
Effect of Propeller Blade Angle -	85
Correlation of Calculated Cowl Pressures -	86
Nacelle Drag	87
Thrust-Minus-Drag Performance	102
Correlation with Existing Data Base -	102
Front End Thrust-Minus-Drag -	102
Configuration Comparison -	105
Effect of Diverter Height -	109
Effect of Mach Number -	109
Effect of Mass Flow Ratio -	111
Propeller Blade Stresses	114
CONCLUDING REMARKS	117
APPENDIX	119
A. Test Configuration Coordinates and Pressure Tap Locations	119
B. Inlet Flow Calibration	137
C. Repeatability Analysis	142
D. Uncertainty Analysis	147
E. Data Reduction Description	150
F. List of Symbols	153
REFERENCES	157



## SUMMARY

As a step toward the development of a generalized technology base, inlets for tractor installations of advanced turboprop (propfan) propulsion systems were tested in three phases, covering a period from November, 1982 to January, 1984. Nacelle inlet configuration types included single-scoop, twin-scoop, and annular arrangements. Tests were performed with and without boundary layer diverters and several different diverter heights were tested for the single-scoop inlet. This same inlet was also tested at two different axial positions. Test Mach numbers ranged from Mach 0.20 to 0.80. Types of data taken were (1) internal and external pressures, including inlet throat total pressure recoveries, (2) balance forces, including thrust-minus-drag, and (3) propeller blade stresses.

Results of the testing showed that inlet performance improved with reducing inlet aspect ratio (i.e., circumferential spread), decreasing propeller-to-inlet separation, and increasing boundary layer diverter height. The best performing design was a forward mounted, single-scoop inlet with a boundary layer diverter that was approximately two-and-a-half times the estimated flat-plate boundary layer height. However, this inlet position produced high blade stresses through dynamic excitation. A trade-off between inlet recovery and blade stress levels as a function of inlet position was found to exist, so a compromise in inlet performance is expected to be necessary for most installations. Inlet-forebody spillage drag was not found to be a serious problem, due to the relatively small size of the inlet for a given installation and the favorable effect of inlet blockage on the propeller operating point. It was also found that calculated pressures on the nacelle and inlet external surfaces agreed well with the measured values.



## INTRODUCTION

Preliminary tests of advanced, high-speed ( $Mo = 0.80$ ) turboprops (propfans) in idealized nacelles show propulsion efficiencies 10 to 20 percent higher than equivalent technology turbofans. Efficient installation of propfans, however, presents some challenging technical problems. These problems generally concern inlet pressure recovery, cowl drag, diffuser performance, and interactions between the propeller and aircraft flow fields. While there are many variations in propfan propulsion system and aircraft installation design, the most aerodynamically challenging combinations generally occur for single-rotation propellers in a wing-mounted tractor arrangement because of the swirl interaction effects on the wing and inlet.

Research on propfans has been underway for over 10 years. During this period, NASA established as a long range, high-priority objective the development of technology for the efficient installation of high-performance propfans. Most of the work performed in this area by Lockheed and other major aerospace firms has been monitored and coordinated by the NASA Lewis Research Center (LeRC) at Cleveland, Ohio. In the 1981-82 time frame, an LeRC sponsored design study was performed by Lockheed under Contract No. NAS3-22751, "Propfan Core Inlet Design" (Reference 1), to generate preliminary designs on single- and twin-scoop inlets. As an outgrowth of this effort, the present program was initiated to perform wind tunnel tests on a series of inlet models for advanced tractor, turboprop installations.

This effort was a cooperative undertaking by three participants: the Lockheed-Georgia Company (Gelac), United Technologies (Pratt and Whitney Aircraft and Hamilton Standard), and NASA. Thus it was designated the GUN Program. Testing was conducted in three phases in the United Technologies Research Center (UTRC), high-subsonic wind tunnel test facility at Hartford, Connecticut in the 1982-84 time period. Inlet pressure recovery and distortion, external cowl forebody drag, and propeller blade stress data were recorded for single-scoop, twin-scoop, and annular inlet configurations. A substantial technology base for the selection and design of inlets for propfan installations was thereby established.

The technology base generated in this program was developed in general for the advancement of propfan installation technology and in particular as a data base for application directly to the development of an inlet installation for the Propfan Testbed Assessment (PTA) Program. This effort is currently the focus of the long range NASA objective to develop the technology for the design of efficient, high-speed propfan installations. The objective of the PTA program is to develop, build, and verify the propfan structural integrity and evaluate its cabin noise and cabin acoustic treatment characteristics on a Gulfstream II airplane.

The principal measurements and calculations for this test program were made in English units. Accordingly, in the body of the report, English units will be given parenthetically following the required SI units. In the first appendix, which contains long listings of highly detailed, dimensional data, however, the English units will be presented alone.

## INLET DESIGN

One of the problems in evaluating propfan inlet concepts is that of establishing an inlet definition parameter against which quantitative performance assessments can be made. As a result of studies conducted under Contract NAS3-22751, "Propfan Core Inlet Design", the parameter Theta,  $\theta$ , was selected to define the aspect ratio, or angular circumferential spread, of the inlet entry (Figure 1). Based on these studies, a value of  $\theta = 55$  degrees was selected for the single-scoop inlet,  $\theta = 2 \times 55$  degrees for the twin-scoop inlets, and  $\theta = 360$  degrees for the annular inlet.

Five basic inlet configurations were selected for design and experimental evaluation with an advanced eight-bladed 45 degree swept (SR-3) propfan (Reference 2). They were two single-scoop, or chin inlet, configurations - one designed with a boundary layer diverter and one without, two twin-scoop configurations with and without a boundary layer diverter, and an annular inlet.

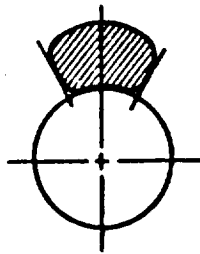
### Design Criteria

The objective in the design of the inlets was to maximize aerodynamic performance at cruise conditions ( $M_o = 0.80$ ), subject to practical structural and aerodynamic constraints. This included providing acceptable performance at off-design cruise Mach numbers up to 0.85 and during simulated ground operations (cross-winds and reverse thrust).

While recognizing the strong asymmetry of the swirling slipstream, one of the initial geometric constraints adopted in the program was to maintain inlet lateral symmetry, so that the drag penalty associated with this simpler geometry could be established. This, then, precluded inlet face canting (sweeping), or other asymmetries, to counter propeller swirl effects.

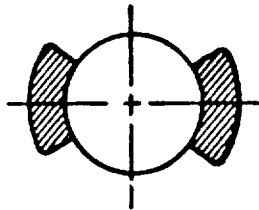
### Inlet Location

The fore-and-aft location of the inlet with respect to the propeller is important, since it impacts inlet total pressure recovery and distortion during forward and reverse thrust conditions, inlet-induced blade cyclic stresses, and external nacelle drag. Since no data were available to assess inlet/propfan-blade dynamic excitation, the inlets were positioned as close behind the propeller as possible without adversely impacting reverse thrust performance. This resulted in a spacing between the blade pitch-change axis and the inlet highlight equal to 11 percent of propeller diameter for most of the inlets. An alternate version of one configuration, the single-scoop inlet with boundary layer diverter, was placed at a spacing of 20 percent behind the blade axis in order to assess the effects of moving an inlet aft.

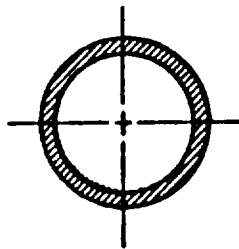


$\theta$

$55^\circ$



$2 \times 55^\circ$



$360^\circ$

Figure 1. - Inlet entry angular definition

## Inlet Sizing

During high-speed cruise conditions, flow-field Mach numbers behind the SR-3 propfan exceed local values of 1.0. The air induction system must, therefore, perform a deceleration of the inlet flow from these high transonic values to a compressor face Mach number of approximately 0.40. For optimum performance, part of this flow diffusion is performed external to the inlet and the remainder internal to it. The question in inlet design is how to select an optimum design point (inlet area), so that losses and propeller-inlet aerodynamic interactions due to external diffusion are balanced against those due to internal diffusion. A large inlet will give low inlet Mach numbers, small internal diffusion area ratios, and thus good quality flow to the engine compressor - all at the risk, however, of creating excessive nacelle drag and large propfan excitation factors. Reducing the inlet size will ease the external drag and propfan blade stress problem, but at the expense of higher inlet Mach numbers, larger diffuser area ratios, and possibly unacceptable flow distortion at the engine compressor face.

The optimum inlet design point was determined based on trade studies performed under NASA Contract NAS3-22751, "Propfan Core Inlet Design". Results from the trade studies (Reference 3) are reproduced in Figure 2. The drag data used here were synthesized from tests of several NACA 1-Series annular inlets, and internal losses were based on data from S-duct diffuser tests conducted at Lockheed Georgia in 1981 (Reference 4). On the basis of this data, a design mass flow ratio (based on inlet highlight area) of 0.70 was chosen. This allows some margin for off-design operation at lower mass flow ratios without significant drag penalties. This mass flow ratio corresponds to an inlet throat Mach number of about 0.55. Other trade-offs were involved in selecting the inlet throat area as a function of disc loading,  $(HP/Dp^2)$ , specific horsepower,  $(HP/Wa)$ , and throat mass flow ratio. They showed a disc loading of 32.0 HP/ft<sup>2</sup> and a specific horsepower of 220 HP/(lb/sec) to be appropriate for the design point, resulting in an inlet throat area equal to 1.12 percent of the propeller disc area for the single and twin-scoop inlets, and 1.23 percent for the annular inlet.

## Design Methodology

The external cowling of the inlets was designed using an analytical procedure that is based on the use of advanced computational tools. The basis for the method is the use of the Lockheed/Jameson FLO49 transonic code (Reference 5) to assess transonic effects, while full three-dimensional effects are included through the subsonic 3-D QUADPAN panel code (Reference 6), which has been modified to include a propeller slipstream. As this methodology is described in detail in References 3, 7 and 8, only an outline of it will be provided here.

Figure 3 illustrates the use of the FLO49 transonic code to design super-critical contours. The initial configuration is a conventional NACA 1-Series cowl section. The shape exhibits a strong leading-edge shock, followed by an expansion and subsequent strong terminal shock. The target Mach number distribution, on the other hand, is one with isentropic or

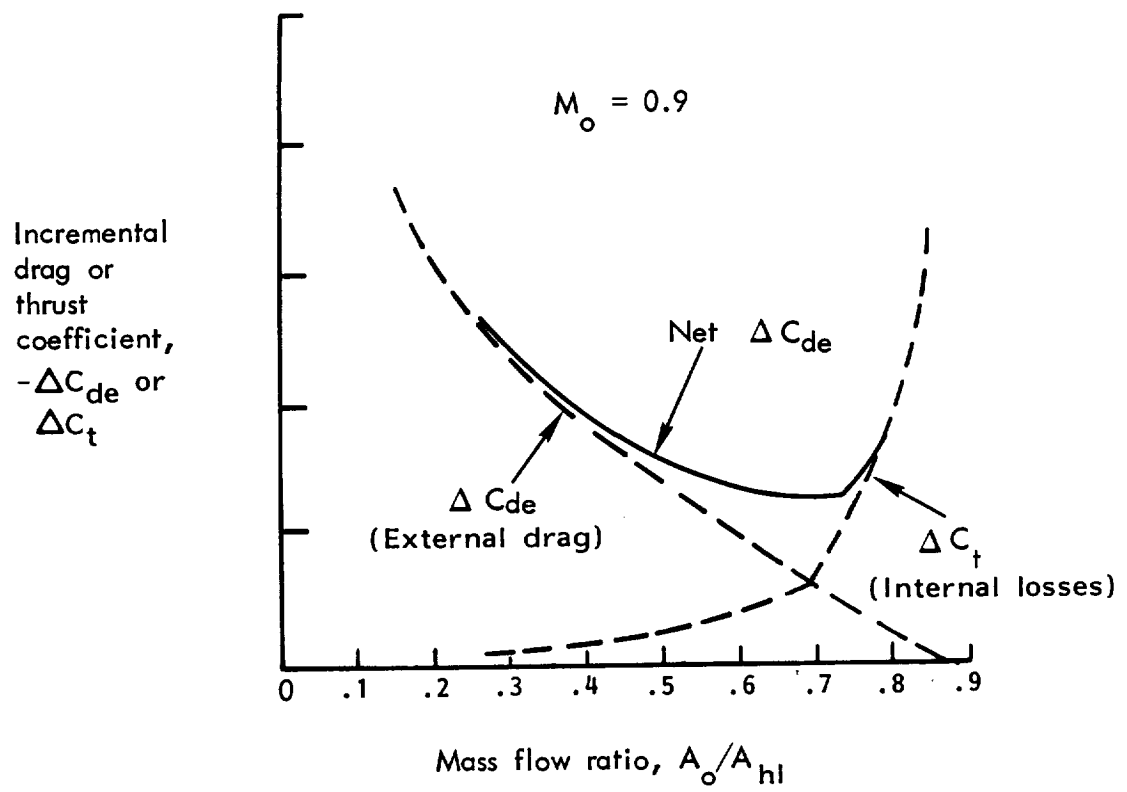


Figure 2. - Inlet design trade study

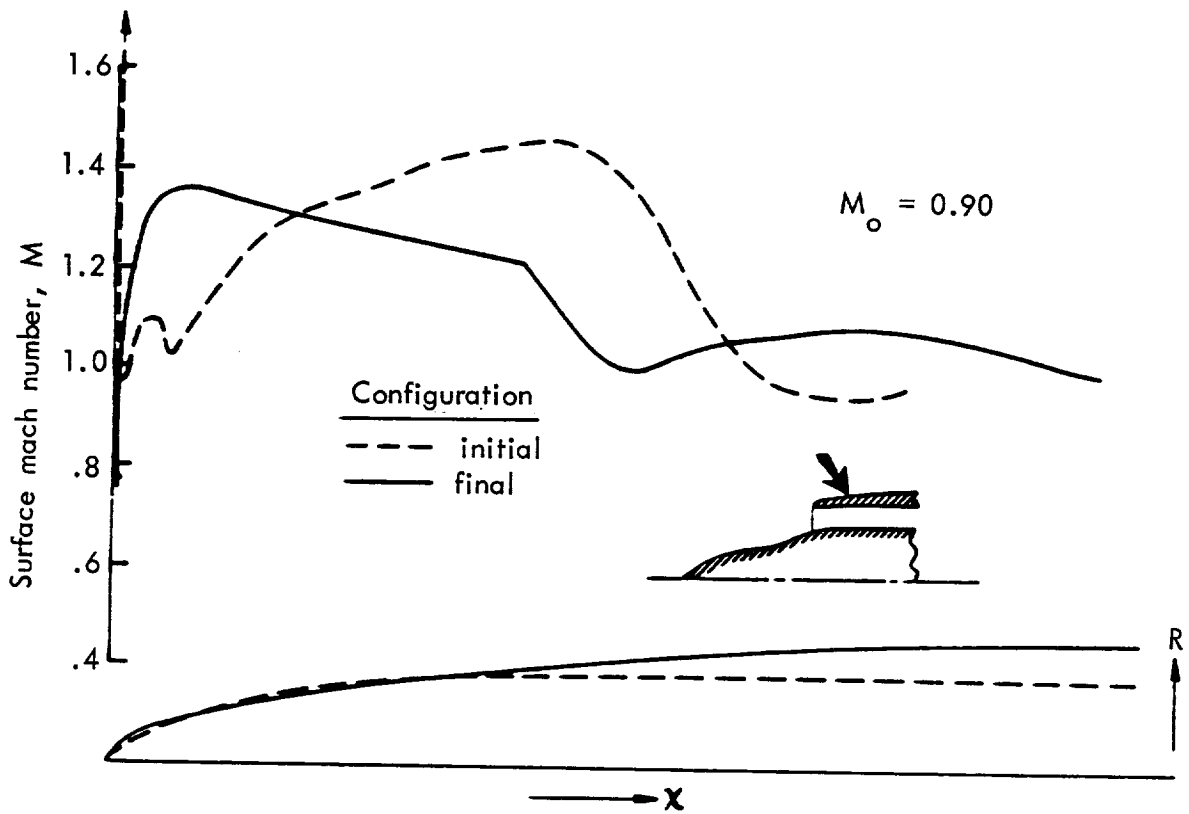


Figure 3. - Inlet external cowl design



near-isentropic recompression with a shock at local Mach numbers no greater than about 1.2. To attain that goal, the initial shape is analytically perturbed in an iterative process to achieve the target Mach number distribution shown. The basic transonic cowl section was designed in isolation from the propeller using the FLO49 code, a process later verified from GUN-I program test data which showed the propfan to have a relatively small effect on the flow over the crown section (meridional plane) of the cowl. However, in adapting the axisymmetric (2-D) FLO49 transonic code to design three-dimensional inlets, it has been found necessary to account for 3-D relief effects by adjusting the inlet mass flow ratio, MFR ( $A_o/A_{h1}$ ) in the FLO49 analysis. It must be increased above the actual value in order to simulate the flow over the crown section of a 3-D inlet.

Following the above procedure, the FLO49 code was used to design supercritical cowl sections for each of the inlets. The sections were then integrated into the three-dimensional nacelle to yield an initial configuration for subsequent iterative design using the 3-D QUADPAN panel code. This code includes a propeller effects calculation, which uses momentum theory and experimentally derived propeller velocity survey data just aft of the propeller plane to provide the slipstream development downstream along the nacelle. Predicted surface pressure distributions for the inlets with and without the propfan are provided later under discussion of cowl pressure distributions.

An objective of iterative design with the QUADPAN code is to predict and reduce pressure peaks over the external inlet surfaces, so as to minimize shock formation and consequent drag at higher subsonic Mach numbers. This is especially important with the propfan present, as the windward and leeward cowl sections respond strongly to flow angle changes caused by swirl, resulting in large negative pressure peaks on the leeward side. This can be alleviated by three-dimensional contouring of the inlet, which involves drooping the windward and leeward leading edge sections of the cowl, so as to better align them with the local swirl flow. Although droop is unnecessary for the windward side of the inlet, both sides of the inlet cowl sections would be drooped equally to maintain lateral symmetry. This procedure was also followed for the twin-scoop inlet designs, and both results from experimental and calculated nacelle pressure data confirm its effectiveness.

Trade studies conducted in the NASA Core Inlet Contract indicated that boundary layer diverters would significantly improve the performance of scoop inlets. Results of this study for a single-scoop inlet are shown in Figure 4 where the parameter  $F_{Dbld}/F_u$  is plotted against height of the boundary layer diverter ( $F_u = \text{thrust at } 100\% \text{ pressure recovery}$ ). The optimum height varies, depending on the assumed diverter drag coefficient. For the baseline single-scoop inlet, a diverter height of 1.3 percent of the propeller diameter was selected. The trade studies also showed that the optimum boundary layer diverter height for a twin-scoop inlet to be approximately three-fourths of that for a single-scoop. Therefore, a diverter height of 1.0 percent was selected as optimum for the twin-scoop inlet.

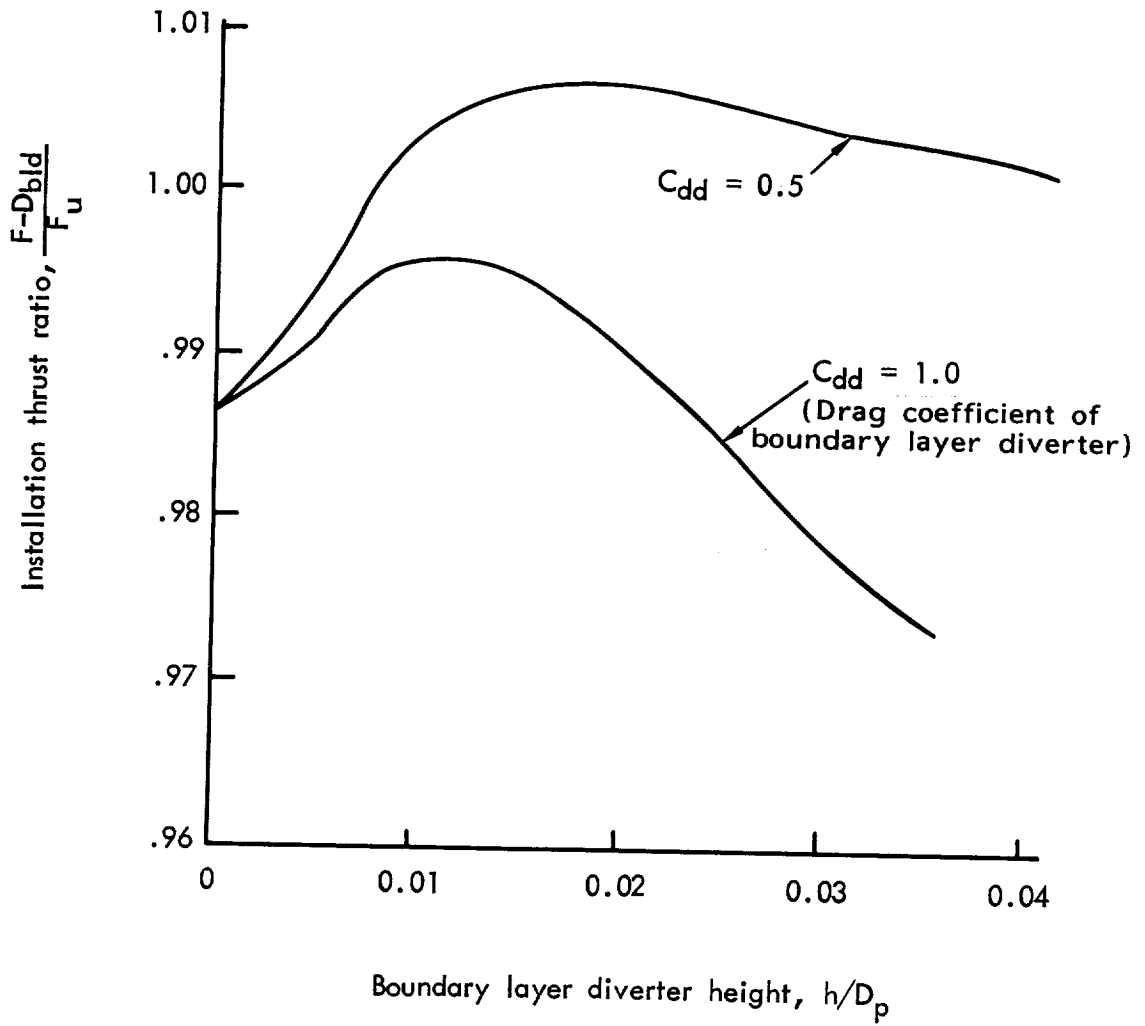


Figure 4. - Thrust gain with boundary layer diverter for single-scoop inlet

The modification of the inlets to accommodate a diverter was accomplished by vertically displacing the inlet entry and changing the cross-sectional shape by "unsagging", or flattening, of the kidney shape to allow efficient diversion of the viscous layer (Figure 5). In planform, the overall proportions and shape of the boundary layer diverter profile are constrained, to a large extent, by internal diffuser geometry. Within these limits, the diverter/channel for the inlet was contoured so that the spinner boundary layer was captured and channeled with minimum losses. Results from the QUADPAN panel code were used to iteratively refine the contour to achieve a pressure field that promotes boundary layer diversion. Specific criteria included minimizing suction peaks to prevent strong shock-boundary layer interactions and tailoring the adverse pressure gradients to minimize boundary layer growth. QUADPAN analysis models of the five basic configurations are presented later in the section entitled "Cowl Pressure Distributions". Detailed coordinates of the configurations are listed in Appendix A.

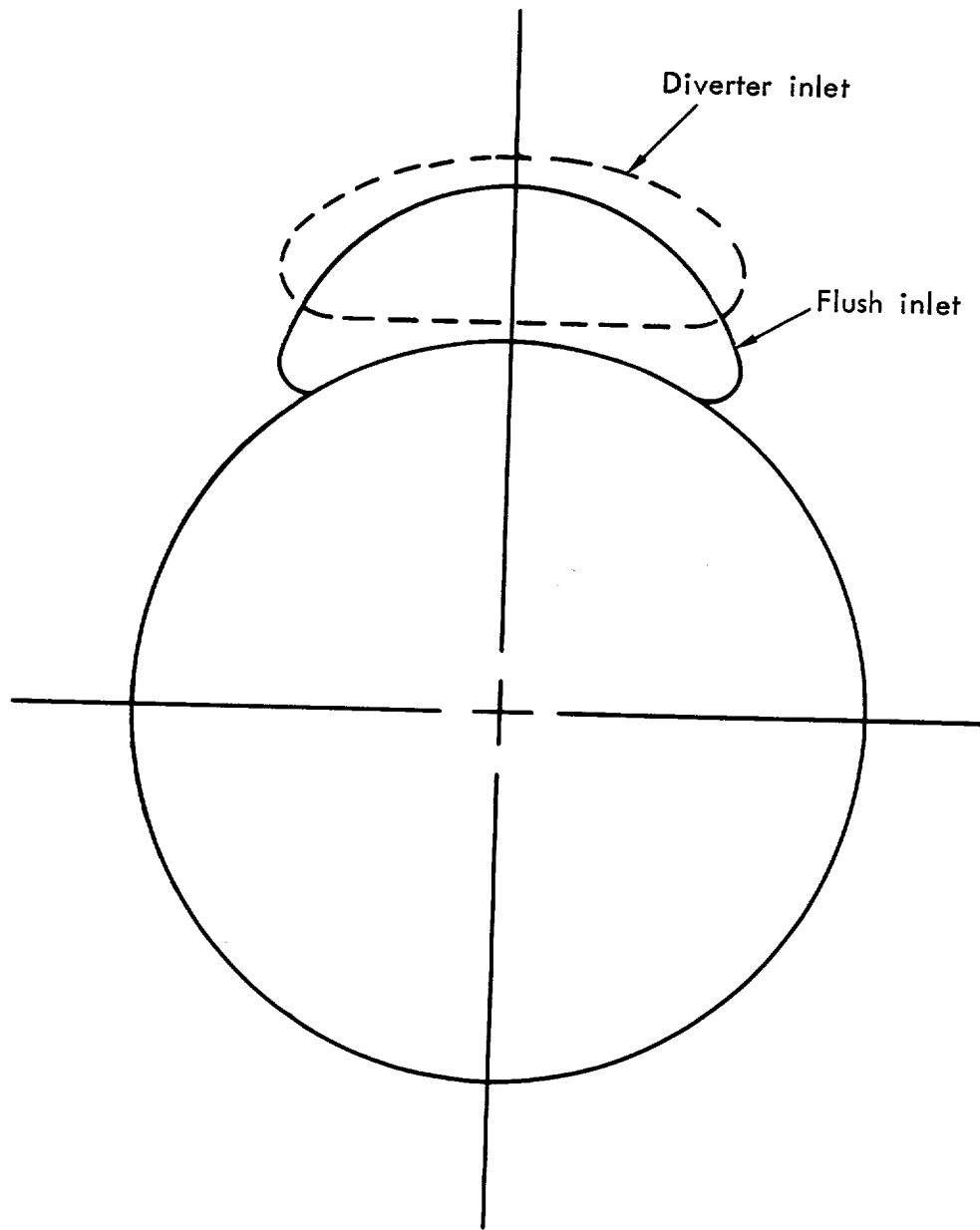


Figure 5. - Inlet entry cross-section

## MODEL DESCRIPTION

### Propeller

The inlets were tested with a 62.23-centimeter (24.5-in.)-diameter variable pitch model of the eight-bladed, SR-3 propeller. Figure 6(a) shows the propeller with the nacelle and inlet mounted on the Propeller Test Rig (PTR) in the UTRC wind tunnel. The direction of rotation of the propeller is counterclockwise, looking forward. Figure 6(b) shows the cowl drag balance installation.

For blade stress tests a slip-ring assembly was installed on the nose of the spinner to transfer the strain gage signals from rotating to stationary hardware. A sting on the axis of rotation carried the wiring upstream to a low-velocity section for exit from the tunnel.

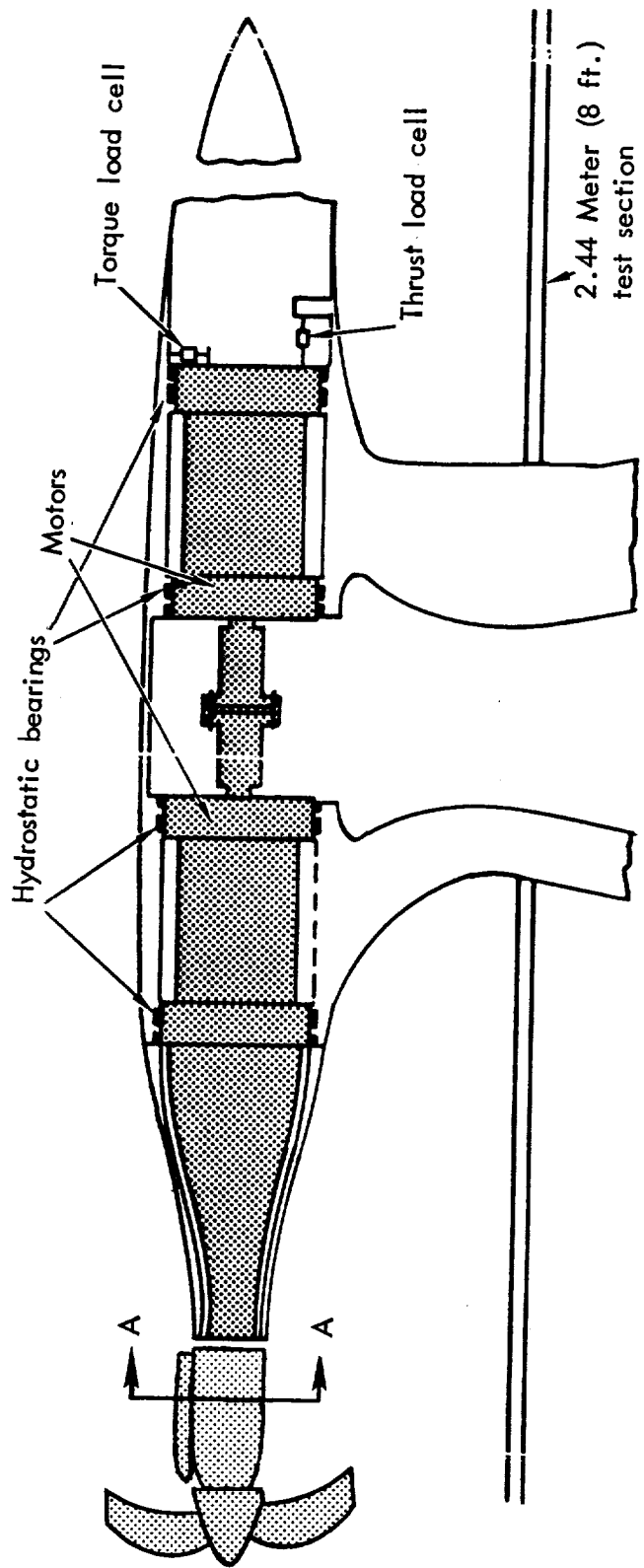
### Nacelle and Inlets

Photographs of representative installations from the GUN-I, II, and III tests are presented in Figure 7. A photo of the single-scoop inlet installed in the aft position is shown in Figure 7(g). The bare nacelle without an inlet, but with a Kiel probe rake installed, is illustrated in Figure 7(h). The major envelope dimensions for all the test configurations are provided in Figure 8. All inlets are positioned .5 inches behind the spinner except for the single-scoop inlet in the aft position shown in Figure 8f. Details of the contours are tabulated in Appendix A. The nacelle maximum cross-sectional reference area for the purpose of computing drag coefficients is 383.55 square centimeters (59.45 sq. in.).

In all phases of the GUN test program, inlet internal performance measurements were taken no further aft than the throat. Internal duct performance simulation was not included, because it was not practical to include the typical "S" duct design arrangement into the PTR as configured for this test. It was also desirable to separate the inlet entry inflow losses from the internal duct losses for analysis purposes.

As built for the GUN-I test, the single-scoop inlets were mounted under the nacelle (Figure 7(a)). The inlet airflow was aspirated through a faired duct on the pylon leading edge to the flow control measurement section and exhaust system under the floor. After GUN-I these inlets were rebuilt with an internal balance that measured the axial aerodynamic force on the inlet forebody. A flow-through arrangement, with exit nozzle control areas sized at 40, 60, 80, and 100 percent of inlet throat area, replaced the ducted exhaust and the inlets were moved to the top of the nacelle (Figure 7(b)). A similar cowl drag balance arrangement was fabricated for the twin-scoop and annular inlets, but, in these cases, exit nozzle areas were sized at 25, 50, and 75 percent of inlet throat area to allow for higher losses with the smaller inlet internal areas.

The pressure distributions on the original 1.3 percent ( $h/D_p=0.013$ ) diverter of the single-scoop inlet showed that the diverter gutter (trough) contour was too sharp, causing supercritical velocities in the

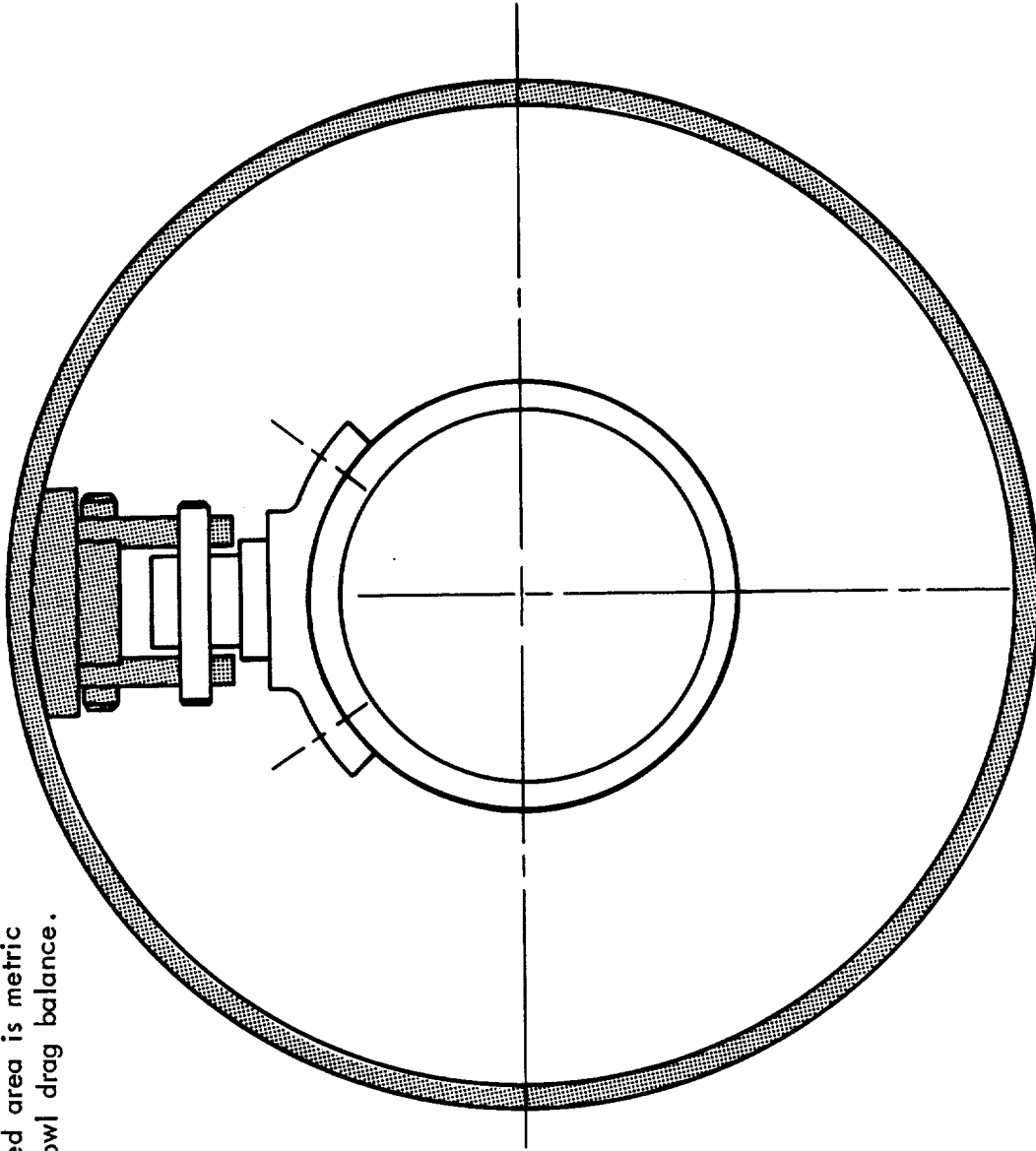


Note: Shaded components are metric on load cells

(a) General arrangement

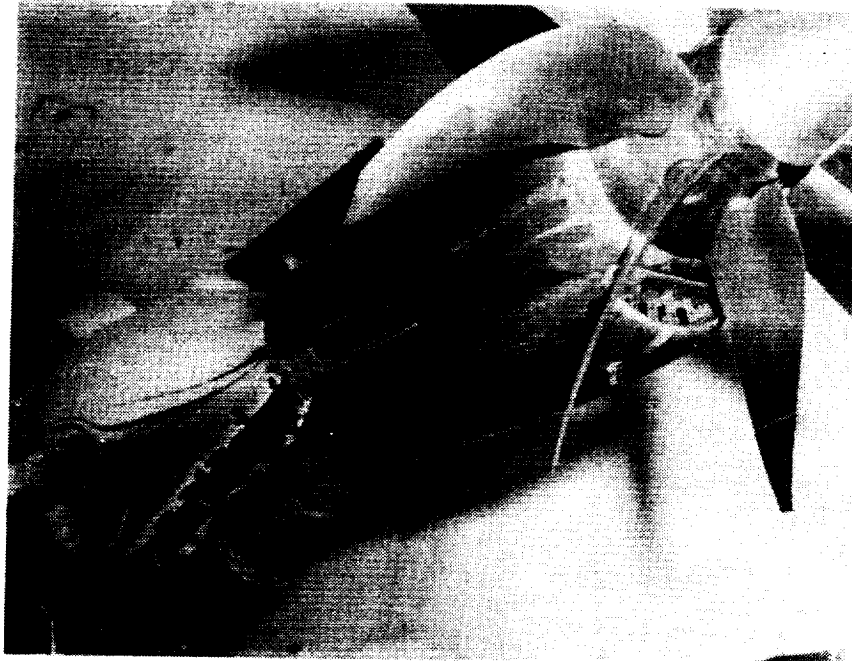
Figure 6. - Propeller test rig in wind tunnel

Note: Shaded area is metric  
on cowl drag balance.

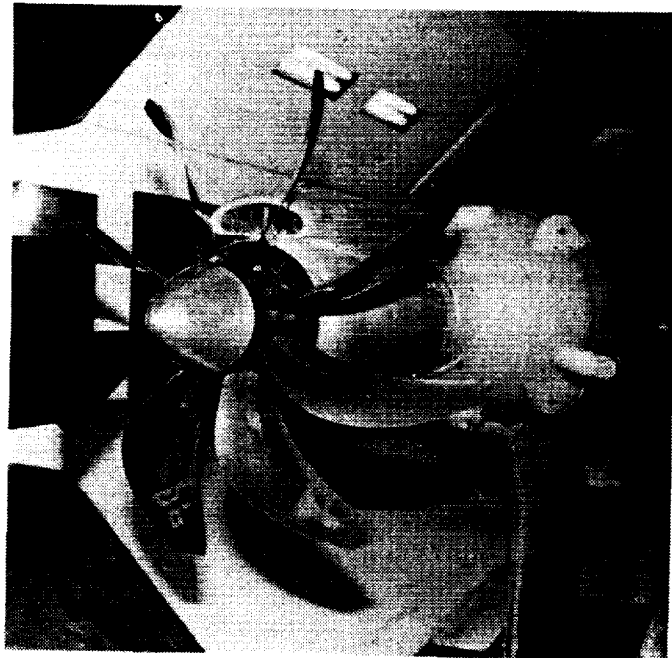


(b) Cowl drag balance detail (section A-A)

Figure 6. - Concluded



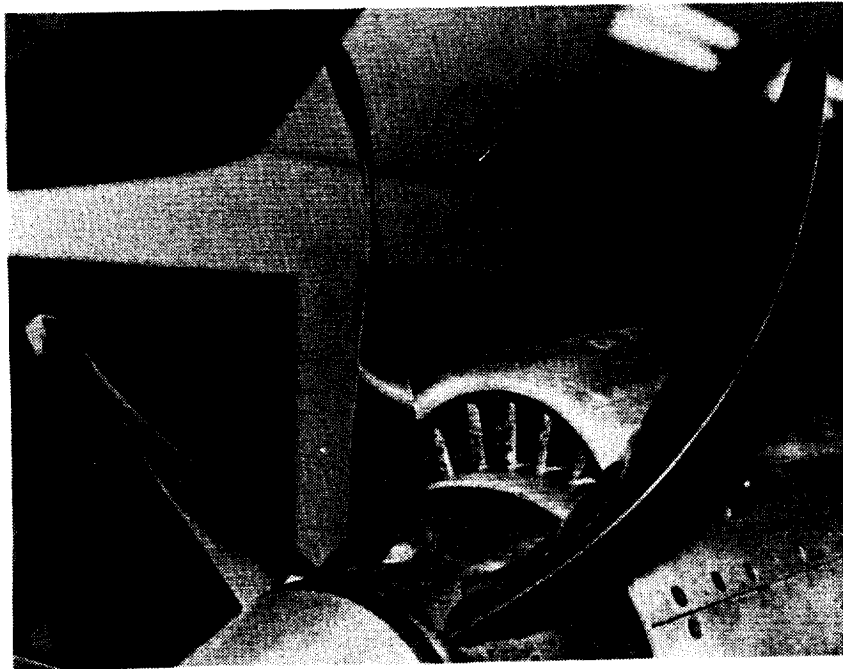
(a) Single-scoop inlet with diverter; GUN I installation.



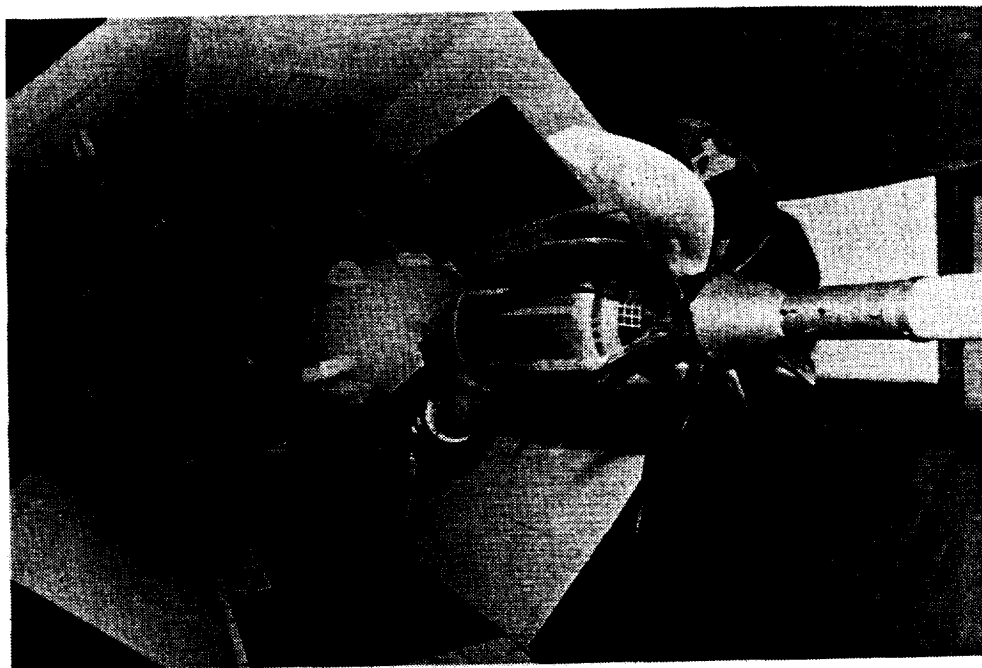
(b) Single-scoop inlet with diverter; GUN II installation.

Figure 7. - Propeller, nacelle, and inlets; photographs of wind tunnel installation.



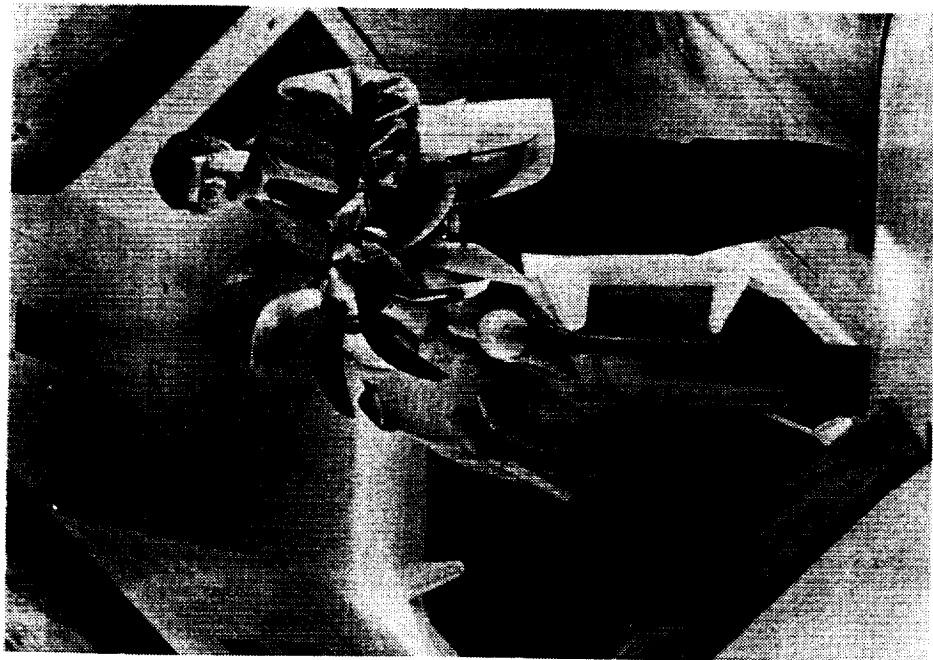


(c) Single-scoop inlet without diverter; GUN-II installation.

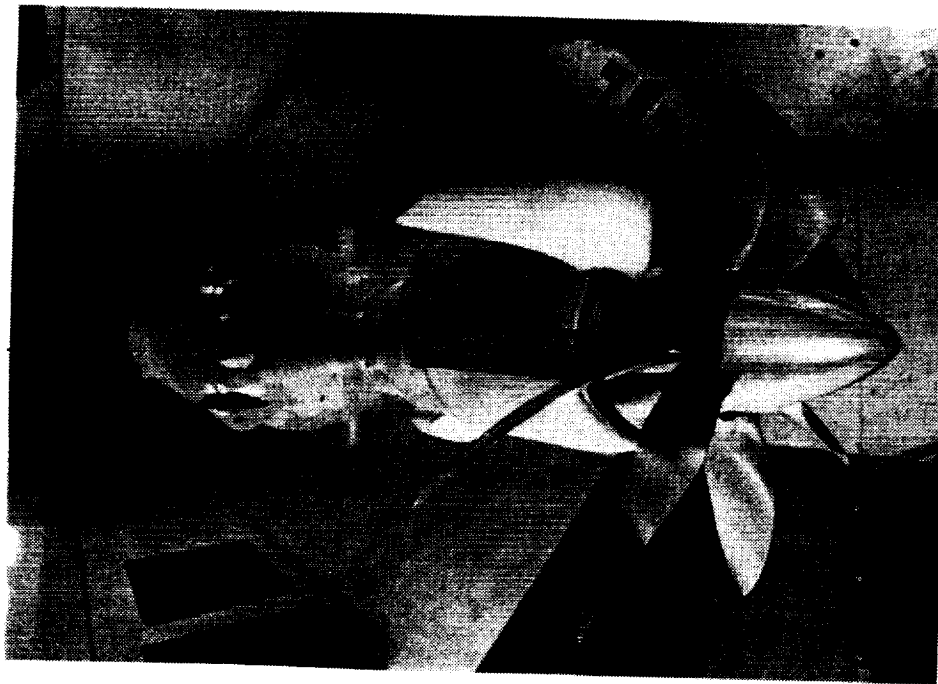


(d) Twin-scoop inlet with diverter; GUN-III installation.

Figure 7. - Continued

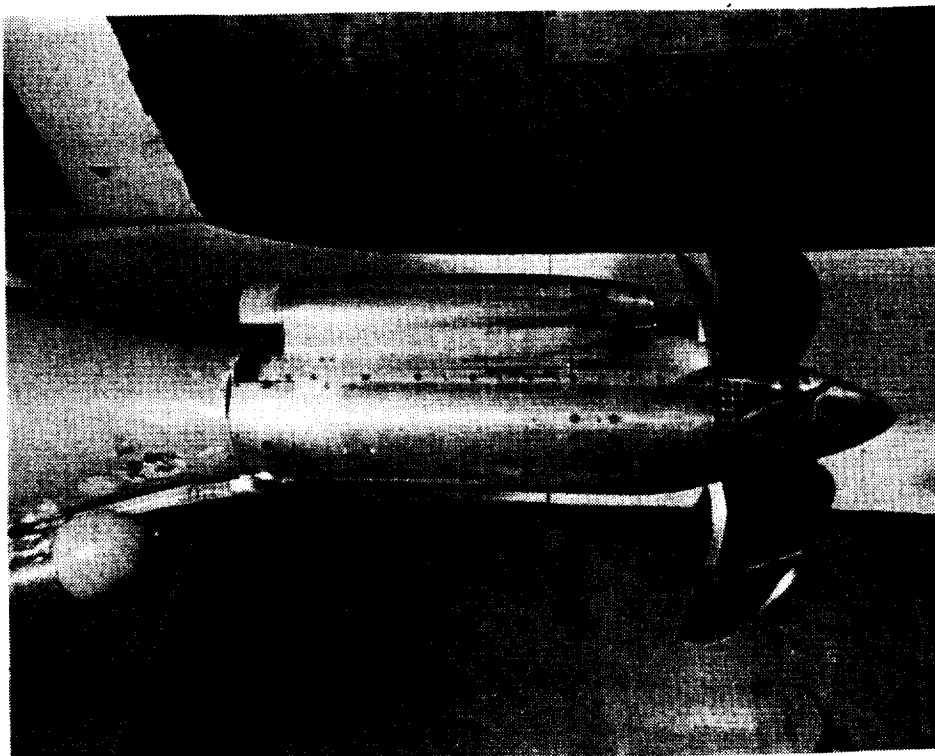


(e) Twin-scoop inlet without diverter ;  
GUN III installation.

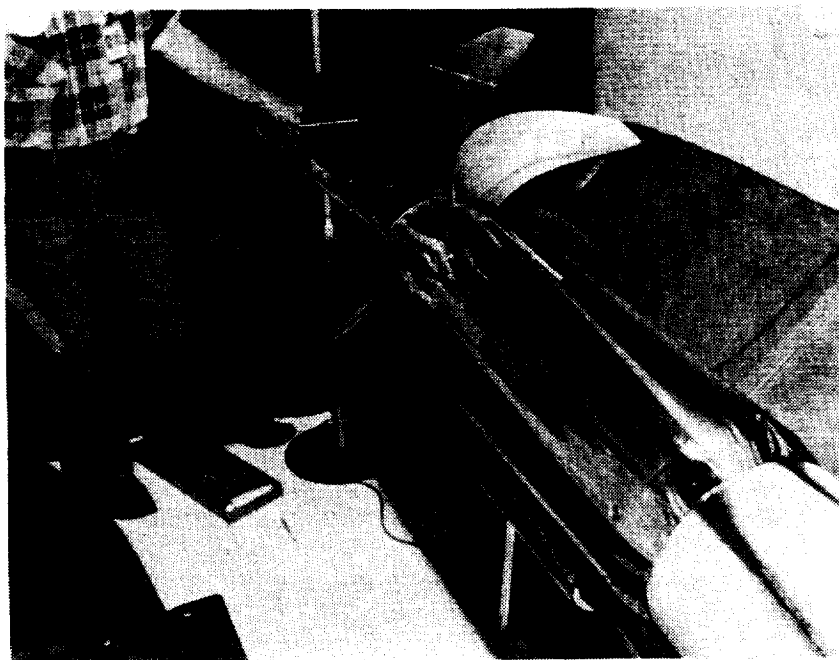


(f) Annular inlet, viewed from above ;  
GUN-III installation.

Figure 7. - Continued

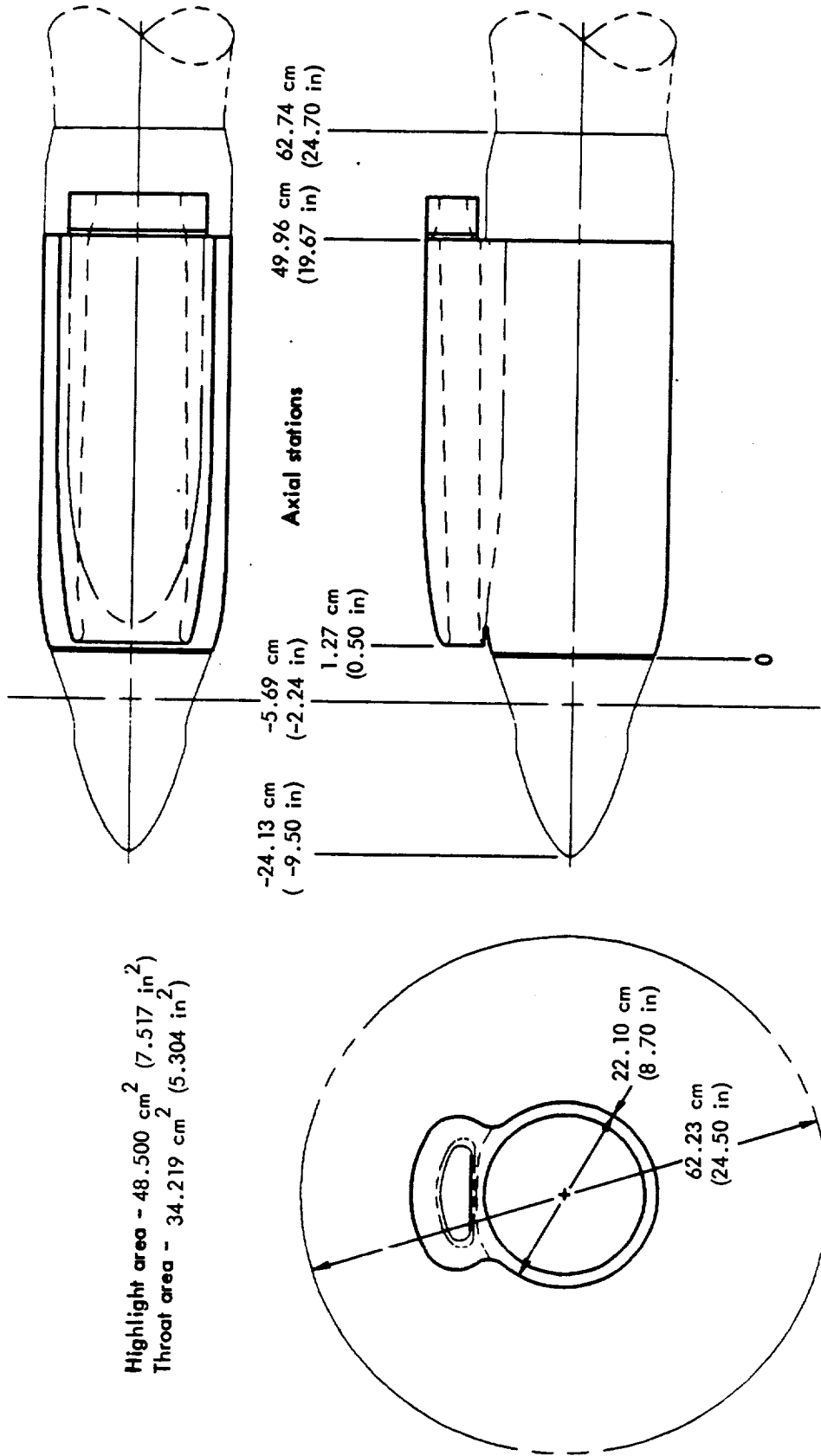


(g) Single-scoop inlet with diverter, in aft position ;  
GUN III installation.



(h) Nacelle without inlet, with Kiel probe rake ;  
GUN III installation.

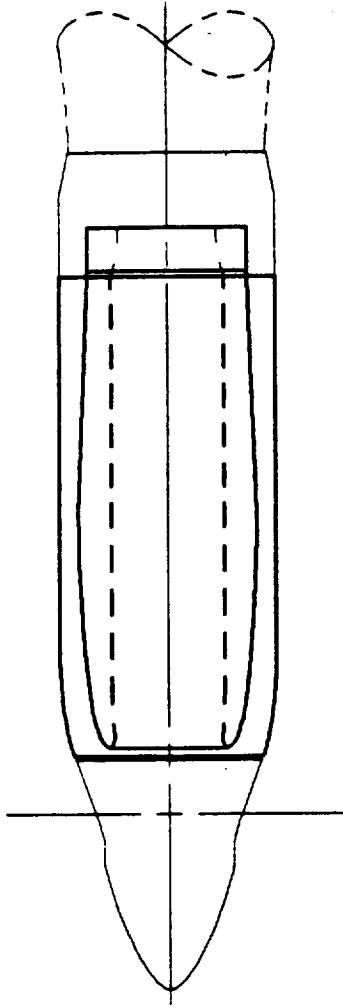
Figure 7. - Concluded



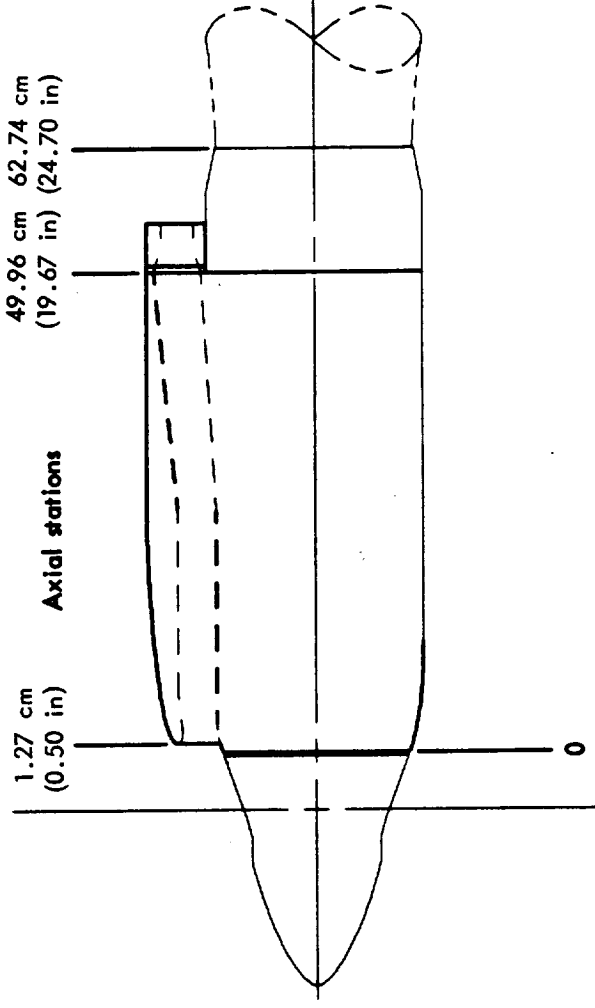
- Notes:
1. Propeller and spinner dimensions apply to all models.
  2. Components in heavy lines are metric on cowl drag balance.

(a) Single-scoop inlet with diverter; in most forward position GUN-II installation.

Figure 8. - Major dimensions of models illustrated by sketches



Highlight area -  $46.690 \text{ cm}^2$  ( $7.237 \text{ in}^2$ )  
 Throat area -  $34.161 \text{ cm}^2$  ( $5.295 \text{ in}^2$ )



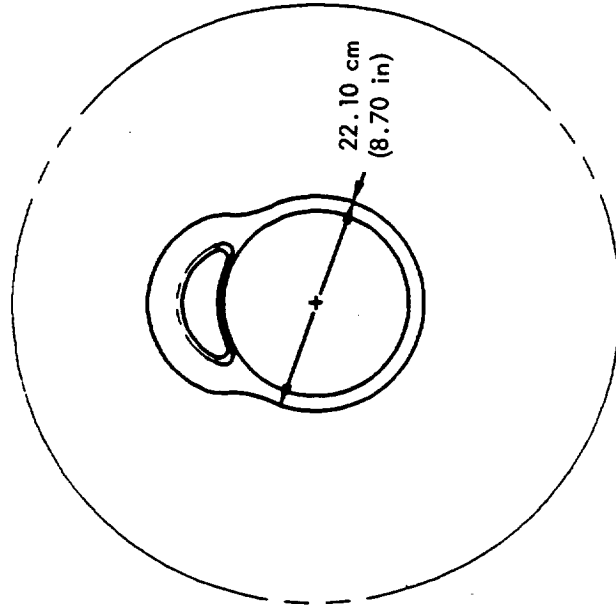
1.27 cm  
(0.50 in)

Axial stations

49.96 cm  
(19.67 in)

62.74 cm  
(24.70 in)

0

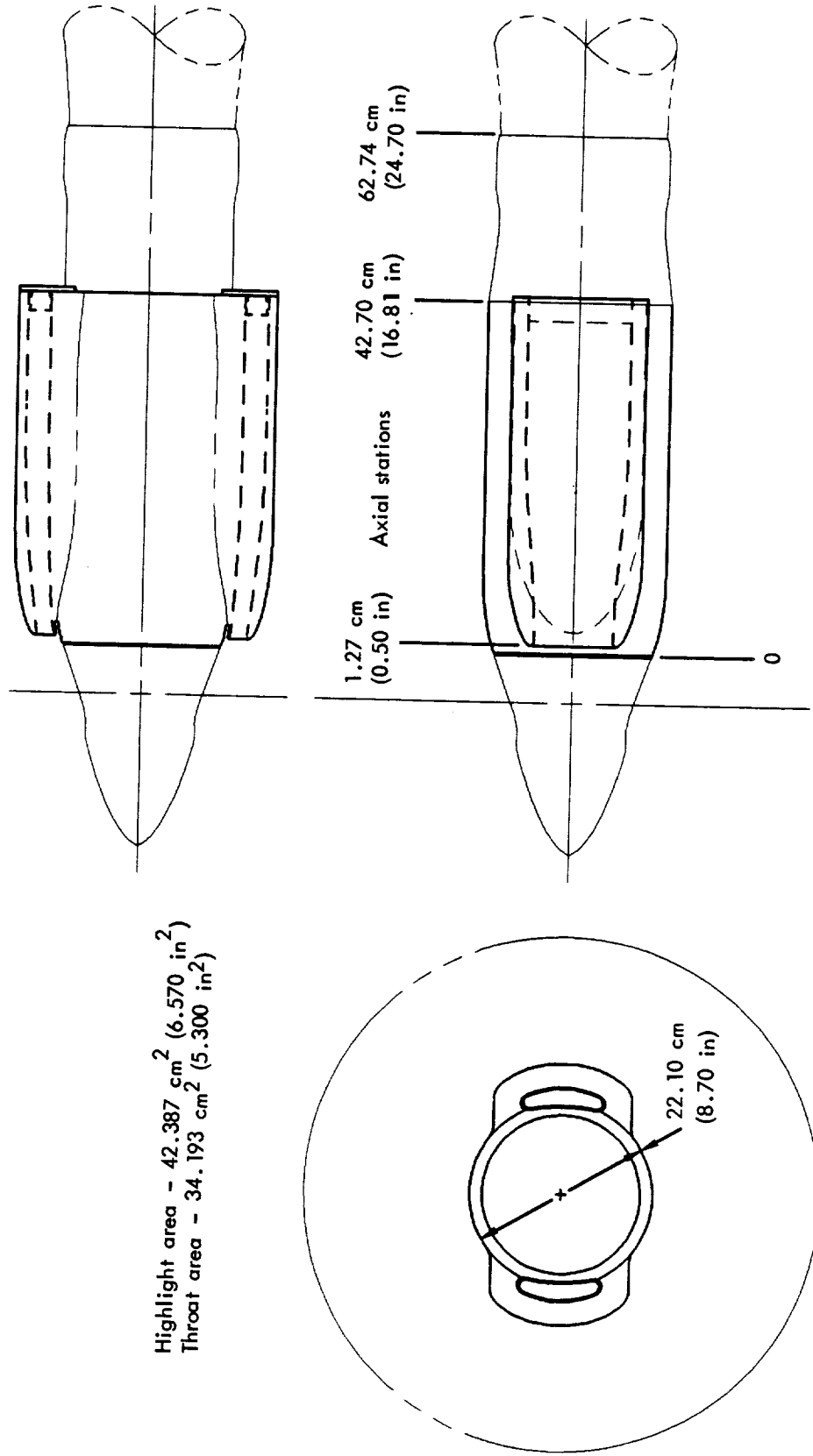


22.10 cm  
(8.70 in)

(b) Single-scoop Inlet without diverter; GUN-II installation.

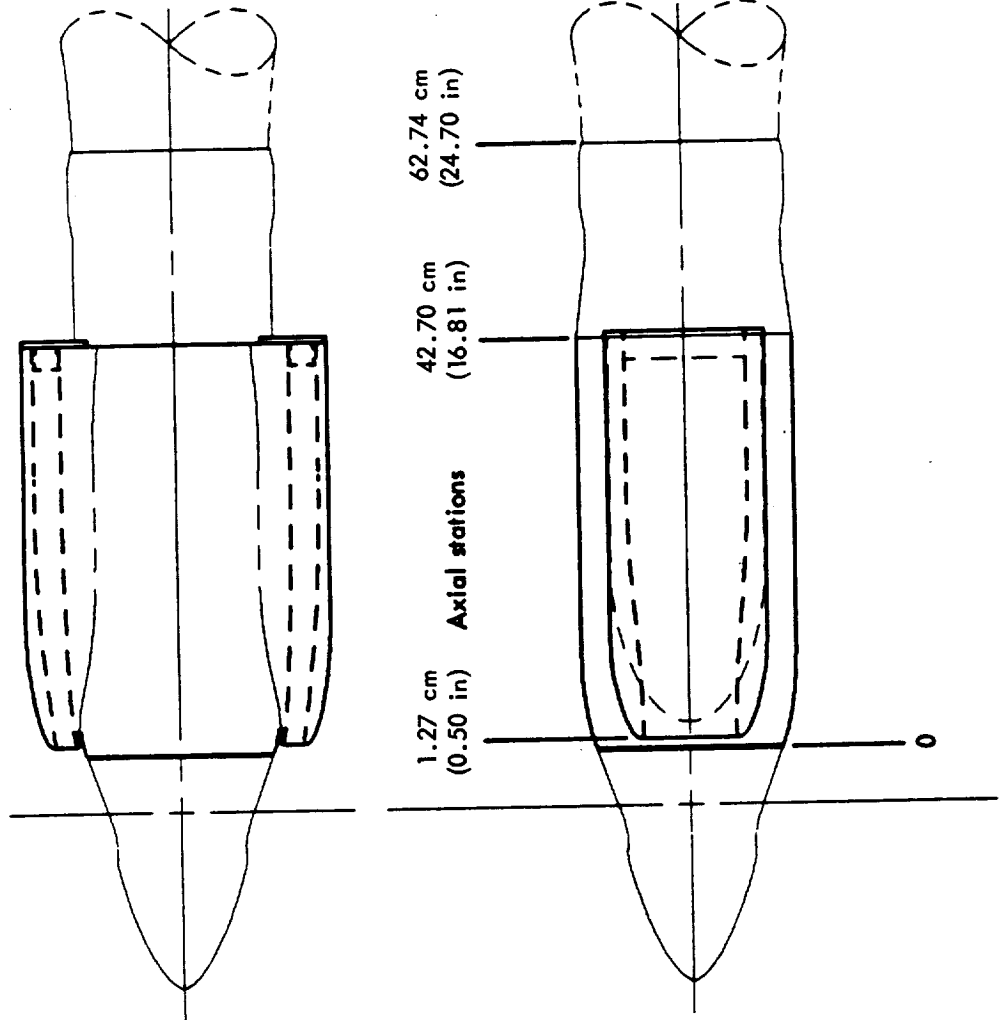
Figure 8. - Continued

Highlight area - 42.387 cm<sup>2</sup> (6.570 in<sup>2</sup>)  
 Throat area - 34.193 cm<sup>2</sup> (5.300 in<sup>2</sup>)

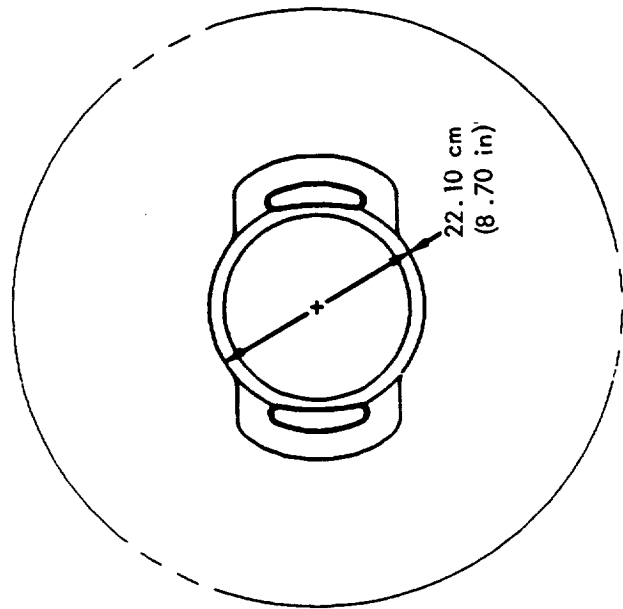


(c) Twin-scoop inlet with diverter ; GUN-II installation.

Figure 8. - Continued

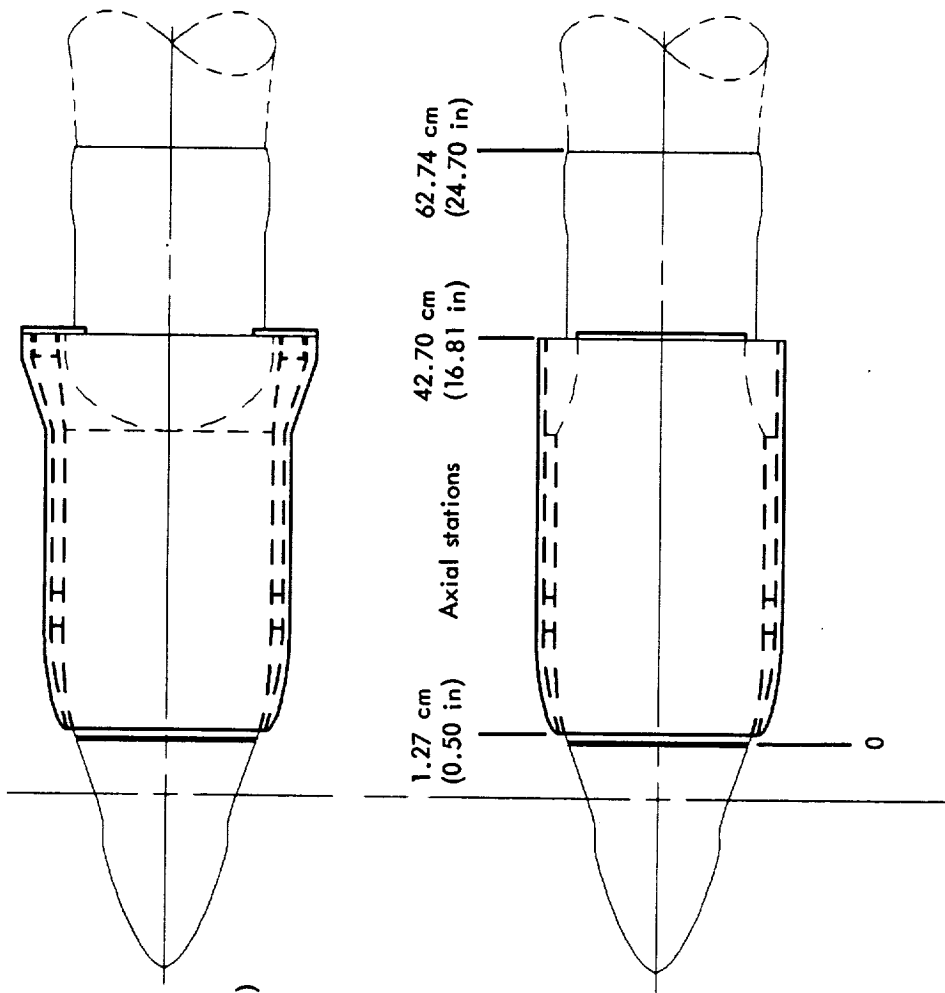


Highlight area - 42.542 cm<sup>2</sup> (6.594 in<sup>2</sup>)  
 Throat area - 34.193 cm<sup>2</sup> (5.300 in<sup>2</sup>)

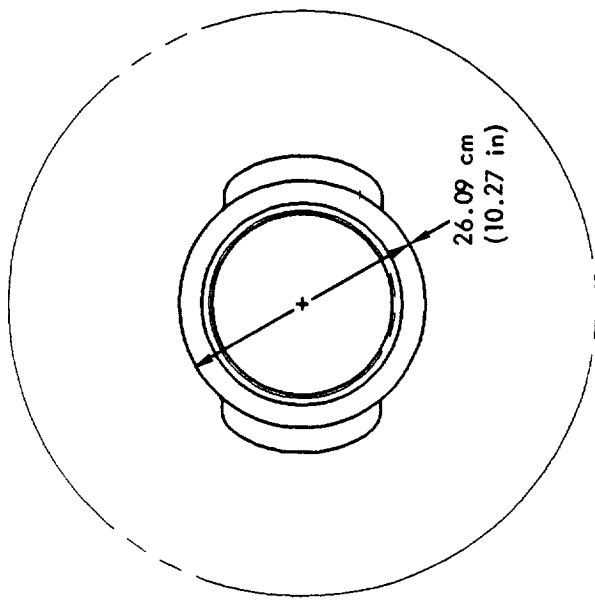


(d) Twin-scoop inlet without diverter; GUN III installation.

Figure 8. - Continued



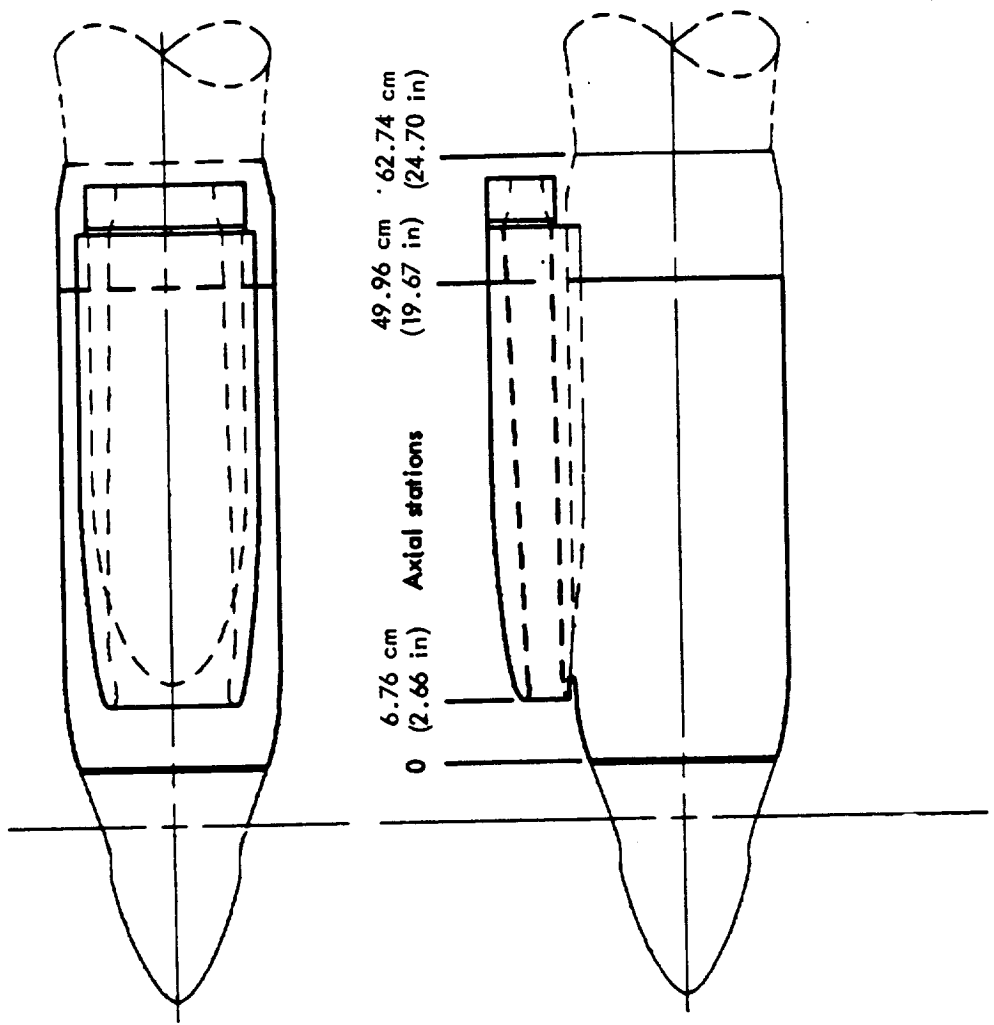
Highlight area -  $43.148 \text{ cm}^2$  ( $6.688 \text{ in}^2$ )  
 Throat area -  $37.426 \text{ cm}^2$  ( $5.801 \text{ in}^2$ )



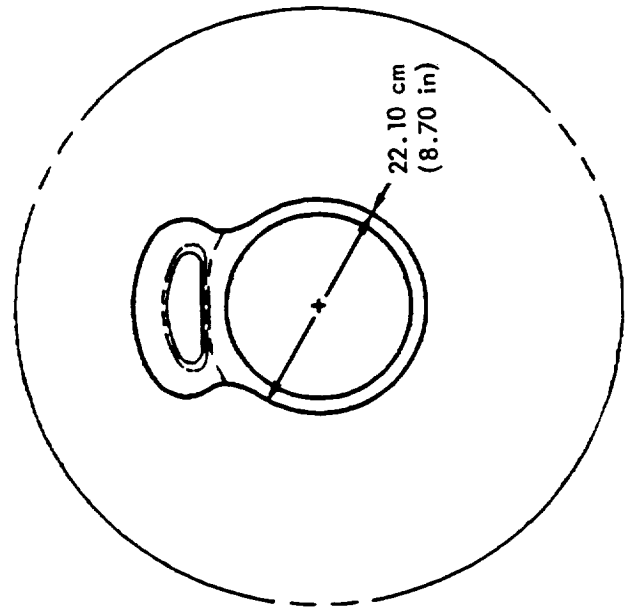
(e) Annular inlet ; GUN III installation.

Figure 8. - Continued



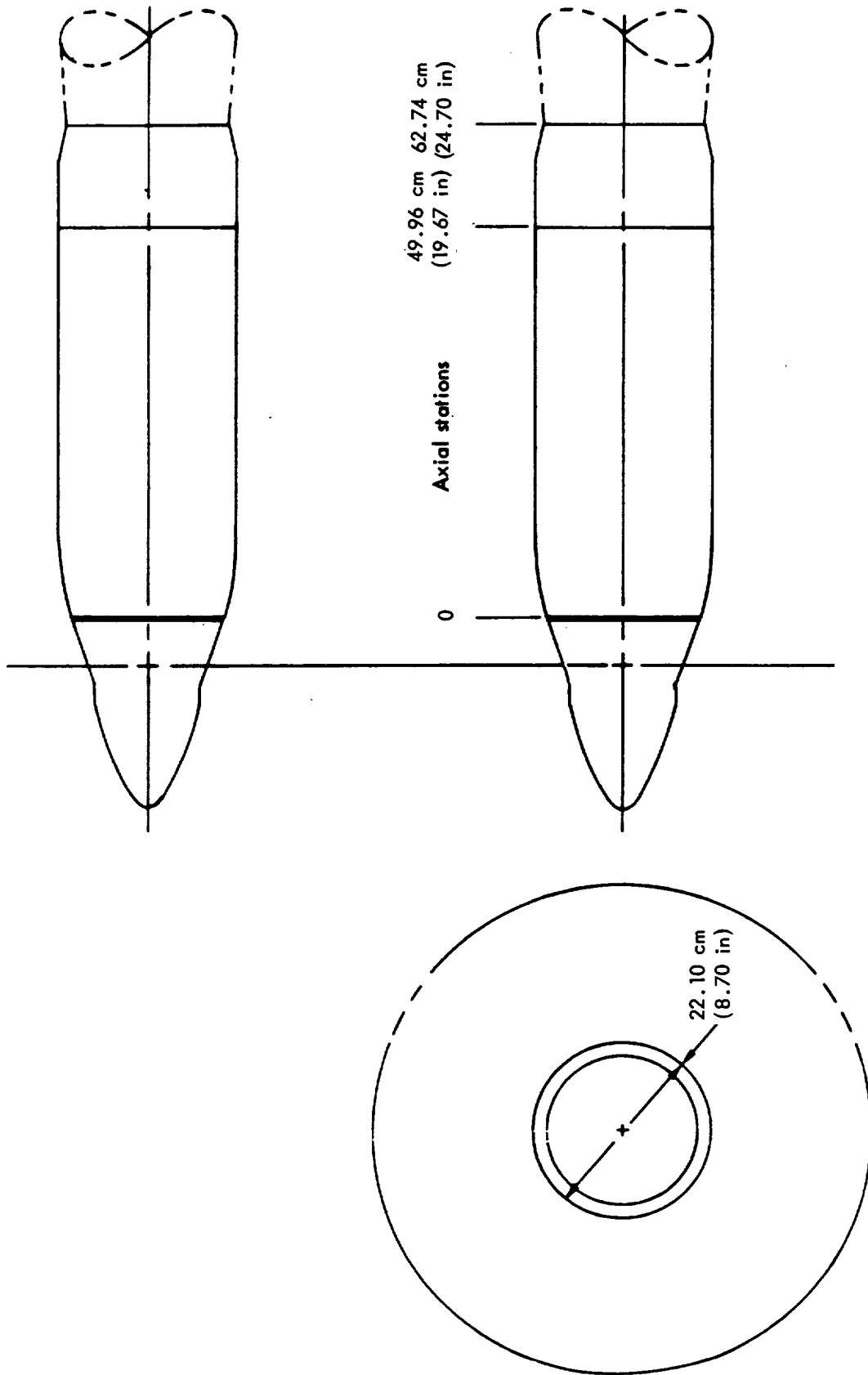


Highlight area - 48.500 cm<sup>2</sup> (7.517 in<sup>2</sup>)  
 Throat area - 34.219 cm<sup>2</sup> (5.304 in<sup>2</sup>)



(f) Single-scoop inlet with diverter, in aft position; GUN III installation.

Figure 8. - Continued



(g) Nacelle without inlet; GUN III installation.

Figure 8. - Concluded

channel region on the leeward side relative to propeller rotation. Using an insert fabricated prior to the start of testing, the diverter was broadened in the plan view and the contour was reblended with filler. The modified diverter was then used throughout the remaining GUN-I tests. When the 1.3 percent inlet was rebuilt to add the cowl drag balance in the GUN-II and GUN-III tests, provision was made to change the height of the boundary layer diverter. The 1.6 and 0.6 percent inlets were the result. The basic axial location of all inlet highlights was immediately behind the spinner. The 1.3 percent inlet was also tested, however, with an insert that moved it aft by 9 percent of the propeller diameter.

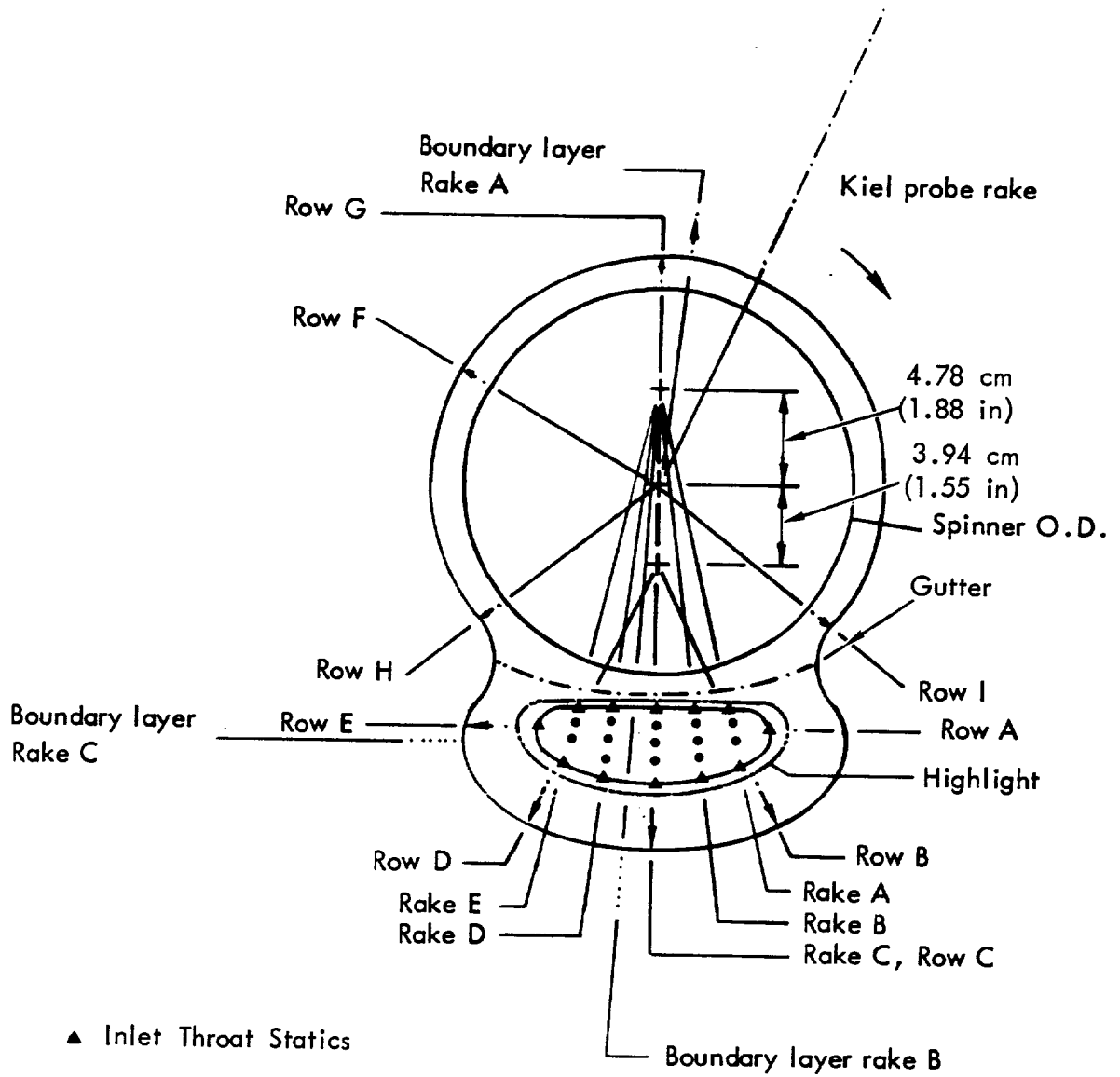
Only two variations of the twin-scoop inlet were tested: one with and the other without the use of a boundary layer diverter. For the diverter configuration, a nominal height ratio of 1.0 percent ( $h/D_p = 0.010$ ) was employed.

In addition to the modifications described above, tests were also made of the effects of sealing the blade-root/spinner gaps since the gaps were much too large when scaled to a full configuration. For the tests that were run with the propeller off, the holes for accommodating the blade roots were faired over with tape.

#### **Instrumentation**

The models incorporated extensive, steady-state, static and total pressure instrumentation. These are pictorially identified in Figure 9, (a) through (f). The coordinates of the pressure measurement points are individually listed in Tables A7 and A8 (Appendix A). Special total and static pressure instrumentation for analysis of the boundary layer diverter are described in Figure 10. In addition to the steady-state, total pressure instrumentation in the inlet throat, three high-frequency response Kulites were utilized for the GUN-I testing.

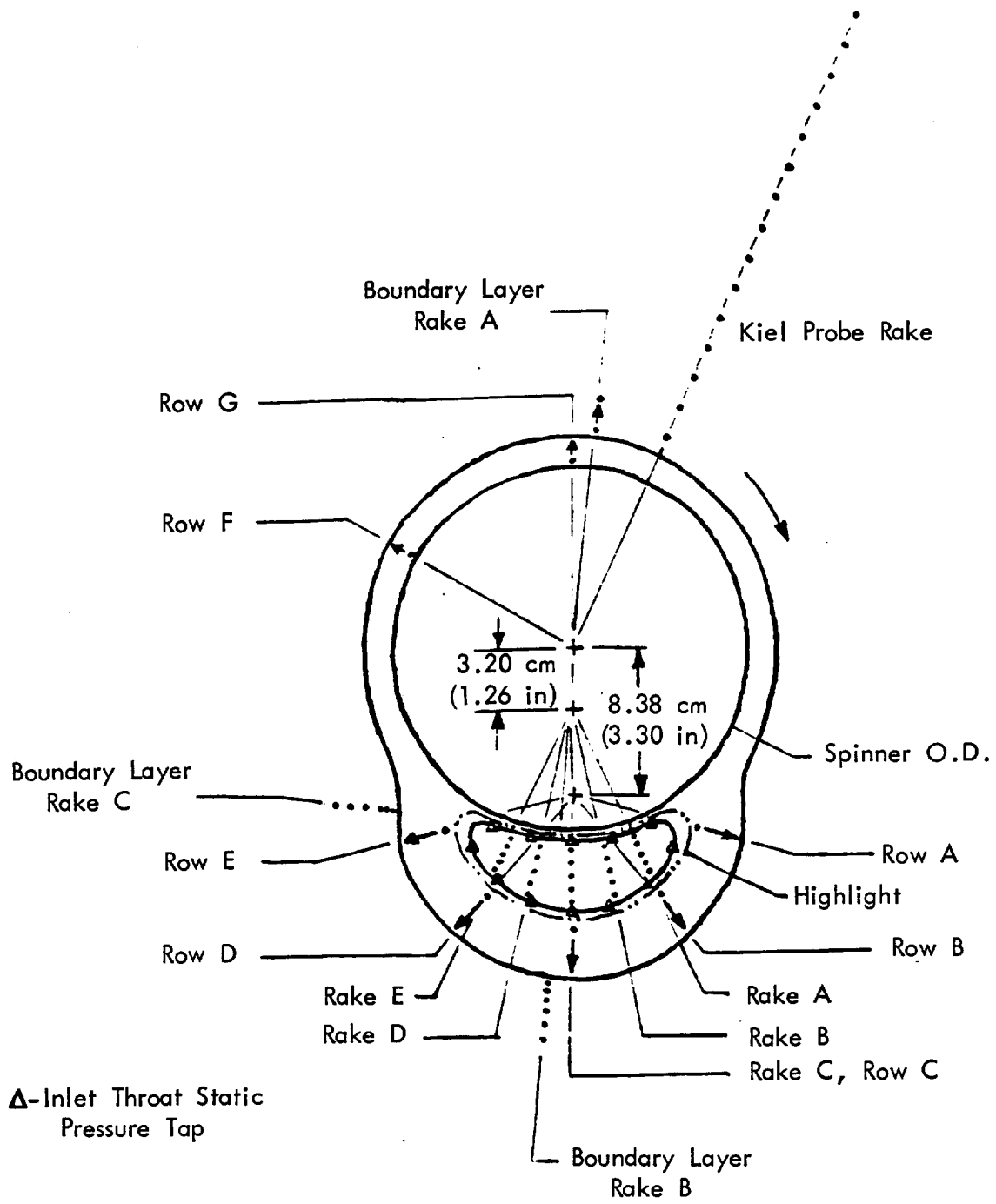
Propeller RPM were acquired from the facility PTR instrumentation. Torque and thrust were obtained from two load cells located behind the aft drive motor, as previously illustrated in Figure 6(a). Both motors, their associated drive train, and the entire nacelle front end/cowling are metric, as indicated in the figure. Additionally, the cowling, which consists of the forward nacelle, aft of the spinner, and inlet fairing, is metric on a special balance, mentioned earlier. Details of the special balance arrangement are provided in Figure 6(b), which is Section A-A from Figure 6(a). Internal cavity pressure is measured to supply the required tare correction. Use of the cowl drag balance provided the means whereby cowl drag and, eventually, spinner drag could be separated out from total front-end thrust-minus-drag.



- Notes: 1. View is shown looking aft  
 2. Arrow shows direction of propeller rotation.

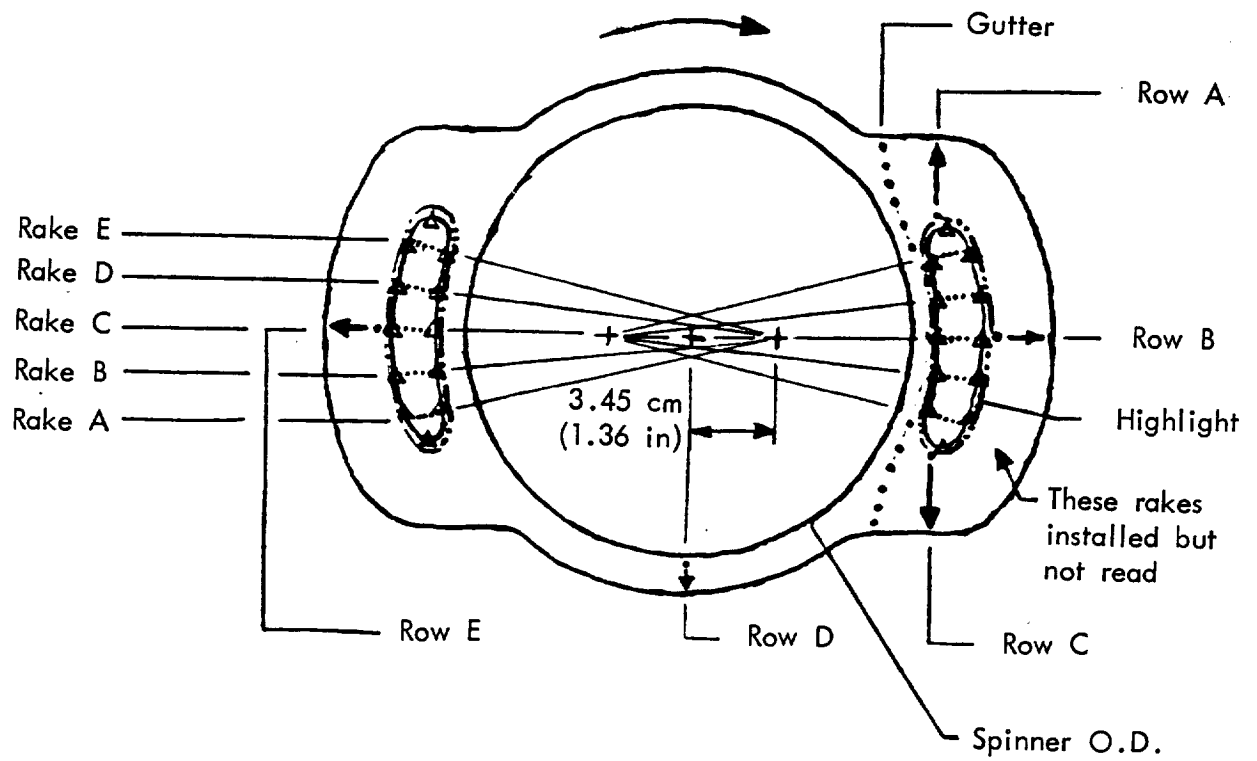
(a) Single-scoop inlet with diverter; GUN-I installation.

Figure 9. - Pressure probe angular locations



(b) Single-scoop inlet without diverter; GUN-1 installation.

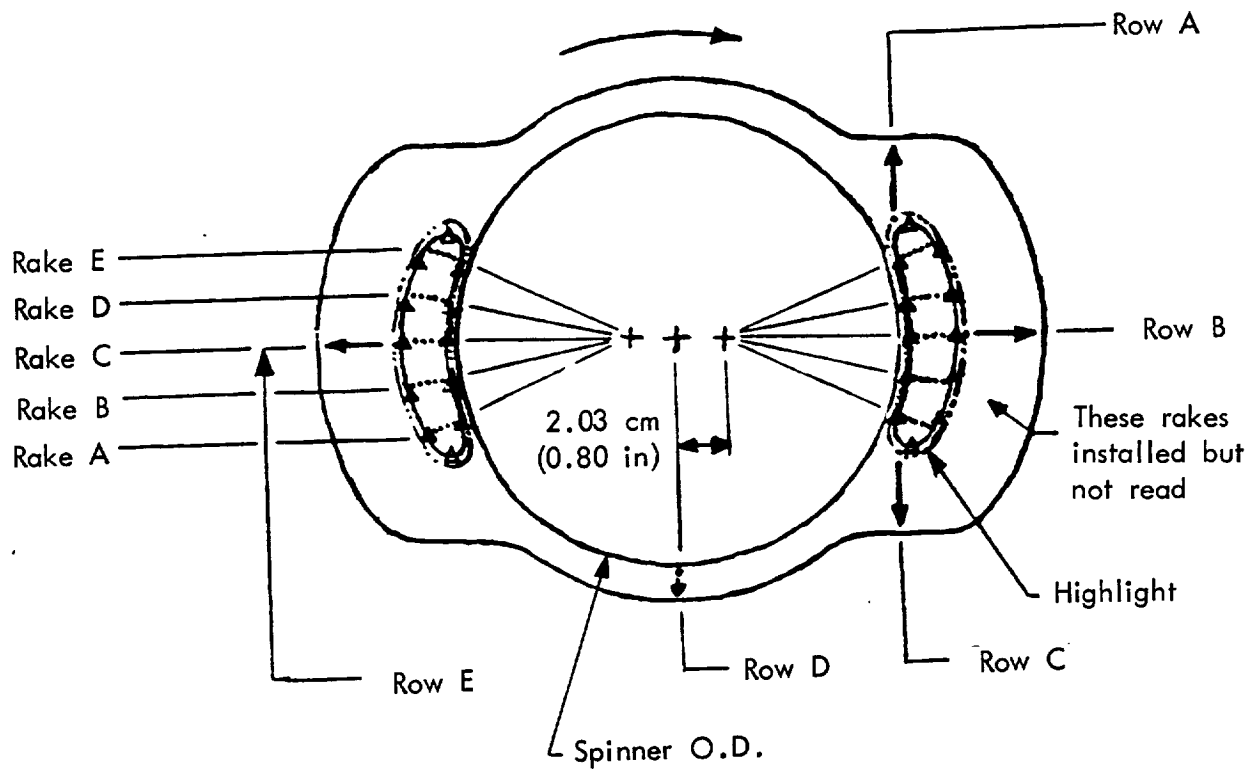
Figure 9. - Continued



△ Inlet throat static pressure tap

(c) Twin-scoop inlet with diverter; GUN III installation.

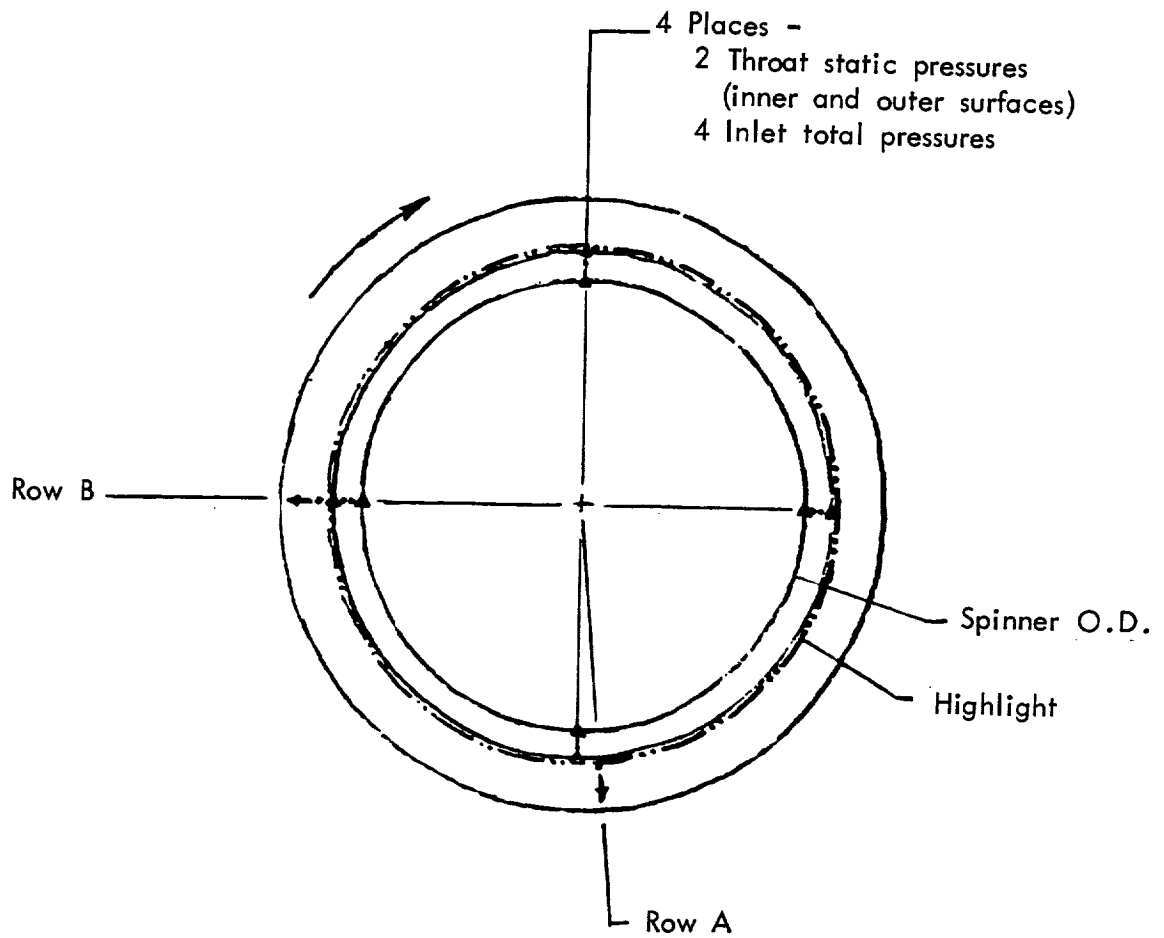
Figure 9. - Continued



△ Inlet throat static pressure tap

(d) Twin-scoop inlet without diverter; GUN-III installation.

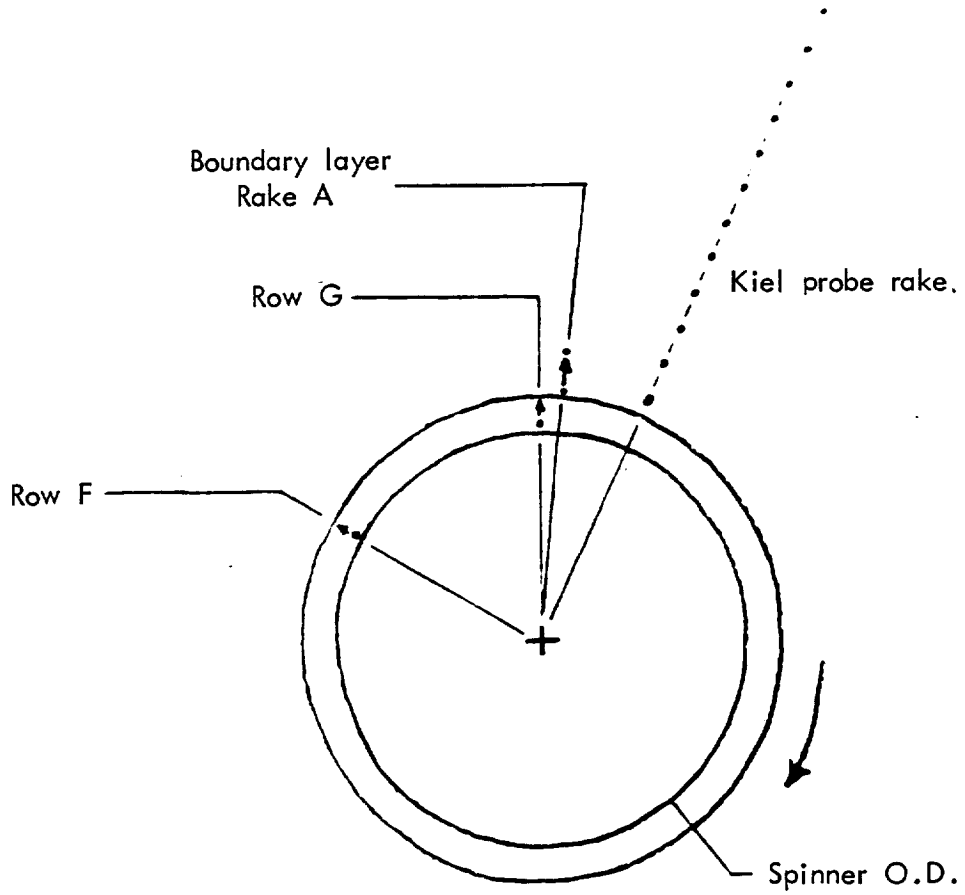
Figure 9. - Continued



(e) Annular inlet, GUN III installation.

Figure 9. - Continued





(f) Nacelle without inlet, GUN-III installation.

Figure 9. - Concluded



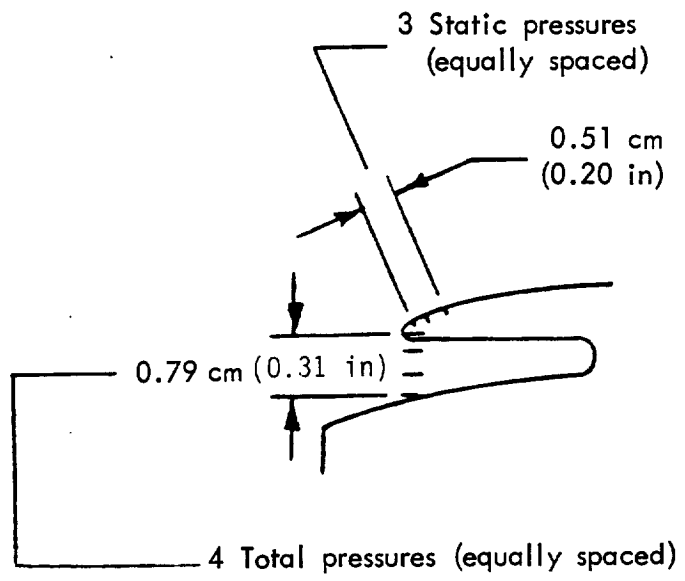


Figure 10. - Pressure probe locations, diverter for single-scoop inlet.

~~PRECEDING PAGE BLANK NOT FILMED~~

## **TEST FACILITY**

### **Wind Tunnel**

The test program was conducted in the United Technologies Research Center (UTRC) Large Subsonic Wind Tunnel, shown in Figure 11. The tunnel is a single-return, closed-throat facility with interchangeable 2.44-meter (8.0-ft.) and 5.49-meter (18.0-ft.) octagonal test sections. The main drive system is a 6714-kilowatt (9000-hp.), synchronous motor with a variable-speed coupling driving a 7.93-meter (26-ft.)-diameter, 20-blade fan. The 2.438-meter (8.0-ft.) test section, used in the GUN tests, is inserted in the 5.49-meter (18.0-ft.) section and provides speeds up to 0.90 Mach number. The tunnel operates with the stagnation pressure at atmospheric, and the stagnation temperature is held within 16 to 60 (60 to 140) degrees Celsius (F.) by air-exchange valves.

Mounted under the test section is the aspiration system, which can be used to withdraw a controllable and measured airflow from the model to simulate engine inlet airflow. A large electromechanical, six-component balance is also located there. It was locked out for the GUN tests.

### **Propeller Test Rig**

The propeller test rig (PTR), as shown in Figure 6(a), consists of two variable-speed motors in tandem in a streamlined-case, steel pod and pylon. Each motor is rated at 280 kilowatts (375 hp.) at 12,000 RPM. Together they provide a maximum torque of 448 newton-meters (330 ft-lbs.) over the entire speed range. The stators for the motors are supported on hydrostatic bearings that allow free axial and rotational movement. Pressures in the pod and on its external surfaces are measured and used to correct the axial thrust reading for unbalanced pressures on test-rig components.





## TEST DESCRIPTION -- CONFIGURATIONS, PROCEDURES, AND RUN SUMMARY

Three basic types of configurations were tested in the GUN Program. These were the single-scoop, twin-scoop, and annular inlet configurations. The single-scoop and twin-scoop inlets were tested both with and without boundary layer diverters; the single scoop was tested with a range of diverter heights varying from 0.6 to 1.6 percent of propeller diameter. Axial position was also varied for the single-scoop inlet and runs were performed with the entry plane at 11 percent and 20 percent of propeller diameter aft of the prop plane. General descriptions of the configurations tested and types of data obtained are provided in Figure 12. Dates for the three phases of the GUN tests are also included.

In the first test (GUN-I), a bare tunnel reference run was made followed by two bare nacelle runs, one without a propeller and the second with a propeller in place. For most of the program, the basic type of data obtained was inlet throat and external cowl surface pressures. Early in the test, however, some limited propeller blade stress testing was performed to define the potential severity of stress level increments imposed by interaction with the inlet. In addition to the standard cruise test cases, some testing with the prop blades in the reverse thrust pitch position was performed to evaluate the effects on recovery and distortion levels. Additional, special tests in GUN-I included flow visualization, both on cowl and blade surfaces, and runs with the prop blades feathered.

In GUN-II and GUN-III, the same kinds of reference runs were made, but not necessarily at the beginning of the tests. This time, both pressure data and cowl drag force data were taken. A special test performed in GUN-II was to compare performance with and without the prop-to-spinner gaps sealed. Most of the testing in GUN-II involved variation of the boundary layer diverter height. GUN-III involved both an expansion of the kinds of models tested and the types of data recorded. A twin-scoop and annular inlet were added to the basic single-scoop configuration. In addition, the effect of inlet axial position was investigated. Blade-stress, pressure, and force data were taken for the configurations covered in this phase of the testing.

A more detailed summary of the three-phase GUN Test Program is provided in Table I. Here the run numbers, configuration descriptions, and objectives are outlined for each of the geometric combinations tested. All runs, including those made for reference only, are included. In cases where the mass flow ratios were varied, the values of the nominal settings are presented. Propeller blade angle  $\beta$  is specified at the 75 percent radius. Also included in GUN-I are a number of runs with different propellers that were made for internal usage by Hamilton Standard. These were all performed with a bare nacelle.

Model	Variations	Data obtained			
		Pressure		Drag	Blade stress
		Int	Ext		
10011		G-1	G-1	G-2	G-1, G-3
11011		G-1	G-1	G-2	
11011 <sub>1</sub>	Modified bld contour	G-1	G-1		
11011 <sub>2</sub>	Bld height = 0.15"	G-2		G-2	
11011 <sub>3</sub>	Bld height = 0.31"	G-2		G-2	
11011 <sub>4</sub>	Bld height = 0.38"	G-2		G-2	
11020		G-3	G-3	G-3	G-3
11040					
20011		G-3	G-3	G-3	
21011	Bld height = 0.25"	G-3	G-3	G-3	G-3
90011		G-3	G-3	G-3	

G-1 November - December, 1982  
G-2 March - April, 1983  
G-3 November, 1983 - January, 1984

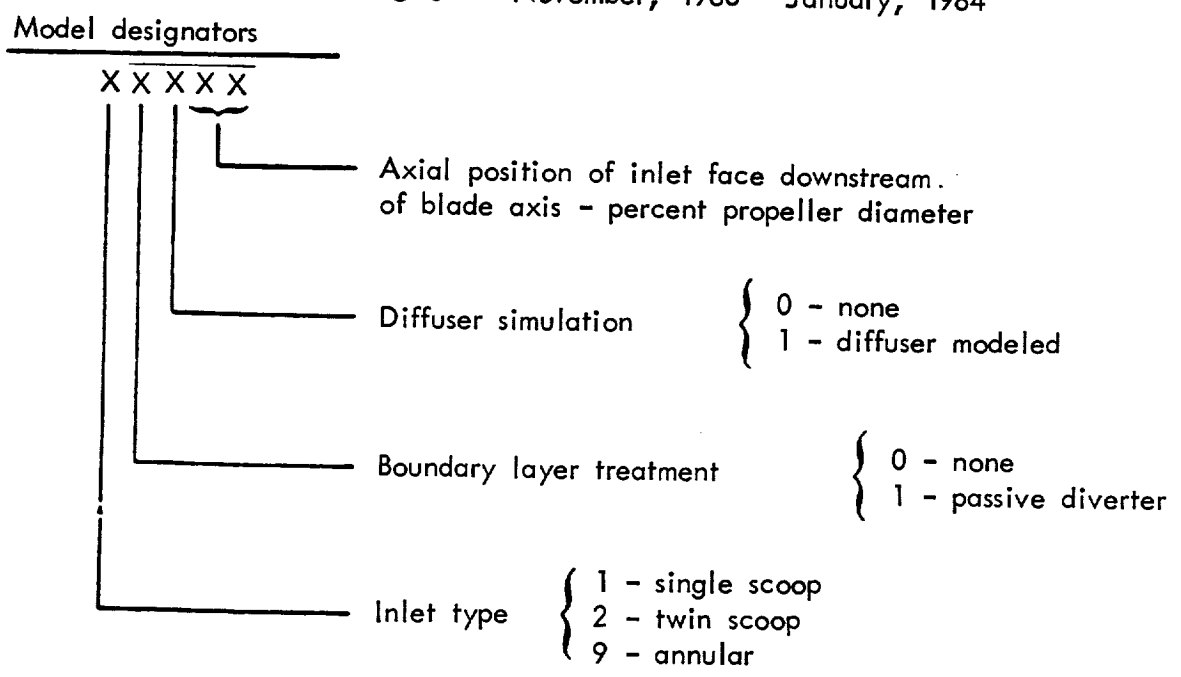


Figure 12. - Test configuration/data summary



TABLE I. - RUN PROGRAM SUMMARY

Gelac/UTRC/NASA cooperative test program

GUN-1 - Single scoop inlets mounted on turboprop nacelle, pressure data + limited blade stresses (most runs in 0.70 to 0.80 Mach range, some low Machs)

Run nos.	Configuration	Objectives
1-7	Bare tunnel, no PTR	Reference data
8-15	Bare nacelle, no prop	Reference data
16-22	Bare nacelle, SR-3 prop	Blade stresses
23-30	Nacelle with inlet plus orig. gutter, SR-3	Blase stresses
31-32	Nacelle with inlet plus orig. gutter, no prop	Thrust tares
33-58	Nacelle with inlet plus orig. gutter, SR-3	Pressures & thrust
60-64	Nacelle with inlet plus new gutter, SR-3 prop	Pressures & thrust
66-79	Nacelle with inlet and no gutter, SR-3 prop	Pressures & thrust
80-84	Nacelle with inlet and no gutter and no prop	Thrust tares
85	Nacelle with inlet and no gutter, SR-3 prop	Flow visualization
86-87	Bare nacelle with no prop	Thrust tares
89-145	Bare nacelle with SR-3	Pressure data
146-147	Bare nacelle with no prop	Pressure data
148-172	Bare nacelle with SR-1M	Pressure data
173-181	Bare nacelle with SR-3	Pressure data
182-198	Bare nacelle with SR-2	Pressure data

TABLE I. - CONTINUED.

199	Bare nacelle with SR-3	Pressure data
200	Bare nacelle with SR-1M	Pressure data
201	Bare nacelle, no prop	Pressure data
202-219	Bare nacelle with SR-2	Pressure data
221-227	Bare nacelle with SR-3, 4 blades	Pressure data
228-232	Bare nacelle with SR-3, 4 blades	No PTR - bare tunnel

GUN-2 - Single scoop inlets with various boundary layer diverter heights, pressure data + forebody drag (most runs in 0.70 to 0.80 mach range, some low machs)

Run nos.	Configuration	Objectives
1-7	Bare nacelle, propeller pitch beta = 55-58 deg	Reference data
8-51	Nacelle with inlet + BLD H=0.384", AN=40, 60, & 80%, beta = 55-58 deg	Pressure + drag data
52-79	Nacelle with flush inlet H=0.000", AN=60, 80, & 100%, beta = 55-58 deg	Pressure + drag data
80-106	Nacelle with inlet + BLD H=0.159", AN=40, 60, & 80%, beta = 55-58 deg	Pressure + drag data
107-110	Nacelle with inlet + BLD H=0.159", AN=40, 60 & 80%, no prop blades	Pressure + drag data
111-114	Nacelle with inlet + BLD H=0.384", AN=40, 60, & 80%, no prop blades	Pressure + drag data
115	Bare nacelle and no propeller blades	Pressure + drag data, reference

TABLE I. - CONTINUED.

116-120	Nacelle with flush inlet H=0.000", AN=40, 60 & 80%, no prop blades	Pressure + drag data
121-129	Nacelle with flush inlet H=0.000", AN=40% beta = 55-58 degrees	Pressure + drag data
130-135	Bare nacelle with prop blades, beta = 55-58 deg	Pressure + drag data, reference
136-155	Nacelle with inlet + BLD H=0.309", AN=40, & 80%, beta = 55-58 degrees	Pressure + drag data
156-157	Nacelle with inlet + BLD H=0.309", AN=40 & 80%, no propeller blades	Pressure + drag data
138-163	Nacelle with inlet + BLD H=0.309", AN=40% beta = 57 deg, bl rake	Pressure + drag data

GUN-3 - Single, twin scoop and annular inlets with provision for pressure, force, and blade stress data (most runs in 0.70 to 0.80 mach range, some low machs)

Run nos.	Configuration	Objectives
1-4	Empty tunnel, no PTR	Mach no. calcs.
5-18	Nacelle with SS + BLD, H=0.350", AN=60 & 80%, prop beta = 58-59 deg	Blade stress data
19-24	Bare nacelle, propeller pitch beta = 58-59 deg	Reference blade stress data
25-37	Nacelle with SS + BLD, inlet in aft position, H=0.350", AN=60 & 80%, prop beta = 58-59 deg	Blade stress data
38-45	Nacelle with TS + BLD inlet aspirated, prop beta = 58-59 deg	Blade stress data

TABLE I. - CONTINUED.

46-56	Nacelle with TS + BLD, range of mass flows	Static calibr. of nozzles
57-62	Nacelle with TS, with & without BL diverter, range of mass flows	Static calibr. of nozzles
63-81	Nacelle with TS + BLD, inlet aspirated, prop beta = 58-59 deg	Cowl surface pressure data
82-99	Nacelle with flush TS, inlet aspirated, prop beta = 58-59 deg	Cowl surface pressure data
100-102	Nacelle with flush TS, inlet aspirated, no propeller blades	Cowl surface pressure data
103-123	Nacelle with annular inlet (AI), aspirated, prop beta = 58-59 deg	Cowl surface pressure data
124-128	Nacelle with annular inlet, various flows	Static calibr. of nozzles
129	Bare nacelle, no blades	Prop hub tares
130-145	Nacelle with SS + BLD, inlet in aft position, H=0.350", AN=60 & 80%, prop beta = 55-59 deg	Inlet total pressure data
146-157	Nacelle with SS + BLD, H=0.350", AN=60 & 80%, prop beta = 55-59 deg	Inlet total pressure data
158-171	Nacelle with flush TS, AN = 50 & 75%, prop beta = 55-59 deg	Inlet total pressure data
172-188	Nacelle with TS and BLD, AN = 50 & 75%, prop beta = 55-59 deg	Inlet drag data

TABLE I. - CONCLUDED

189-203	Nacelle with annular inlet, AN=50 & 75%, prop beta = 55-59 deg	Inlet drag data
204-205	Nacelle with annular inlet, AN=50 & 75%, no propeller blades	Inlet drag data
206	Nacelle with annular inlet, AN=50 & 75%, no blades, gaps filled	Inlet drag data
207-213	Bare nacelle, propeller pitch beta = 55-59 deg	Inlet drag data
214	Bare nacelle, no blades	Inlet drag data
215-223	Nacelle with annular inlet, AN=50 & 75%, prop beta = 58-59 deg	Propeller blade stress data



## TEST RESULTS AND DISCUSSION

The number of parameter combinations associated with combined propfan / inlet testing is very large and, hence, not all the potential variations can be covered in detail. Therefore, except where noted, the data in this report are limited to specific combinations of propeller CP, J, and inlet airflow that have been selected to match the anticipated cruise range. Estimated requirements have been based on assuming the use of the Pratt and Whitney study engine, STS-589-4 (Reference 9).

### Inlet Total Pressure Recovery

For this evaluation, the inlet throat was instrumented with a set of five total pressure rakes containing five probes per rake, as described in the instrumentation section. The objective was to obtain the effects of propeller supercharging, induced swirl, slipstream distortion, and spinner boundary layer ingestion.

Effect of Peripheral Extent - Both the total pressure recovery and its variation with mass flow ratio were found to depend heavily upon the inlet design selection for turboprop installations. Generally speaking, as inlet peripheral extent (aspect ratio) diminished, total pressure recovery increased. This result had been predicted by analytical studies described in Reference 3. Figure 13 illustrates the comparison between the predicted effect of peripheral extent and the actual measured effect on total pressure recovery. For the plot shown, mass flow ratio ( $A_0/A_{h1}$ ) was held constant at the design cruise value of 0.60. The upper curve shows how the use of a full boundary layer diverter provides a discrete level of improvement, regardless of inlet aspect ratio.

There are a number of reasons why reducing inlet aspect ratio (peripheral extent) improves recovery so dramatically. First, the 360 degree annular inlet ingests all of the minimum pressure portion of the spinner-ramp boundary layer. Even if there were no spinner surface friction, however, the inner-most layer of the slipstream would be relatively low in energy, because of the design of the propeller root section to avoid choking. So as peripheral extent is reduced, the average height of the inlet is increased and the average total pressure of the captured slipstream improves significantly. As peripheral extent is reduced to a level approaching that of the twin-scoop inlet, another effect begins to assert itself. Here the reflected blockage of the inlet itself begins to locally shift the propeller operating line. This results in the measured recovery crossing over the predicted characteristic and increasing at a faster rate than anticipated (Figure 13). At the peripheral extent of the single-scoop inlet, the test recovery exceeds the predicted value by a substantial margin. The relatively large recovery improvement shown by the boundary layer diverter inlets (Figure 13) results from (1) the elimination of boundary layer ingestion, (2) the further shift of the inlet radially outward into the higher pressure region of the slipstream, and (3) the increased blockage due to the larger frontal area of the diverter inlet which creates a higher pressure flowfield.

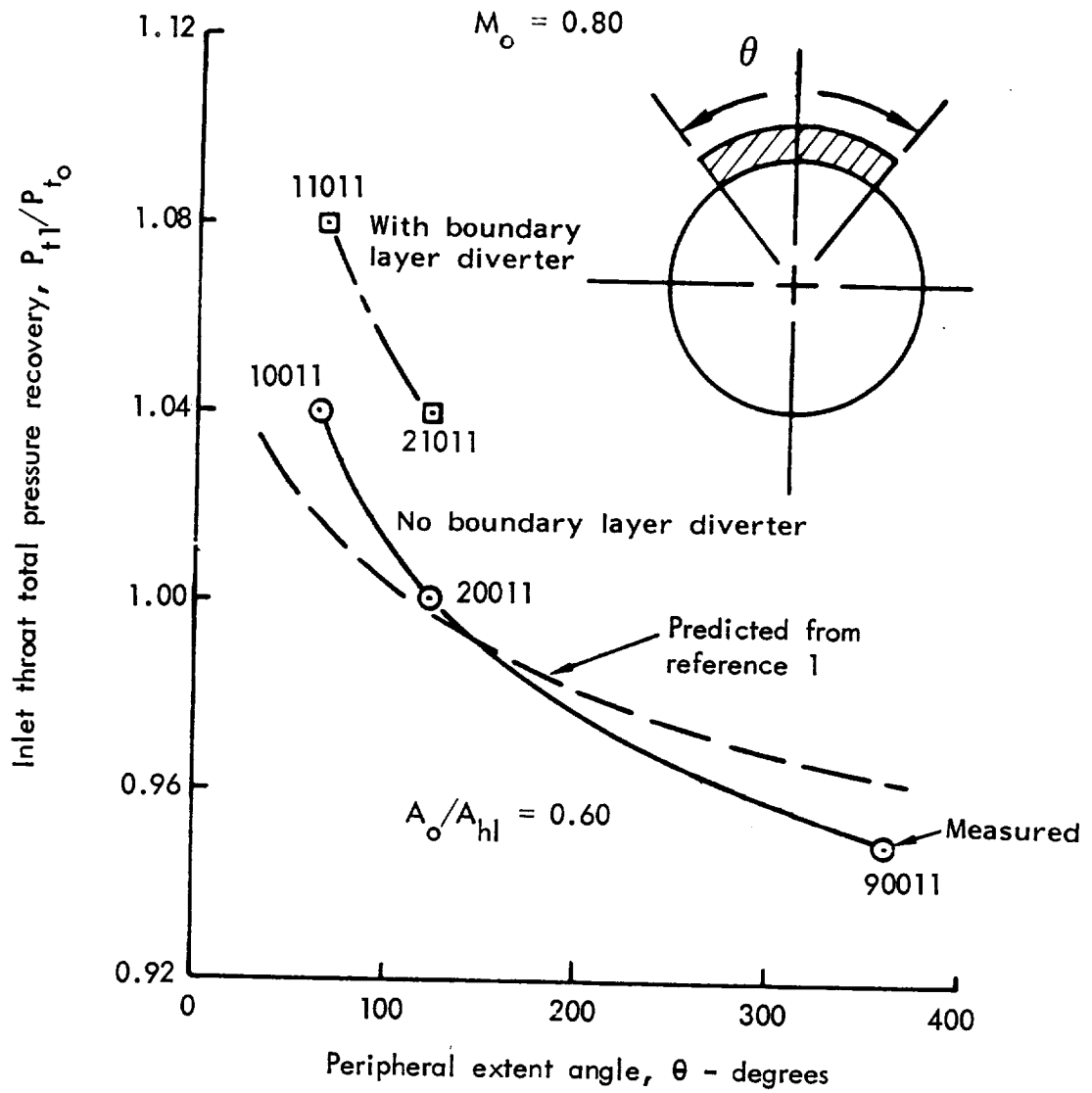


Figure 13. - Effect of peripheral extent on inlet total pressure recovery.



Effect of Boundary Layer Diverter Height - When it was determined in GUN-I that the use of a boundary layer diverter was effective in improving inlet total pressure recovery, it was decided to perform a special study in GUN-II to define optimum diverter height. Since a small drag penalty was expected to result from the use of a diverter, it was anticipated that the optimum height would be the lowest height at which boundary layer effects could be eliminated. Accordingly, single-scoop inlet model variations were designed and fabricated to extend diverter height up to three times the estimated flat plate boundary layer thickness.

Results from testing the various diverter heights at the cruise design point are shown in Figure 14. The flush-scoop inlet data were used for the zero diverter height case and, as such, represented a slight departure from consistency with the other models. The difference was in the fact that the flush scoop had a curved inside wall representing an extension of cowl surface aft of the spinner. With finite diverter heights, however, this wall was flattened, so that the lower entry lip diverged from the cowl surface with circumferential movement away from top dead center.

As Figure 14 shows, the use of a diverter rapidly improves the recovery as height is increased above zero. The initially very rapid improvement probably results from two things: (1) the diversion of the ultra-low energy air near the surface, and (2) the anomaly just discussed in the previous paragraph. Maximum improvement is seen to be reached at  $h/D_p = 0.013$ , which is about 2.7 times the flat plate boundary layer height. Requirement for a height ratio this large could result from blade-root / spinner interference wakes interacting with the boundary layer and greatly magnifying its adverse effect.

Effect of Mass Flow Ratio - The inlet performance characteristics as a function of mass flow ratio depend heavily upon the inlet design selection. More than anything else, this variation is a function of peripheral extent. Figure 15 summarizes the effects of mass flow ratio on recovery, as obtained from the testing at Mach 0.80. The top performing configuration, which was the single-scoop inlet with boundary layer diverter, (11011), showed a sharply negative slope as a function of mass flow ratio. Thus reducing mass flow ratio below design point would enhance recovery, while increasing mass flow ratio would lower it. The principal mechanism for this change is believed to be the reflected backpressure effect on the propeller operating line. The evidence for this conclusion can be seen by looking at the characteristic curve for the same inlet moved aft from  $X/D_p = 0.11$  to 0.20. This configuration, which is labeled 11020, has a nominal design point recovery over three percent lower than for the forward position. Its slope is also substantially flatter than for the forward location.

The annular inlet configuration (90011) showed a distinctly positive slope with mass flow ratio, although the nominal recovery value was almost 14 percent lower than for the top performer. The primary losses here are associated with boundary layer buildup on the spinner and ramp surface, the low performance of the propeller root section, and the interference vortices generated by the prop-spinner intersections and their associated gaps. The key to the positive slope shown in Figure 15 is the streamwise

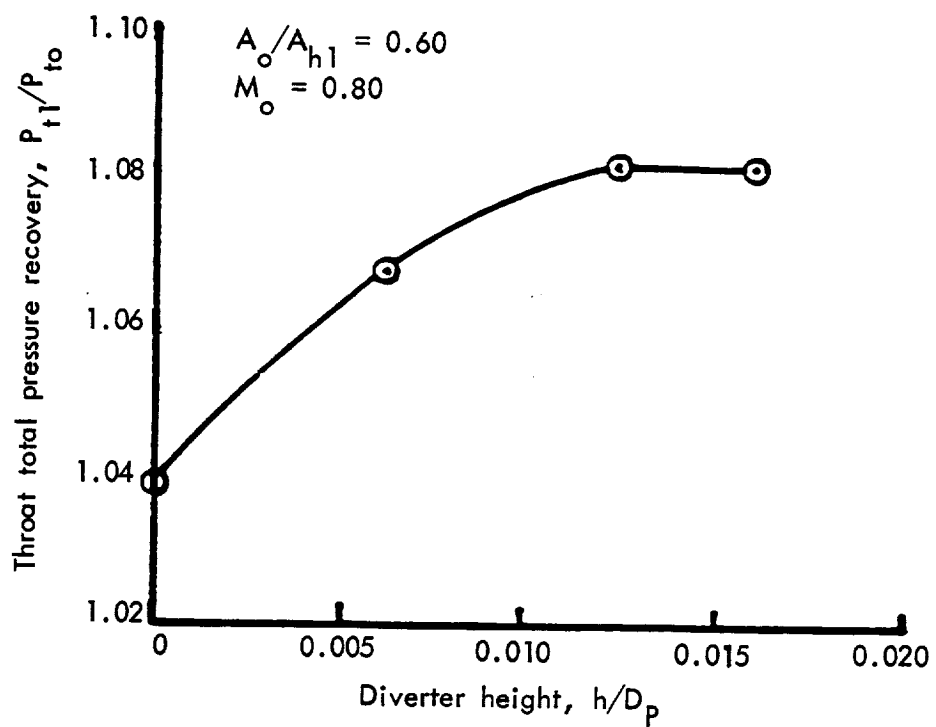


Figure 14. - Effect of boundary layer diverter height on inlet recovery, single-scoop forward inlet.

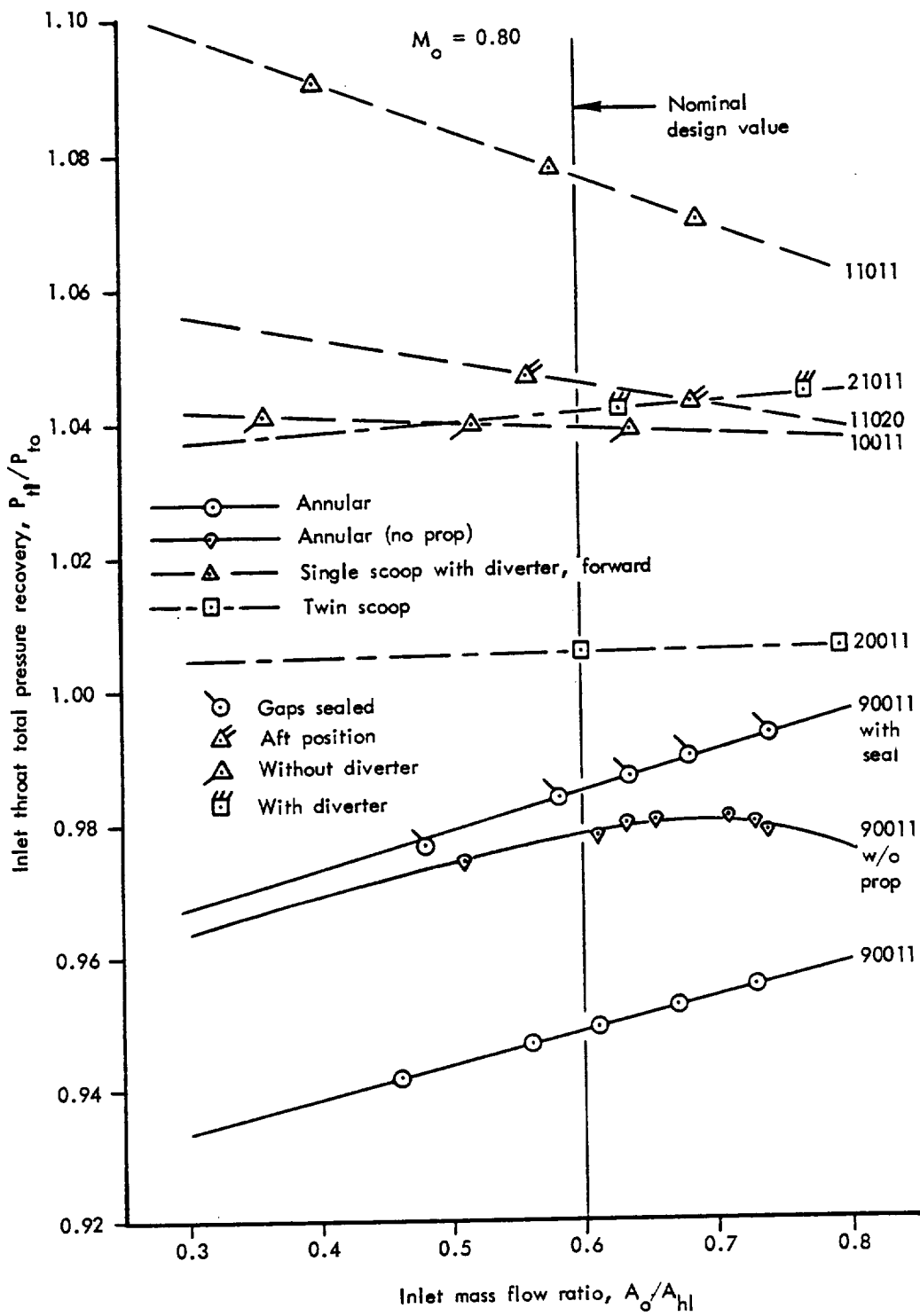


Figure 15. - Effect of mass flow ratio on inlet total pressure recovery.

pressure gradient in the boundary layer, which is severely adverse at the lower mass flow ratios. This gradient diminishes as mass flow ratio is increased and the amount of external compression is reduced, thereby reducing the tendency of the approaching flow to separate.

By examining the photographs shown in Figure 7, it can be seen that significant annular gaps exist between the spinner surface and propeller blade roots. Sealing of these gaps was found to have a very positive effect on annular inlet recovery (90011, flagged symbols) providing, as shown, an almost 4 percent improvement. Indications are that the effects of these vortices are substantially greater for the annular inlet than for the other, better performing configurations. With the gaps unsealed, the propeller supercharging effect was found to actually be negative, as evidenced by the comparison with the prop-off data. Sealing the gaps, on the other hand, provided a slightly positive supercharging effect.

The twin-scoop inlet (20011) was found to be a mid-range performer, with a nominal recovery around 100 percent for the flush installation with the entry in the forward position. Use of a boundary layer diverter (21011) yields a full 4 percent improvement in nominal, design point recovery. The slope, however, which would have been expected to become negative, remained positive. The best recorded performance of the twin scoop does not measure up to that of the single-scoop inlet, because its backpressure effect on the propeller operating line is substantially less. With a combination of both the boundary layer diverter and prop-spinner gap sealing, the recovery could be pushed up by about one more percent. The same approach, however, could also be applied to the single-scoop inlet configuration.

Effect of Mach Number - Since the inlet design mass flow ratio is substantially less than 1.0, variations in Mach number do not have a large effect on recovery. To evaluate the effect that does exist, test results for two inlets from GUN-III were examined closely. These were the annular and twin-scoop inlet configurations, both with their entries in the forward location. The boundary layer diverter version of the twin-scoop inlet was selected for the study. Also, the single-scoop inlet with boundary layer diverter from GUN-I was examined.

At a constant mass flow ratio, the effect of Mach number is to increase scrubbing velocity for the annular inlet and to increase the reflected blockage effect on the propeller operating point for the twin-scoop, diverter inlet. The results of these effects are shown in Figure 16. With an increase in Mach number, the annular inlet recovery is shown to decrease. This results from a combination of the effects of the higher average velocity, the increased pressure gradient in the boundary layer, and the more severe interference penalty associated with the prop-spinner intersection. This trend does not change with variation in mass flow ratio above or below the the design point level.

In contrast to the annular inlet, recovery for the twin-scoop diverter inlet tends to increase as Mach number goes up. Although not fully substantiated, it is believed that there is a greater shift in the propeller pressure ratio due to flow blockage at the higher Mach number.

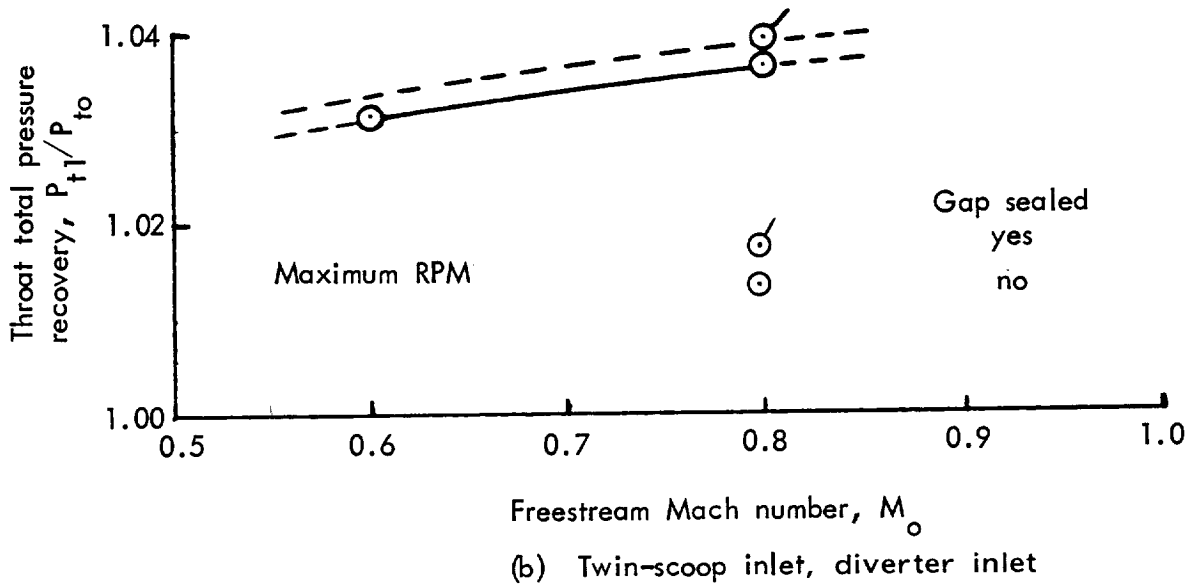
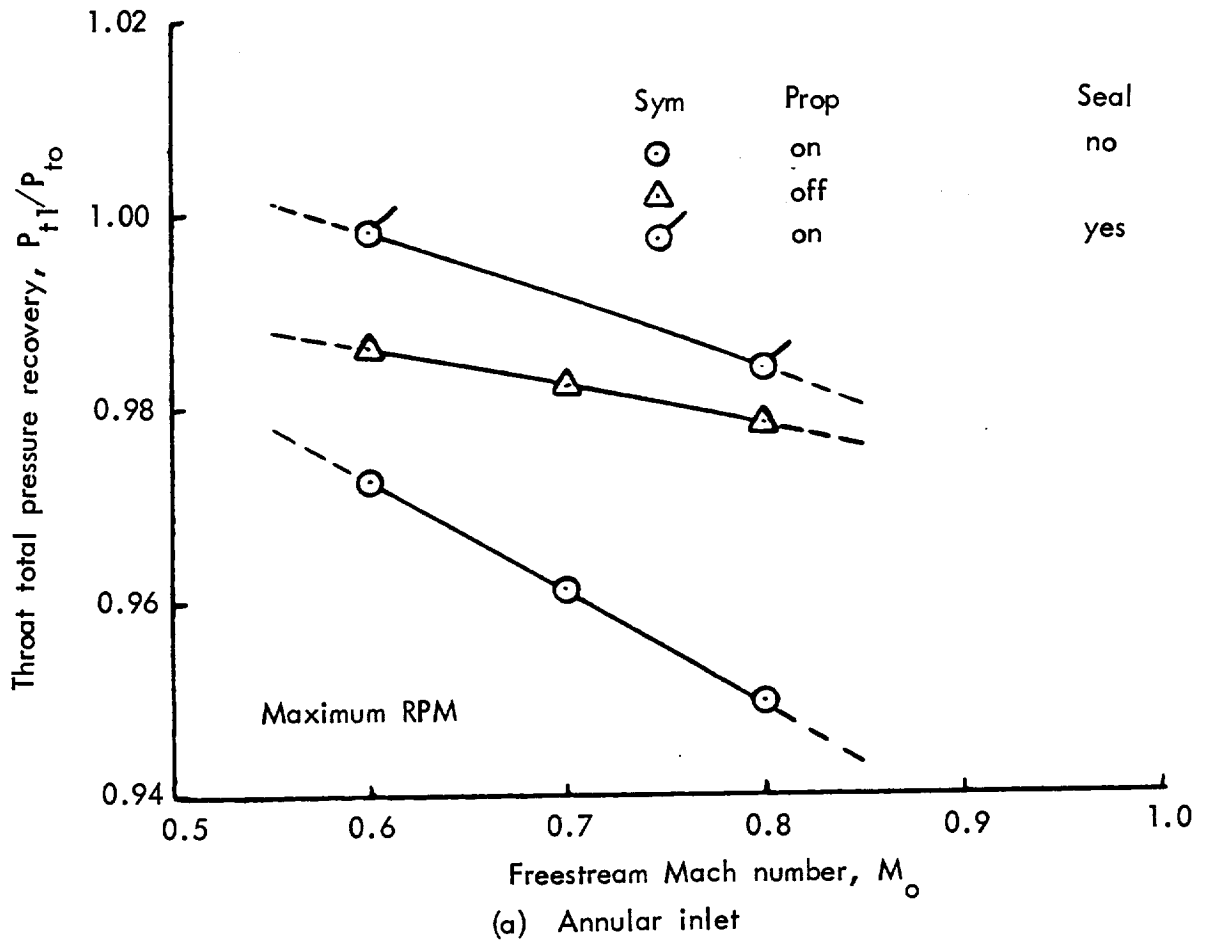
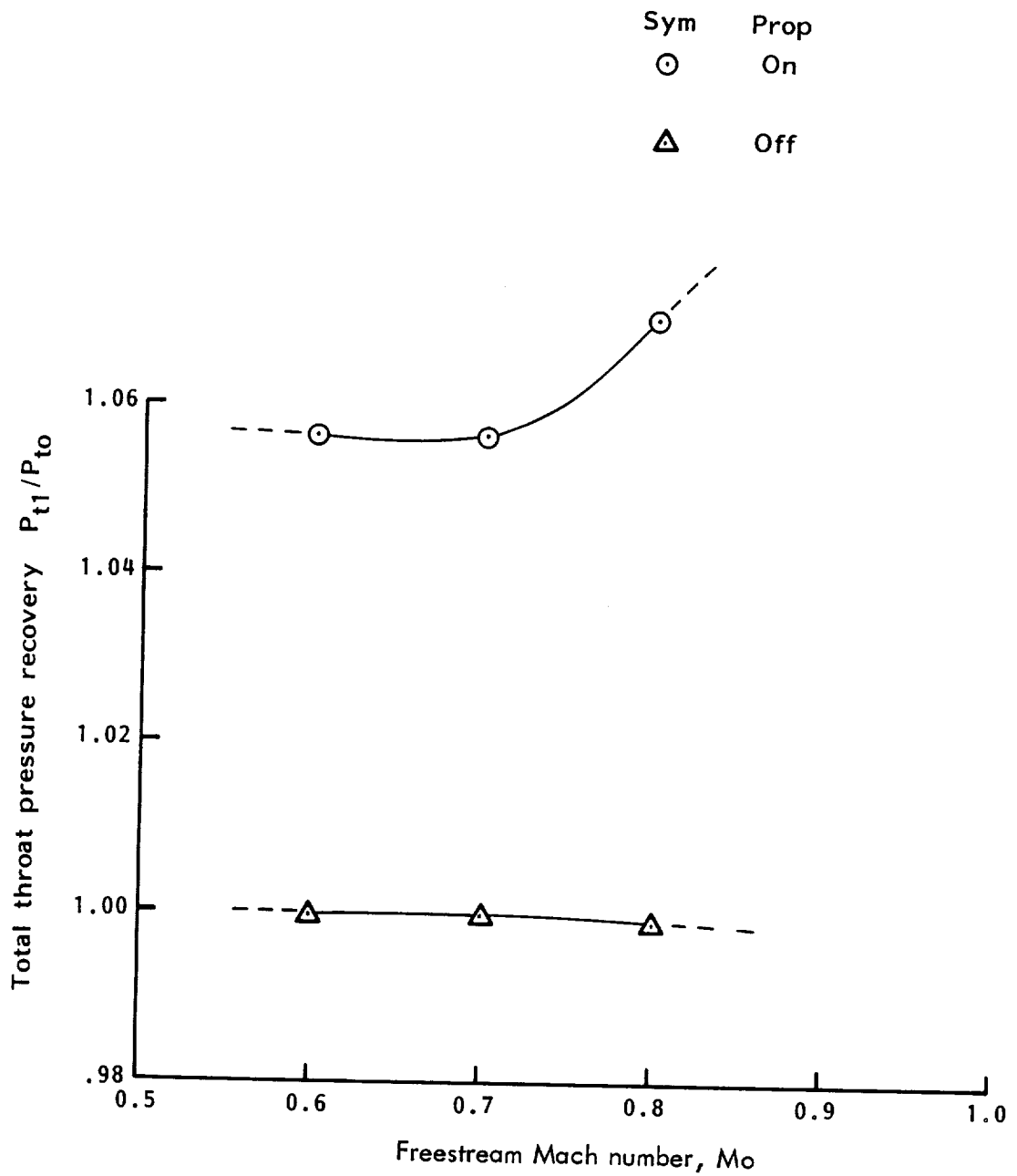


Figure 16. - Effect of Mach number on throat total pressure recovery.



(c) Single-scoop inlet, diverter inlet

Figure 16. - Continued.

This would be expected, since the effect of local blockage becomes more pronounced at higher speeds. It is also possible that, unless there is a substantial margin in the boundary layer diverter height, the combination of wake vorticity from the root-spinner intersection and swirl acting on the boundary layer could result in more low-energy air being ingested at higher Mach numbers.

Pressure recovery for the single-scoop inlet, as shown in Figure 16(c), also tends to increase as Mach number goes up, at least for the propeller on case. Again, this is probably due to flow blockage at the higher Mach number. Because of the greater diverter heights for the single-scoop inlet, the recovery levels are higher than was the case for the twin-scoop inlet. Pressure recoveries without the propeller are constant with Mach number.

### **Inlet Pressure Distortion**

Evaluation of the average total pressure available at the inlet throat does not provide complete insight into the mechanism that causes the loss to occur or the potential for inlet-engine incompatibility. These things can only be obtained through a study of the actual pressure distributions. To accomplish the desired analyses, static and total pressure data were obtained at the inlet throat using the instrumentation described in Figure 9. As noted before, the scope of this testing did not include the measurement of duct losses and compressor face pressure distributions.

Inlet Static Pressure Patterns - Throat static pressure profiles measured at Mach 0.80 are presented for the single-scoop, diverter inlet in Figure 17, where it can be seen that the windward lip (relative to the direction of propeller rotation) experienced a lower static pressure than the leeward lip. This is due to the propeller generating swirl which, in turn, causes local acceleration of the flow around the windward lip and a corresponding deceleration on the inside of the leeward lip. Looking at it another way, since the circumferential swirl component is traveling in the same direction as the propeller blade, there is an inlet stagnation line shift toward the direction from which the propeller blade is moving. For the case shown in Figure 17, the static pressure isobars indicate a discontinuity near the windward lip and at a static pressure approximately equal to 50 percent of the freestream total. It is likely that the region on the upwind side of this discontinuity is locally separated, while the region on the downwind side is attached, but distorted. The potential for significant improvement through local tailoring to a specific inflow direction can be clearly seen here.

Static pressure pattern contours have been generated at Mach 0.80 cruise for five separate configuration geometries. These were the annular, twin-scoop flush and diverter inlets, and the single-scoop, diverter inlets in the forward and aft positions. Their pattern plots are presented in Figures 18, (a) through (e), respectively. All inlets are presented at the same scale. Since the pattern for the annular inlet is axially symmetric, only a partial sector of its periphery is presented. An interesting characteristic of the annular and flush inlet patterns is that the static pressure increased from the outer to the inner wall. This

$$M_o = 0.80$$

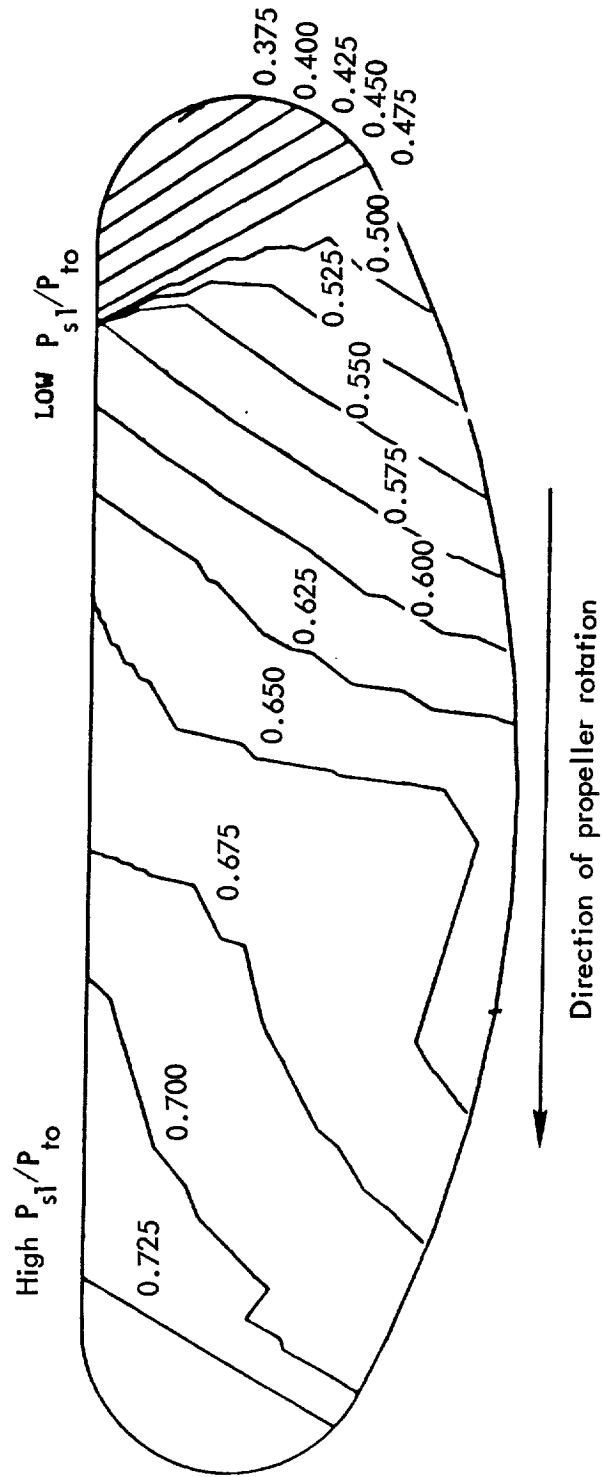
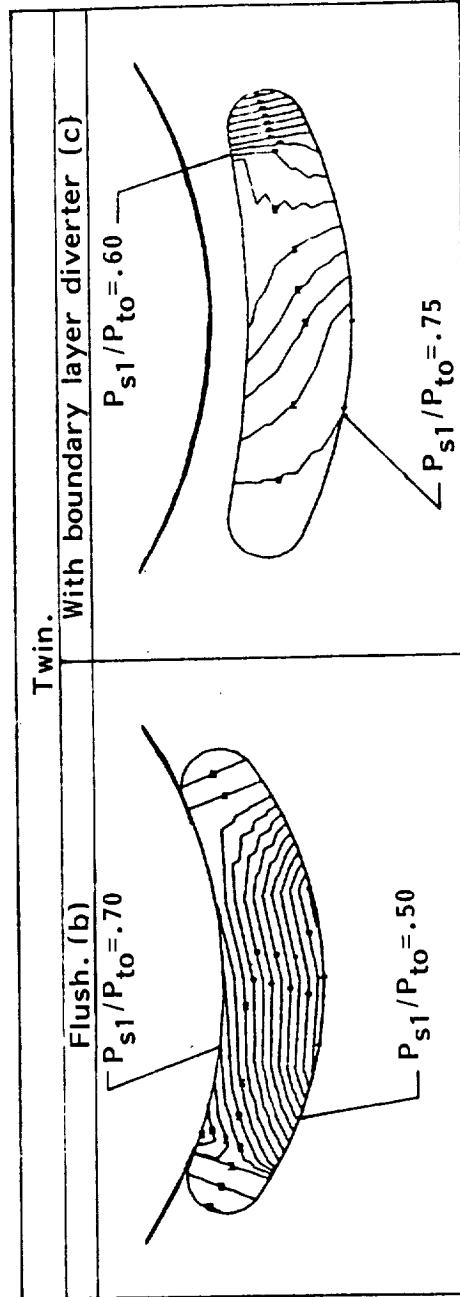
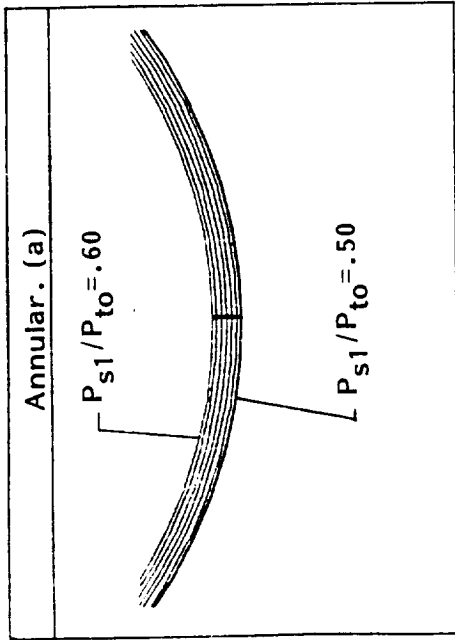


Figure 17. - Static pressure pattern for GUN-1 single-scoop, diverter inlet in cruise operation.



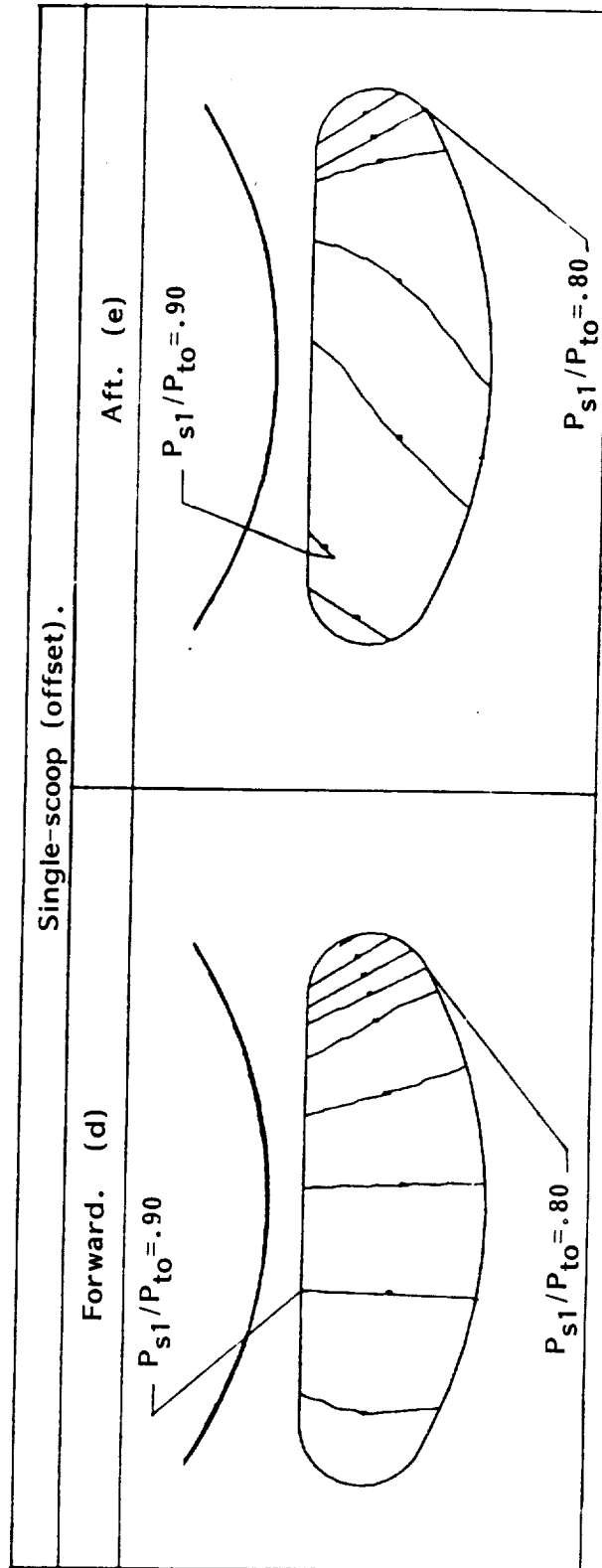
$M_0 = 0.80$



Note: Isobar increments are 0.025

Figure 18. Static pressure patterns for GUN-III inlets in cruise operation.

$$M_o = 0.80$$



Note: Isobar increments are 0.025

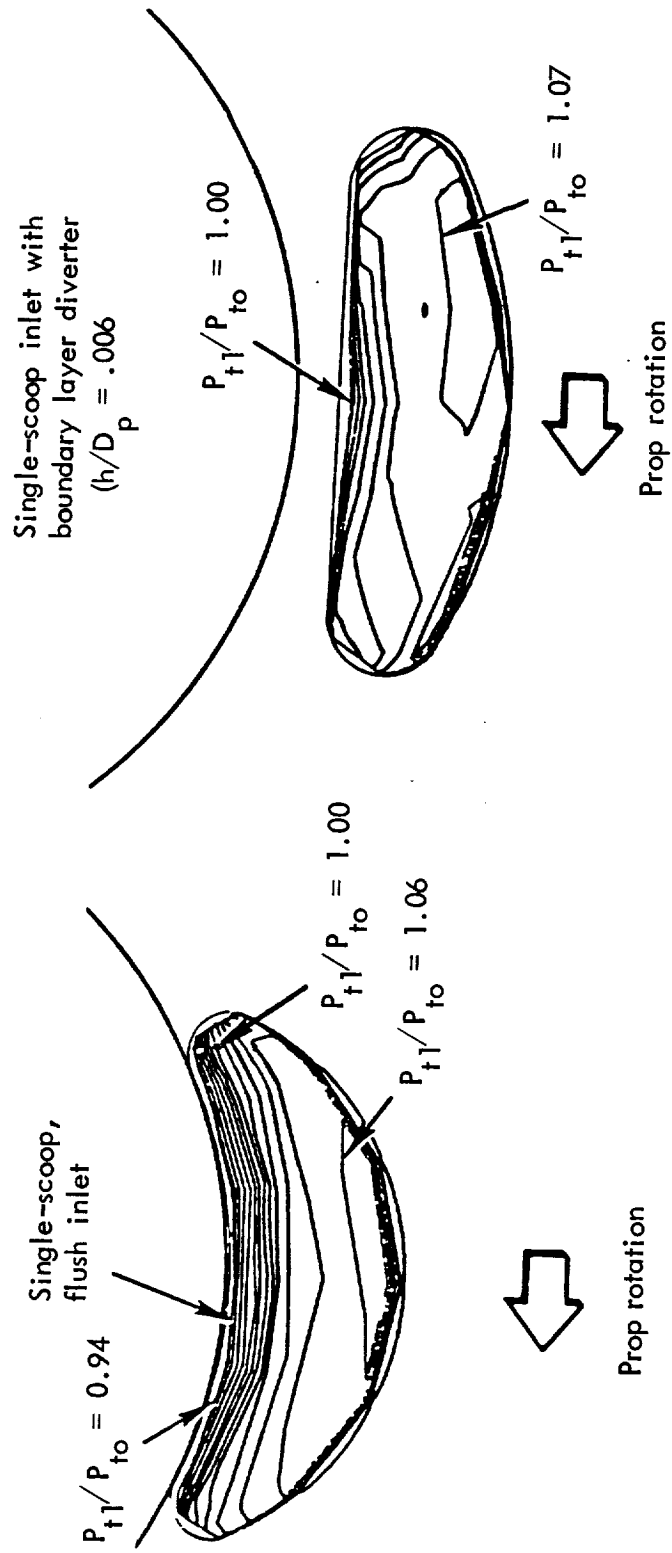
Figure 18. - Continued.

results from the fact that the streamlines along the flow boundary between the spillage and inlet inflow curve sharply near the outer lip with associated higher velocities and lower static pressures. For the twin-scoop, diverter and single-scoop, diverter inlets, the isobars are largely vertical indicating that here the flow field is dominated by the slipstream swirl, which is more strongly induced by the propeller at the greater distance from the nacelle centerline typical for the diverter inlets. Highly accelerated flow, with potential separation, is indicated locally on the windward side of the twin-scoop diverter inlet, but it does not appear to exist on the flush version of that inlet. The single-scoop inlet as shown in Figure 18(d) is at a different mass flow ratio from the inlet shown in Figure 17. In comparing the forward and aft positions for the single-scoop diverter inlet, two things are immediately apparent. The first is that static pressures are generally lower in the aft position, and the second is that the slopes of the isobars change from almost vertical on the windward side to a positive slope of about 45 degrees in the region enclosed by the center and leeward sides.

Inlet Total Pressure Contours - Using measured throat total pressure data, isobar plots were generated from data for the single-scoop inlet at selected conditions. Figure 19 shows a comparison between contour plots constructed from measured data for the flush versus diverter versions of the single-scoop inlet. For the flush inlet, the pressure gradient due to ingestion of the boundary layer extends outward a significant distance from the inner wall. An interesting feature of the flush inlet pattern relative to the diverter inlet is that the pressure pattern near the nacelle surface is more symmetrical. Apparently, the combination of the boundary layer and the root-spinner interference pattern reduces the impact of the swirl component. Also, propeller induced swirl is reduced for the flush inlets with their smaller radial displacement from the nacelle centerline. Moving away from the inlet inner wall toward the outer wall of the throat, the centroid of the peak pressure region can be seen on the upwind side. This effect is slightly more pronounced for the boundary layer diverter than for the flush inlet. It illustrates how the center of pressure is skewed along a line that generally follows the path of the ingested streamtube.

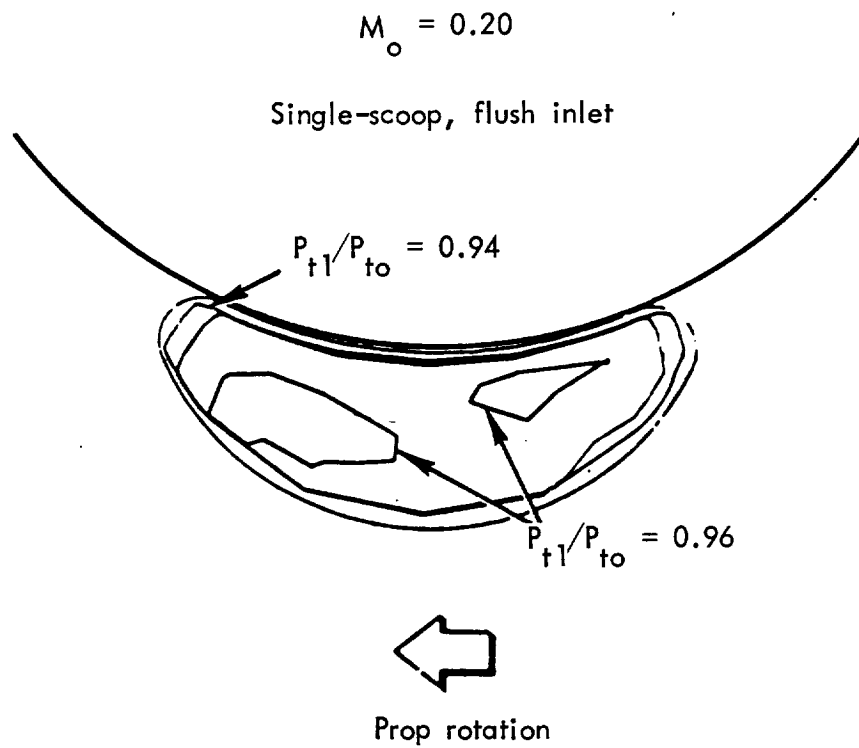
In addition to evaluating inlet characteristics at or near cruise conditions, a limited number of test points were obtained at reverse thrust conditions for the flush inlet. These data have been used to generate the total pressure contour plot shown in Figure 20. Based on these results, it has been concluded that inlet distortion is acceptable during reverse thrust operation. This is true for two reasons. First, the twist of the blades is such that substantial reverse thrust levels can be obtained with average pitch angles that do not actually reverse the local blade pitch at the roots. Second, when reverse pitch is commanded, the trailing edges of the blades rotate away from the inlet, leaving sufficient space for ambient air to backfill the gap with relatively low distortion airflow. While the overall recovery thus obtained is not good, it appears to be adequate to avoid compressor stall. Because of the high level of effectiveness of a propfan in the reverse mode, the engine can be operated at a relatively low power setting and, therefore, adequate throttle margin is available to compensate for low recovery.

$M_o = 0.80$



Note: Isobar increments are  $\Delta P_f/P_{to} = 0.01$

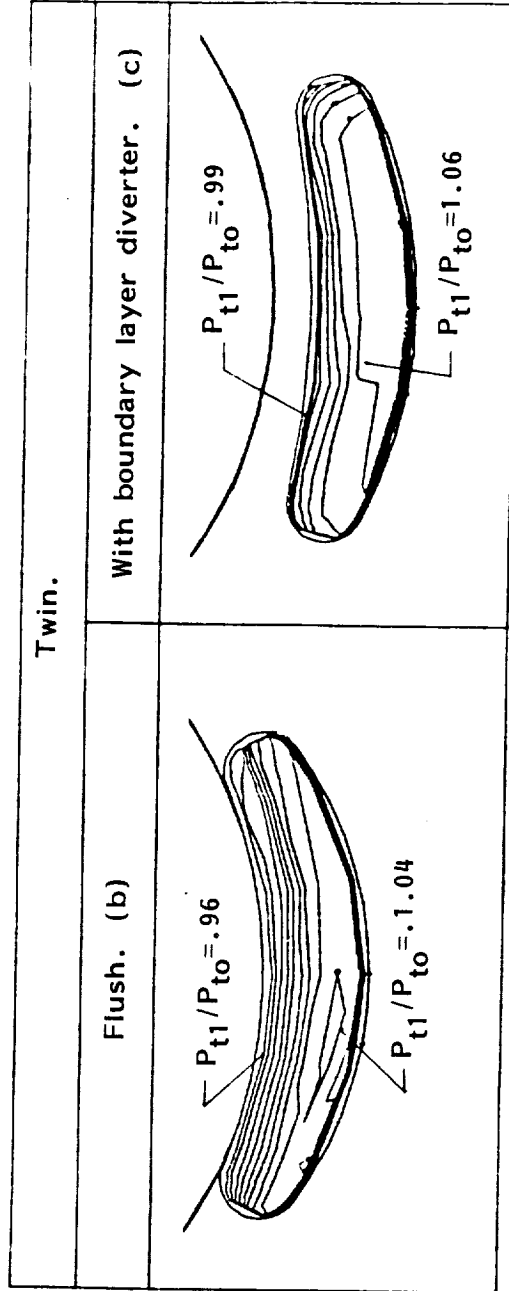
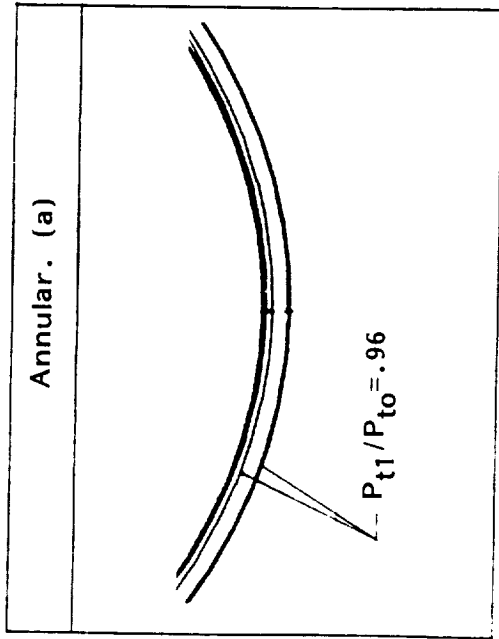
Figure 19. - Total pressure contour map comparison--effect of boundary layer diverter.



Note: Isobar increments are  $\Delta P_t/P_{to} = 0.01$

Figure 20. - Total pressure contour map for reverse thrust operation.

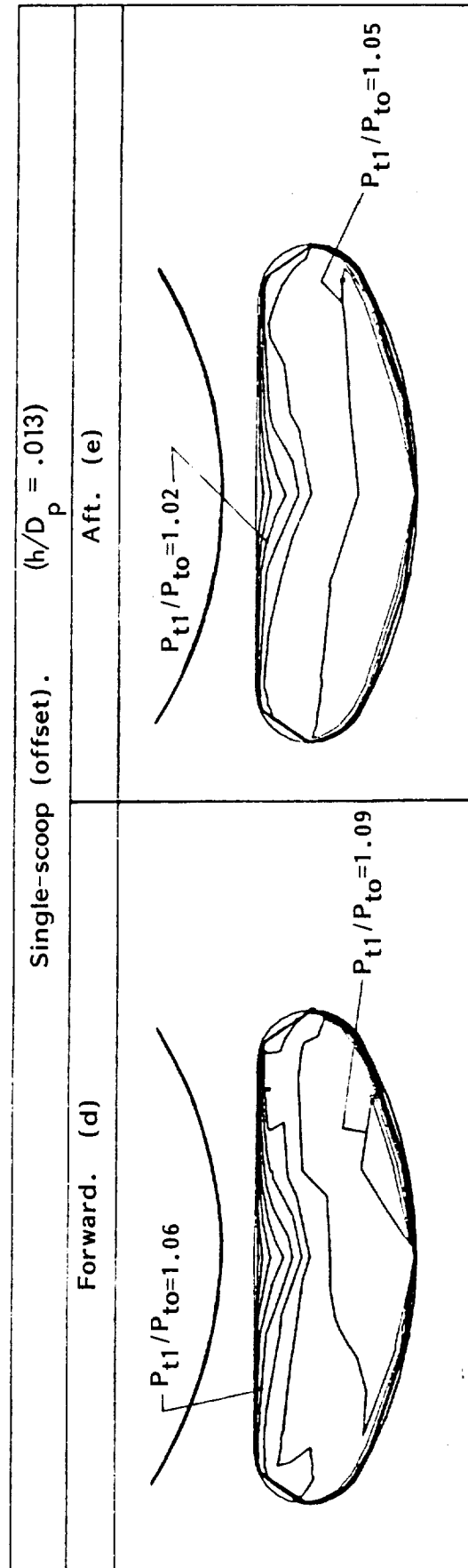
$M_0 = 0.80$



Note: Isobar increments are 0.01

Figure 21. Total pressure contour maps for GUN-III inlets in cruise operation.

$$M_o = 0.80$$



Note: Isobar increments are 0.01

Figure 21. - Continued.

Total pressure contours were also generated at Mach 0.80 cruise for five separate configuration geometries. These were the annular, twin-scoop flush and diverter inlets, and the single-scoop, diverter inlets in the forward and aft positions. These contour plots are presented in Figures 21, (a) through (e), respectively. The first note of interest is that the annular inlet has a very low energy level, with an average recovery of only 0.95. This level is less than would be expected of a boundary layer generated by the nacelle ramp plus SR-3 spinner with no propeller mounted. The root of the blade, although not heavily loaded, should have energized the flow to some extent. The fact that there is no evidence that the propeller did energize the flow indicates that adverse blade/spinner/gap interaction more than offset the supercharging of the blade. The total pressure isobars for the twin-scoop flush installations clearly illustrate the boundary layer ingestion. The ingested boundary layer for the twin, of course, is a smaller percentage of the overall flow than for the annular inlet. This is consistent with the better recovery actually measured for the twin compared to the annular.

Figure 21(c) shows how diverting the boundary layer eliminates most of the reduced energy flow and allows a large portion of the inlet to experience the full benefit of the propeller pressure rise. As shown in Figure 21(d), the total pressure contour pattern for the single-scoop inlet in the forward position is very similar to that of the twin. It does, however, exhibit a higher peak pressure. This results from both the blockage effect and the improved average slipstream pressure obtained at a greater radial displacement from the hub. The inlet shown in Figure 21(d) had a diverter height of 1.3 percent ( $h/D_p=0.013$ ), while the diverter inlet shown in Figure 19 had a diverter height of .6 percent and a corresponding lower total pressure contour map. The pattern for the single-scoop, aft position, as shown in Figure 21(e), is substantially more symmetrical, indicating a reduced impact of the slipstream swirl.



## Cowl Pressure Distributions

Static pressure distributions were obtained for the single-scoop inlet, with and without boundary layer diverter, for the twin-scoop inlet, with and without boundary layer diverter, and for the annular inlet. Pressure taps were placed on the nacelle body, on the top and sides of the inlet scoops, and in the boundary layer diverter channel (Figure 9). No pressure data were obtained for the single-scoop inlet in the aft position. All pressure data below are presented in terms of non-dimensional nacelle ordinates  $X/L$ , with  $L$  as the total length of the cowl for the single-scoop inlet - 48.69 centimeters (19.169 in.).

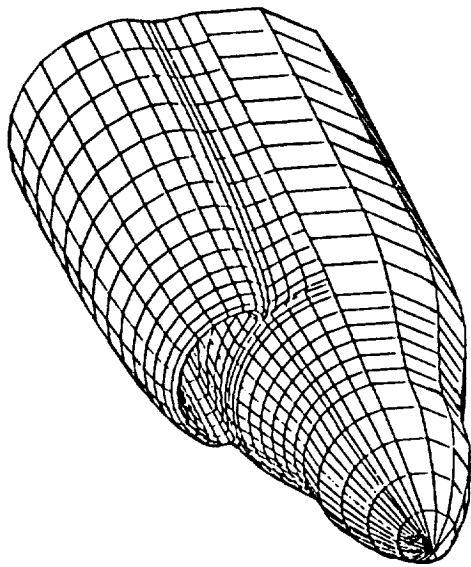
To assist in the analysis of pressure data, all of the nacelle configurations were analyzed with the Lockheed QUADPAN panel program (Reference 6), and the panel models are shown in Figure 22.

Effect of Inlet Type - All of the inlet configurations share the characteristic of having peaky pressure distributions at their design conditions. The annular inlet has moderate pressure peaks on the front of the cowl (Figures 23 and 24) and, for  $Mo = 0.80$ , another pressure peak farther downstream associated with a shock formation.

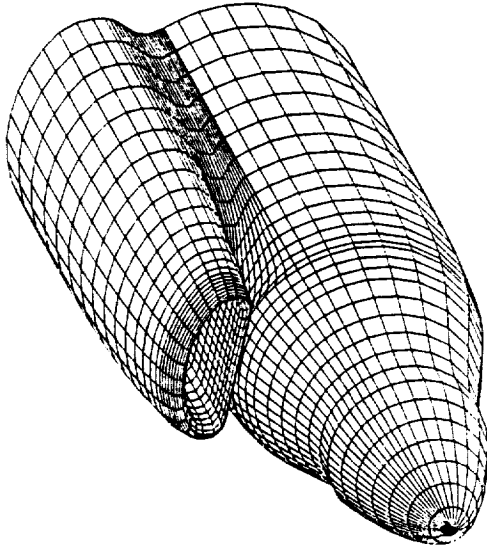
The flush single-scoop inlet typically shows higher pressure peaks at the front of the cowl (Figures 25 and 26). Also, as is the case with all inlets, except the annular inlet, this inlet has higher pressure peaks on the leeward side of the scoop with the propeller on, because of the propeller induced swirl angle. This effectively places the leeward side of the scoop at a higher angle of attack, while the windward side of the scoop is effectively at a lower angle of attack. Figures 25(a), 25(b), and 25(c) show this effect for the windward side, top, and leeward side of the single-scoop inlet.

The single-scoop inlet with boundary layer diverter has similar pressure distributions on the cowl (Figures 27 through 31). With the propeller on, it also has the highest pressure peaks on the leeward side of the scoop. This effect is shown in Figures 30(a) and 30(b), which contrasts propeller off and propeller-on cases for the windward side, top, and leeward side of the scoop.

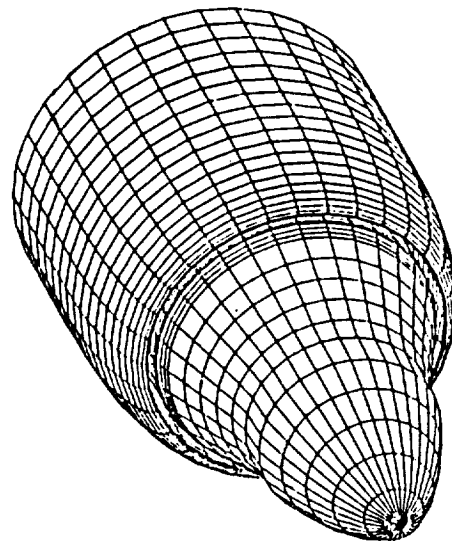
The twin-scoop inlets were designed to reduce the pressure peaks and consequent shocks by cambering the cowl at its front. As a result, the twin-scoop inlets have lower pressure peaks there. This is especially true for propeller-on cases, as the side of the inlet was thickened and effectively turned into the propeller induced swirl flow. The pressure distributions for the flush twin-scoop inlet are shown in Figure 32. Its pressure peaks are markedly lower than those for the single-scoop inlets, and there is much less difference in pressure levels for the left and right sides of the scoop. For the top of the cowl, there is a pressure peak at the front of the cowl and a peak farther downstream due to a shock formation, similar to the case of the annular inlet. Pressure distributions for the twin-scoop inlet with boundary layer diverter are shown in Figure 33 and are comparable to the flush inlet data.



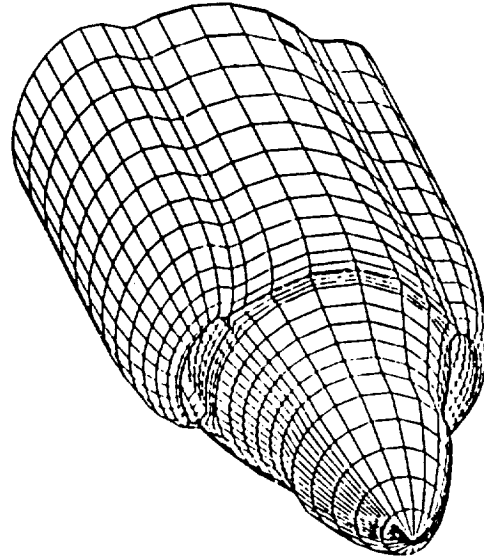
(a) Flush inlet



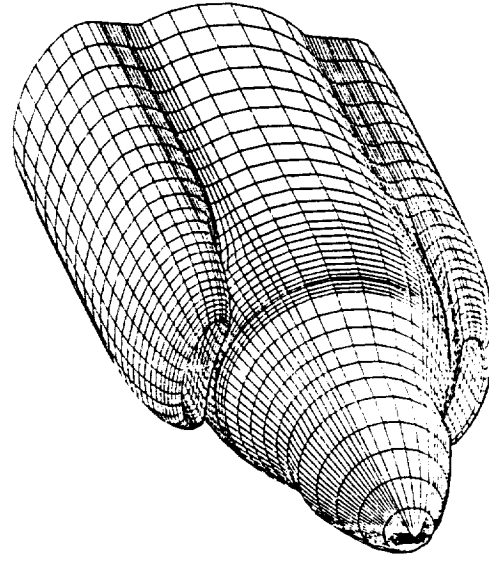
(b) Boundary-layer-diverter inlet



(c) Annular inlet

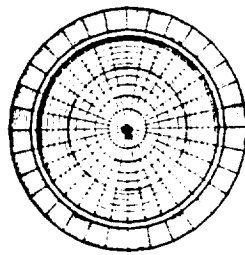


(d) Twin scoop flush inlet



(e) Twin scoop bld inlet

Figure 22. - Propfan nacelle configurations



○ } Row A  
 △ }

Sym	Run	Point	$M_o$	MFR
○	106	6	0.61	0.52
△	109	1	0.81	0.49

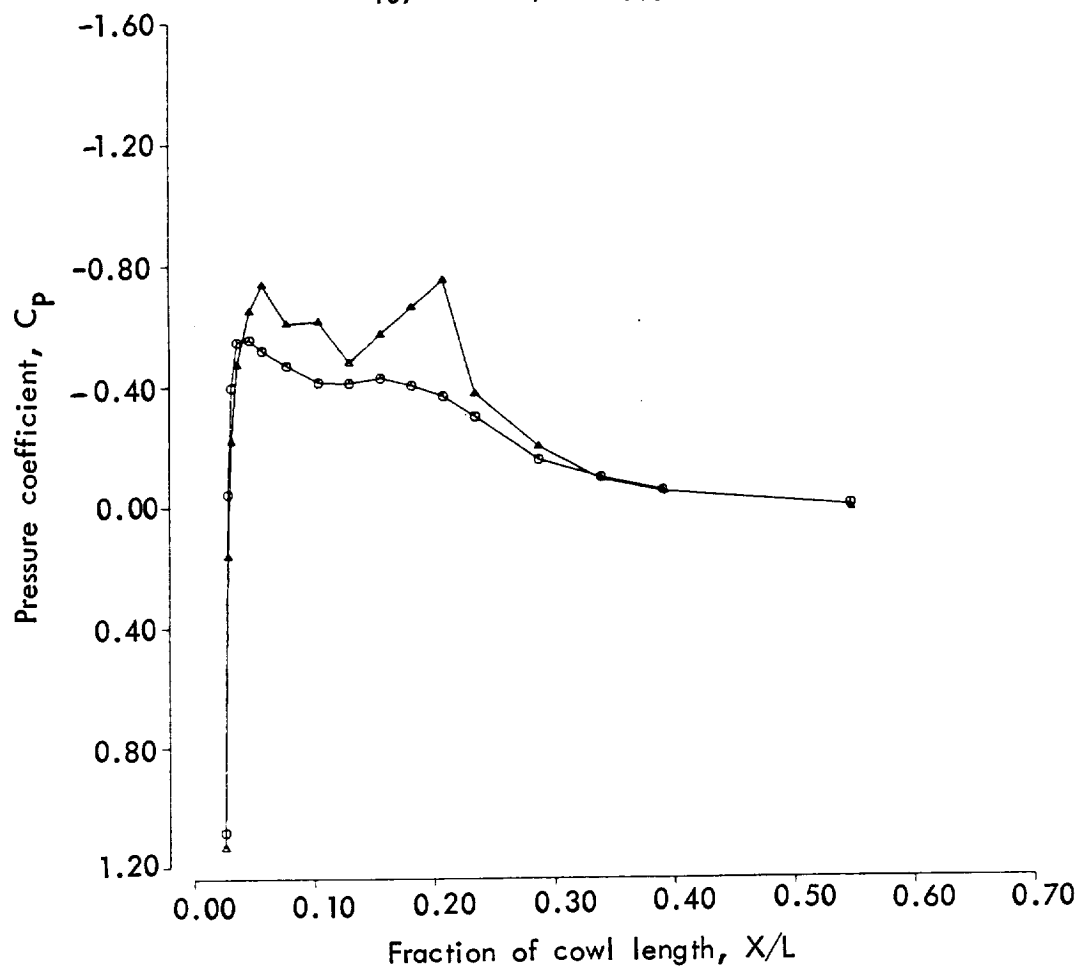
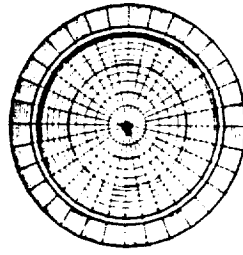


Figure 23. - Pressure distribution for annular inlet, effect of Mach number, propeller on, MFR = 0.5



○ } Row A  
 △ }

Sym	Run	Point	$M_o$	MFR
○	108	5	0.80	0.49
△	108	1	0.81	0.74

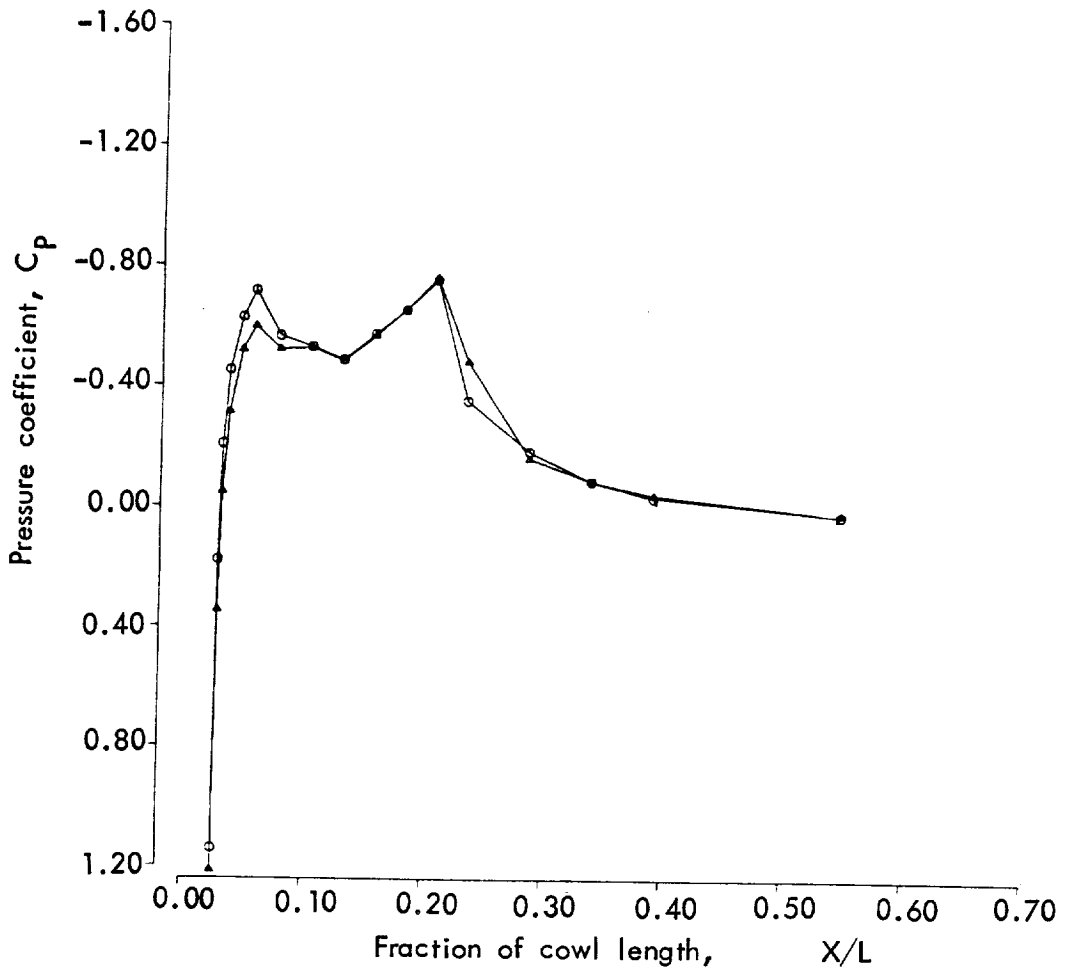
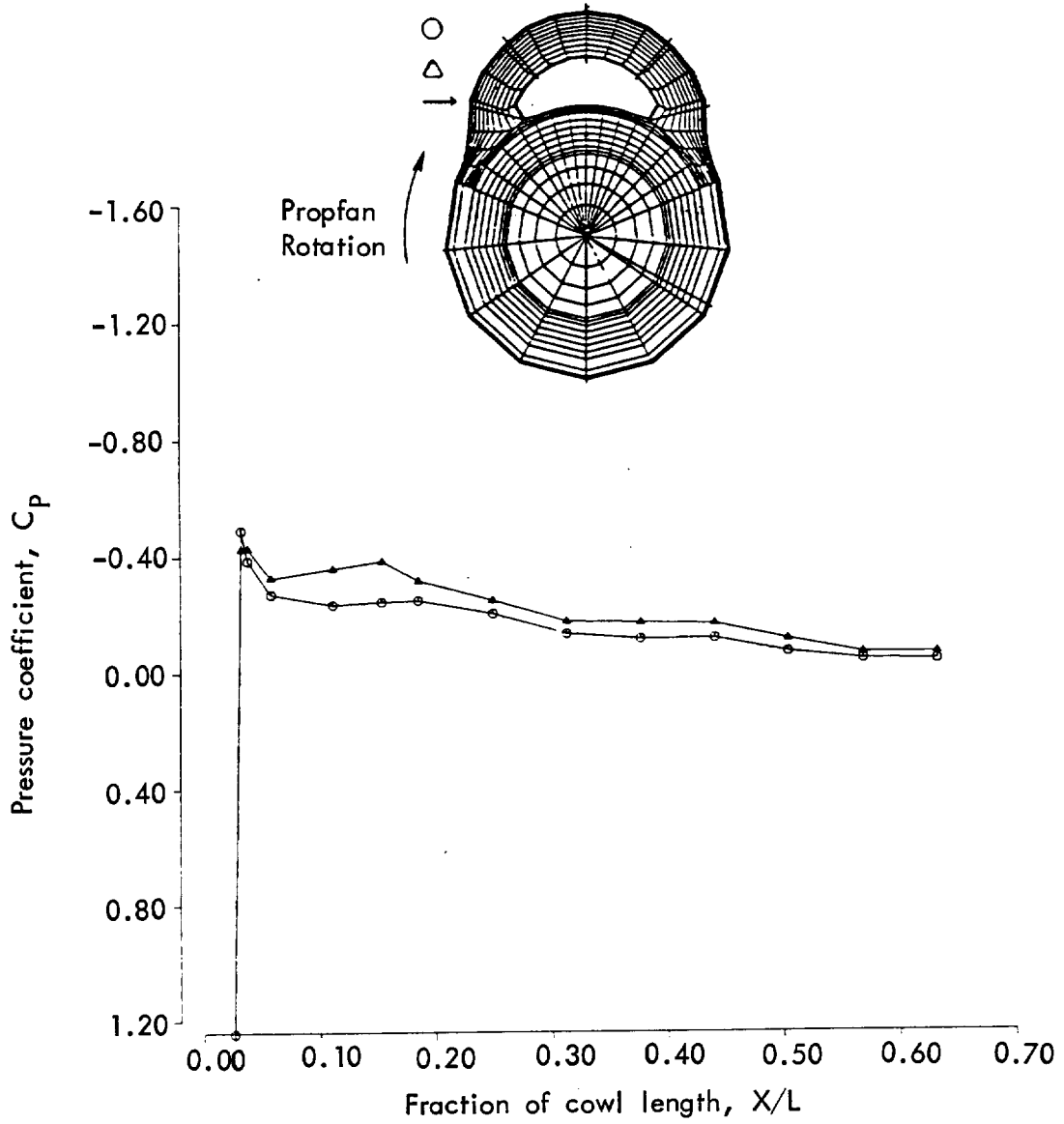


Figure 24. - Pressure distribution for annular inlet, effect of mass flow ratio, propeller on, Mach = 0.8

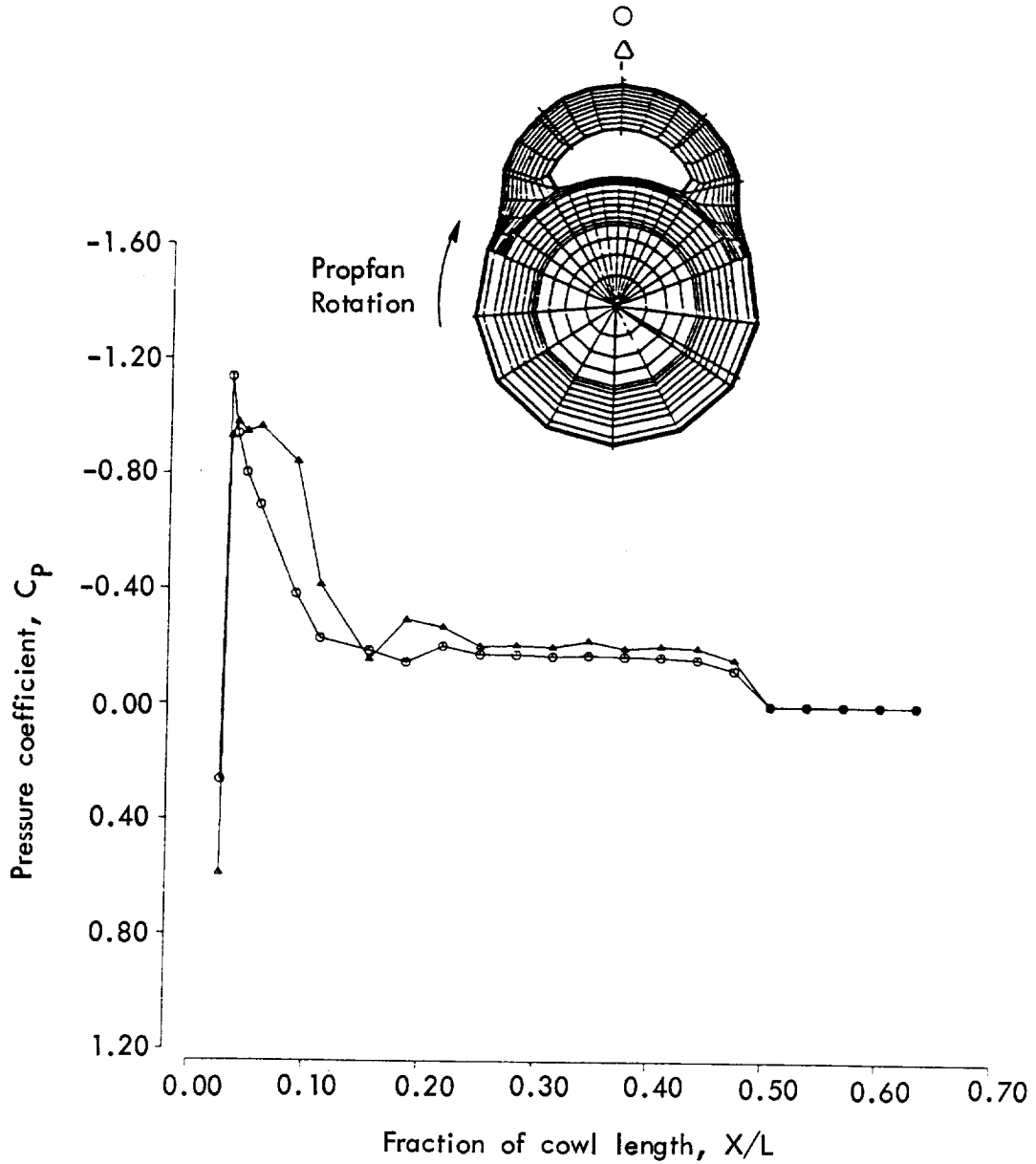
Sym	Run	Point	$M_o$	MFR
○	67	1	0.61	0.43
△	75	1	0.81	0.40



(a) Effect of Mach number, propeller on, MFR = 0.4, windward side of cowl.

Figure 25. - Pressure distribution for flush single-scoop inlet

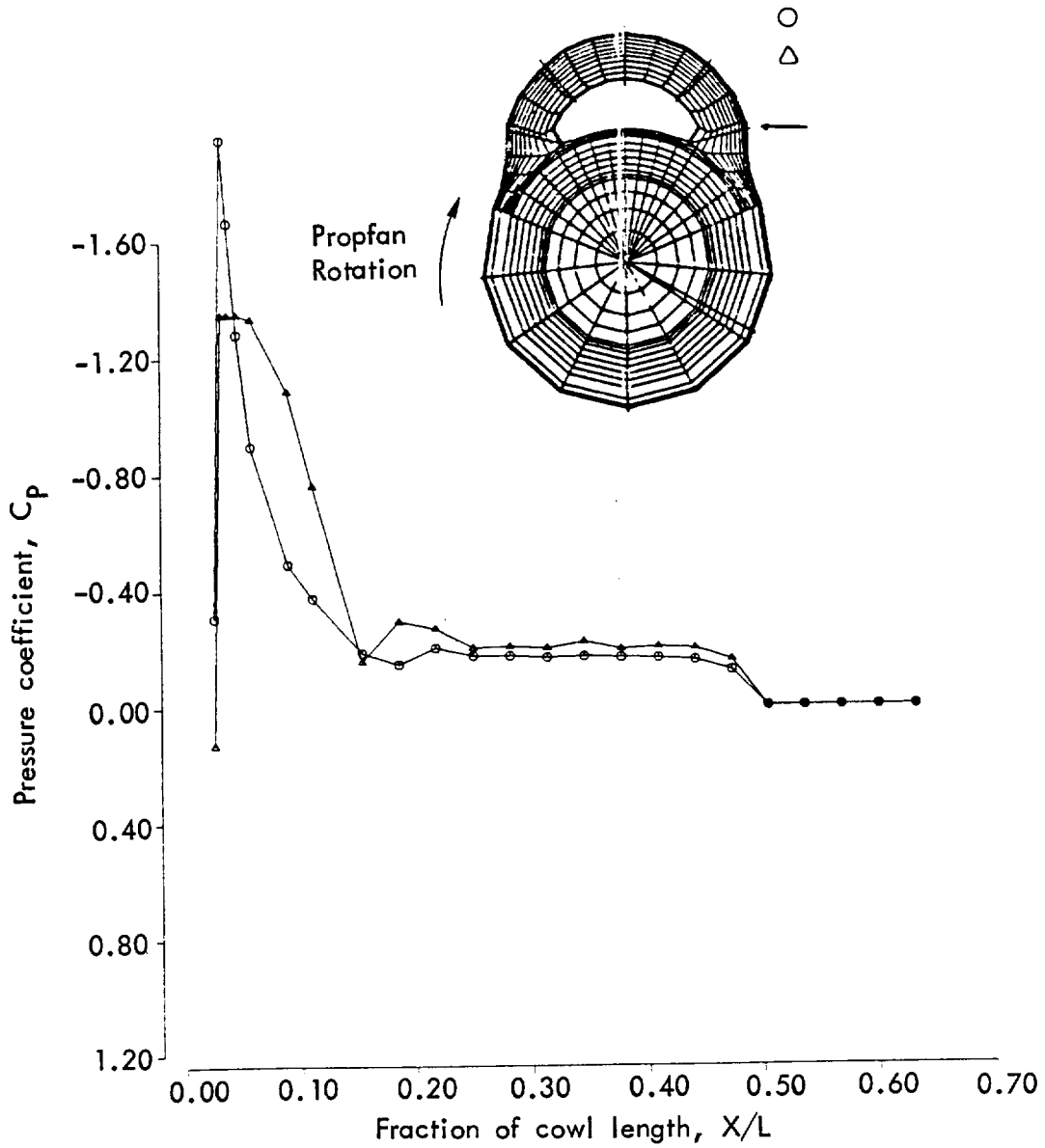
Sym	Run	Point	$M_o$	MFR
○	67	1	0.61	0.43
△	75	1	0.81	0.40



(b) Effect of Mach number, propeller on, MFR = 0.4, top of cowl.

Figure 25. - Continued.

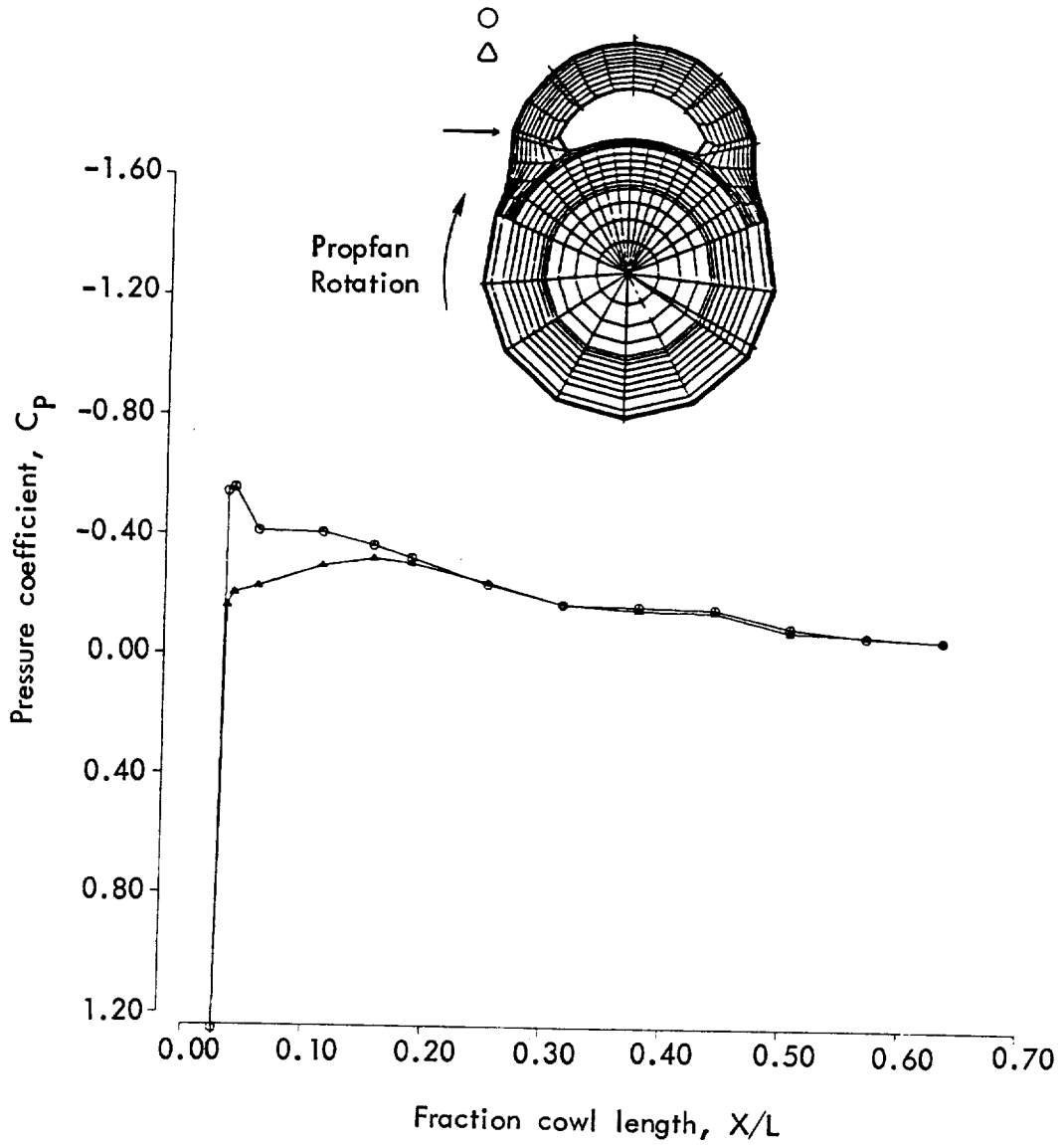
Sym	Run	Point	$M_o$	MFR
○	67	1	0.61	0.43
△	75	1	0.81	0.40



(c) Effect of Mach number, propeller on, MFR = 0.4, leeward side of cowl.

Figure 25. - Concluded.

Sym	Run	Point	$M_o$	MFR
○	77	1	0.81	0.35
△	75	5	0.81	0.70

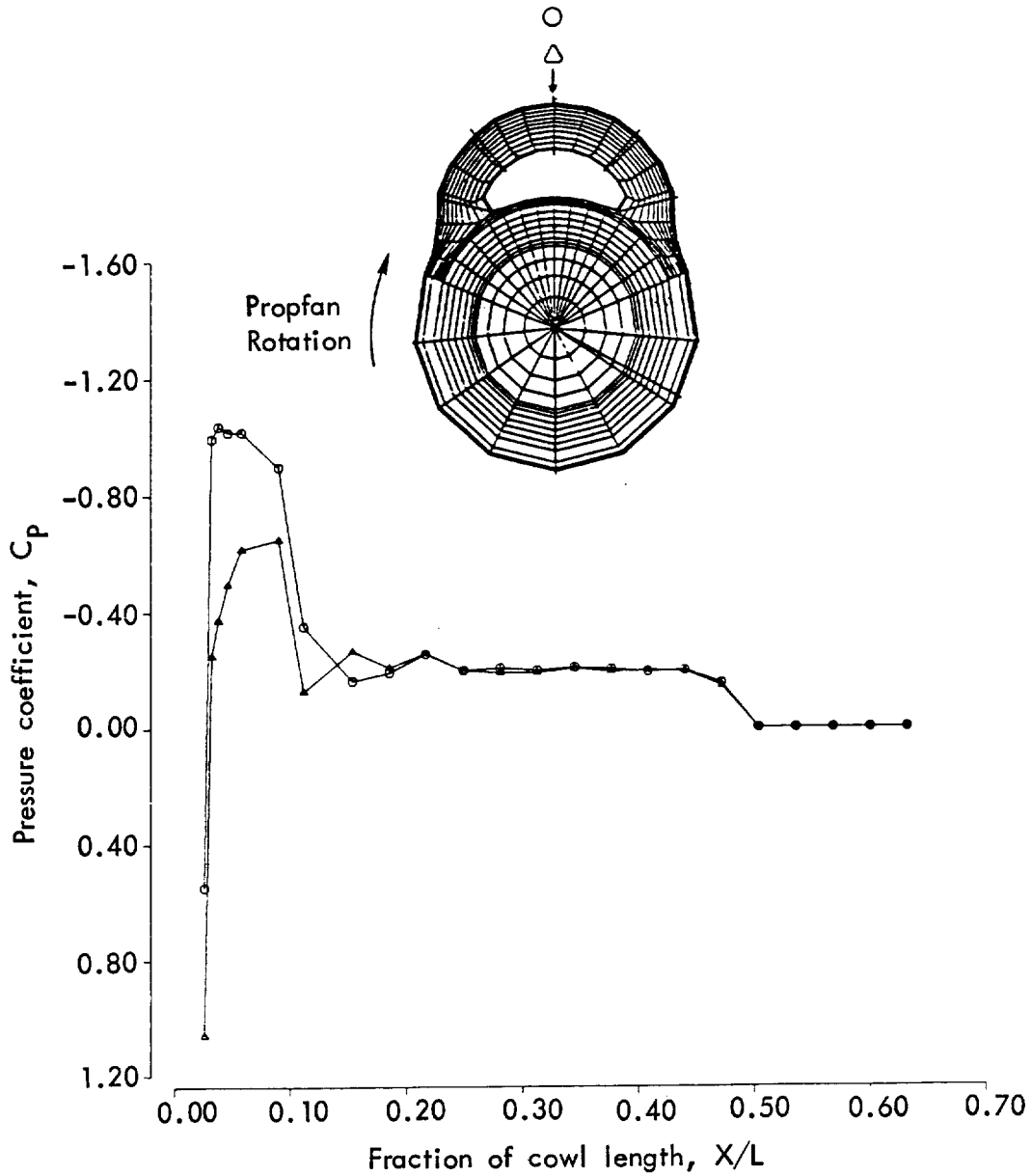


(a) Effect of mass flow ratio, propeller on, Mach = 0.8, windward side of cowl.

Figure 26. - Pressure distribution for flush single-scoop inlet.



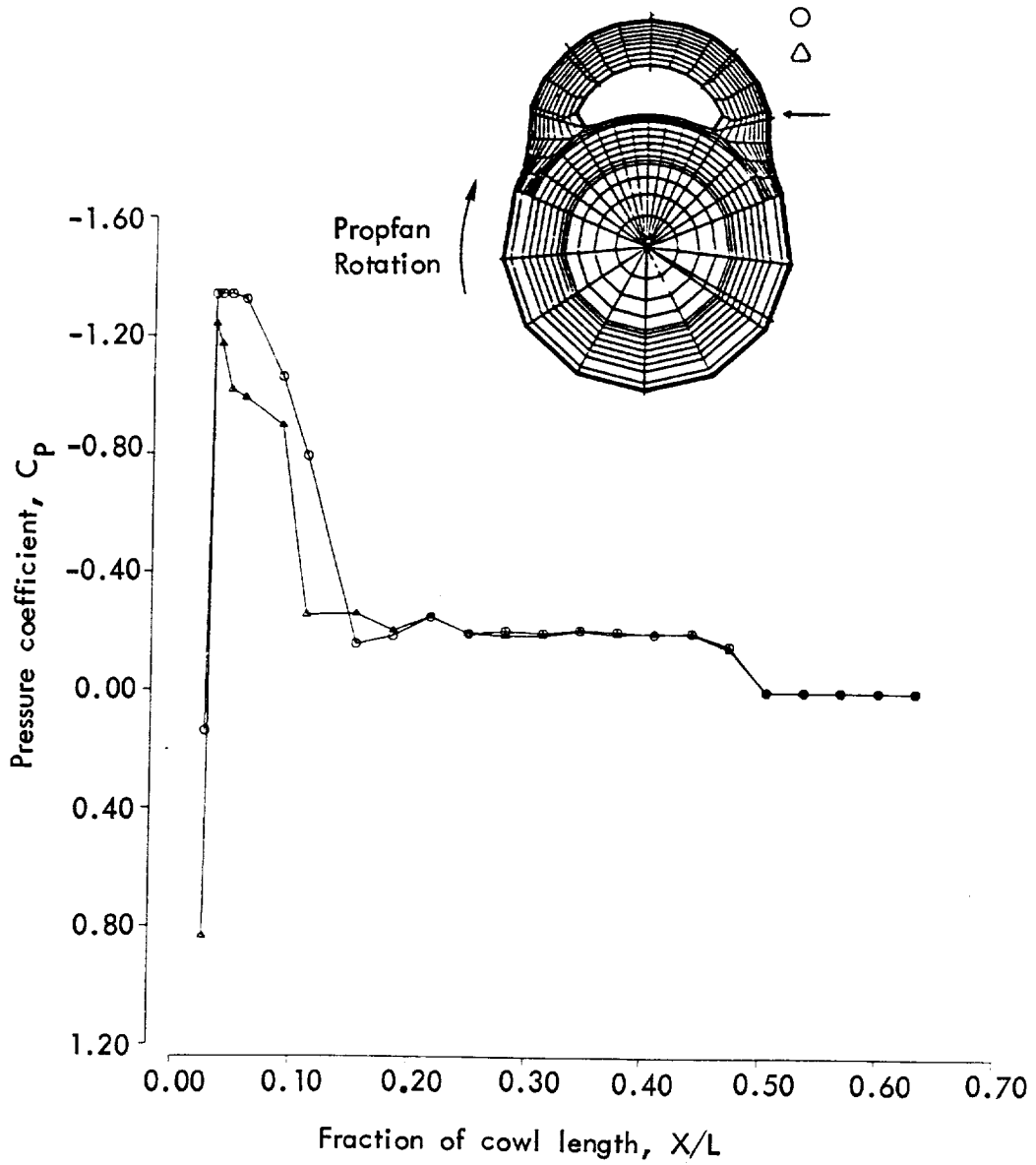
Sym	Run	Point	$M_o$	MFR
○	77	1	0.81	0.35
△	75	5	0.81	0.70



(b) Effect of mass flow ratio, propeller on, Mach = 0.8, top of cowl.

Figure 26. - Continued.

Sym	Run	Point	$M_o$	MFR
○	77	1	0.81	0.35
△	75	5	0.81	0.70



(c) Effect of mass flow ratio, propeller on, Mach = 0.8, leeward side of cowl.

Figure 26. - Concluded.

Sym	Run	Point	$M_o$	MFR
○	35	5	0.61	0.63
△	51	5	0.81	0.60

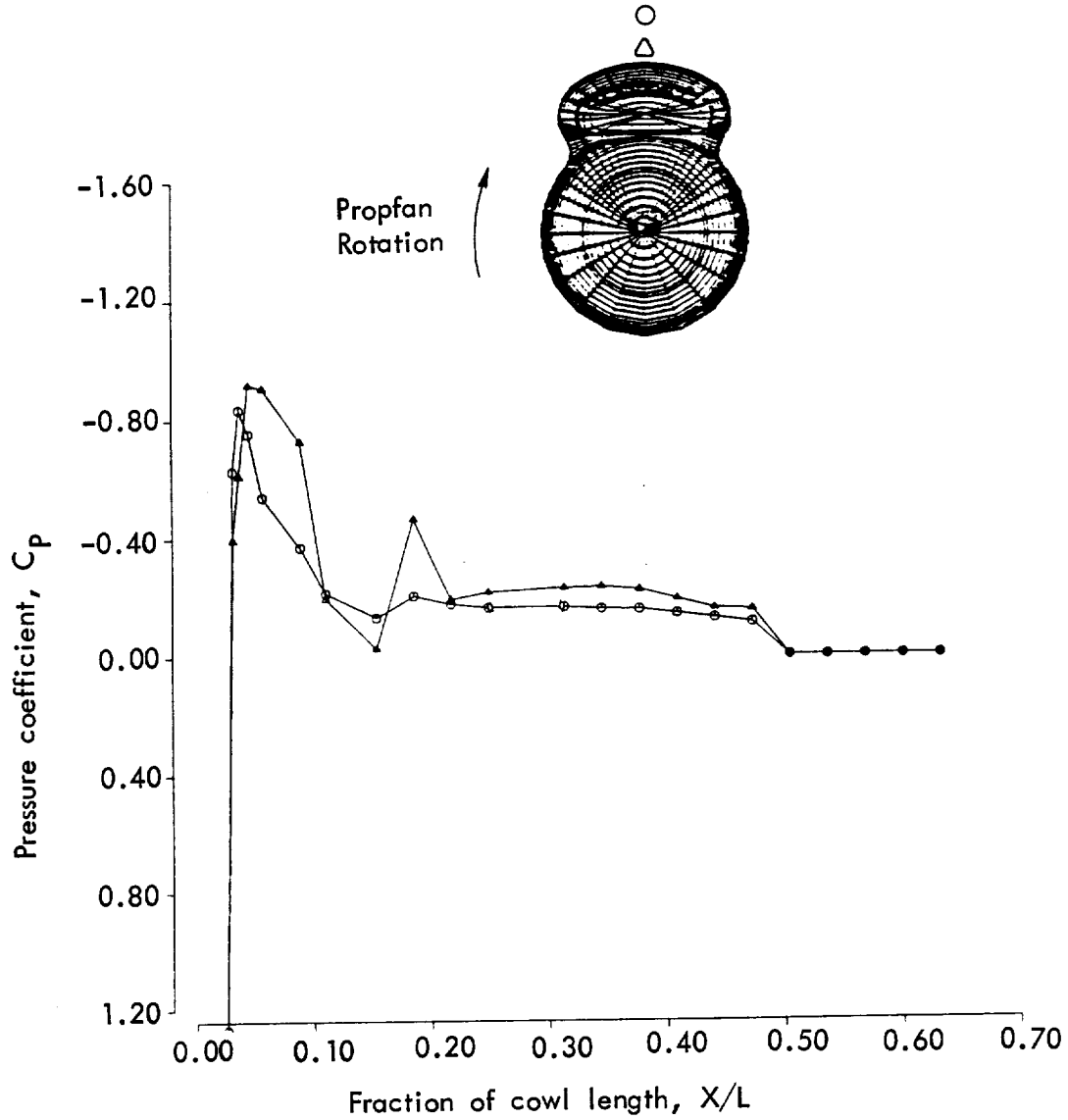
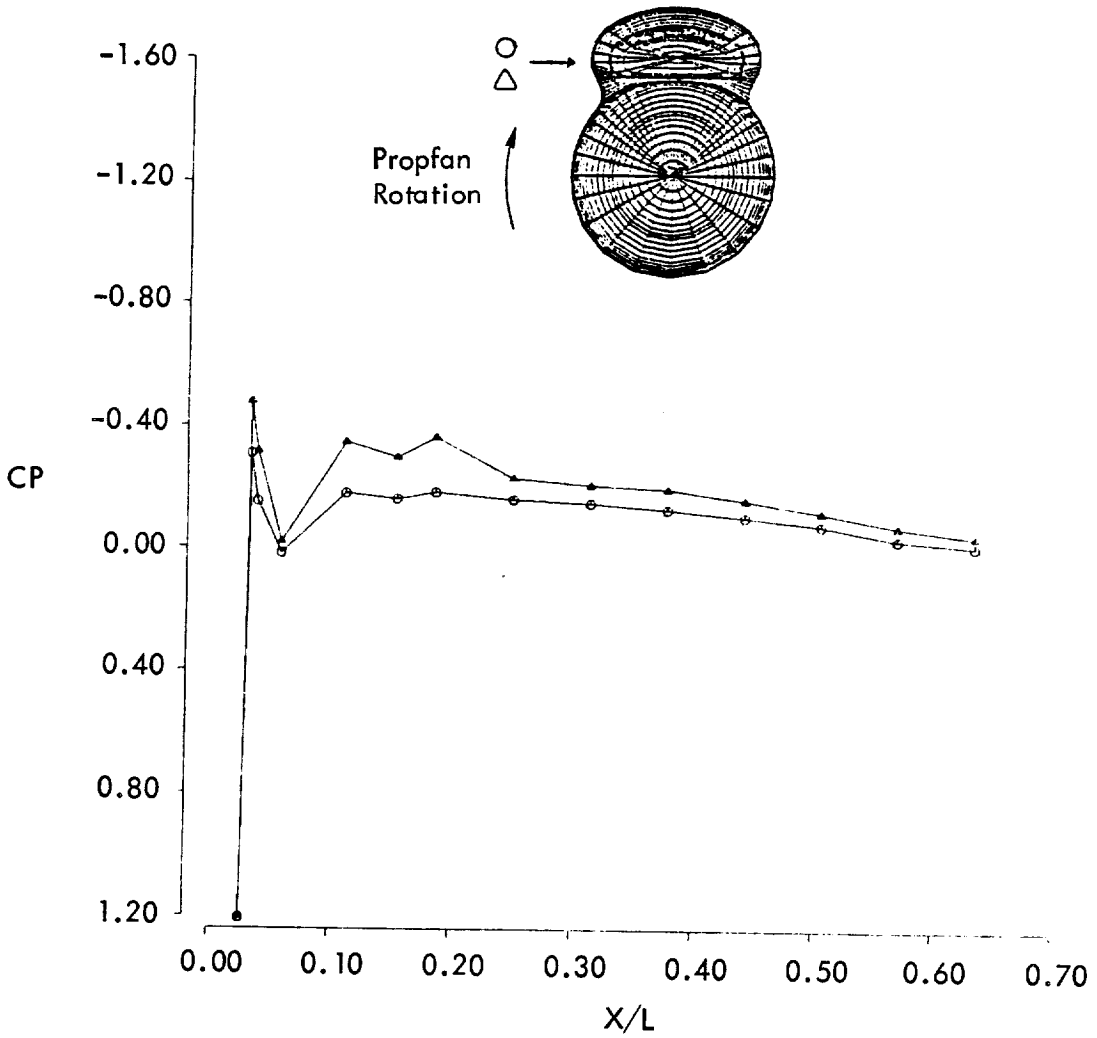


Figure 27. - Pressure distribution for single-scoop inlet with boundary layer diverter, effect of Mach number, propeller on, MFR = 0.6, top of cowl.

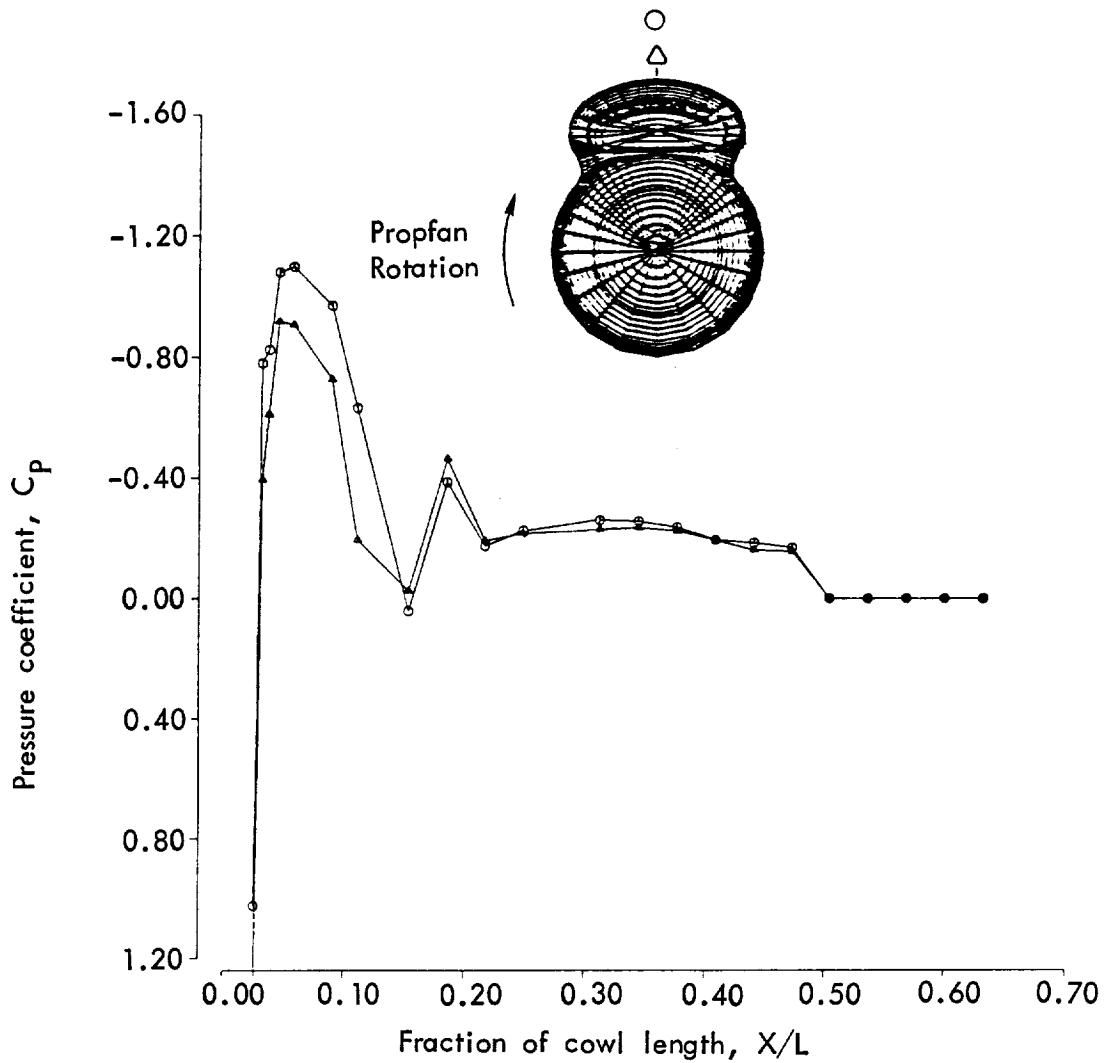
Sym	Run	Point	$M_\infty$	MFR
○	51	1	0.81	0.40
△	51	1	0.81	0.60



(a) Effect of mass flow ratio, propeller on, Mach = 0.81, windward side of cowl.

Figure 28. Pressure distribution for single-scoop inlet with boundary layer diverter.

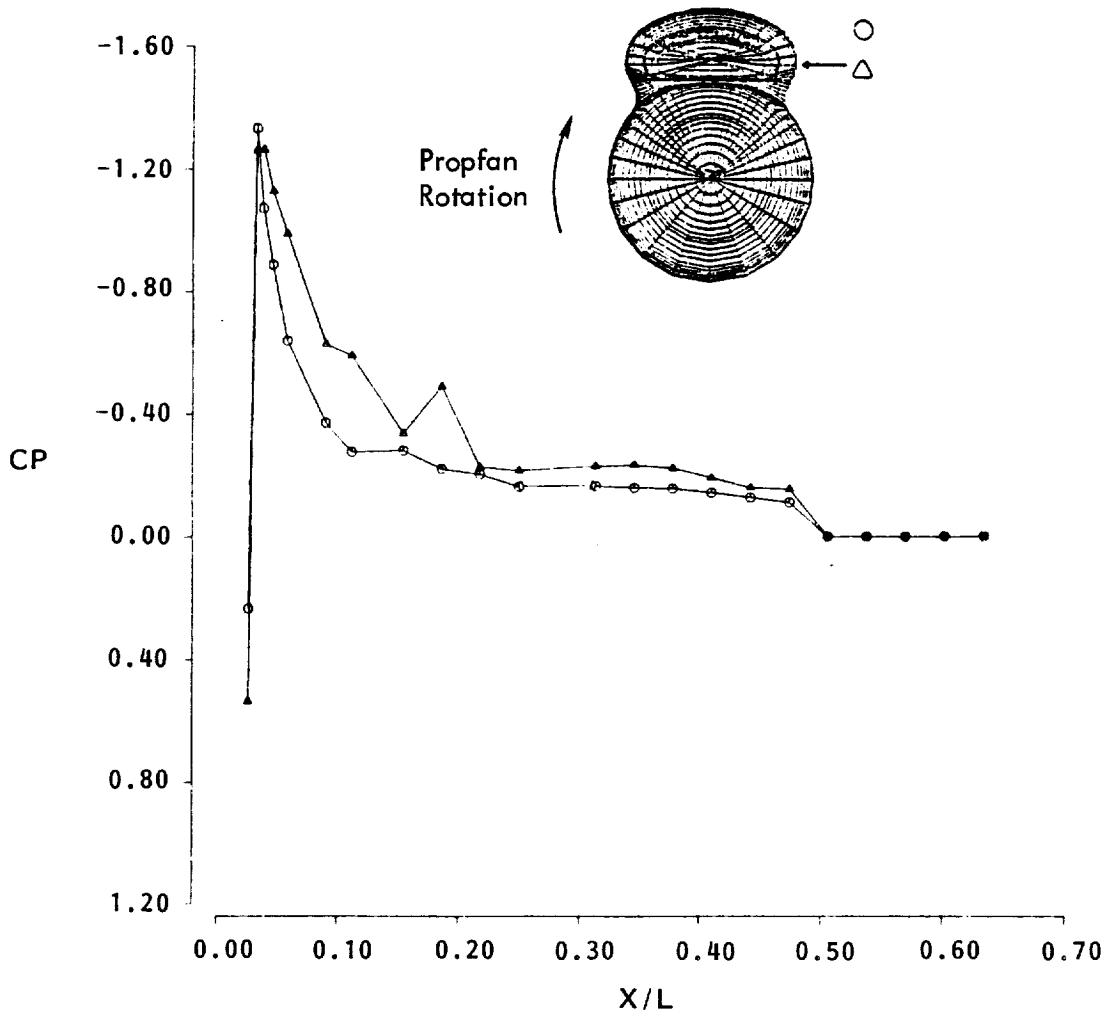
Sym	Run	Point	$M_o$	MFR
○	51	1	0.81	0.40
△	51	5	0.81	0.60



(b) Effect of mass flow ratio, propeller on, Mach = 0.81, top of cowl.

Figure 28. - Continued.

Sym	Run	Point	$M_o$	MFR
○	51	1	0.81	0.40
△	51	5	0.81	0.60



(c) Effect of mass flow ratio, propeller on, Mach = 0.81, leeward side of cowl.

Figure 28. - Continued.

$\beta^\circ$	$C_T$	Sym	Run	Point	$M_\infty$	MFR
56.5	.225	○	49	1	0.81	0.44
58.5	.318	△	53	7	0.81	0.47

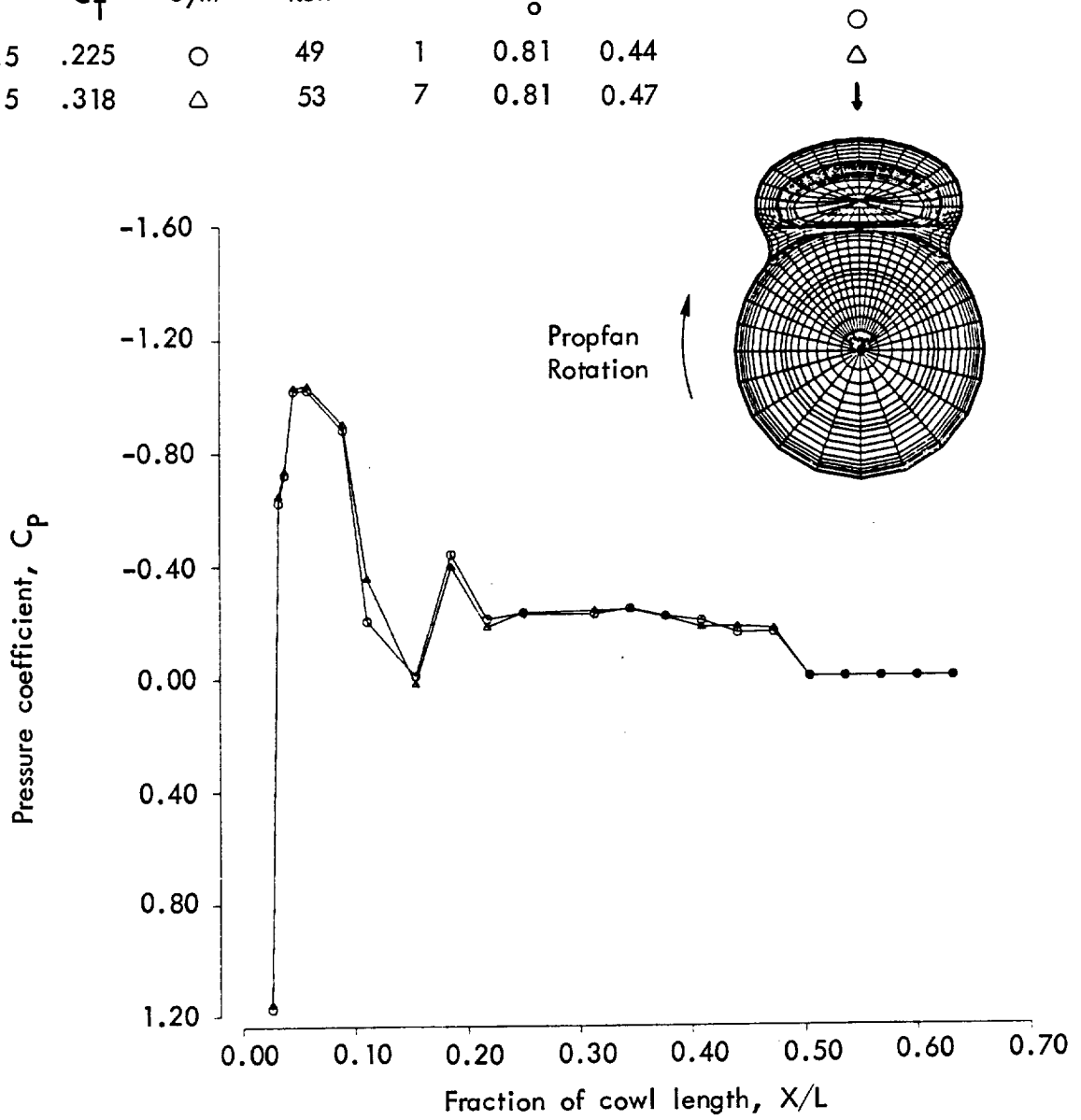
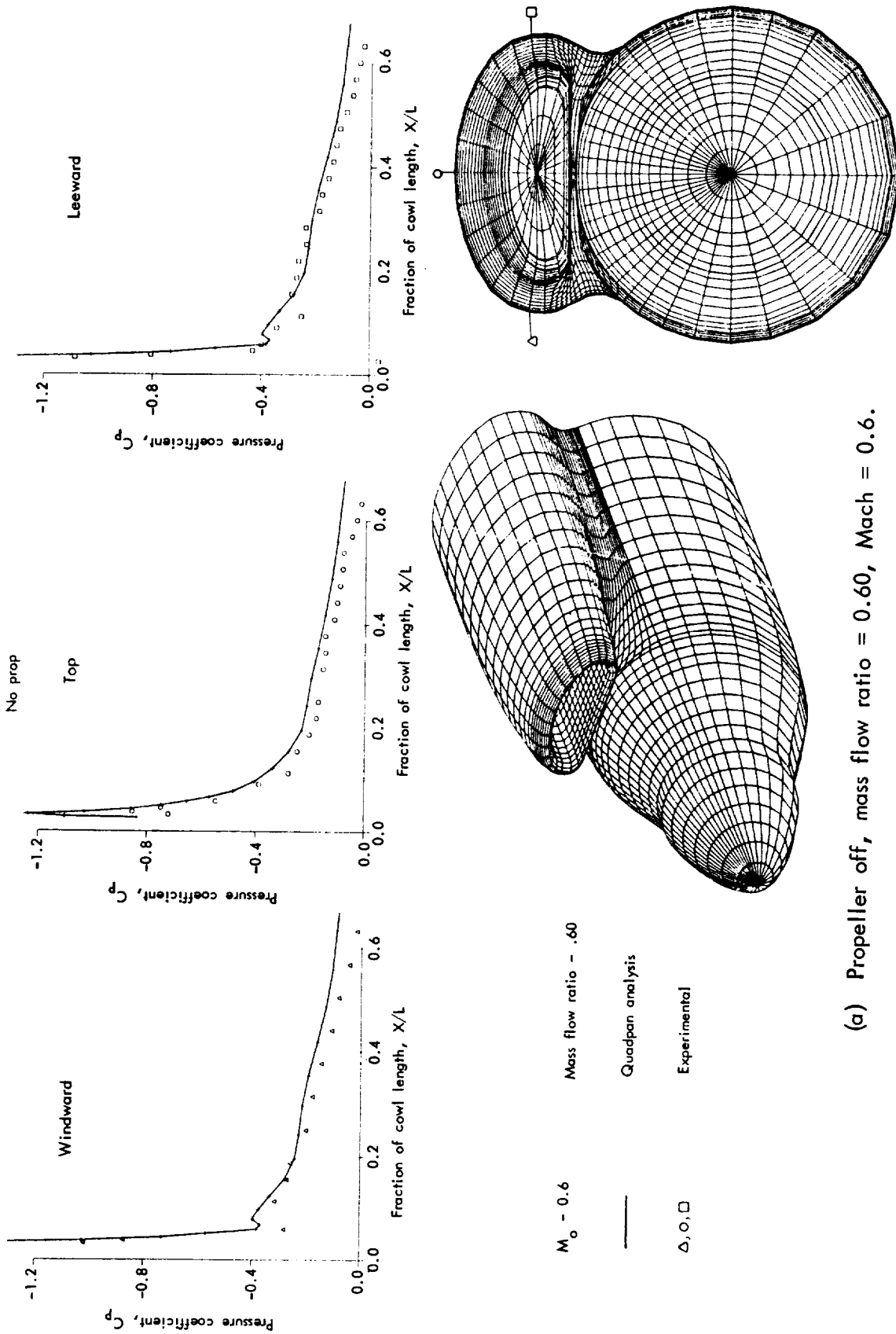


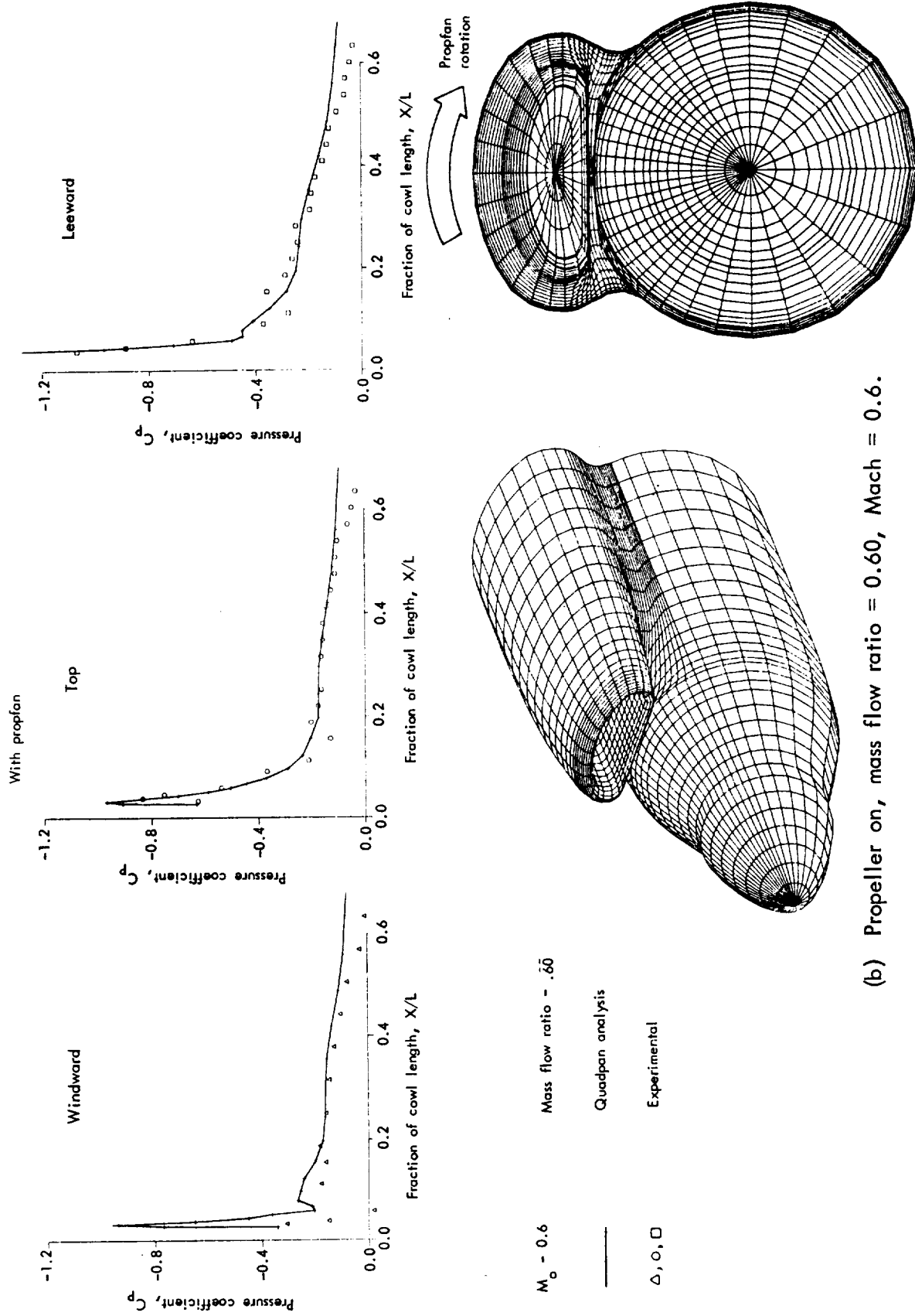
Figure 29. - Pressure distribution for single-scoop inlet with boundary layer diverter, effect of propeller blade angle, top of cowl.



(a) Propeller off, mass flow ratio = 0.60, Mach = 0.6.

Figure 30. - Calculated and experimental pressure distributions for single-scoop inlet with boundary layer diverter.





(b) Propeller on, mass flow ratio = 0.60, Mach = 0.6.

Figure 30. - Concluded.

$M_o = 0.60$   
 $MFR = 0.7$   
 No prop

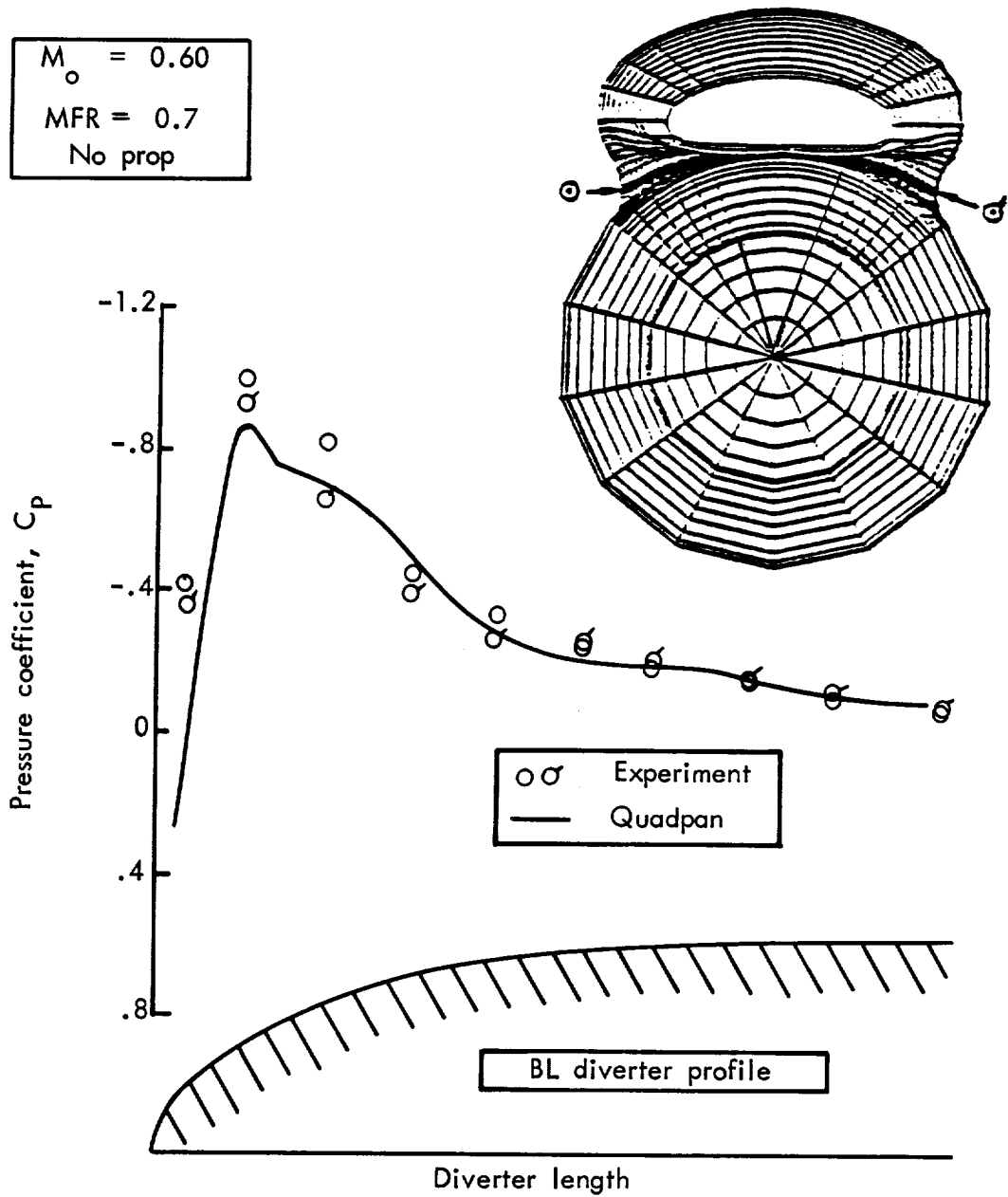
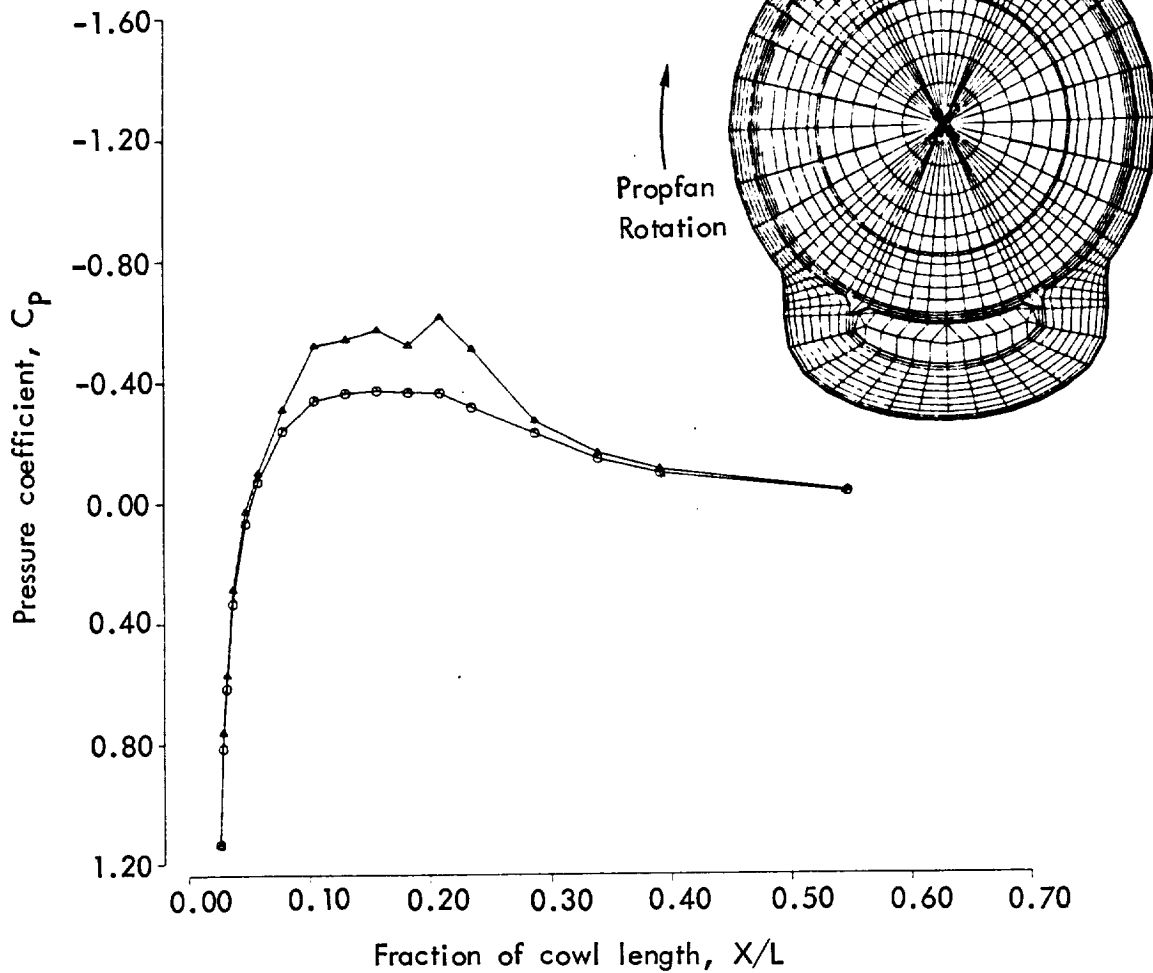


Figure 31. - Calculated and experimental pressure distributions for the boundary layer diverter of the single-scoop inlet.

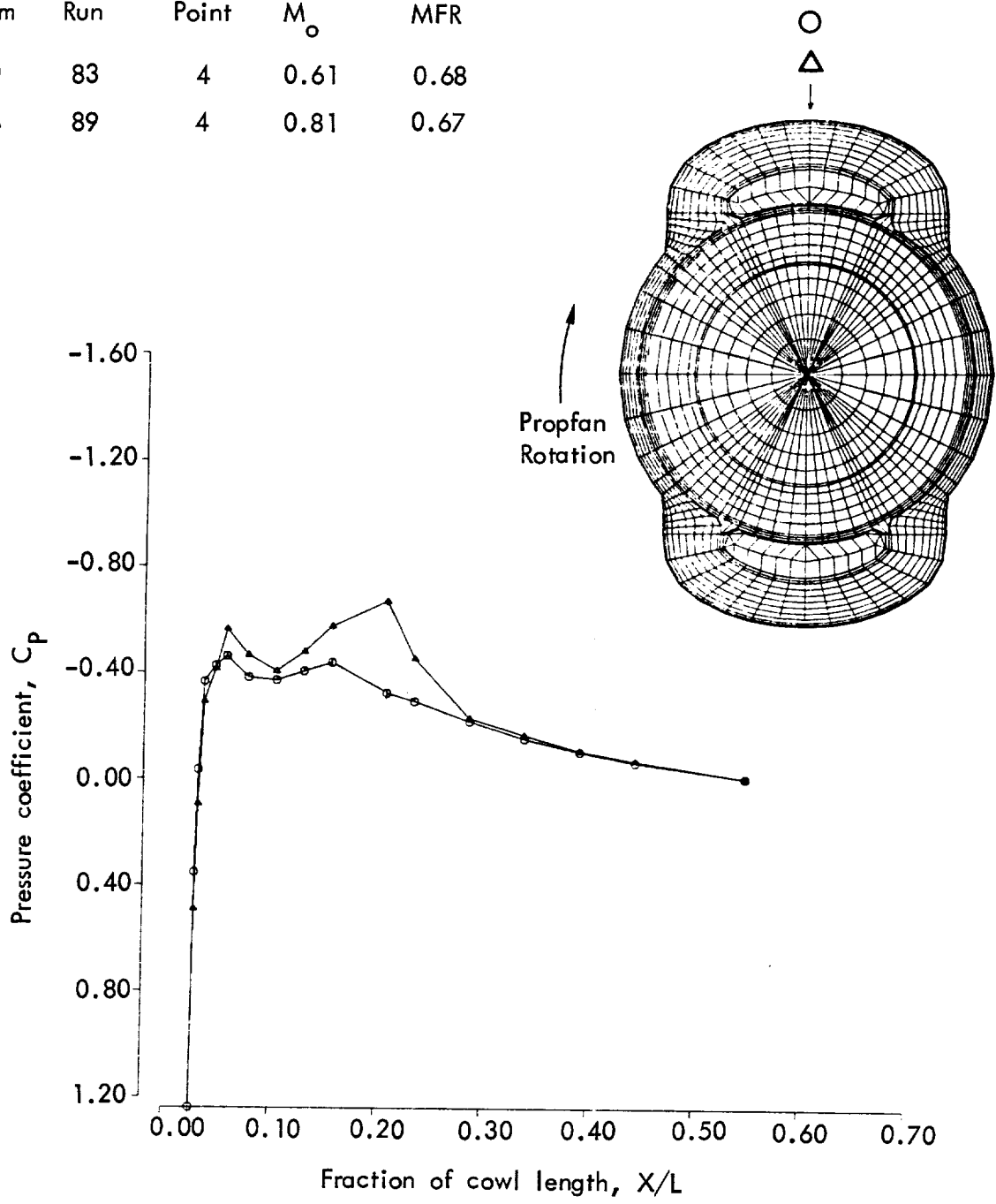
Sym	Run	Point	$M_o$	MFR
○	83	4	0.61	0.68
△	89	4	0.81	0.67



(a) Effect of Mach number, propeller on, MFR = 0.68, windward side of cowl.

Figure 32. - Pressure distribution for flush twin-scoop inlet.

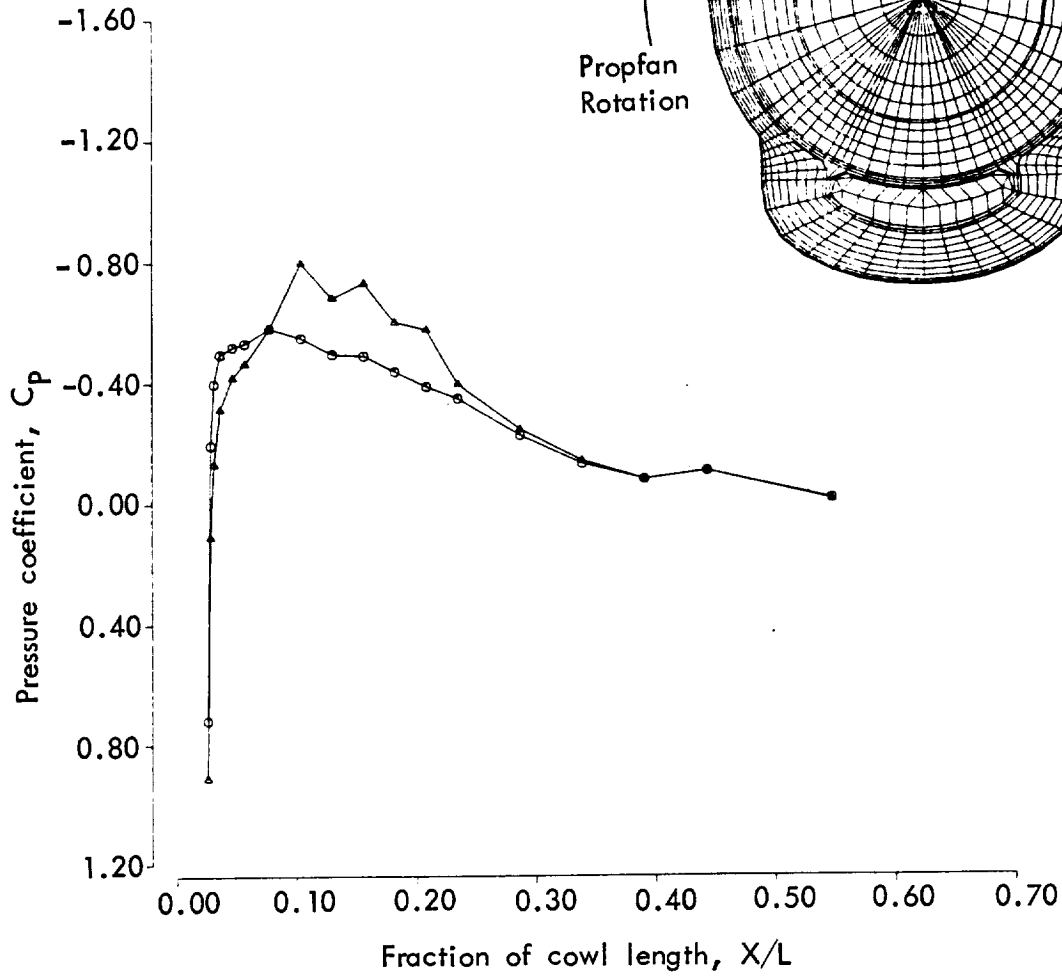
Sym	Run	Point	$M_o$	MFR
○	83	4	0.61	0.68
△	89	4	0.81	0.67



(b) Effect of Mach number, propeller on, MFR = 0.68, top of cowl.

Figure 32. - Continued.

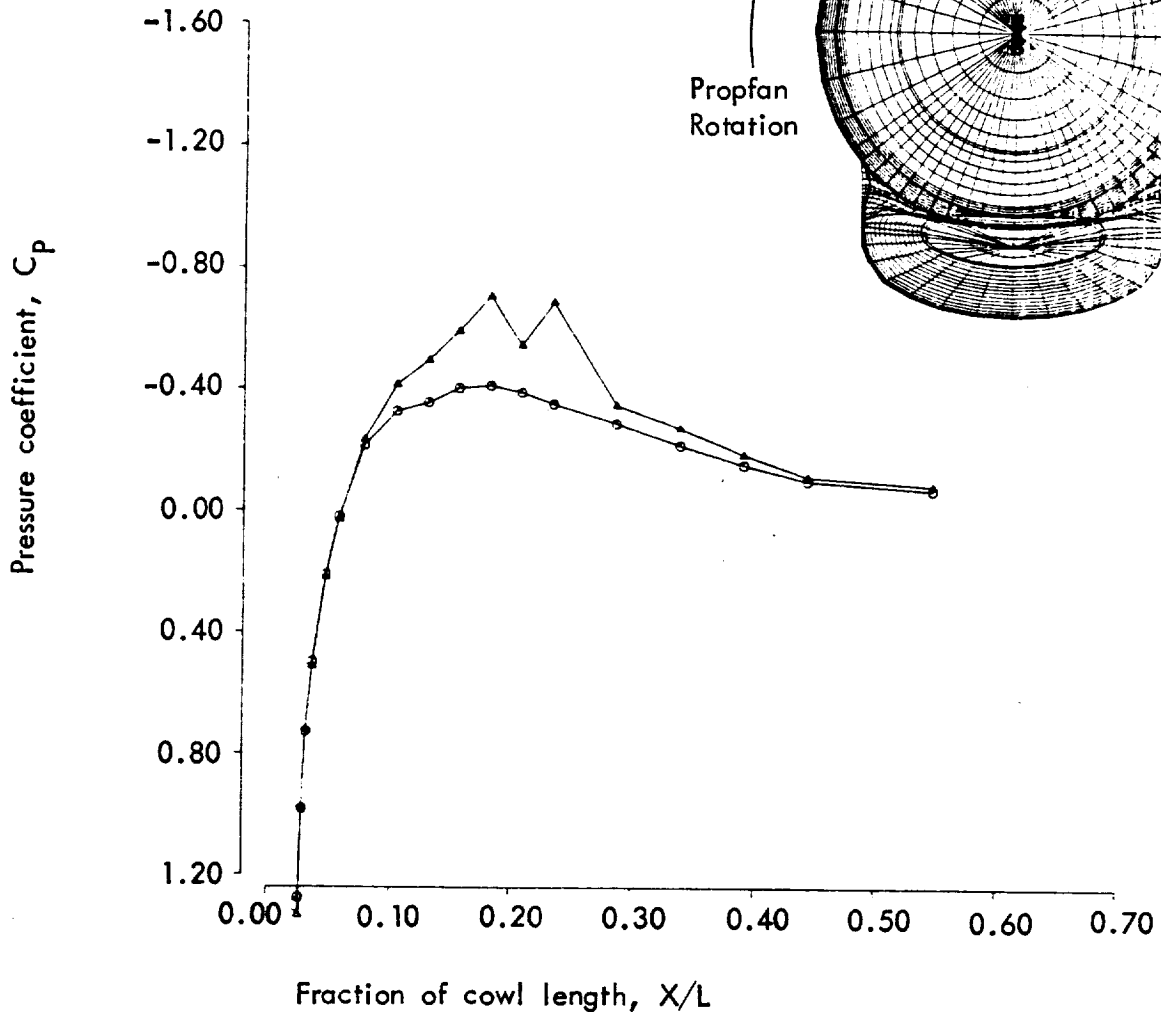
Sym	Run	Point	$M_o$	MFR
○	83	4	0.61	0.68
△	89	4	0.81	0.67



(c) Effect of Mach number, propeller on, MFR = 0.68, leeward side of cowl.

Figure 32. - Concluded.

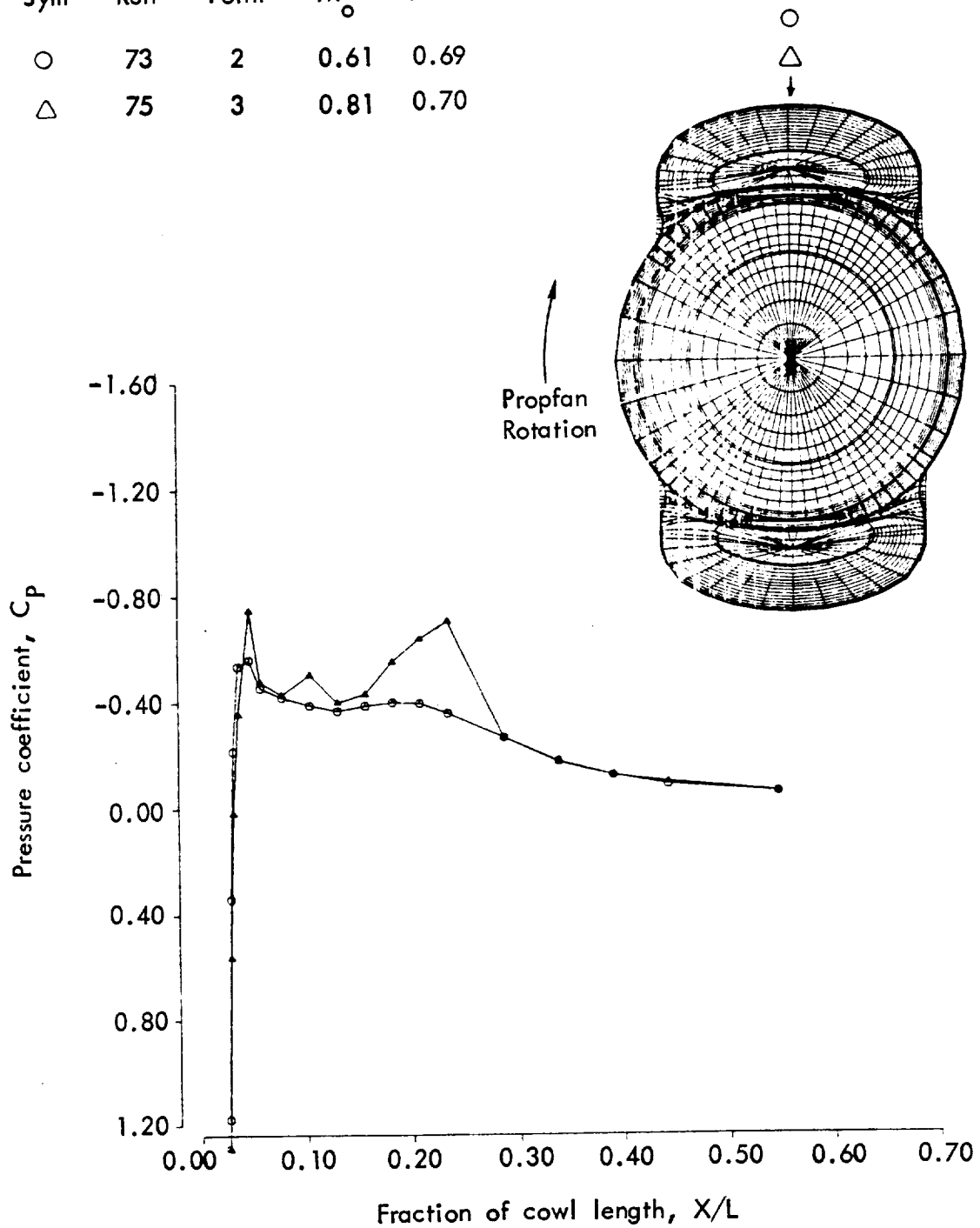
Sym	Run	Point	$M_o$	MFR
○	73	2	0.61	0.69
△	75	3	0.81	0.70



(a) Effect of Mach number, propeller on, MFR = 0.70, windward side of cowl.

Figure 33. - Pressure distribution twin-scoop inlet with boundary layer diverter.

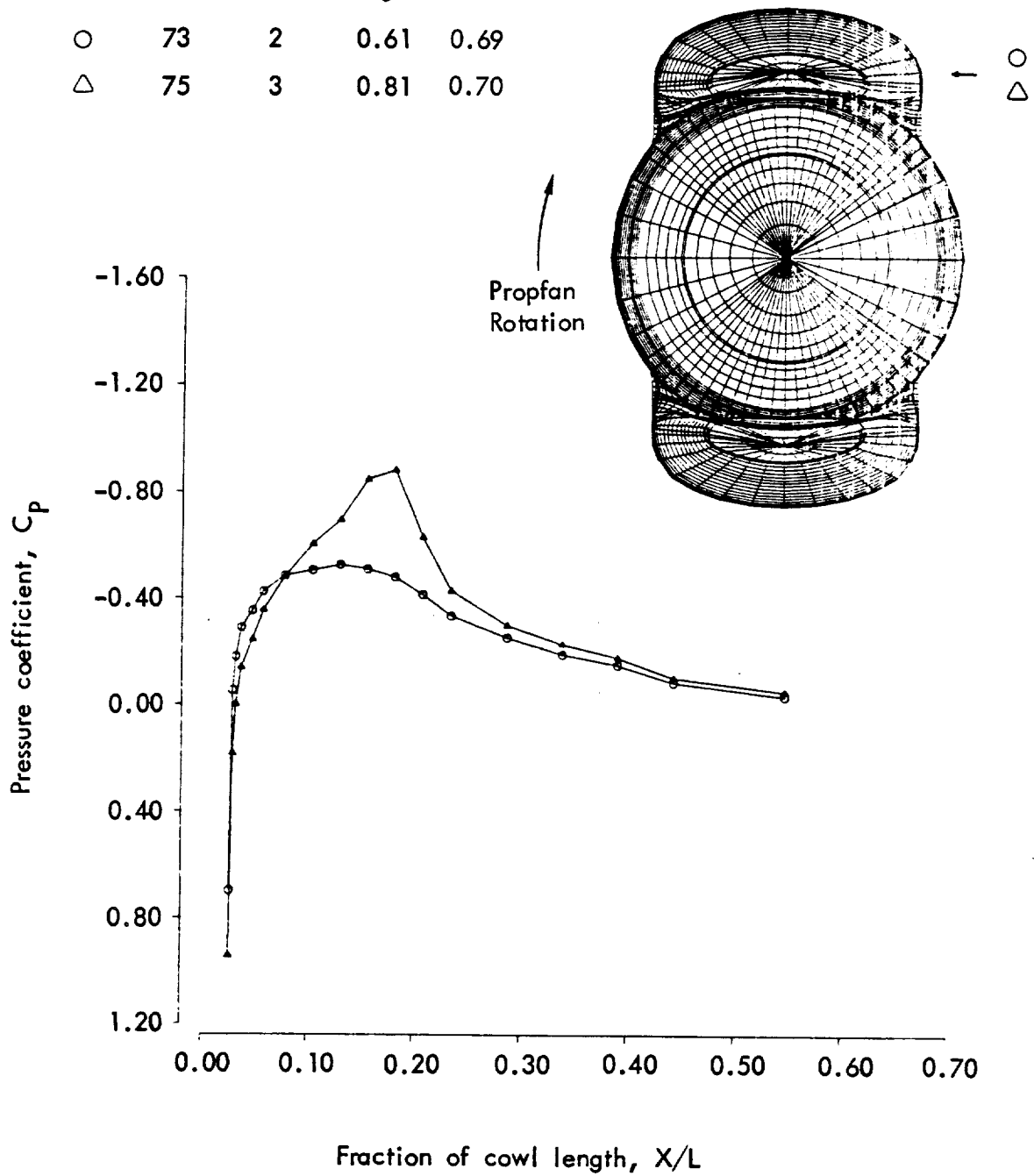
Sym	Run	Point	$M_o$	MFR
○	73	2	0.61	0.69
△	75	3	0.81	0.70



(b) Effect of Mach number, propeller on, MFR = 0.70, top of cowl.

Figure 33. - Continued.

Sym	Run	Point	$M_o$	MFR
○	73	2	0.61	0.69
△	75	3	0.81	0.70



(c) Effect of Mach number, propeller on, MFR = 0.70, leeward side of cowl.

Figure 33. - Concluded.



Effect of Mach Number - The pressure distributions for the Mach = 0.80 cases differ from the pressure distributions at lower Mach numbers, because of shocks forming on the cowl. Consequently, both the pressure peaks at the front of the cowl and the pressure distributions farther aft on the cowl can be substantially altered. The effect of Mach number is shown in Figure 23 (presented earlier) for the annular inlet, for a mass flow ratio of 0.5, propeller on. For a Mach Number of 0.60, the pressure distribution is entirely subsonic. However, the pressure distribution for Mach = 0.80 has a higher peak at the front of the cowl and a strong shock farther aft.

Pressure distributions for the flush single-scoop inlet are shown in Figures 25(a), 25(b), and 25(c) for the windward side, top, and leeward side of the scoop. The effect of Mach number is minor for the windward side, but for the top and leeward side, the peak pressure at the inlet highlight is reduced somewhat and a shock forms just downstream of the highlight. The cowl pressure distributions for the single-scoop inlet with boundary layer diverter are similar, as shown for the cowl top in Figure 27.

For the flush twin-scoop inlet, similar Mach number effects are present, but not as strongly as for any of the single-scoop inlets. As shown in Figures 32(a), 32(b), and 32(c), the pressure levels are higher for Mach = 0.80, with some evidence of shocks. However, there is less of a difference between Mach = 0.60 and Mach = 0.80 than for a single-scoop inlet. In fact, the twin-scoop inlet at the cowl top has a pressure distribution more similar to the annular inlet. The same is true for the twin-scoop inlet with boundary layer diverter, but it has slightly stronger shocks (Figures 33(a), 33(b), and 33(c)).

Effect of Mass Flow Ratio - The effect of lowering mass flow ratio, and thereby increasing flow spillage, is similar for all inlets. As the flow spills out of the blocked inlet, velocities are increased over the front of the cowl and pressure coefficients become more negative. Figure 24 shows this effect for the annular inlet, propeller on. This effect is much the same for the single-scoop inlet without boundary layer diverter, as presented in Figures 26(a), 26(b), and 26(c) for the top and sides of the cowl. Again, higher velocities at the front of the cowl are the result of the lower mass flow ratio, but there would appear to be more spillage from the top of the cowl than from the sides. This same effect is present for the single-scoop inlet with boundary layer diverter (Figure 28(a), 28(b), and 28(c)).

Effect of Propeller Blade Angle - The effect of propeller blade angle appears to be minor in terms of nacelle surface pressures. Typical data are presented in Figure 29 for the single-scoop inlet with boundary layer diverter with a propeller blade pitch angle change of two degrees - from 56.6 to 58.5 degrees, corresponding to thrust coefficients of 0.225 and 0.318, respectively. Although this is a significant increase in thrust coefficient, very little change in the pressure distribution is evident for the cowl top, which is shown in the figure, or for the windward and leeward sides of the cowl.

Correlation of Calculated Cowl Pressures - Figures 30 and 31 present typical correlations of calculated nacelle surface pressures with experiment for the single-scoop nacelle with boundary layer diverter. The calculations were made with Lockheed's QUADPAN panel program (Reference 6). Propeller off data are presented in Figure 30(a) for the windward side, top, and leeward sides of the scoop inlet and show excellent correlation. Good correlation was also obtained for the propeller on case (Figure 30(b)), and the higher (more negative) pressure coefficient levels on the leeward side of the scoop due to propeller induced swirl are predicted in theory. Correlation is also good for pressures predicted in the channel of the boundary layer diverter Figure 31. This predictive capability was of value in shaping the profile of the boundary layer diverter to avoid sharp pressure peaks and associated shocks.

## Nacelle Drag

The single-scoop inlets were tested for pressure data and total thrust in GUN-I. In GUN-II these inlets were modified to incorporate an inlet/forebody cowl drag balance. This balance, as described earlier, was designed to measure the force on the cowl between the spinner and the nacelle maximum cross-section, including the inlet. By removing the inlet internal drag and the tare due to static pressure acting on the internal cowl surface, the net force on the external cowl surface was determined. Good cowl drag data were obtained, both with the propeller operating and with the blades removed. When the twin-scoop and annular inlets were designed and built for GUN-III, the same cowl drag balance arrangement was also utilized for them. The GUN-III drag data are incomplete, however, because serious strain gage problems occurred frequently during the test. The drag data on the twin-scoop inlet with diverter and on the nacelle with no inlet are considered to be of high quality, but no drag information is available for the annular inlet or the twin-scoop inlet without diverter.

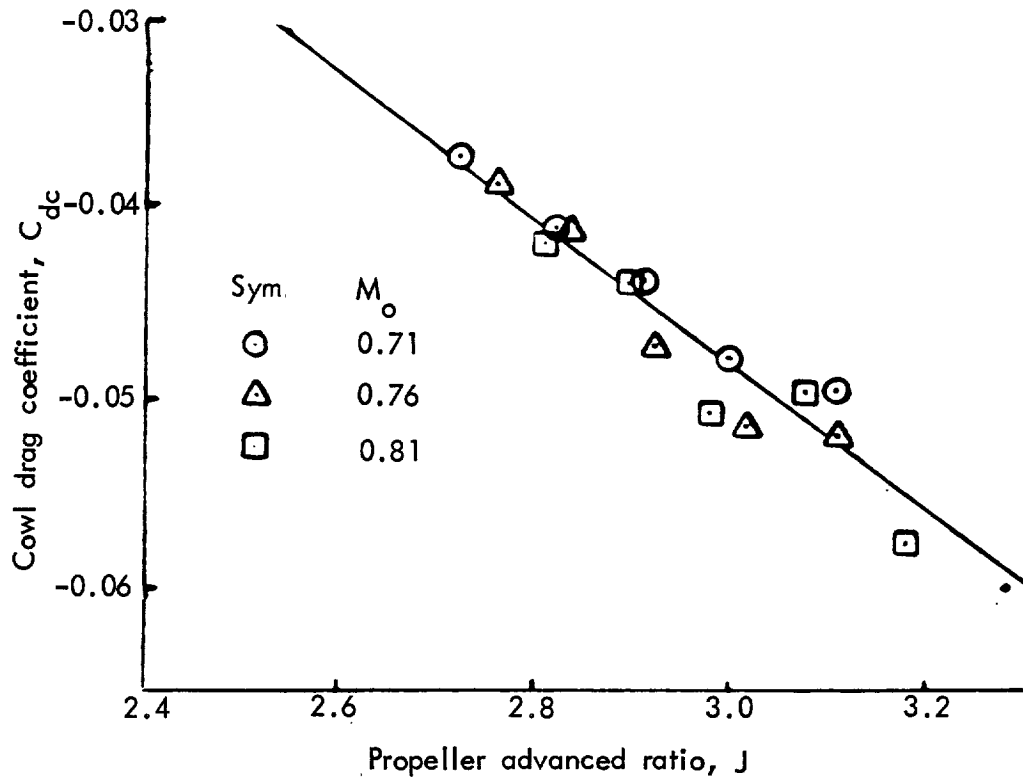
The drags measured by the cowl drag balance and presented here are all negative, reflecting the forward thrust developed by the accelerated flow over the forward-facing area. Of course, in an isolated installation, the net arithmetic sum of the cowl and spinner drag will always be positive. Even though they do not represent the net drag of the installation, it is of value to look at the cowl drags separately. This is because changes in propeller performance due to different blockage-induced, back-pressure patterns are not included herein. Changes in spinner surface pressures, however, are also not included and this is a disadvantage. At the present time, there is no real good way to obtain the breakdown between back-pressure effects on the spinner drag and those same effects on the propeller performance.

Both with the propeller operating and with the blades removed, the measured coefficients become more negative with increasing forward speed. Figure 34, (a) through (i), shows typical variations of cowl drag coefficient,  $C_{dc}$ , with propeller advance ratio,  $J$ . The slope of  $C_{dc}$  versus  $J$  is seen to be independent of blade angle, mass flow ratio (controlled by the restriction imposed by the size of the flow-through nozzle), and freestream Mach number, although blade angle and mass flow ratio significantly affect the levels of the curves.

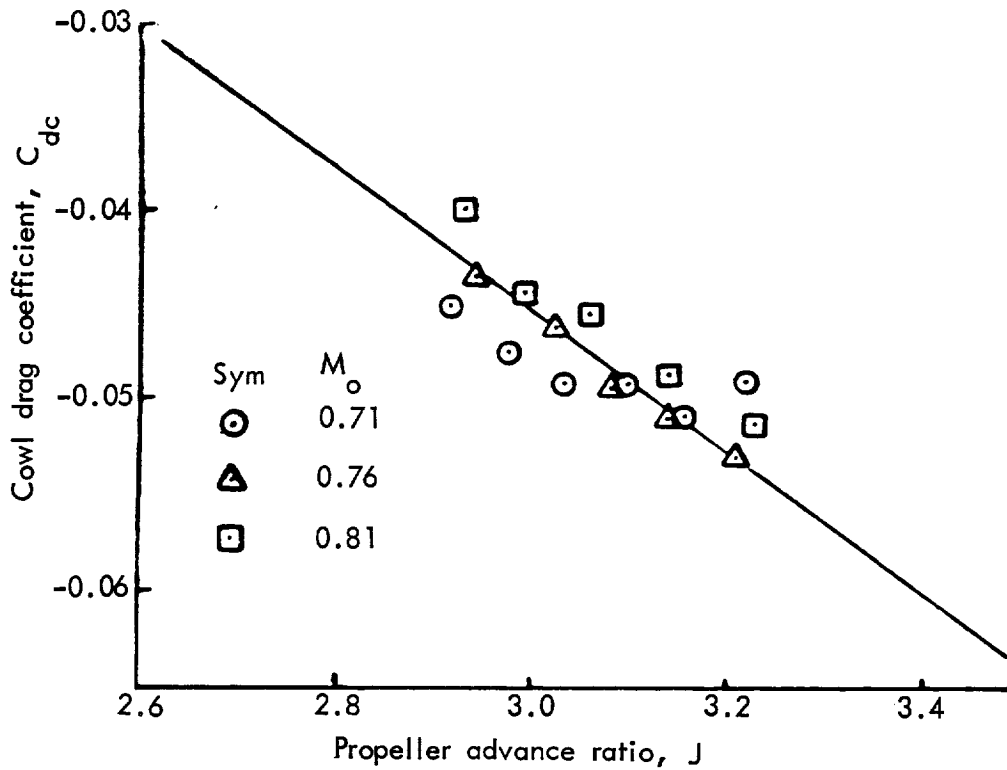
The  $C_{dc}$  versus  $J$  slopes are equally consistent for the other configurations, not shown. This makes it possible to reduce the volume of the cowl drag data by eliminating  $J$  as a plotted variable. First the following slopes of  $C_{dc}$  versus  $J$  were selected from the plots of all runs.

Configuration	Slope
Single-Scoop Inlet, with and without Diverter	-0.0375
Twin-Scoop Inlet with Diverter	-0.0500
Nacelle without Inlet	-0.0250

These slopes were then used to project the drag coefficients at all test

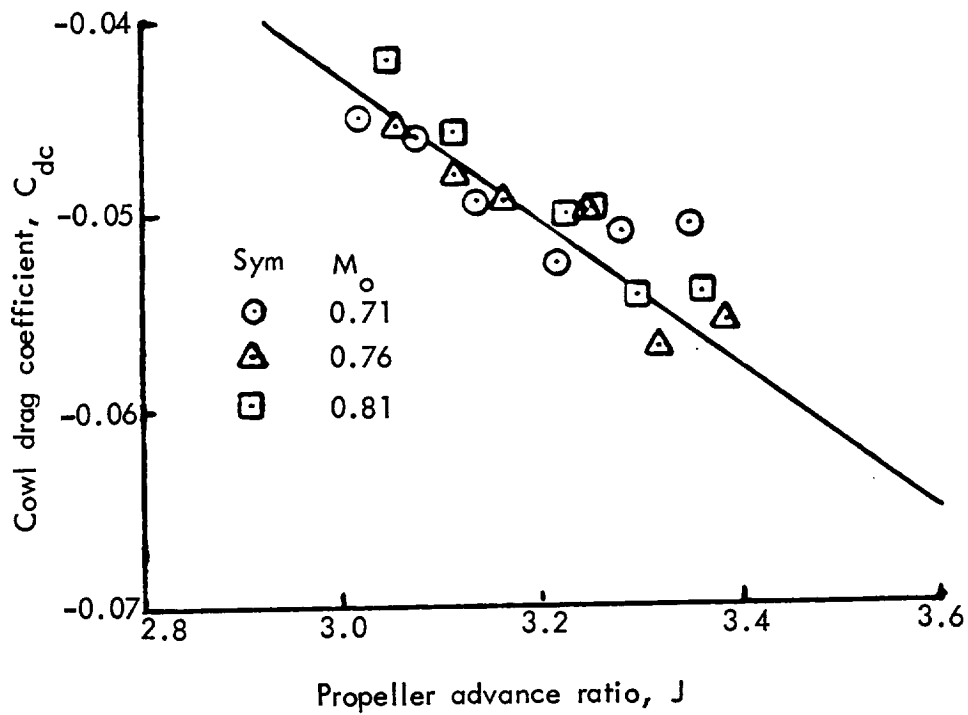


(a) Runs 101-103,  $A_{ex}/A_{th} = 0.40$ ,  $\beta = 55.2$  deg.

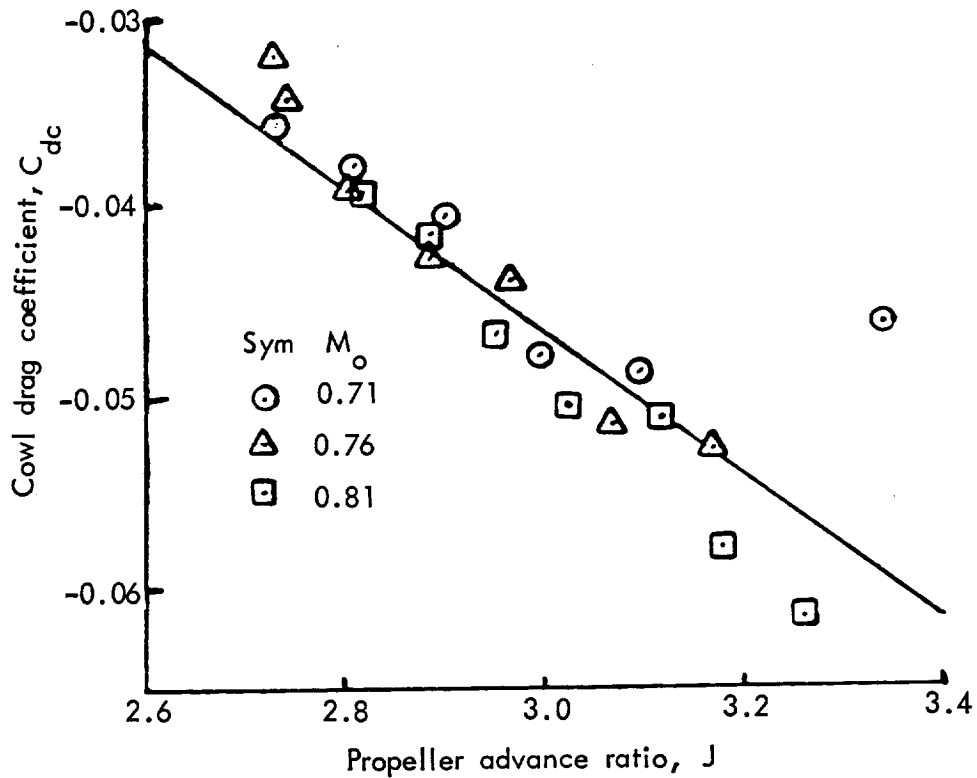


(b) Runs 104-106,  $A_{ex}/A_{th} = 0.40$ ,  $\beta = 57.2$  deg.

Figure 34. - Measured cowl drag coefficients versus propeller advance ratio, single-scoop inlet with diverter,  $h/D_p = 0.006$ , GUN II test.

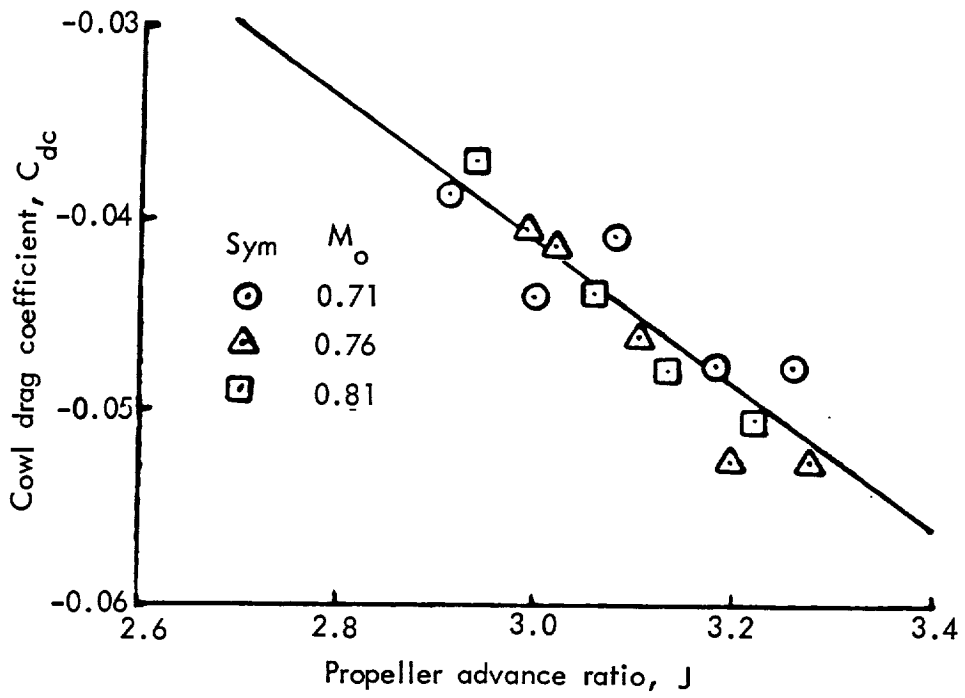


(c) Runs 98-100,  $A_{ex}/A_{th} = 0.40$ ,  $\beta = 58.2$  deg.

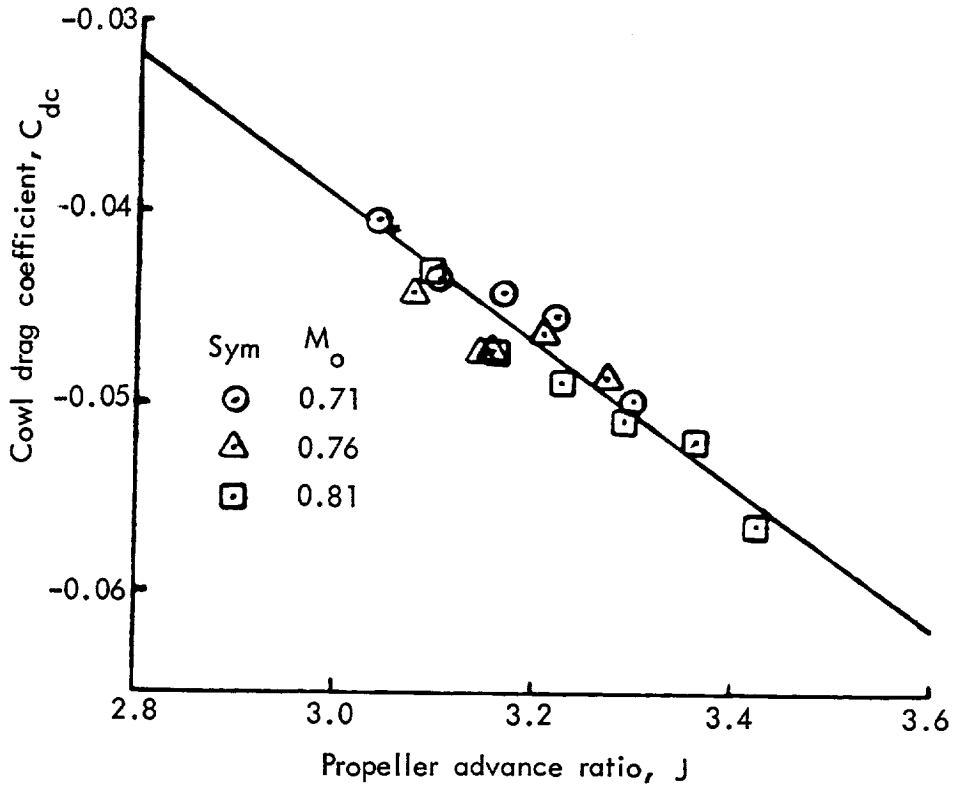


(d) Runs 92-94,  $A_{ex}/A_{th} = 0.60$ ,  $\beta = 55.2$  deg.

Figure 34. - Continued.

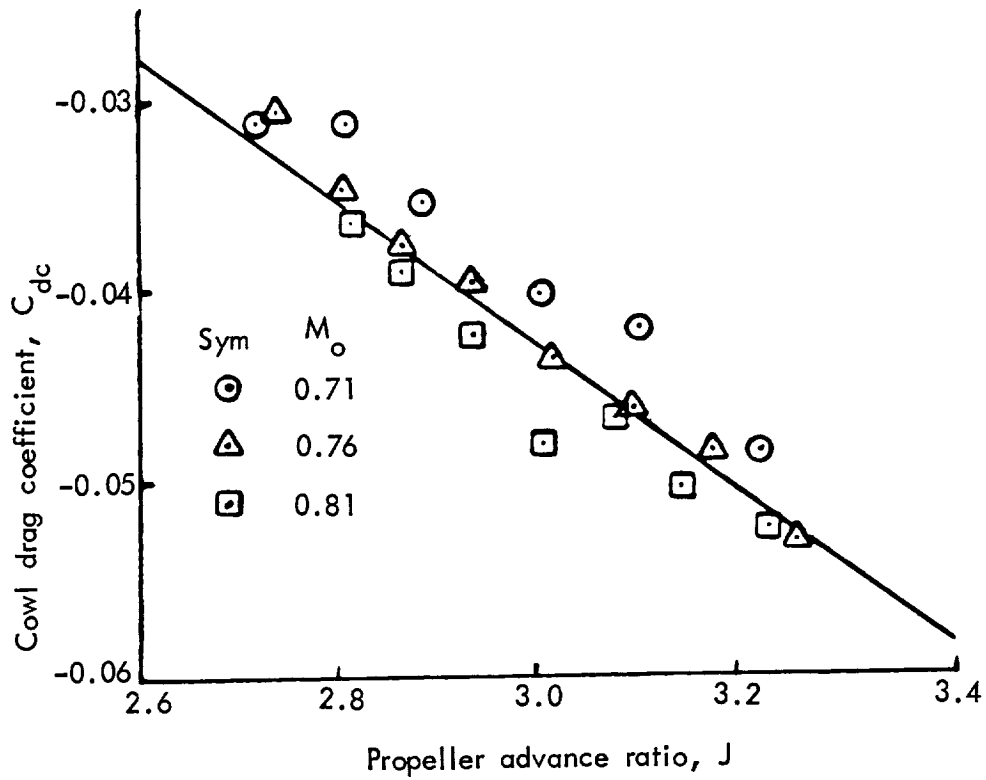


(e) Runs 89-91,  $A_{ex}/A_{th} = 0.60$ ,  $\beta = 57.2$  deg.

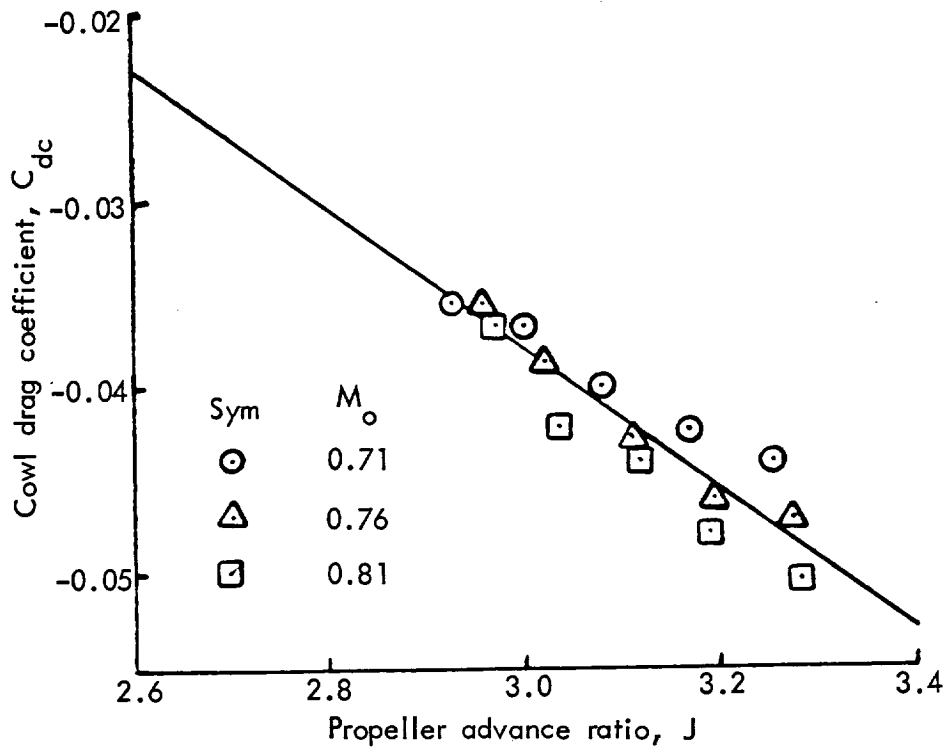


(f) Runs 95-96,  $A_{ex}/A_{th} = 0.60$ ,  $\beta = 58.2$  deg.

Figure 34. - Continued.

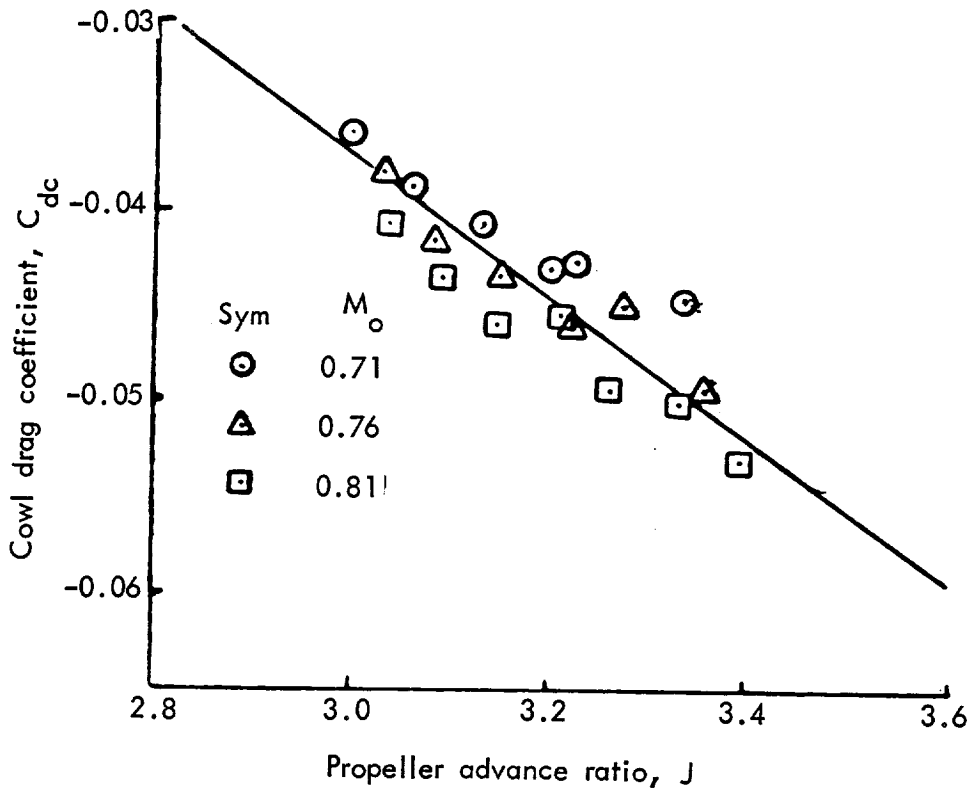


(g) Runs 83-85,  $A_{ex}/A_{th} = 0.80$ ,  $\beta = 55.2$  deg.



(h) Runs 86-88,  $A_{ex}/A_{th} = 0.80$ ,  $\beta = 57.2$  deg.

Figure 34. - Continued.



(i) Runs 80-82,  $A_{ex}/A_{th} = 0.80$ ,  $\beta = 58.2$  deg

Figure 34. - Concluded.

*[Handwritten signature]*

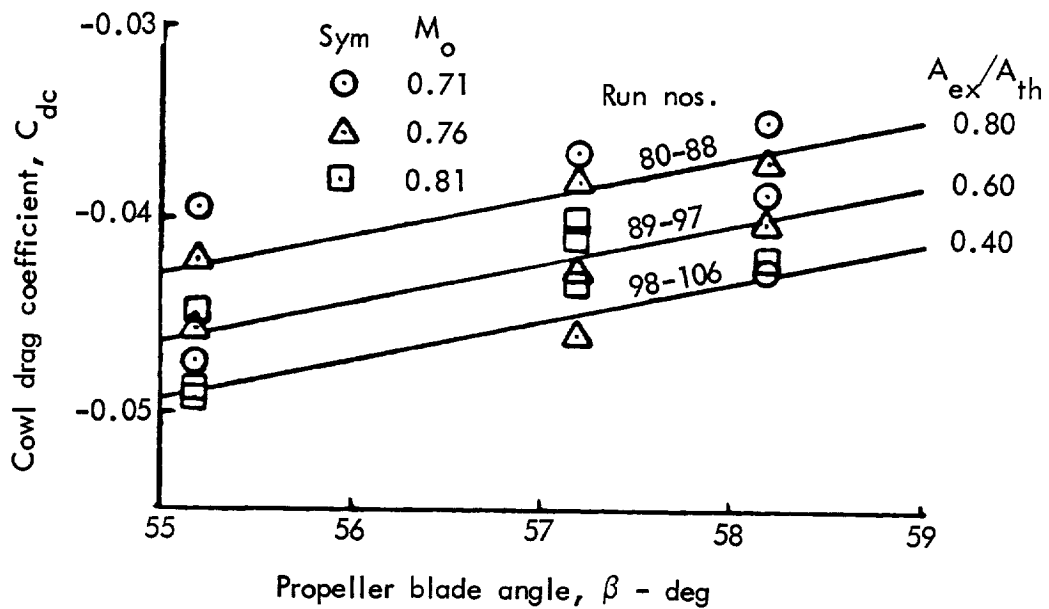


points in each run to the expected intercepts at  $J = 3$ , which is a typical advance ratio for Mach = .8 cruise. Wild points were deleted and the  $J = 3$  intercepts in each run were averaged. Figure 34(a), for example, was reduced to the following data elements.

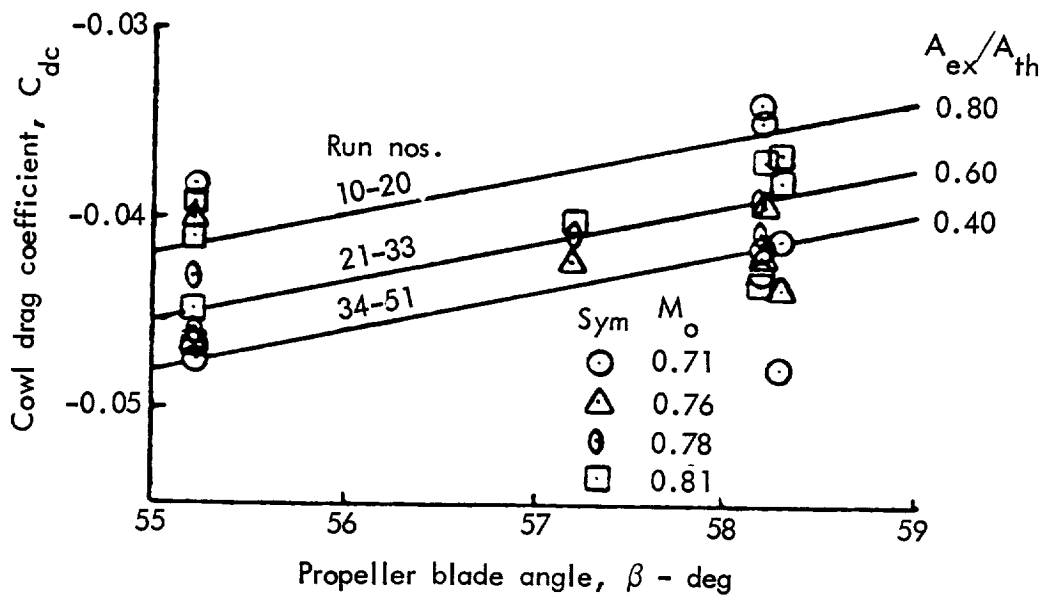
Run No.	No. of Pts.	Mo	Avg. Cdc at $J = 3$	Cdc/J
101, GUN-II	5	0.81	-0.0493	-0.0375
102, GUN-II	5	0.76	-0.0489	-0.0375
103, GUN-II	5	0.71	-0.0474	-0.0375

The drag coefficients at  $J = 3$  are plotted against blade angle in Figure 35. Using the slope of Cdc at  $J = 3$  versus blade angle from Figure 35, which is 0.002/degree, the expected drag coefficients at Beta = 57 degrees were calculated for all runs, eliminating blade angle as a plotted variable and arriving at the final drag coefficient curves, Figures 36 and 37. Both figures plot Cdc at  $J = 3$  and Beta = 57 degrees versus Mach number. In Figure 36 the drag scale is the same as in the preceding drag plots; in Figure 37, both the drag scale and the Mach number scale cover wider ranges, so that the operating and no-blades results can be compared.

0-2

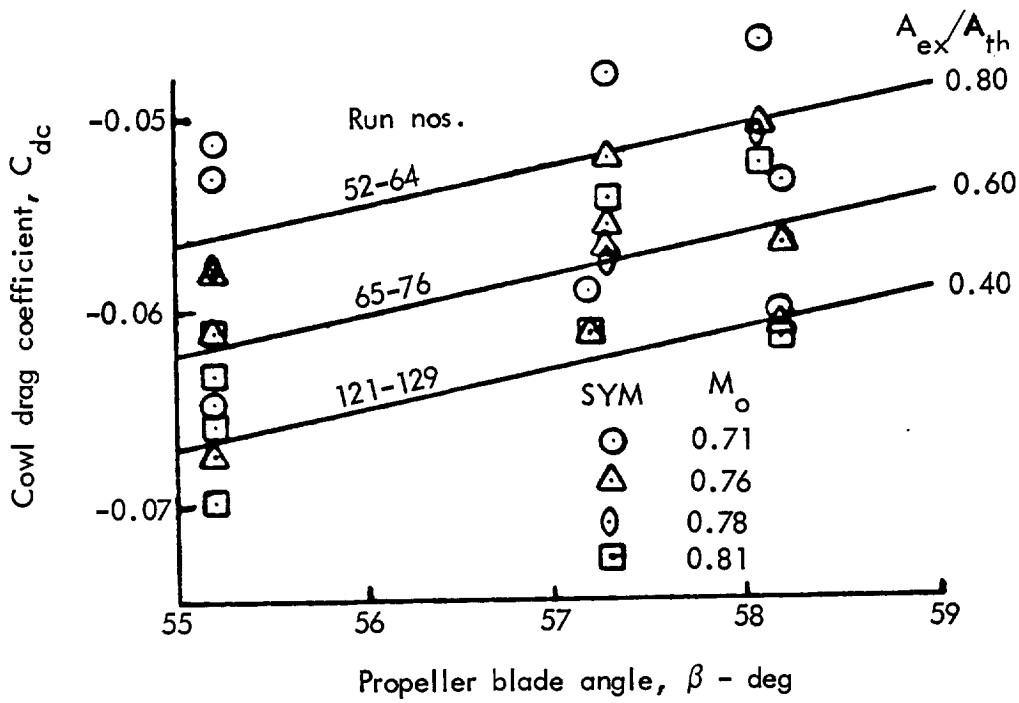


(a) GUN-II, single-scoop inlet with diverter,  $h/D_p = 0.006$ .

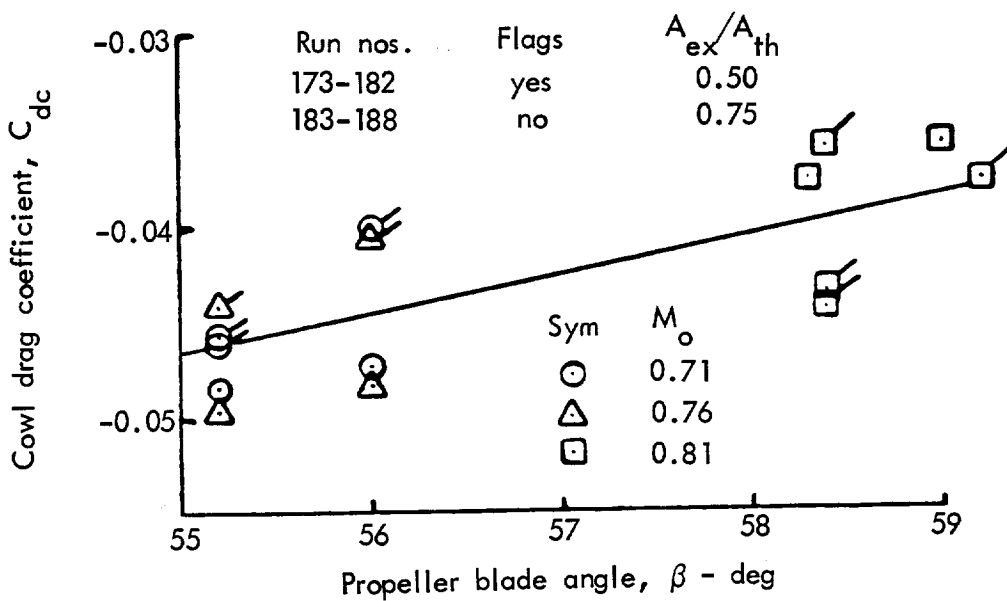


(b) GUN-II, single-scoop inlet with diverter,  $h/D_p = 0.013$ .

Figure 35. - Measured cowl drag coefficients at propeller advance ratio,  $J = 3$  versus propeller blade angle.



(c) GUN II, single-scoop inlet without diverter.



(d) GUN III, twin-scoop inlet with diverter.

Figure 35. - Continued.

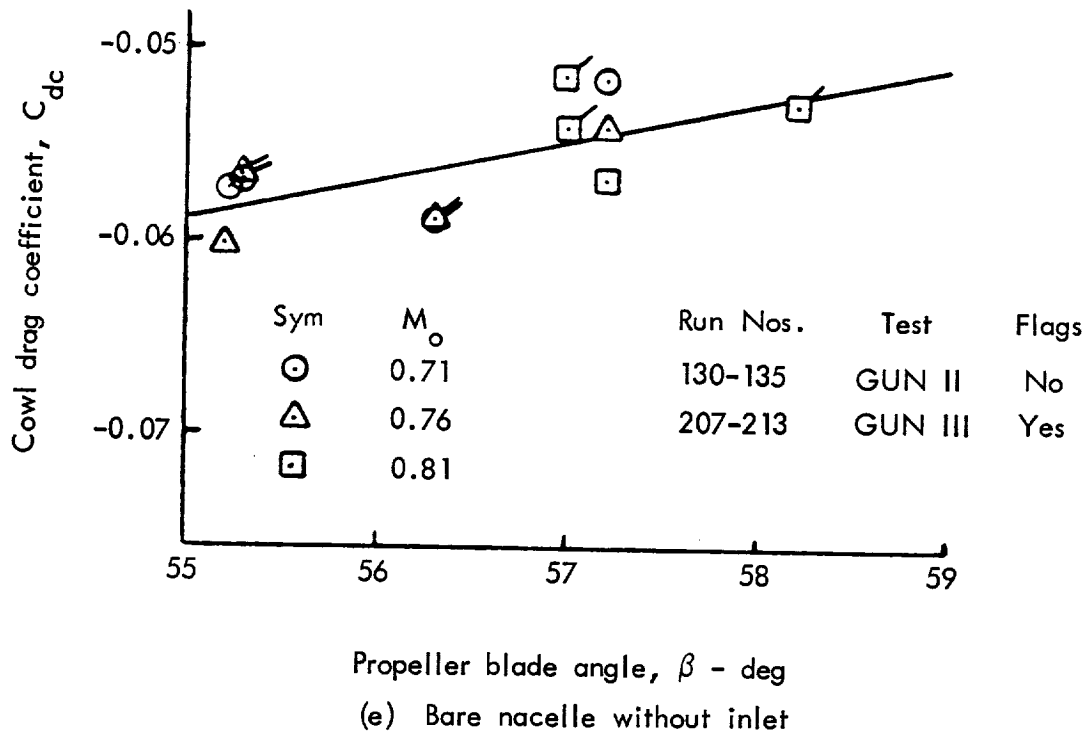
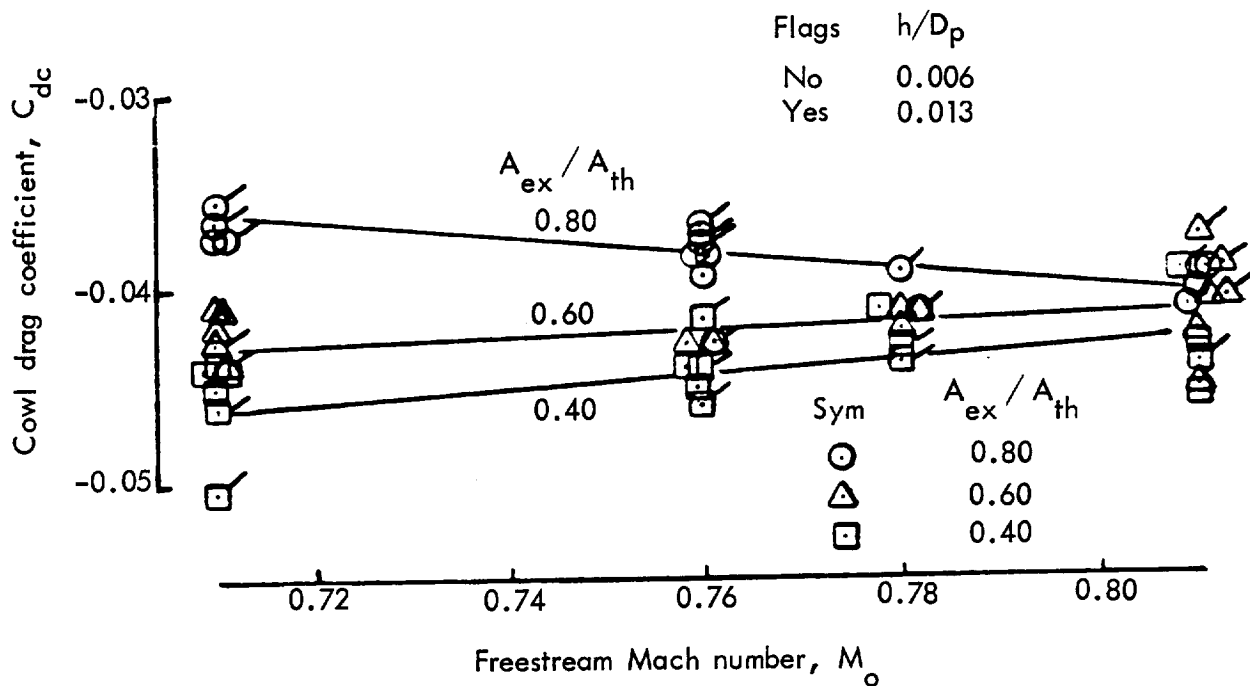
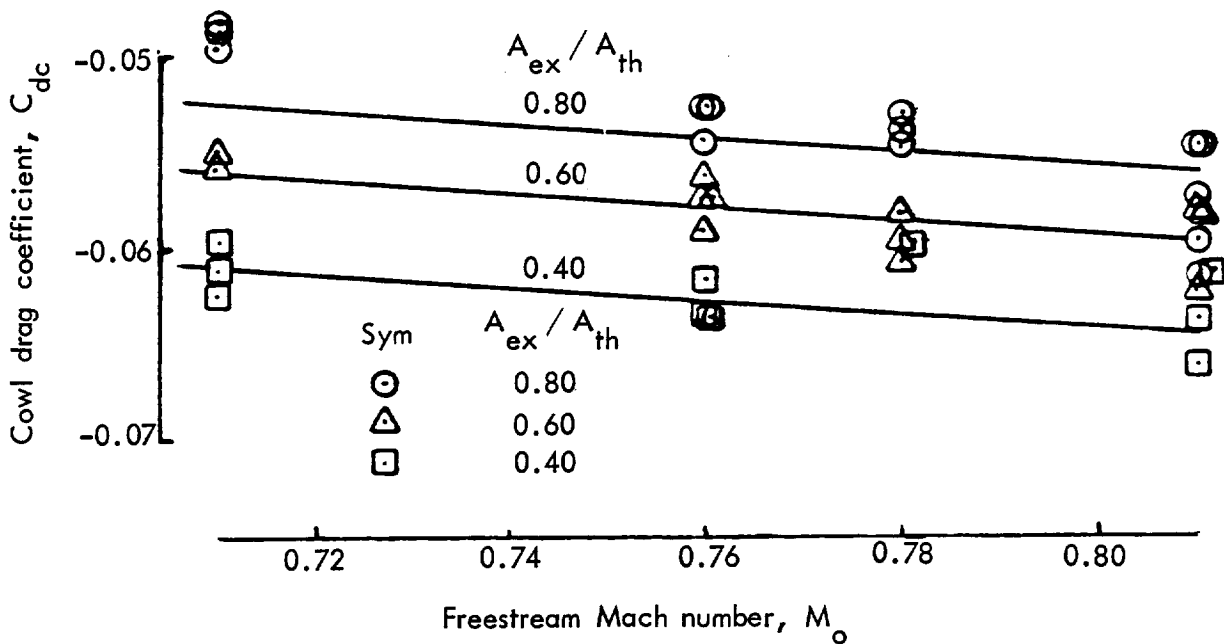


Figure 35. - Concluded.

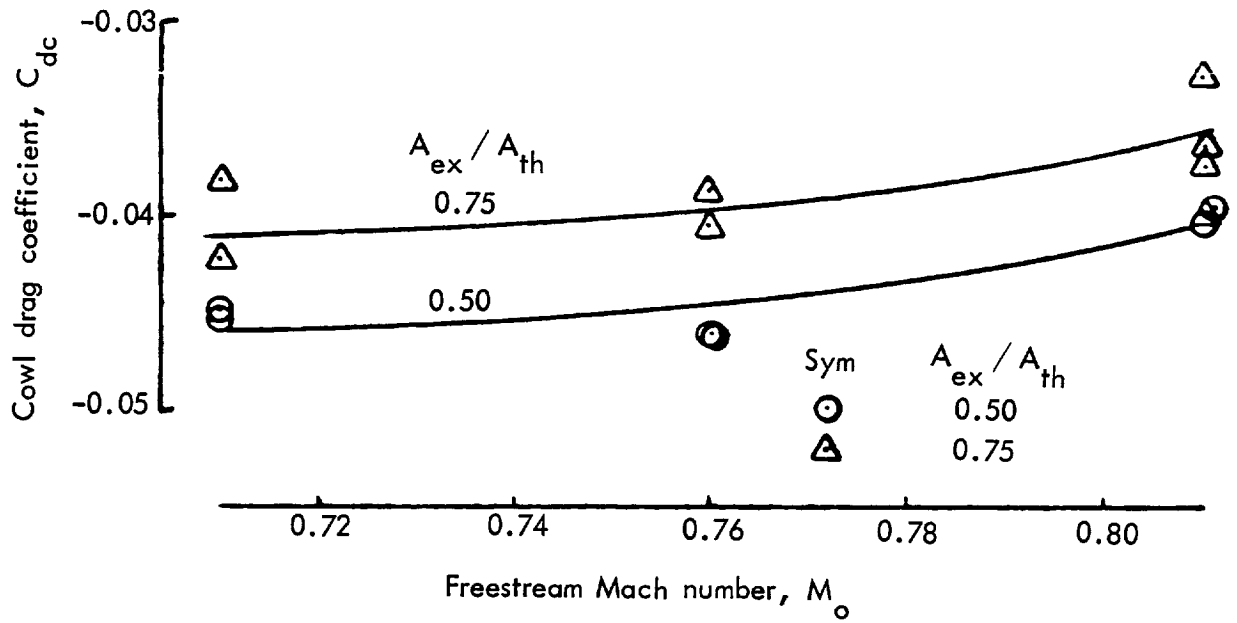


(a) Single-scoop inlet with diverter,  $h/D_p$  variable.

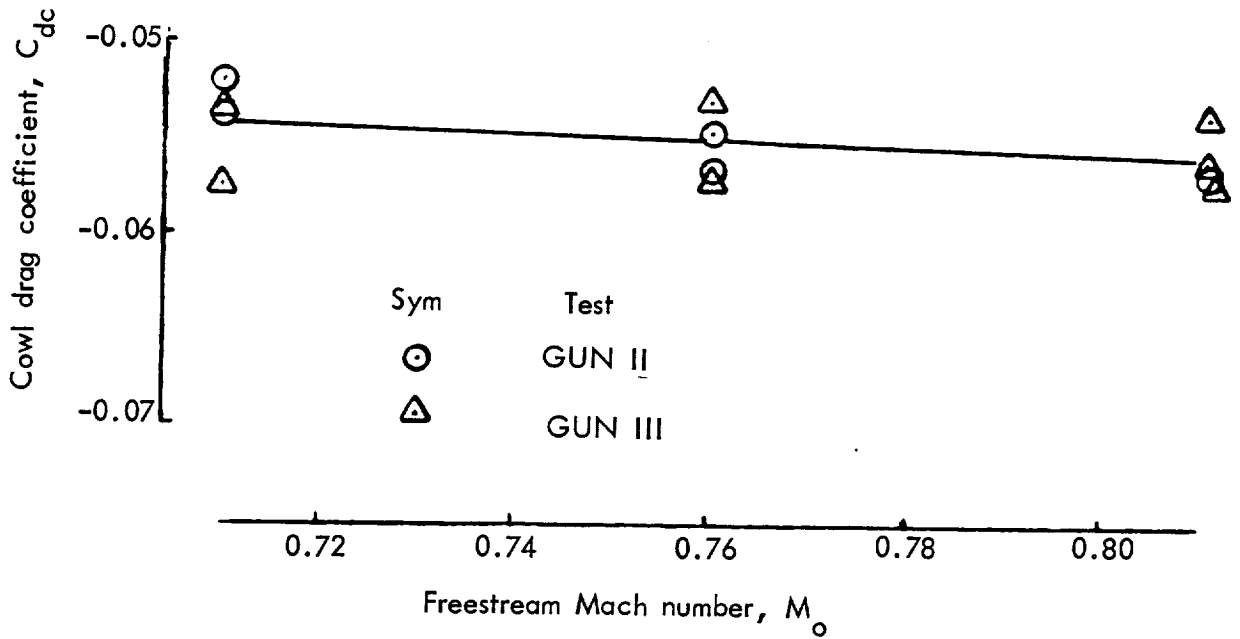


(b) Single-scoop inlet without diverter.

Figure 36. - Measured cowl drag coefficients at propeller advance ratio,  $J = 3$  and propeller angle  $\beta = 57$  degrees versus freestream Mach.

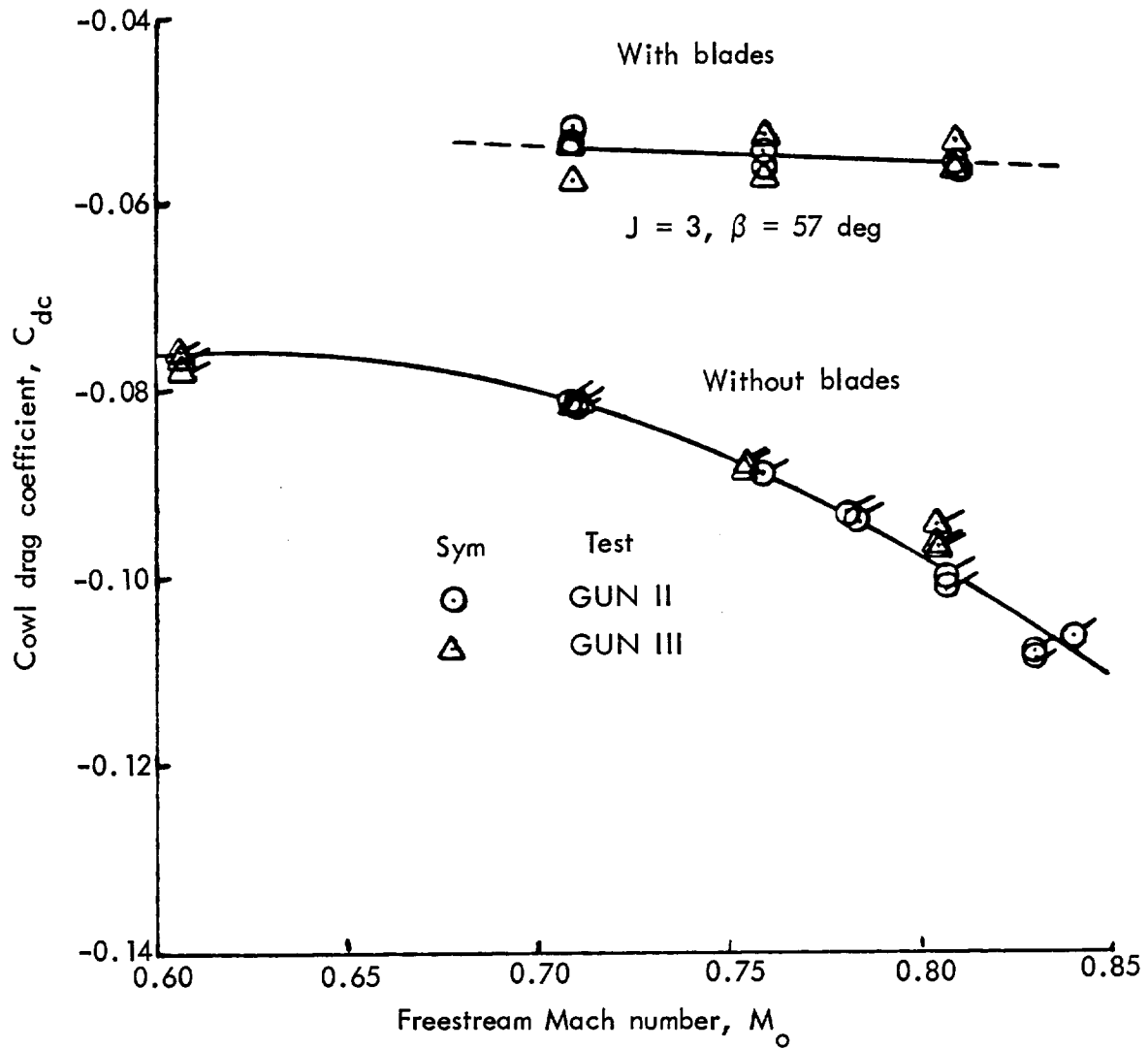


(c) Twin-scoop inlet with diverter.



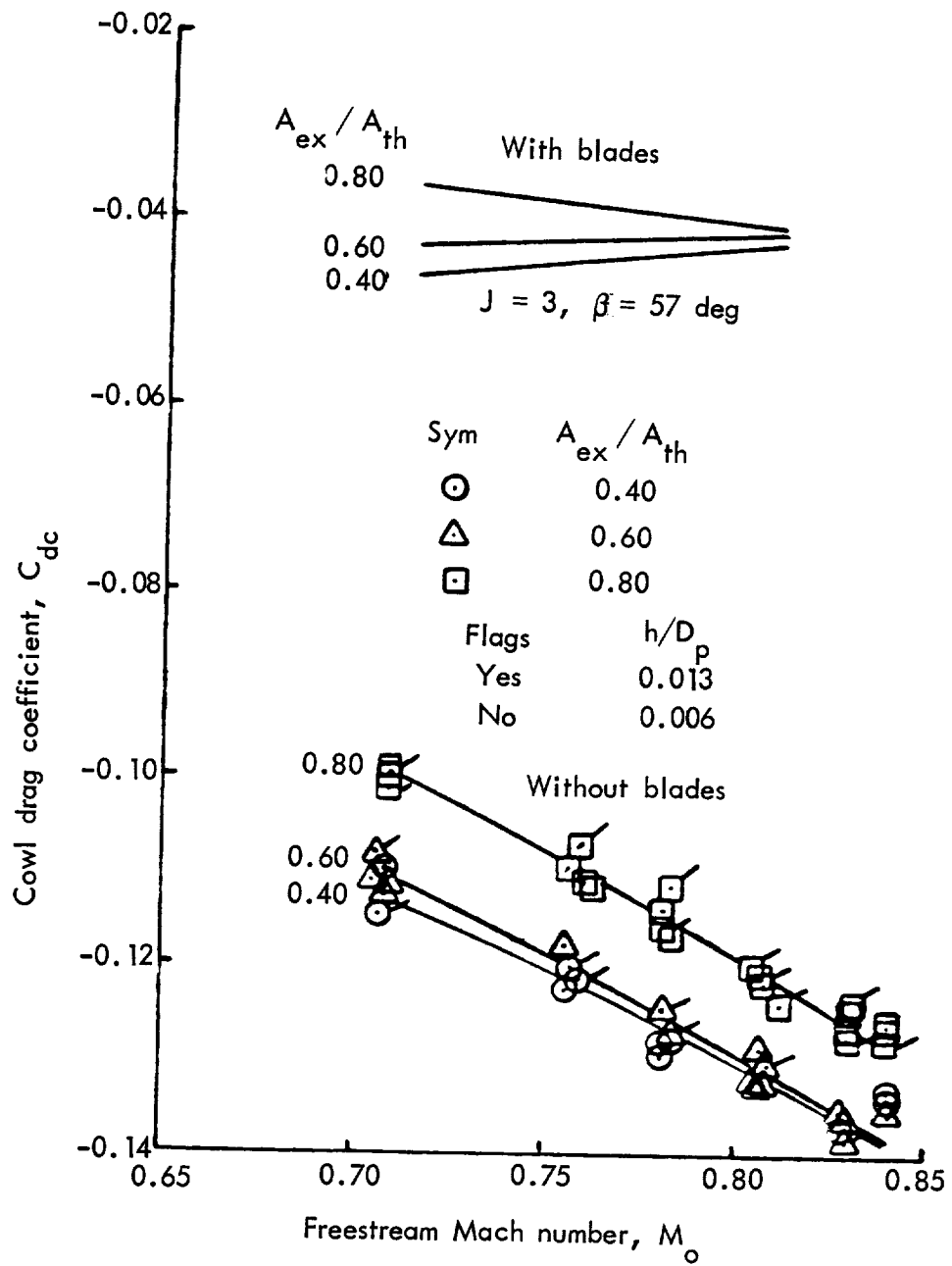
(d) Bare nacelle without inlet.

Figure 36. - Concluded.



(a) Bare nacelle without inlet.

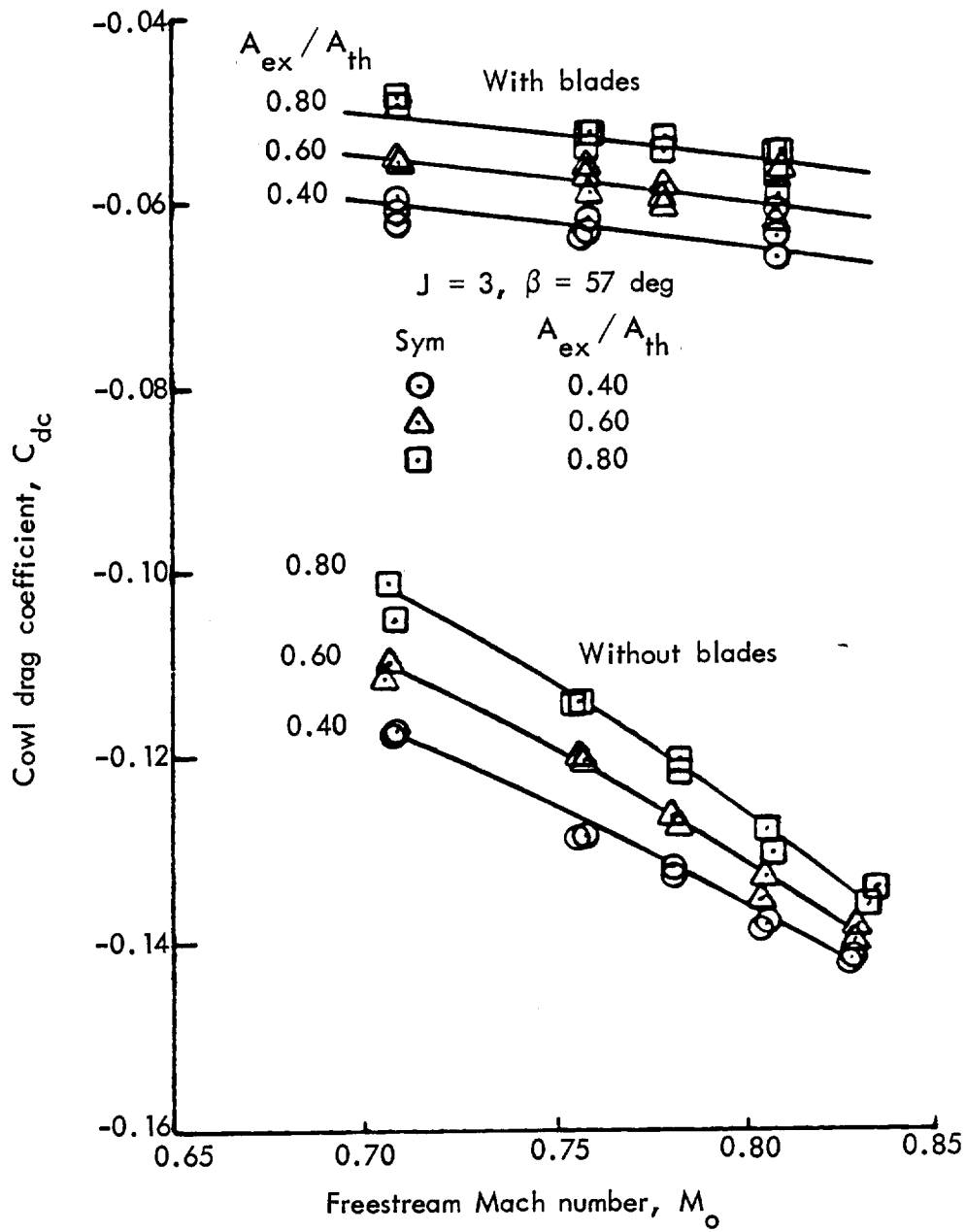
Figure 37. - Cowl drag coefficient comparison, with and without operating propeller blades.



(b) Single-scoop inlet with diverter.

Figure 37. - Continued.





(c) Single-scoop inlet without diverter.

Figure 37. - Concluded.

## Thrust-Minus-Drag Performance

In addition to the separate cowl drag balance for measuring force on the inlet-forebody, the entire nacelle front end was metric. The arrangement, which utilized the propeller test rig (PTR) load cells, was described earlier and is illustrated in Figure 6. The measurement produced was the net value of propeller thrust minus nacelle front-end drag.

Correlation with Existing Data Base - Hamilton Standard has established a precedent for the bookkeeping system which is used to quote propeller performance. In order to compare the present data for a bare nacelle without an inlet to previous testing of the SR-3, the data had to be converted into the Hamilton Standard format. Hamilton Standard "uninstalls" their blades by measuring the performance of a propeller assembly and then subtracting out the pressure and friction forces of the spinner. These are determined by removing the propeller blades and measuring the spinner forces on a balance. Because the metric spinner has not yet reached a maximum nacelle diameter, Hamilton Standard does not want to take credit for the back-pressuring caused by the nacelle cowling from the spinner trailing edge to  $D_{max}$ . So they pressure tap and integrate to get the force on this cowling, assuming an equal and opposite force is also acting on the prop. They then subtract this out of their data. For the GUN II and III tests, however, the separate cowl drag balance eliminated the need for pressure integration and greatly simplified the acquisition of this force correction. The spinner drag, obtained from the GUN testing, is compared to previous test results in Figure 38 (also Figure 8, Reference 10), where it can be noted that it agrees reasonably well with previous tests (Reference 2).

Getting the isolated blade performance, then, merely required subtracting the cowl drag, obtained from the special cowl drag balance, and subtracting the spinner drag, obtained as described above, from the thrust-minus-drag data of the propeller test rig (PTR) assembly. Applying this approach, isolated propeller efficiency was computed and compared to data from previous entries. An efficiency map generated for Mach 0.80 is presented in Figure 39. Here, the newly measured data (dashed lines) are compared to the solid line data from the previous entry. While the comparison lines are fairly close, the differences do appear to be significant. Consultation with Hamilton Standard, however, indicated that repeatability this close is generally considered to be acceptable.

Front End Thrust-Minus-Drag - The initial discussion will address the inlet drag acquired with the spinner / nacelle / inlet installation without a propeller. These data were acquired by utilizing both balances to separate inlet/nacelle drag from that of the spinner. The selected tests were performed on the flush and  $h/D_p = 0.013$  single-scoop inlet. The data are presented in Figure 40, where it is noted that the spinner drag increases slightly with decreasing mass flow ratio. However, this trend is negated by the increase of inlet lip suction with decreasing mass flow ratio. The net effect is insensitivity of total front end drag to mass flow ratio. In an installation of the Pratt and Whitney STS-589-4, the total nacelle drag at  $M_o = 0.80$  is worth 3.67 percent thrust specific fuel consumption.

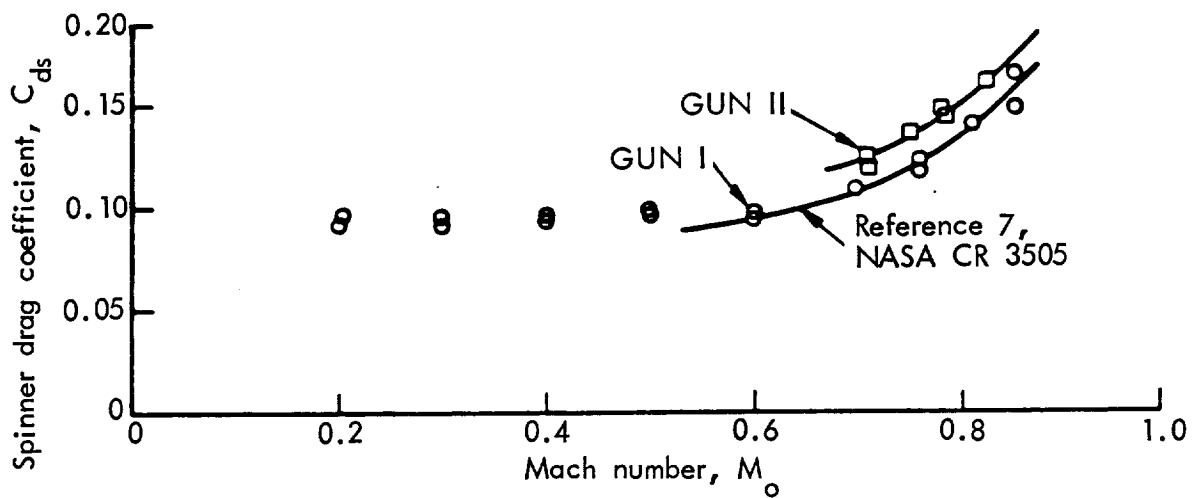


Figure 38. - Spinner drag coefficient, bare nacelle and no propeller.

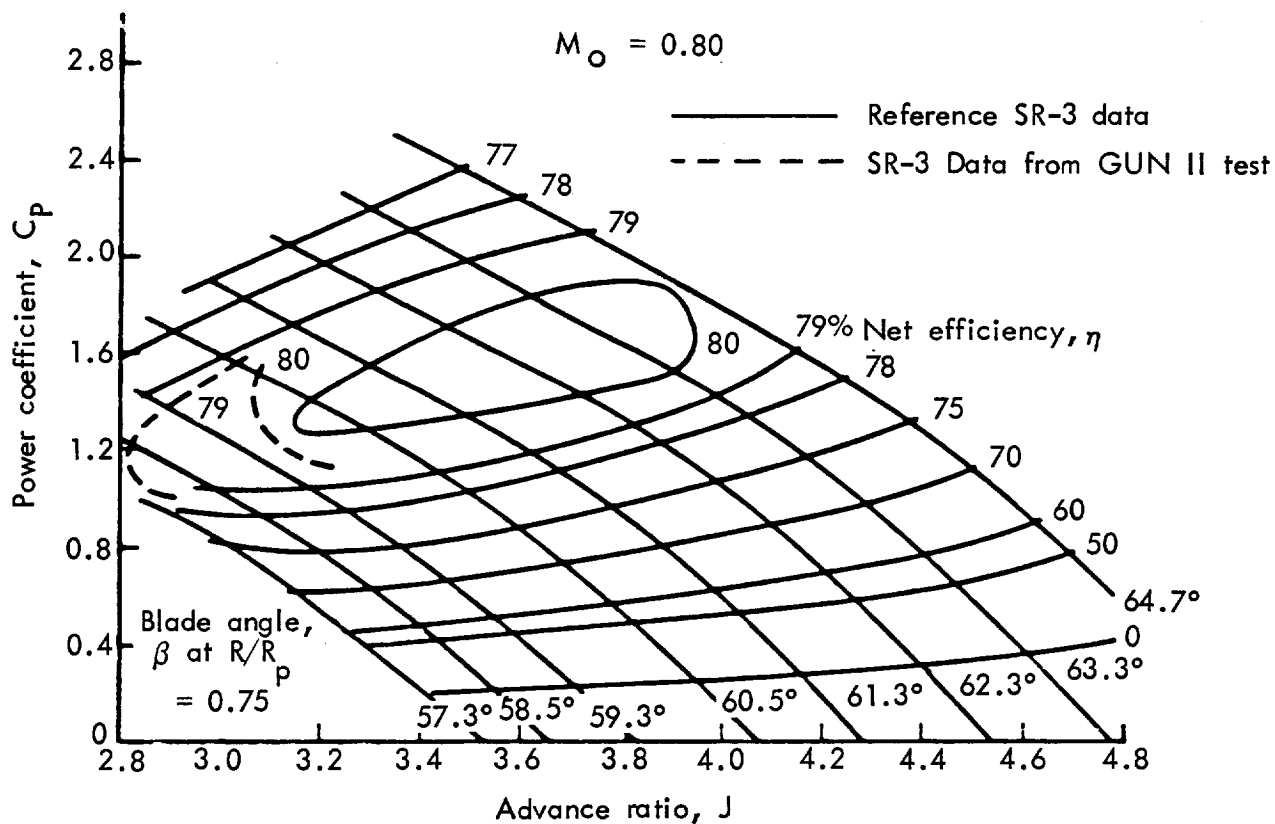


Figure 39. - Comparison of isolated propeller blade performance.

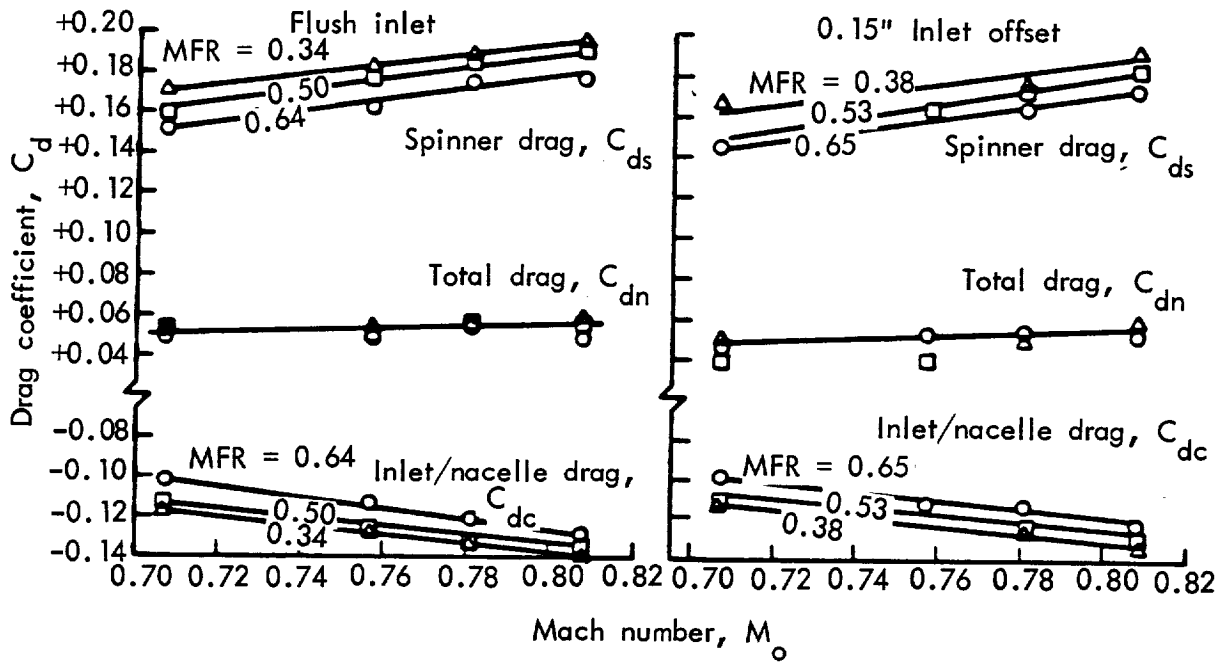


Figure 40. - Component drag as a function of mass flow ratio and Mach number (single-scoop inlet, no propeller).

A perplexing question at the beginning of this program was how to bookkeep the installation of Hamilton Standard's isolated blade performance. To gain insight into this, a propulsion system control volume was formulated, as shown in Figure 41, analogous to the manner in which turbofan installations are bookkept. Organizing the thrust terms in this manner provides a straight forward segregation of inlet drag, nozzle drag, and ram drag, which is a product of known terms: engine airflow and flight speed. In the propfan installation, however, as shown in Figure 42, the control volume not only encompasses the stream tube of the gas generator, but envelops the spinner and cuts through the propeller. Using this control volume, the equation on the bottom of Figure 42 can be derived and arranged into familiar propulsion system terms. The collection of terms included in the horizontal bracket is called "Front End Thrust-minus-Drag". As mentioned earlier, the net value of this term is measured with the main PTR balance. Similar to turbofan nacelle tests, propeller/inlet testing simulates and measures the front-end forces, but does not yield the correct back-end drags or nozzle coefficients. Therefore, back-end terms that were not properly simulated were analytically subtracted out of the data.

Configuration Comparison - During the preliminary data reduction for GUN III, where the configuration comparison tests were made, the relative performance of several of the test configurations was contrary to expectations and could not be explained with other measurements. As a result, a diagnostic effort was initiated and several measurement parameters were investigated and cleared. Finally, a cavity tare force between metric and non-metric components was found to have increased to an order of magnitude relative to the same force measured in the previous tunnel entry (GUN II). An attempt was made to correct the data, but this proved to be impossible because of the spurious tare force behavior and because of the lack of instrumentation to accurately quantify the tare. The root cause of the tare force change has not been found. However, it has been speculated that, with the model changes to accommodate the other inlet types or with certain model assembly procedures, the gap between the metric / non-metric section would change, allowing more leakage into and more pressurization inside the cavity. Hence, a larger and more unstable tare was created. With these factors in mind, the performance comparison, as measured, is discussed below.

Design point performance is summarized in Figure 43 in the form of a bar chart comparison. The parameter  $\lambda_j$ , employed for comparison is defined as the force (thrust-minus-drag) increment for the nacelle / inlet combination versus the isolated blade thrust, divided by the isolated blade alone force. As presented, the data show the thrust-minus-drag penalty to be maximum for the annular inlet, intermediate for the twin-scoop inlet, and minimum for the single-scoop inlet. Since the annular inlet should have been a relatively low-drag installation, the result obtained for this installation is not easy to explain. Study of the pressure data (Figure 23) shows no indication of a loss mechanism.

No penalty was shown for installation of the twin-scoop, flush inlet relative to the isolated nacelle. A relatively strong sensitivity to the installation of a boundary layer diverter is shown, however, and this is

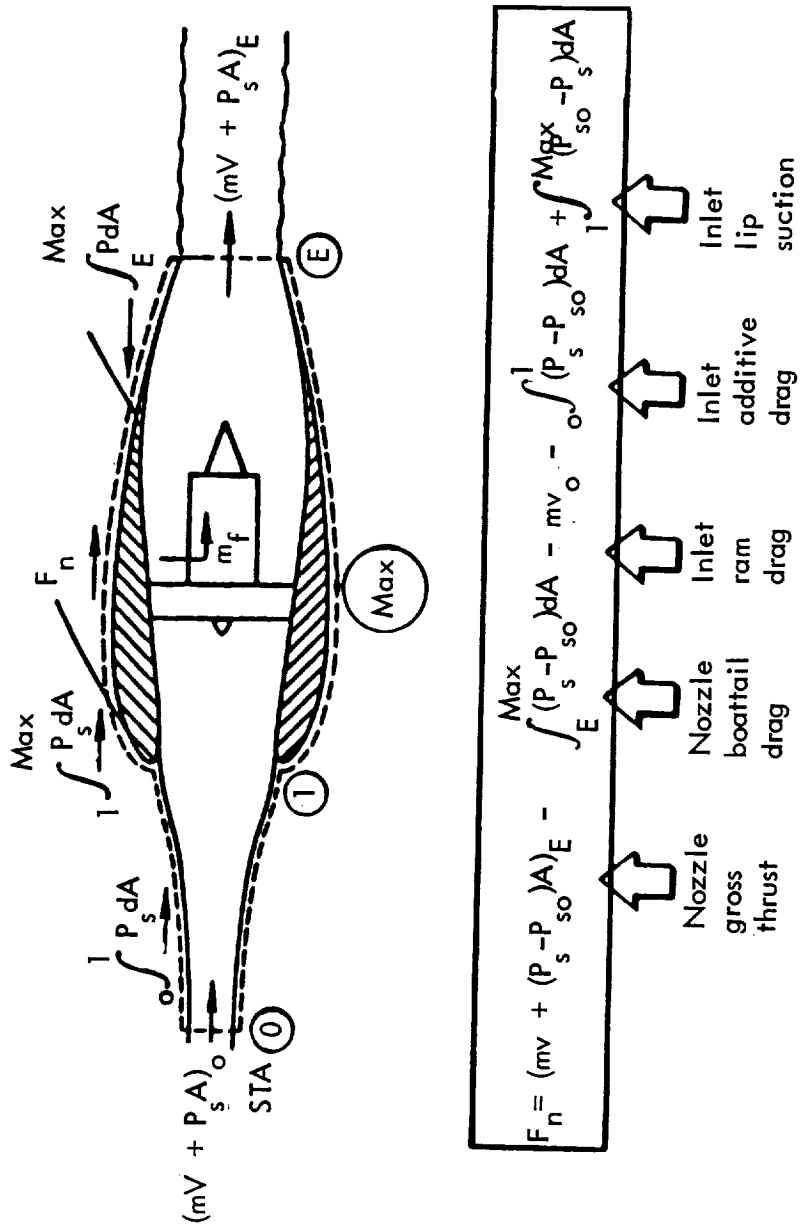
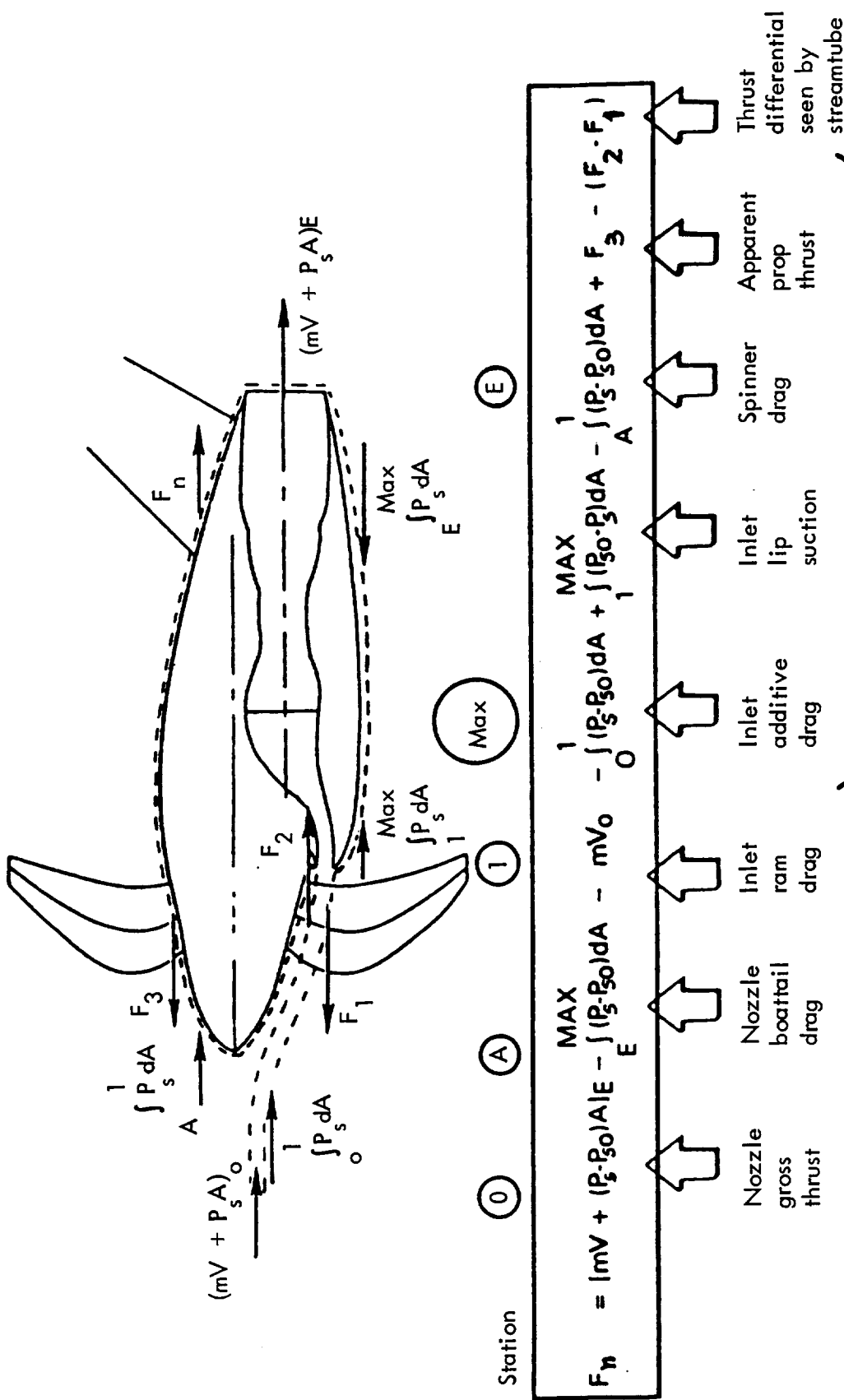


Figure 41. Standard thrust/drag accounting system for turbo-fans.



Front end thrust-drag

Figure 42. - Recommended propulsion thrust-minus-drag accounting system for a tractor propfan installation.

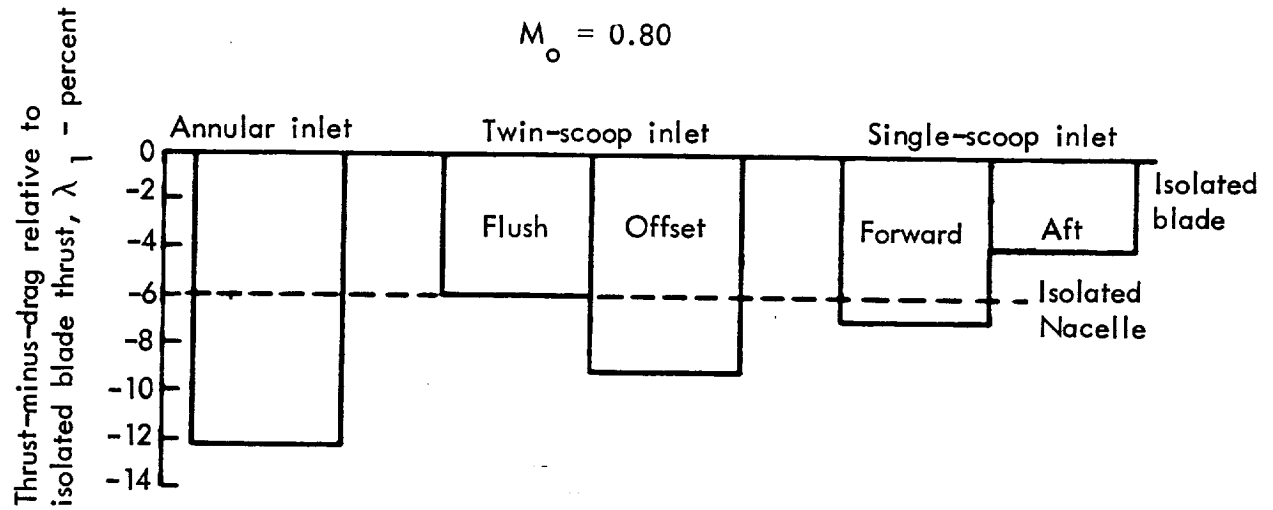


Figure 43. - Summary of GUN-III installation penalties relative to isolated propeller blade performance.

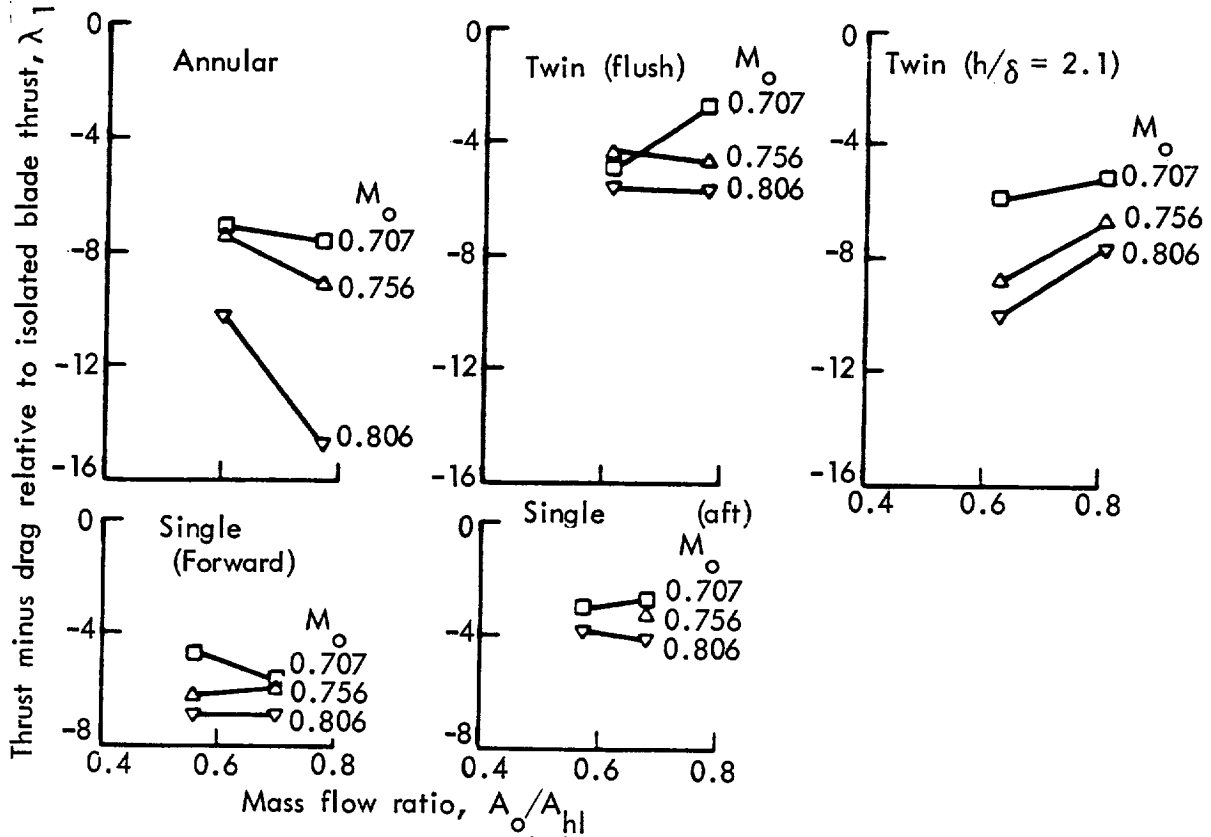


Figure 44. - Impact of mass flow ratio produces inconsistent thrust minus drag variations.



contrary to the results from the GUN II testing of the single-scoop inlet for the effect of diverter height.

The single-scoop inlet in the forward position showed only a small drag increment relative to an isolated nacelle. The same inlet in the aft position, on the other hand, showed a lower thrust-minus-drag penalty than no inlet at all.

During the comparison testing, data were generated across a range of Mach numbers and mass flow ratios for the five inlets discussed here. These results, which are presented in Figure 44, were badly scattered and did not show consistent trends. In fact, increasing mass flow ratio greatly reduced the annular inlet drag, but produced the opposite effect on the twin-scoop inlet. Varying mass flow ratio had little effect on the single-scoop inlet performance. This particular finding agreed with the GUN II test results.

Effect of Diverter Height - It was recognized early in the program that the single-scoop inlet was a leading candidate for best overall installation performance. Consequently, special studies such as the effect of diverter height variation, were done for this configuration. Fortunately, most of this work was performed in GUN II, where the data obtained were believed to be reasonably reliable. The discussion in the following paragraphs is based on these more reliable GUN II data.

It has been established in an earlier discussion that inlet recovery is improved as diverter height is increased up to better than two-and-a-half times the equivalent flat-plate boundary layer height. At the same time, as diverter height is increased, it would be anticipated that nacelle drag would gradually increase. Although a slight trend is indicated, a buildup in thrust-minus-drag penalty as a function of boundary layer diverter height is not clearly defined. Figure 45 illustrates the variation in  $\lambda_2$  with normalized boundary layer height ( $h/\delta$ ) for two different Mach numbers. Data were taken with mass flow ratio held at a constant value of 0.60, which approximates the design cruise operating point. The curves show  $\lambda_2$  to be fairly constant across the range examined, although there is some variation at the lower Mach number of 0.71. It is virtually certain that some increased drag will result from increasing the boundary layer diverter height, but if it is properly designed, the penalty should be small. In this case, it is probable that there is a definite penalty, but that it is within the scatter of the data. Some verification of this conclusion can be seen in the next plot to be discussed.

Figure 46 shows  $\lambda_2$  plotted as a function of Mach number for two different boundary layer diverter heights, zero and 2.7. An  $h/\delta$  of 2.7 is the normalized diverter height at which the recovery improvement reaches its maximum value. Here, a small penalty for diverter height can be clearly seen. It appears to average about a quarter percent across the range covered by the plot.

Effect of Mach Number - As shown in Figure 46, relative to the nacelle alone, the complete single-scoop inlet / nacelle combination exhibited a significant, although not prohibitive, drag rise characteristic. Compared

Thrust-minus-drag relative to isolated nacelle,  $\lambda_2$  - percent

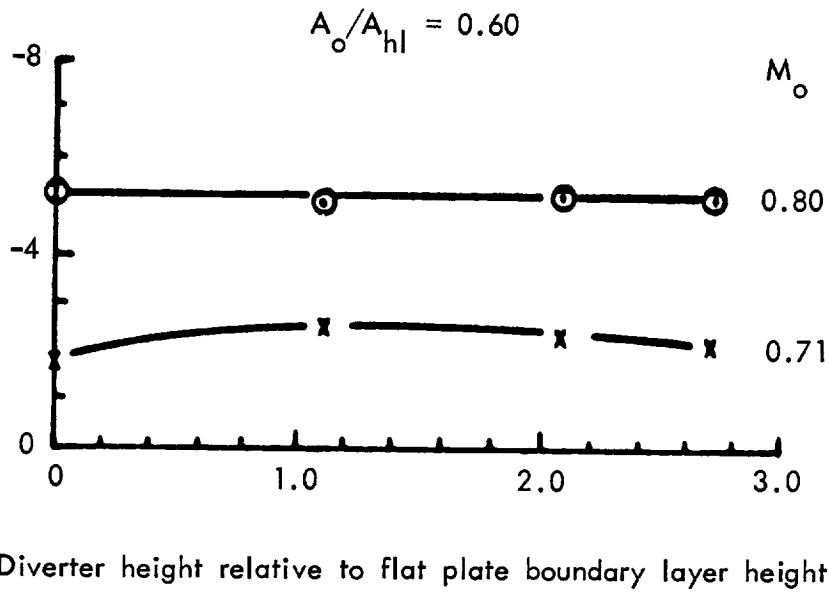


Figure 45. - Effect of boundary layer diverter height on thrust parameter for single-scoop inlet.

Thrust-minus-drag relative to isolated nacelle,  $\lambda_2$  - percent

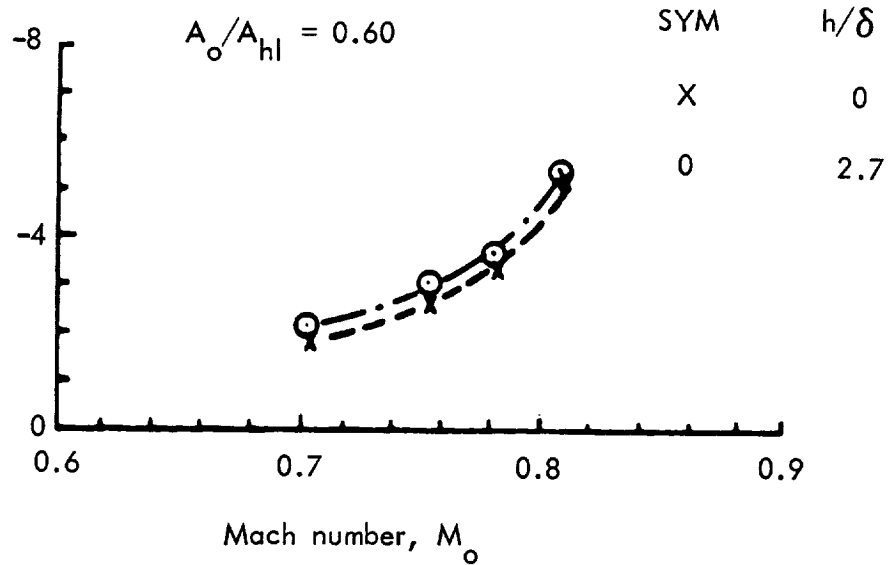


Figure 46. - Effect of Mach number on thrust parameter at two boundary layer diverter heights.

to a base level increment for the inlet of about 2 percent at Mach 0.70, the increment increases to 4 percent at Mach 0.80. Beyond that, the divergence is very sharp. In assessing this result, it should be kept in mind that the effective nacelle Mach number at  $M_o = 0.80$  is really close to 0.90 and propeller swirl imposes an effective yaw angle of 4 to 6 degrees. Local tailoring could improve the inlet-forebody tolerance for swirl, but the price would be the requirement for right- and left-hand nacelles, depending upon the direction of propeller rotation.

To gain a better insight into thrust-minus-drag effect, the actual thrust-minus-drag coefficient data are plotted in Figure 47. For reference purposes, the isolated blade performance, as quoted by Hamilton Standard, is shown in the figure (top curve). The second curve from the top depicts the levels measured on the PTR with the propfan assembly on the balance (spinner blades and nacelle), but without an inlet. Finally, the dotted line is the result of applying an analytical adjustment of the isolated nacelle performance to account for the additional wetted area (friction drag) for adding the inlets. By far the largest drag degradation is due to the spinner and nacelle, which is seen in the figure as the difference between the isolated blade and isolated nacelle curves. The friction and pressure drag increments are about equal at Mach 0.80. At the lower Mach numbers, there does not appear to be any appreciable pressure drag.

Effect of Mass Flow Ratio - A plot of  $\lambda_2$  versus mass flow ratio for two Mach numbers and a number of different diverter heights is presented in Figure 48. The classical shape for these curves calls for spillage drag to increase significantly as mass flow ratio is reduced below the design point. Spillage drag is the difference between inlet additive drag and lip suction, as illustrated in Figure 42. For most of the test cases, an increase did occur for mass flow ratios down to about 0.50. Below this level, however, the drag level either remained flat or began to fall off. Reducing mass flow ratio effectively increases the local blockage, so that the prop is working harder as it passes the inlet, thereby enhancing the total pressure of the stream in this region. A more detailed explanation of this phenomena is contained in Reference 11. Here it is explained how a propeller, operating in a reduced velocity flow-field, can deliver increased levels of both thrust coefficient and efficiency. Again referring to Figure 48, at Mach 0.81 and the highest mass flow ratio shown (0.70), there is some drag divergence for the larger boundary layer diverter height. Since this effect is clearly a function of a difference in diverters, the drag is possibly due to shocking in the gutter passage itself. An analytical study of the pressure distributions in this area should help to clarify this phenomenon.

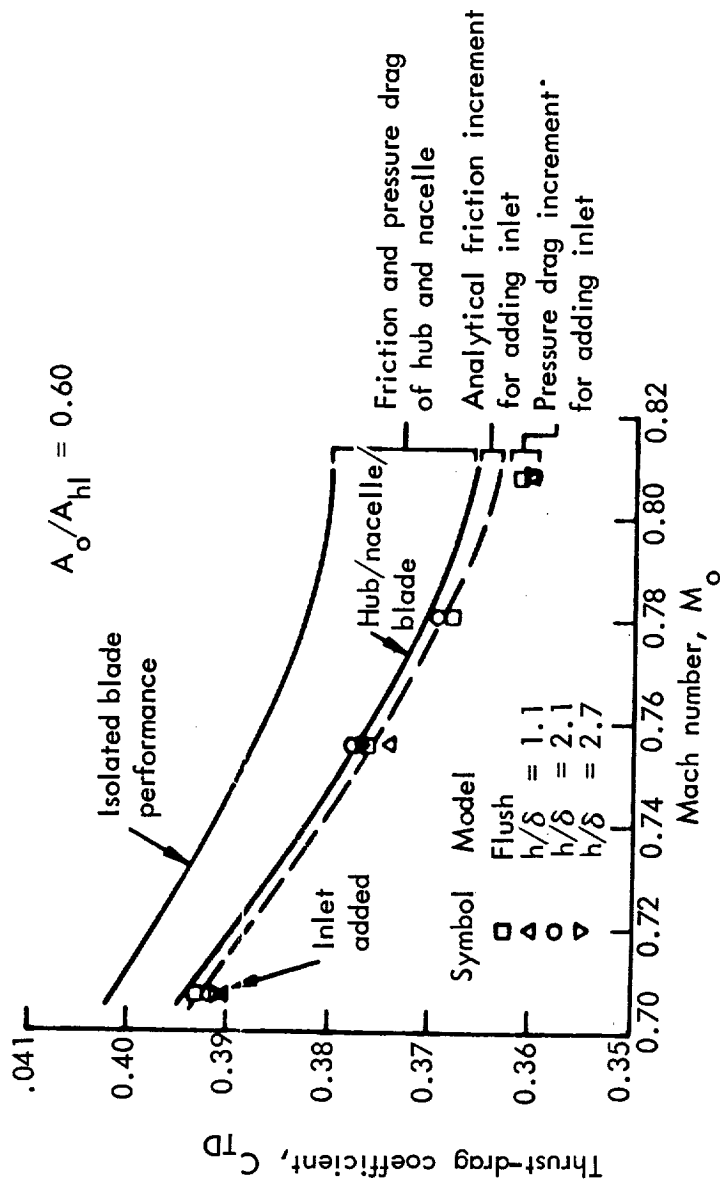


Figure 47. - Mach number effect on front end thrust-minus-drag.

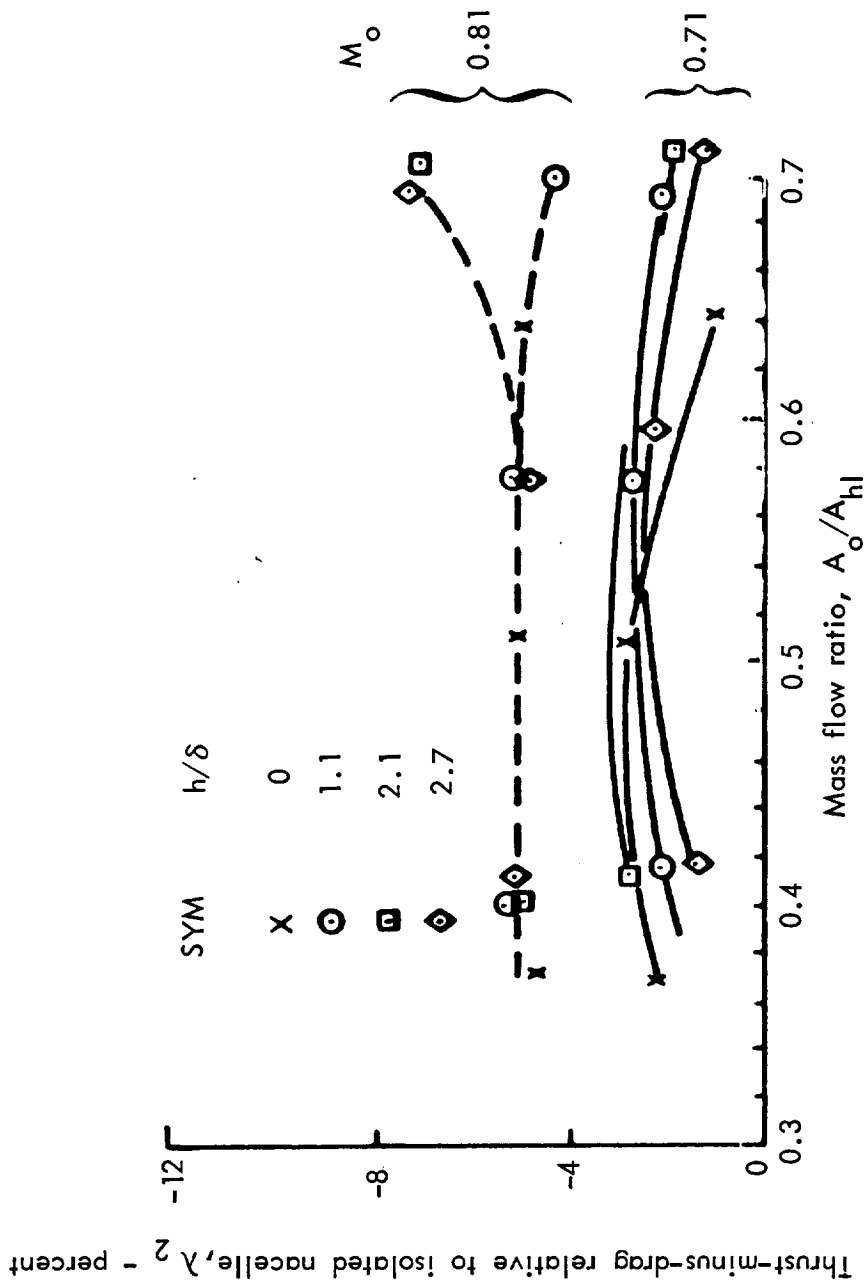


Figure 48. - Effect of inlet mass flow ratio on thrust parameter at various Mach numbers and boundary layer diverter heights.

## Propeller Blade Stresses

To determine the impact of inlet design on blade cyclic loading, five strain gages were placed on the inside cambered surface of one of the blades. Positions were selected to permit comparison with SR-3 test data previously taken at NASA-Lewis. The basic layout is illustrated in Figure 49. Initial testing showed blade root bending (gage no. 1) to be critical, so the subsequent discussion will deal exclusively with the results taken for this position.

Blade stress data were measured for the single-scoop inlet on both the forward and aft positions, the twin-scoop inlet in the forward position, the annular inlet in the forward position, and for no inlet at all. Summarized results of the blade stress testing are presented in Table II. For each configuration, stresses (total vibratory plus 1P and 2P components) are listed at two operating conditions. The maximum total and 2P vibratory stresses were measured near the first mode critical speed, which was 6100  $\pm$ 120 RPM. The maximum 1P stresses, however, were produced at much higher rotational speeds.

From the table it is clear that the 2P vibratory response near the first mode critical speed was an order of magnitude higher than the corresponding 1P response. The single-scoop forward inlet produced 40 to 60 percent higher stresses than the single-scoop, aft inlet. The highest measured 1P stress for the single-scoop, forward inlet was  $\pm$ 12611 K Pa ( $\pm$ 1829 psi) at 0.80 Mach number, 8392 RPM, 0.81 throat mass flow ratio, and 57.8 degrees blade angle. For the single-scoop, aft inlet, the highest 1P stress was  $\pm$ 8998 K Pa ( $\pm$ 1305 psi) at 0.80 Mach number, 8204 RPM, 0.81 throat mass flow ratio, 58 degrees blade angle. The 1P stress environment for the twin-scoop inlet was very mild. However, the 2P stresses near the first mode critical speed were the highest among all the inlets tested. The stress environment produced by the annular inlet was only slightly higher than for the no-inlet configuration. These results indicate that inlet-induced blade stress can be significant and must be considered in the design of a prop-fan installation. A more complete analysis of the data, as performed by Hamilton Standard, is contained in Reference 12.

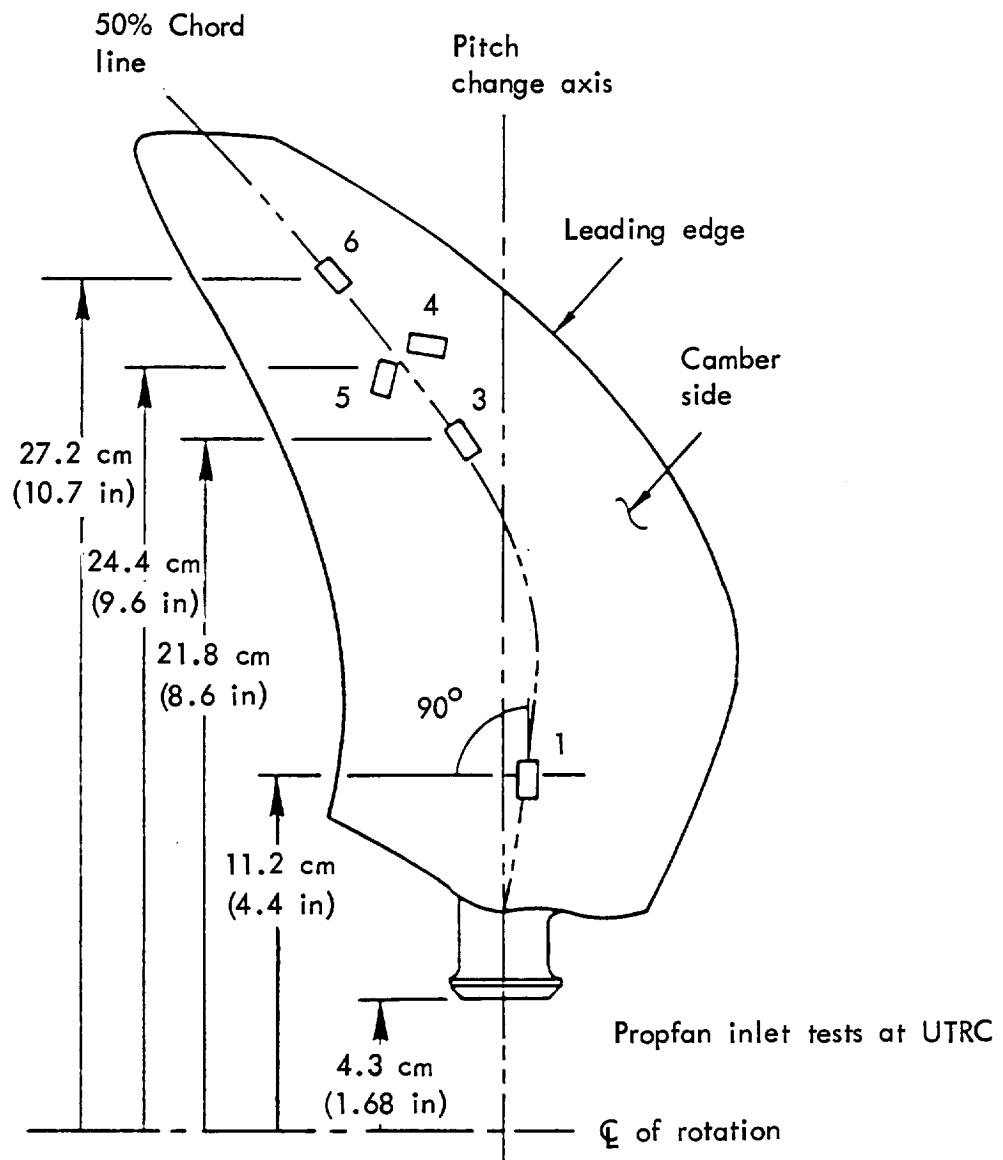


Figure 49. - SR-3 propfan blade strain gage layout.

TABLE II. - SR-3 BLADE ROOT BENDING VIBRATORY TEST STRESSES FOR VARIOUS INLETS.

Type of Inlet	$M_o$	$\beta$ 3/4 (Deg)	MFRT	RPM	GUN III Test/ Run No.	Total Stress ±K Pa (±psi)	1P Stress ±K Pa (±psi)	2P Stress ±K Pa (±psi)
Single-scoop Forward	0.8	57.8	0.81	6221	11/5	126506 (18348)	8715 (1264)	108738 (15771)
	0.8	57.8	0.81	8392	11/7	22890 (3320)	12611 (1829)	7820 (1134)
Single-Scoop Aft	0.8	58.0	0.81	8204	37/3	14186 (2057)	8998 (1305)	4971 (721)
	0.8	58.0	0.97	6110	27/1	76511 (11097)	6509 (944)	61226 (8880)
Twin-Scoop Forward	0.6	58.3	0.75	6927	40/4	24710 (3584)	3413 (495)	17900 (2596)
	0.8	58.3	0.0	6127	42/1	187249 (27158)	1834 (266)	173487 (25162)
Annular Forward	0.6	59.0	0.86	6432	215/3	13535 (1963)	3689 (535)	8715 (1264)
	0.6	59.0	0.86	6234	215/4	17209 (2496)	2840 (412)	12052 (1748)
No-Inlet	0.7	58.0		7655	23/2	6550 (950)	2524 (366)	1950 (283)
	0.8	59.0		5981	21/1	15472 (2244)	1393 (202)	9963 (1445)

Note 1: The blade stresses listed herein are measured values and have not been adjusted for the tare stresses seen with no inlet.

Note 2: MFRT is throat mass flow ratio.  
MFR inlet mass flow ratio = MFRT x  $A_t/A_{h1}$   
where  $A_t$  and  $A_{h1}$  are listed in Figure 8 for each inlet.



## CONCLUDING REMARKS

As a step toward the development of a generalized technology base, inlets for tractor installations of advanced turboprop (propfan) propulsion systems were tested in the UTRC large subsonic wind tunnel. Nacelle inlet configuration types included single-scoop, twin-scoop, and annular arrangements. Tests were performed with and without boundary layer diverters, and several different diverter heights were tested for the single-scoop inlet. This same inlet was also tested at two different axial positions. Test Mach Numbers ranged from Mach 0.20 to 0.80. Types of data taken were (1) internal and external pressures, including inlet throat total pressure recoveries, (2) balance forces, including thrust-minus-drag, and (3) propeller blade stresses. The following results were obtained:

1. For a given inlet axial position, the single-scoop inlet showed the highest recovery, the twin-scoop inlet was second, and the annular inlet had the lowest recovery of all.

2. Increasing boundary layer diverter height improved total pressure recovery up to a height of 2.7 times the flat plate boundary layer thickness.

3. Although tare problems were experienced in some of the force testing, thrust-minus-drag penalties  $\lambda_1$  for the single-scoop inlet were generally the lowest. Thrust-minus-drag penalties for the twin-scoop inlet were slightly higher and, for the annular inlet, were highest of all. This result for the annular inlet was not predicted and is suspected of being in error.

4. Thrust-minus-drag levels were found to be relatively insensitive to mass flow ratio, indicating that spillage drag is not a serious problem for this type of installation.

5. Mach number variations performed during the testing indicated that a significant drag rise would begin around Mach 0.80 for the single-scoop installation.

6. Measured cowl surface pressure data correlated well with pressures predicted using an analytical model.

7. Propeller blade stress levels could be reduced by shifting the inlet entry position in the aft direction. The 1P stress, for example, was reduced about 30 % for the single-scoop inlet. This was found to result in a tradeoff against total pressure recovery, which was reduced from 1.08 to 1.05. The aft position, (20 % in propeller diameters), would be acceptable, but it might be possible to place the inlet somewhat forward of this to improve total pressure recovery and stay within propeller stress limits. These limits need to be more clearly defined.

8. The best inlet type, considering both total pressure recovery and thrust-minus-drag, was the single-scoop inlet with boundary layer diverter. The thrust-minus-drag data for the twin-scoop and annular

inlets were not reliable enough to rank them with the single-scoop flush inlet.

## Appendix A

### Test Configuration Coordinates and Pressure Tap Locations

The coordinates of the spinner and inlets, as well as the locations of the external surface static pressure taps, are defined in this appendix. The origin of the coordinates is on the axis of rotation in the plane of the base of the rotating spinner. The positive directions are: X, aft; Y, left; and Z up. A sketch is included with each of the tables to illustrate the application of the coordinate system described here. All dimensions are in inches.

Table A1 presents coordinates of the spinner and front of the nacelle. This part of the nacelle, which extends aft to the highlight, is axisymmetric. The propeller blade axis plane is 2.245 inches forward of the origin and the spinner leading edge is 9.495 inches forward of the origin. The inlet highlight is positioned at  $X = 0.500$  inches. Coordinates presented in Tables A2 through A6 begin at this station.

Tables A2 and A3 provide coordinates for the single-scoop inlet with and without a boundary layer diverter respectively. Since the inlet was positioned at the top for most of the testing, the positive Z axis is shown passing through the cowl. The inlet is symmetrical about the Z plane, so only the positive Y coordinates are given.

Tables A4 and A5 present coordinates for the twin-scoop inlet with and without a boundary layer diverter respectively. In this case, the scoops are positioned on either side of the nacelle. Since the inlets are symmetrical about the Y and Z planes, only the positive coordinates are presented.

The annular inlet is described using cylindrical coordinates in Table A6. It is completely axisymmetric, so the tabular presentation is greatly simplified. Both external and internal coordinates are presented, as appropriate.

External surface static pressure tap angular locations are presented in Table A7. The associated axial and radial locations are provided in Table A8.

TABLE A1. - COORDINATES OF SPINNER AND FRONT OF NACELLE.

X	Radius
-9.495	.000
-9.145	.520
-8.895	.730
-8.395	1.070
-7.895	1.350
-6.895	1.800
-5.895	2.160
-4.895	2.470
-4.745	2.510
-4.495	2.570
-4.245	2.600
-3.995	2.595
-3.745	2.590
-3.495	2.595
-3.245	2.635
-2.995	2.695
-2.745	2.765
-2.495	2.845
-2.245	2.928
-1.995	3.017
-1.245	3.285
-.245	3.642
.000	3.730
.100	3.766
.200	3.797
.300	3.833
.400	3.864
.500	3.895

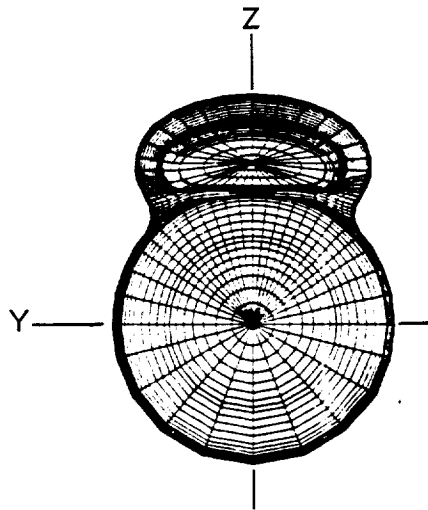
The diagram illustrates the geometry of the spinner and nacelle. The spinner is a tapered, conical structure with a grid of lines representing its surface. The nacelle is a larger, more complex structure that encompasses the spinner. Key features and labels include:

- Inlet highlight:** Located at the top of the nacelle.
- Blade axis plane:** A vertical plane passing through the center of the spinner.
- X = 9.495:** A coordinate value indicating the position of the blade axis plane.
- R, Y, OR Z = 0:** Coordinate axes originating from the center of the spinner.
- Rear of spinner (X = 0):** The base of the spinner.
- Spinner:** The tapered conical structure.
- Nacelle:** The larger structure housing the spinner.
- Inlet highlight:** Also indicated by an arrow pointing to the top of the nacelle.

TABLE A2. - COORDINATES OF SINGLE-SCOOP INLET WITH DIVERTER.

(a) X = 0.500 through 0.750.

X = .500		X = .510		X = .525		X = .600		X = .750	
Y	Z	Y	Z	Y	Z	Y	Z	Y	Z
3.895	.000	3.898	.000	3.902	.000	3.924	.000	3.965	.000
3.600	1.486	3.600	1.494	3.600	1.506	3.600	1.561	3.600	1.662
3.000	2.484	3.000	2.489	3.000	2.495	3.000	2.529	3.000	2.593
2.400	3.068	2.400	3.071	2.400	3.077	2.400	3.104	2.400	3.156
1.800	3.454	1.800	3.457	1.800	3.462	1.800	3.487	1.800	3.533
1.200	3.705	1.200	3.708	1.200	3.713	1.202	3.735	1.200	3.779
.600	3.843	.600	3.846	.600	3.849	.600	3.887	.600	3.897
.000	3.881	.000	3.884	.000	3.887	.000	3.904	.000	3.932
.000	4.19	.000	4.169	.000	4.163	.000	4.162	.000	4.162
2.002	↓	2.002	↓	2.002	↓	2.003	↓	2.005	↓
2.212	4.226	2.340	4.265	2.400	4.291	2.400	4.261	2.400	4.235
2.400	4.339	2.502	4.407	2.524	4.407	2.583	4.407	2.646	4.407
2.516	4.515	2.614	4.727	2.643	4.729	2.714	4.743	2.782	4.769
2.555	4.726	2.530	5.060	2.569	5.062	2.682	4.991	2.746	5.063
2.518	4.946	2.400	5.252	2.400	5.306	2.570	5.244	2.647	5.298
2.400	5.167	2.087	5.495	2.093	5.527	2.400	5.427	2.400	5.547
2.266	5.308	1.800	5.631	1.800	5.667	2.119	5.607	2.169	5.687
2.082	5.434	1.200	5.846	1.200	5.880	1.200	5.969	1.800	5.860
1.800	5.574	.600	5.970	.600	6.003	.600	6.089	1.200	6.064
1.200	5.794	.000	6.011	.000	6.043	.000	6.129	.600	6.182
.600	5.921							.000	6.221
.000	5.962								



- Notes: (1) Gutter has been modified for performance improvements.  
 (2)  $h/D_p = 0.013$ .

TABLE A2. - CONTINUED

(b) X = 0.900 through 1.450.

X = .900		X = 1.000		X = 1.200		X = 1.350		X = 1.450	
Y	Z	Y	Z	Y	Z	Y	Z	Y	Z
4.003	.000	4.026	.000	4.068	.000	4.098	.000		
3.600	1.750	3.600	1.802	3.600	1.894	3.600	1.957	3.600	1.996
3.000	2.650	3.000	2.685	3.000	2.747	3.000	2.791	3.000	2.819
2.400	3.204	2.400	3.232	2.400	3.285	2.400	3.321	2.400	3.344
1.800	3.575	1.800	3.601	1.800	3.648	1.800	3.668	1.800	3.690
1.200	3.807	1.200	3.824	1.200	3.849	1.200	3.877	1.200	3.895
.600	3.922	.600	3.936	.600	3.955	.600	3.978	.600	3.985
.000	3.956	.000	3.969	.000	3.987	.000	4.001	.536	3.989
.000	4.162	.000	4.162	.000	4.162	.000	4.152	.420	4.015
2.011	↓	2.017	↓	2.032	↓	.600	4.162	.372	4.043
2.400	4.224	2.400	4.217	2.400	4.206	2.046	↓	.348	4.076
2.683	4.407	2.705	4.407	2.750	4.407	2.400	4.199	.370	4.109
2.824	4.791	2.849	4.803	2.864	4.617	2.645	4.294	.425	4.137
2.691	5.332	2.806	5.139	2.895	4.823	2.781	4.407	.536	4.160
2.400	5.625	2.717	5.350	2.868	5.108	2.928	4.833	.600	4.168
2.210	5.739	2.400	5.668	2.765	5.384	2.799	5.407	2.057	↓
1.800	5.930	2.229	5.769	2.258	5.824	2.645	5.601	2.400	4.195
1.200	6.131	1.800	5.969	1.800	6.035	2.400	5.788	2.746	4.353
.600	6.247	1.200	6.168	1.200	6.232	1.800	6.078	2.866	4.503
.000	6.286	.600	6.284	.600	6.346	1.200	6.272	2.949	4.837
		.000	6.322	.000	6.383	.600	6.385	2.866	5.325
						.000	6.422	2.746	5.527
								2.283	5.881
								1.800	6.103
								1.200	6.297
								.600	6.409
								.000	6.446

TABLE A2. - CONCLUDED

(c) X = 1.564 through 10.100.

X = 1.564		X = 2.500		X = 3.067		X = 5.319		X = 10.100	
Y	Z	Y	Z	Y	Z	Y	Z	Y	Z
4.137	.000	4.259	.000	4.303	.000	4.350	.000	4.350	.000
3.600	2.038	4.200	.707	4.200	.936	4.200	1.133	4.200	1.133
3.000	2.848	3.600	2.276	3.600	2.357	3.600	2.442	3.947	1.828
2.400	3.369	3.000	3.023	3.000	3.085	3.000	3.150	3.600	2.442
1.800	3.712	2.400	3.518	2.400	3.572	2.858	3.280	3.530	2.542
1.200	3.911	1.800	3.852	2.119	3.745	2.688	3.469	3.335	2.792
.967	3.956	1.693	3.891	2.052	3.782	2.643	3.660	3.140	3.131
.762	3.981	1.622	3.913	1.965	3.828	2.688	3.850	3.094	3.425
.656	4.011	1.574	3.940	1.894	3.891	2.858	4.030	3.140	3.718
.626	4.039	1.538	4.028	1.869	3.978	3.000	4.105	3.335	4.060
.611	4.073	1.574	4.114	1.894	4.065	3.196	4.270	3.530	4.428
.625	4.107	1.622	4.143	1.965	4.127	3.366	4.547	3.611	4.902
.664	4.137	1.693	4.154	2.052	4.142	3.425	4.867	3.530	5.430
.787	4.162	1.800	↓	2.400	↓	3.366	5.301	3.335	5.849
2.070	↓	2.400	4.162	2.711	4.190	3.196	5.699	3.140	6.101
2.400	4.191	3.000	4.438	3.000	4.430	3.000	5.963	3.000	6.236
2.618	4.260	3.094	4.645	3.121	4.506	2.858	6.101	2.400	6.599
2.821	4.407	3.120	4.846	3.189	4.850	2.688	6.229	1.800	6.843
2.936	4.618	3.094	5.134	3.121	5.285	2.400	6.388	1.200	7.010
2.971	4.839	3.000	5.435	3.000	5.561	1.800	6.641	.600	7.108
2.936	5.181	2.400	6.040	2.711	5.917	1.200	6.815	.000	7.141
2.841	5.435	1.800	6.314	2.400	6.129	.600	6.917		
2.618	5.693	1.200	6.499	2.119	6.266	.000	6.950		
2.400	5.846	.600	6.607	1.800	6.397				
1.800	6.132	.000	6.643	1.200	6.579				
1.200	6.324			.600	6.685				
.600	6.436			.000	6.720				
.000	6.472								

TABLE A3. - COORDINATES OF SINGLE-SCOOP INLET WITHOUT DIVERTER.

(a)  $X = 0.500$  through 1.300.

X = .500		X = .600		X = .700		X = .900		X = 1.300	
Y	Z	Y	Z	Y	Z	Y	Z	Y	Z
3.894	.000	3.924	.000	3.951	.000	4.002	.000	4.088	.000
3.670	1.299	3.600	1.561	3.900	.634	3.900	.897	3.600	1.936
3.047	2.423	3.000	2.529	3.600	1.628	3.600	1.748	3.244	2.487
2.424	3.047	2.773	2.777	3.000	2.571	3.300	2.264	3.172	2.578
2.113	3.270	2.746	2.847	2.858	2.729	2.988	2.662	3.032	2.984
2.112	3.344	2.752	3.078	2.836	2.757	2.923	2.772	3.000	3.468
2.225	3.368	2.745	3.236	2.821	2.788	2.904	2.899	2.695	4.419
2.337	3.441	2.726	3.406	2.812	2.823	2.906	3.100	2.400	4.882
1.801	3.452	2.657	3.748	2.810	2.858	2.883	3.400	1.800	5.469
2.442	3.659	2.561	4.038	2.814	2.927	2.828	3.700	1.200	5.813
1.179	3.711	2.400	4.376	2.815	3.077	2.700	4.106	.600	6.001
.556	3.854	1.800	5.111	2.809	3.227	2.400	4.669	.000	6.061
.000	3.894	1.200	5.506	2.771	3.527	1.800	5.311		
2.413	3.905	.600	5.715	2.700	3.827	1.200	5.677		
2.329	4.135	.000	5.781	2.643	4.000	.600	5.873		
2.113	4.507			2.400	4.501	.000	5.936		
1.801	4.874			1.800	5.194				
1.179	5.323			1.200	5.576				
.556	5.547			.600	5.780				
.000	5.607			.000	5.844				

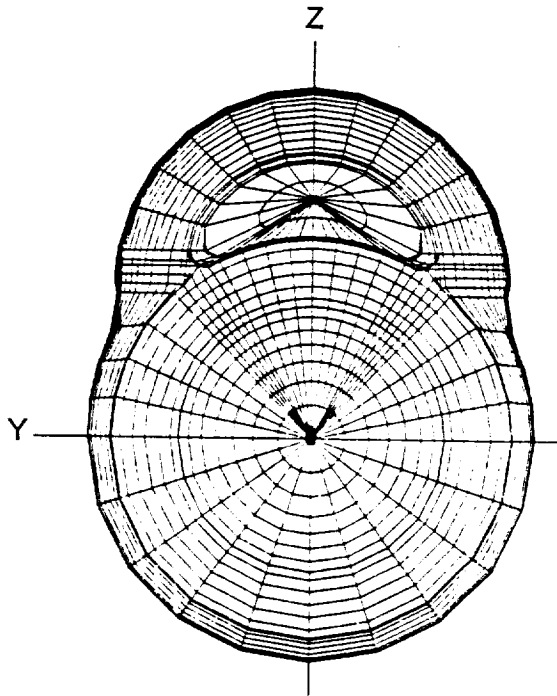




TABLE A3. - CONCLUDED

(b) X = 1.900 through 10.095.

X = 1.900		X = 2.900		X = 4.700		X = 7.300		X = 10.095	
Y	Z	Y	Z	Y	Z	Y	Z	Y	Z
4.193	.000	4.292	.000	4.350	.000	4.350	.000	4.350	.000
4.046	1.098	4.200	.885	4.200	1.132	4.200	1.132	4.200	1.289
3.600	2.149	3.900	1.793	3.900	1.926	3.900	1.926	3.900	2.004
3.300	2.598	3.600	2.338	3.792	2.132	3.810	2.200	3.849	2.2
3.210	2.800	3.499	2.500	3.600	2.590	3.740	2.500	3.794	2.5
3.161	3.100	3.428	2.650	3.551	2.800	3.703	2.800	3.766	2.8
3.140	3.400	3.375	2.800	3.519	3.100	3.698	3.100	3.761	3.1
3.090	3.700	3.321	3.100	3.499	3.400	3.678	3.400	3.743	3.4
3.000	4.028	3.300	3.391	3.454	3.700	3.600	3.867	3.701	3.7
2.895	4.300	3.251	3.700	3.382	4.000	3.471	4.300	3.600	4.120
2.700	4.675	3.175	4.000	3.300	4.250	3.300	4.694	3.300	4.835
2.400	5.088	3.000	4.451	3.149	4.600	3.000	5.188	3.000	5.298
1.800	5.629	2.700	4.960	3.000	4.868	2.700	5.553	2.700	5.648
1.200	5.954	2.400	5.323	2.700	5.285	2.400	5.840	2.400	5.926
.600	6.133	1.800	5.818	2.400	5.602	1.800	6.257	1.800	6.332
.000	6.191	1.200	6.124	1.800	6.052	1.200	6.525	1.200	6.594
		.600	6.294	1.200	6.337	.600	6.676	.600	6.742
		.000	6.349	.600	6.496	.000	6.725	.000	6.790
				.000	6.548				

TABLE A4. - COORDINATES OF TWIN-SCOOP INLET WITH DIVERTER.

(a) X = 0.500 through 0.800.

X = .500		X = .550		X = .600		X = .700		X = .800	
Y	Z	Y	Z	Y	Z	Y	Z	Y	Z
.000	3.893	.000	3.908	.000	3.923	.000	3.951	.000	3.978
2.753	2.753	2.763	2.763	.640	3.870	.622	3.901	.628	3.928
3.893	.000	3.905	.000	1.263	3.714	1.230	3.755	1.240	3.780
3.967	1.699	3.929	1.791	1.852	3.457	1.761	3.537	1.820	3.537
3.973	1.606	3.941	1.606	2.392	3.109	2.449	3.100	2.492	3.100
3.980	1.791	3.951	1.941	2.867	2.676	2.917	2.664	2.954	2.664
3.988	1.513	3.980	1.392	3.266	2.173	3.263	2.227	3.296	2.227
4.011	1.392	4.017	1.169	3.577	1.610	3.521	1.791	3.552	1.791
4.047	1.169	4.024	2.065	3.792	1.005	3.698	1.392	3.726	1.392
4.048	1.910	4.048	.940	3.887	.507	3.837	.940	3.863	.940
4.079	.940	4.073	.705	3.916	.000	3.913	.466	3.925	2.017
4.103	.705	4.091	.466	3.929	1.832	3.928	1.904	3.926	1.895
4.121	.466	4.101	.224	3.937	1.682	3.934	.000	3.931	.466
4.132	.224	4.105	.000	3.949	1.980	3.936	1.754	3.939	1.774
4.135	.000	4.150	2.136	3.960	1.534	3.945	2.053	3.944	2.137
4.163	1.985	4.317	2.153	3.987	1.392	3.959	1.606	3.950	.000
4.298	2.011	4.444	2.132	4.020	2.111	3.989	2.158	3.970	1.606
4.438	1.984	4.562	2.084	4.023	1.169	4.000	1.392	3.989	2.238
4.556	1.904	4.666	2.009	4.055	.940	4.037	1.169	4.012	1.392
4.644	1.791	4.798	1.800	4.080	.705	4.068	2.241	4.049	1.169
4.734	1.606	4.883	1.606	4.098	.466	4.069	.940	4.068	2.316
4.821	1.392	4.965	1.392	4.108	.224	4.093	.705	4.081	.940
4.892	1.169	5.036	1.169	4.112	.000	4.111	.466	4.106	.705
4.952	.940	5.095	.940	4.145	2.191	4.122	.224	4.124	.466
5.001	.705	5.142	.705	4.242	2.212	4.125	.000	4.134	.224
5.035	.466	5.175	.466	4.335	2.213	4.172	2.288	4.138	.000
5.056	.224	5.195	.224	4.502	2.177	4.286	2.304	4.170	2.360
5.062	.000	5.200	.000	4.653	2.098	4.361	2.300	4.281	2.373
				4.771	1.976	4.450	2.284	4.375	2.367
				4.865	1.791	4.606	2.227	4.533	2.330
				4.945	1.606	4.744	2.135	4.681	2.262
				5.025	1.392	4.849	2.007	4.810	2.162
				5.095	1.169	4.901	1.910	4.908	2.032
				5.154	.940	4.955	1.791	4.980	1.886
				5.199	.705	5.032	1.606	5.022	1.791
				5.232	.466	5.110	1.392	5.098	1.606
				5.250	.224	5.178	1.169	5.174	1.392
				5.256	.000	5.235	.940	5.241	1.169
						5.279	.705	5.297	.940
						5.310	.466	5.340	.705
						5.328	.224	5.370	.466
						5.333	.000	5.387	.224
								5.392	.000

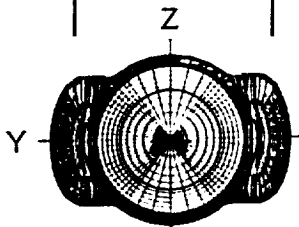


TABLE A4. - CONTINUED.

(b) X = 1.000 through 4.000.

X = 1.000		X = 1.500		X = 2.000		X = 3.000		X = 4.000	
Y	Z	Y	Z	Y	Z	Y	Z	Y	Z
.000	4.027	.000	4.129	.000	4.208	.000	4.307	.000	4.345
.656	3.973	.567	4.090	.377	4.191	.567	4.269	.578	4.366
1.455	3.755	1.124	3.973	.889	4.113	1.125	4.158	1.146	4.191
1.925	3.537	1.718	3.755	1.387	3.973	1.663	3.973	1.759	3.973
2.570	3.100	2.131	3.537	1.900	3.755	2.110	3.755	2.187	3.755
3.020	2.664	2.457	3.318	2.281	3.537	2.458	3.537	2.524	3.537
3.355	2.227	2.727	3.100	2.588	3.318	2.745	3.318	2.805	3.318
3.606	1.791	2.957	2.882	2.845	3.100	2.990	3.100	3.044	3.100
3.779	1.392	3.155	2.664	3.066	2.882	3.201	2.882	3.252	2.882
3.905	.940	3.327	2.446	3.258	2.664	3.384	2.664	3.328	2.793
3.911	2.086	3.477	2.227	3.424	2.446	3.462	2.562	3.410	2.692
3.924	2.241	3.607	2.009	3.570	2.227	3.569	2.410	3.450	2.642
3.925	1.931	3.720	1.791	3.697	2.009	3.636	2.309	3.493	2.592
3.954	1.779	3.804	1.606	3.808	1.791	3.713	2.183	3.558	2.554
3.958	.466	3.871	2.372	3.840	2.567	3.730	2.163	3.608	2.546
3.971	.000	3.886	2.223	3.850	2.446	3.761	2.142	3.657	2.554
3.989	2.380	3.887	1.392	3.869	2.685	3.803	2.132	3.716	2.592
3.992	1.606	3.897	2.519	3.888	1.606	3.816	2.739	3.750	2.642
4.034	1.392	3.923	2.077	3.921	2.228	3.828	2.622	3.763	2.692
4.071	1.169	3.930	1.169	3.923	1.527	3.842	2.142	3.769	2.793
4.103	.940	3.941	2.009	3.962	2.791	3.846	2.562	3.798	2.894
4.117	2.465	3.944	1.075	3.987	2.009	3.850	2.865	3.852	2.995
4.127	.705	3.962	1.027	3.992	1.492	3.859	2.507	3.889	3.045
4.145	.466	3.981	2.630	4.042	1.511	3.870	2.163	3.940	3.100
4.156	.224	3.993	.987	4.045	1.791	3.878	2.410	3.993	3.146
4.159	.000	4.000	1.791	4.070	1.675	3.883	2.183	4.074	3.196
4.271	2.486	4.039	.967	4.072	1.557	3.886	2.928	4.209	3.231
4.402	2.476	4.045	1.606	4.079	1.612	3.891	2.309	4.369	3.222
4.578	2.430	4.090	1.392	4.092	2.845	3.895	2.241	4.527	3.194
4.741	2.351	4.093	.999	4.233	2.860	3.969	3.016	4.681	3.151
4.883	2.238	4.109	2.686	4.517	2.825	4.050	3.067	4.816	3.100
4.990	2.092	4.120	1.059	4.755	2.744	4.215	3.104	5.023	2.995
5.070	1.928	4.124	1.169	4.972	2.617	4.426	3.086	5.184	2.882
5.129	1.791	4.126	1.125	5.153	2.442	4.604	3.044	5.396	2.664
5.202	1.606	4.249	2.698	5.284	2.227	4.690	3.016	5.532	2.446
5.276	1.392	4.465	2.675	5.379	2.009	4.973	2.882	5.645	2.201
5.340	1.169	4.718	2.592	5.466	1.791	5.240	2.664	5.726	2.009
5.393	.940	4.943	2.448	5.532	1.606	5.395	2.446	5.806	1.791
5.434	.705	5.115	2.245	5.597	1.392	5.500	2.227	5.866	1.606
5.462	.466	5.233	2.006	5.652	1.169	5.593	2.009	5.924	1.392
5.478	.224	5.322	1.791	5.697	.940	5.677	1.791	5.973	1.169
5.483	.000	5.391	1.606	5.730	.705	5.738	1.606	6.011	.940
		5.460	1.392	5.752	.466	5.798	1.392	6.040	.705
		5.519	1.169	5.765	.224	5.849	1.169	6.059	.466
		5.567	.940	5.768	.000	5.888	.940	6.069	.224
		5.604	.705			5.917	.705	6.072	.000
		5.628	.466			5.936	.466		
		5.642	.224			5.946	.224		
		5.646	.000			5.949	.000		

TABLE A4. - CONCLUDED.

(c) X = 6.000 through 16.942.

X = 6.000		X = 8.000		X = 10.700		X = 12.942		X = 16.942	
Y	Z	Y	Z	Y	Z	Y	Z	Y	Z
.000	4.350	.000	4.350	.000	4.350	.000	4.350	.000	4.350
.392	4.332	.606	4.308	.436	4.328	.436	4.328	.473	4.324
.782	4.279	1.200	4.181	.868	4.263	.868	4.263	.941	4.247
1.165	4.191	1.771	3.973	1.291	4.154	1.291	4.154	1.398	4.119
1.771	3.793	2.196	3.755	1.701	4.004	1.701	4.004	1.838	3.942
2.196	3.755	2.533	3.537	2.094	3.813	2.094	3.813	2.256	3.719
2.533	3.537	2.813	3.318	2.466	3.584	2.466	3.584	2.648	3.451
2.813	3.318	2.918	3.243	2.813	3.318	2.814	3.317	2.787	3.367
2.969	3.179	3.075	3.173	2.880	3.267	2.984	3.208	2.942	3.314
3.070	3.100	3.306	3.137	3.002	3.200	3.176	3.148	3.104	3.297
3.198	3.040	3.538	3.173	3.096	3.166	3.377	3.140	3.473	3.296
3.365	3.014	3.758	3.243	3.216	3.142	3.573	3.185	4.443	
3.531	3.040	3.982	3.286	3.306	3.137	3.886	3.271	4.633	3.281
3.654	3.100	4.209	3.300	3.397	3.142	4.209	3.300	4.815	3.224
3.803	3.184	4.426	3.286	3.517	3.166	4.441	3.284	5.038	3.100
3.997	3.256	4.640	3.243	3.615	3.200	4.631	3.245	5.258	2.882
4.209	3.283	4.814	3.187	3.867	3.267	4.815	3.187	5.418	2.664
4.517	3.256	5.008	3.100	4.209	3.300	5.008	3.100	5.552	2.446
4.783	3.189	5.319	2.882	4.415	3.287	5.318	2.882	5.669	2.227
4.996	3.100	5.507	2.664	4.618	3.249	5.507	2.664	5.771	2.009
5.317	2.882	5.632	2.446	4.815	3.187	5.632	2.446	5.859	1.791
5.507	2.664	5.729	2.228	5.008	3.100	5.725	2.238	5.925	1.606
5.632	2.446	5.818	2.009	5.319	2.882	5.818	2.009	5.990	1.392
5.727	2.228	5.896	1.791	5.507	2.664	5.896	1.791	6.047	1.169
5.814	2.009	5.954	1.606	5.632	2.446	5.954	1.606	6.093	.940
5.891	1.791	6.011	1.392	5.729	2.228	6.011	1.392	6.127	.705
5.950	1.606	6.059	1.169	5.818	2.009	6.059	1.169	6.147	.466
6.007	1.392	6.097	.940	5.896	1.791	6.097	.940	6.155	.224
6.055	1.169	6.126	.705	5.954	1.606	6.126	.705	6.156	.000
6.093	.940	6.144	.466	6.011	1.392	6.144	.466		
6.121	.705	6.154	.224	6.059	1.169	6.154	.224		
6.139	.466	6.157	.000	6.097	.940	6.157	.000		
6.149	.224			6.126	.705				
6.152	.000			6.144	.466				
				6.154	.224				
				6.157	.000				

TABLE A5. - COORDINATES OF TWIN-SCOOP INLET WITHOUT DIVERTER.

(a) X = 0.500 through 0.800.

X = .500		X = .550		X = .600		X = .700		X = .800	
Y	Z	Y	Z	Y	Z	Y	Z	Y	Z
.000	3.893	.000	3.908	.000	3.923	.000	3.951	.000	3.978
2.753	2.753	2.763	2.763	2.774	2.774	2.794	2.794	2.813	2.813
3.570	1.606	3.400	1.928	3.334	2.069	3.250	2.251	3.188	2.386
3.578	1.791	3.443	1.904	3.418	2.026	3.332	2.196	3.315	2.307
3.615	1.449	3.486	1.927	3.488	2.050	3.429	2.179	3.462	2.281
3.637	1.894	3.542	2.009	3.634	2.155	3.512	2.193	3.538	2.289
3.638	1.392	3.716	2.120	3.916	2.215	3.565	2.228	3.618	2.323
3.709	1.954	3.901	2.154	3.923	.000	3.647	2.257	3.722	2.353
3.715	1.169	3.908	.000	4.148	2.155	3.724	2.281	3.852	2.372
3.780	.940	4.079	2.120	4.338	2.009	3.857	2.303	3.976	2.367
3.794	1.993	4.256	2.009	4.495	1.791	3.946	2.301	3.978	.000
3.831	.705	4.429	1.791	4.603	1.606	3.951	.000	4.156	2.320
3.867	.466	4.539	1.606	4.706	1.392	4.196	2.227	4.317	2.227
3.886	2.009	4.645	1.392	4.793	1.169	4.441	2.009	4.518	2.009
3.888	.224	4.735	1.169	4.866	.940	4.587	1.791	4.659	1.791
3.893	.000	4.809	.940	4.922	.705	4.690	1.606	4.759	1.606
3.895	.000	4.867	.705	4.963	.466	4.790	1.392	4.856	1.392
4.031	1.983	4.909	.466	4.988	.224	4.875	1.169	4.938	1.169
4.156	1.905	4.934	.224	4.995	.000	4.945	.940	5.006	.940
4.251	1.791	4.941	.000			4.999	.705	5.059	.705
4.368	1.606					5.039	.466	5.097	.466
4.483	1.392					5.062	.224	5.120	.224
4.581	1.169					5.069	.000	5.126	.000
4.662	.940								
4.725	.705								
4.769	.466								
4.796	.224								
4.804	.000								

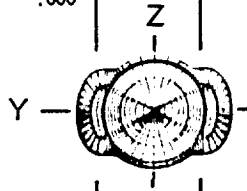


TABLE A5. - CONTINUED.

(b) X = 1.000 through 4.000.

X = 1.000		X = 1.500		X = 2.000		X = 3.000		X = 4.000	
Y	Z	Y	Z	Y	Z	Y	Z	Y	Z
.000	4.032	.000	4.133	.000	4.209	.000	4.306	.000	4.348
.745	3.963	.406	4.113	.389	4.191	.497	4.277	.583	4.308
1.470	3.755	.808	4.053	.897	4.113	.987	4.191	1.156	4.191
1.936	3.537	1.137	3.973	1.390	3.973	1.660	3.973	1.766	3.973
2.290	3.318	1.726	3.755	1.902	3.755	2.107	3.755	2.192	3.755
2.578	3.100	2.138	3.537	2.283	3.537	2.456	3.537	2.529	3.537
2.820	2.882	2.463	3.318	2.590	3.318	2.638	3.403	2.822	3.318
3.083	2.598	2.733	3.100	2.742	3.194	2.812	3.260	3.005	3.238
3.151	2.533	2.986	2.857	2.889	3.062	2.958	3.162	3.203	3.210
3.247	2.470	3.111	2.758	2.986	2.984	3.123	3.100	3.825	3.210
3.354	2.428	3.256	2.691	3.095	2.924	3.302	3.078	4.108	3.181
3.468	2.413	3.413	2.666	3.212	2.882	3.828		4.381	3.100
3.573	2.430	3.472	2.670	3.403	2.857	4.194	3.027	4.570	3.009
3.622	2.446	3.653	2.690	3.832		4.533	2.882	4.756	2.882
3.730	2.472	3.836	2.698	4.087	2.831	4.813	2.664	4.979	2.664
3.840	2.484	4.122	2.664	4.330	2.752	4.997	2.446	5.139	2.446
3.877	2.485	4.195	2.642	4.490	2.664	5.073	2.332	5.271	2.228
3.958	2.481	4.374	2.561	4.734	2.446	5.137	2.227	5.386	2.009
4.038	2.469	4.534	2.446	4.892	2.228	5.257	2.009	5.484	1.791
4.130	2.446	4.725	2.227	5.022	2.009	5.359	1.791	5.556	1.606
4.476	2.227	4.863	2.009	5.134	1.791	5.433	1.606	5.625	1.392
4.644	2.009	4.981	1.791	5.214	1.060	5.506	1.392	5.683	1.169
4.776	1.791	5.068	1.606	5.294	1.392	5.567	1.169	5.729	.940
4.870	1.606	5.152	1.392	5.361	1.169	5.617	.940	5.764	.705
4.963	1.392	5.224	1.169	5.416	.940	5.655	.705	5.788	.466
5.041	1.169	5.283	.940	5.458	.705	5.682	.466	5.801	.224
5.106	.940	5.328	.705	5.488	.466	5.697	.224	5.804	.000
5.156	.705	5.359	.466	5.504	.224	5.701	.000		
5.192	.466	5.377	.224	5.509	.000				
5.213	.224	5.383	.000						
5.219	.000								

TABLE A5. - CONCLUDED.

(c) X = 6.000 through 16.942.

X = 6.000		X = 7.750		X = 12.942		X = 16.942	
Y	Z	Y	Z	Y	Z	Y	Z
.000	4.350	.000	4.350	.000	4.350	.000	4.350
.588	4.310	.588	4.310	.392	4.332	.588	4.310
1.165	4.191	1.165	4.191	.782	4.279	1.165	4.191
1.771	3.973	1.771	3.973	1.165	4.191	1.771	3.973
2.196	3.755	2.196	3.755	1.771	3.973	2.196	3.755
2.533	3.537	2.533	3.537	3.196	3.755	2.533	3.537
2.905	3.318	2.928	3.318	2.533	3.537	2.646	3.453
3.345	3.289	3.102	3.298	2.646	3.453	2.928	3.318
3.788	3.289	3.742	↓	2.780	3.371	3.102	3.298
4.227	3.247	4.061	3.281	2.928	3.318	4.443	↓
4.637	3.085	4.375	3.204	3.102	3.298	4.790	3.251
4.900	2.882	4.658	3.066	3.612	↓	5.051	3.100
5.088	2.664	4.899	2.882	3.868	3.297	5.258	2.882
5.234	2.446	5.095	2.664	4.121	3.271	5.414	2.664
5.363	2.228	5.244	2.446	4.367	3.205	5.553	2.446
5.475	2.009	5.373	2.227	4.599	3.100	5.669	2.227
5.571	1.791	5.485	2.009	4.733	3.017	5.768	2.009
5.640	1.606	5.580	1.791	4.899	2.882	5.861	1.791
5.708	1.392	5.650	1.606	5.095	2.664	5.927	1.606
5.764	1.169	5.717	1.392	5.244	2.446	5.990	1.392
5.809	.940	5.774	1.169	5.373	2.227	6.045	1.169
5.843	.705	5.819	.940	5.485	2.009	6.092	.940
5.865	.466	5.853	.705	5.580	1.791	6.128	.705
5.878	.224	5.876	.466	5.650	1.606	6.148	.466
5.882	.000	5.889	.224	5.717	1.391	6.155	.224
		5.893	.000	5.774	1.169	6.157	.000
				5.819	.940		
				5.853	.705		
				5.876	.466		
				5.889	.224		
				5.893	.000		

TABLE A6. - COORDINATES OF ANNULAR INLET.

X	Radius	
	Internal	External
.5000	4.1840	4.1840
.5040	---	4.2166
.5200	---	4.2554
.5296	4.1517	---
.5400	---	4.2904
.5734	4.1543	---
.5800	---	4.3394
.6000	4.1610	---
.6600	---	4.4075
.7800	↓	4.4810
.9000	↓	4.5388
1.1000	↓	4.6174
1.3000	↓	4.6828
1.5000	↓	4.7395
1.7000	↓	4.7902
2.1000	↓	4.8773
2.5000	↓	4.9495
2.9000	↓	5.0085
3.3000	↓	5.0550
3.7000	↓	5.0891
4.1000	↓	5.1108
4.5000	↓	5.1201
4.9000	↓	5.1248
5.5000	↓	5.1297
6.5000	↓	5.1328

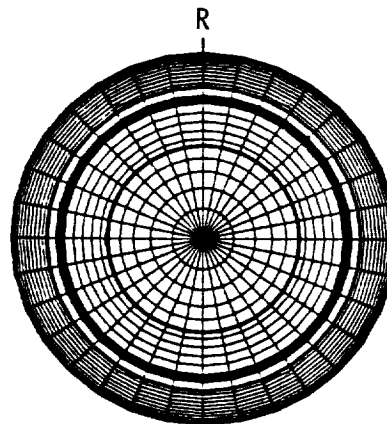




TABLE A7. - PRESSURE PROBE ANGULAR LOCATIONS

	Single-scoop inlet			Twin-scoop inlet			Annular inlet			Nacelle without inlet			
	With diverter (Figure 1-5 (a)) No. of Probes Angle*	X or R Loc.**	No. of Probes Angle*	Without diverter (Figure 1-5 (c)) No. of Probes Angle*	X or R Loc.**	No. of Probes Angle*	Without diverter (Figure 1-5 (d)) No. of Probes Angle*	X or R Loc.**	No. of Probes Angle*	Without inlet (Figure 1-5 (f)) No. of Probes Angle*	X or R Loc.**	No. of Probes Angle*	
Row A	14	A-1	100°	14	A-1	0°	14	A/C-2	18	A/C-2	175°	18	A-Ann
Row B	23	B/E-1	160°	23	B/E-1	90°	23		18		270°	10	B-Ann
Row C	23		180°	23		180°	23		18				
Row D	23		221°	23		180°	23	D-2	10	D-2			
Row E	23		255°	23		270°	23	E-2	7	E-2			
Row F	26	F/I-1	300°	26	F/I-1	0°	26						
Row G	26		0°	26			26						
Row H	26		231°	26									
Row I	26		129°	26									
Gutter	21	GTR-1					17	GTR-2				8	
Inlet throat	12			12			24						
Inlet lip	3												
Row A	5	TA-1D	154°	5	TA-1ND	256°	5	TA-2D	5	TA-2ND	0°	4	
Row B	5	TB-1D	167°	5	TB-1ND	264°	5	TB-2D	5	TB-2ND	90°	4	
Row C	5	TC-1D	180°	5	TC-1ND	270°	5	TC-2D	5	TC-2ND	180°	4	
Row D	5	TB-1D	193°	5	TB-1ND	276°	5	TB-2D	5	TB-2ND	270°	4	
Row E	5	TA-1D	206°	5	TA-1ND	288°	5	TA-2D	5	TA-2ND			
Diverter	4												
Row A	10	BL-A	6°	10	BL-A								6°
Row B	6	BL-B	185°	6	BL-B								
Row C	6	BL-C	275°	6	BL-C								
Row D	15	K	25°	15	K								25°
Row E	15	K		15	K								15
Row F	15	K		15	K								15

Surface static pressures

Row A  
Row B  
Row C  
Row D  
Row E  
Row F  
Row G  
Row H  
Row I  
Gutter  
Inlet throat  
Inlet lip

Inlet and diverter total pressures

Row A  
Row B  
Row C  
Row D  
Row E  
Diverter

External static pressures

Boundary layer rake A  
Boundary layer rake B  
Boundary layer rake C  
Exit probe rake

\* Clockwise from top, looking aft, with centers as shown in figures. For single-scoop inlets, top is defined as 180° from inlet, in accordance with GUN-1 installation.

\*\* Refer to indicated column in table III for axial or radial locations.

TABLE A8. - PRESSURE PROBE AXIAL AND RADIAL LOCATIONS.

Dimensions in inches. Refer to Figure T-5 and TABLE A7 for annular locations.

(a) Surface static pressure locations, axial distance aft of highlight.

Single-scoop inlet				Twin-scoop inlet				Annular inlet	
Row A-1	Rows B/E-1	Rows F/I-1	Row GTR-1	Rows A/C-2	Row D-2	Row E-2	Row GTR-2	Row A-Ann	Row B-Ann
.00	.00	-.28	.00	.00	.00	.00	.00	.00	.00
.12	.12	-.18	.41	.05	.40	.05	.40	.05	.40
.22	.22	-.09	1.16	.10	1.00	.10	.80	.10	1.00
.61	.38	.00	2.33	.20	1.50	.20	1.40	.20	1.50
1.64	.61	.12	3.49	.40	2.00	.40	2.00	.40	2.00
2.45	1.22	.22	4.65	.60	3.00	.60	3.00	.60	3.00
3.06	1.64	.38	5.82	1.00	4.00	1.00	4.00	1.00	4.00
4.29	2.45	.61	6.98	1.50	6.00		6.00	1.50	6.00
5.51	3.06	1.22	8.14	2.00	8.00		8.00	2.00	8.00
6.74	3.67	1.64	9.31	2.50	10.00			2.50	10.00
7.96	4.29	2.45	10.74	3.00				3.00	
9.18	4.90	3.06		3.50				3.50	
10.41	5.51	3.67		4.00				4.00	
11.63	6.12	4.29		5.00				5.00	
	6.74	4.90		6.00				6.00	
	7.35	5.51		7.00				7.00	
	7.96	6.12		8.00				8.00	
	8.57	6.74		10.00				10.00	
	9.18	7.35							
	9.80	7.96							
	10.41	8.57							
	11.02	9.18							
	11.63	9.80							
		10.41							
		11.02							
		11.63							

TABLE A8. - CONTINUED.

(b) Throat total pressure locations, distance from inner surface.

Single-scoop inlet					
With Diverter			Without Diverter		
Rake TA-1D	Rake TB-1D	Rake TC-1D	Rake TA-1ND	Rake TB-1ND	Rake TC-1ND
.11	.13	.14	.10	.13	.14
.32	.40	.43	.30	.40	.43
.54	.67	.71	.49	.67	.72
.75	.94	.99	.69	.94	1.01
.96	1.21	1.28	.89	1.21	1.30

Twin-scoop inlet					
With Diverter			Without Diverter		
Rake TA-2D	Rake TB-2D	Rake TC-2D	Rake TA-2ND	Rake TB-2ND	Rake TC-2ND
.06	.08	.08	.06	.08	.08
.20	.23	.24	.19	.22	.23
.32	.38	.40	.32	.37	.39
.46	.54	.56	.45	.52	.54
.58	.69	.72	.58	.67	.70

TABLE A8. - CONCLUDED.

(c) External rake total pressure locations, distance from surface.  
 x = axial distance aft of highlight.

Rake BL-A (X = -.28)	Rake BL-B (X = 2.00)	Rake BL-C (X = 2.00)	Rake K (X = 3.42)
.02	.05	.05	.72
.07	.10	.10	1.44
.11	.14	.14	2.16
.16	.25	.25	2.87
.21	.50	.50	3.59
.34	.75	.75	4.31
.47			5.03
.60			5.74
.72			6.46
.84			7.18
			7.90
			8.62
			9.33
			10.05
			10.77

## Appendix B

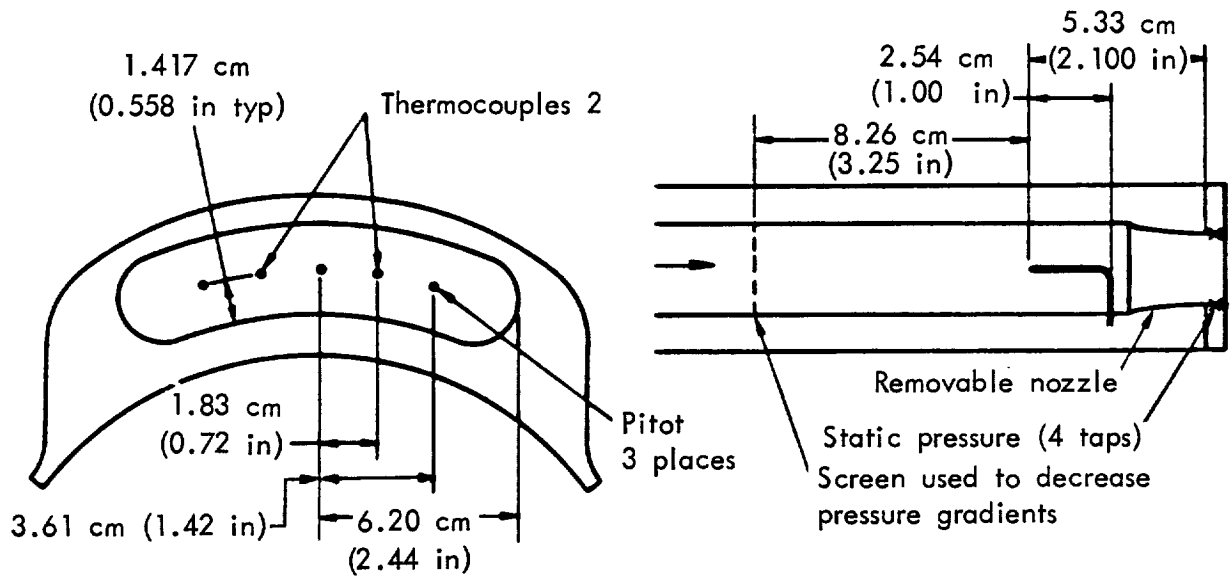
### Inlet Airflow Calibration

The force measurement portions of the program were performed with the inlets mounted on either the top or the sides of the PTR as flow-through configurations. Exit nozzle inserts were used to vary inlet mass flow. In the GUN II single-scoop inlet tests, the inserts provided exit areas that were 60, 80, and 100 percent of the inlet throat area. For the GUN-III twin-scoop and annular inlet tests, similar inserts were fabricated with exit areas of 25, 50, and 75 percent of the inlet throat area. To calibrate these nozzles, connections were made with the aspiration system in the UTRC balance chamber outside the main tunnel. Since this was a static calibration, the inlets were fitted with bellmouths to eliminate lip losses.

Because the propeller produced total pressure gradients across the inlet and the static test would not have these same gradients, the model was fitted with screens of 20 percent solidity to produce a flat total pressure profile entering the nozzle in both the static and propeller testing. (Subsequent testing showed that these were quite effective.) Approximately 3 duct heights downstream of the screens, a total pressure rake was installed to determine the absolute average total pressure levels. No discernible pressure gradients were noted. Thermocouples and nozzle static pressure taps were also installed to allow calculation of an ideal airflow. The model arrangement and instrumentation are shown in Figure B1.

The single-scoop inlet, flow-through model calibration is shown in Figure B2. The data for all the nozzles were correlated and fell within  $\pm 1.0$  percent of each other. The bellmouths were removed and repeat tests showed the levels to be unaffected; the only change was that for the larger nozzle throat areas, the inlet apparently choked sooner without the bellmouth. This prevented achieving as high a pressure ratio and airflow as was achieved with the bellmouth in place. In both cases, the airflows achieved in the static calibrations bracketed the airflow that was anticipated in the ensuing wind tunnel tests. Comparing the levels of the flush versus diverter versions of the single-scoop inlet showed that the flush had the lower flow coefficient. This result was at least partially due to the fact that different nozzles had to be used with each inlet, because of the way that the models were fabricated.

In the GUN III testing, the twin-scoop and annular inlet exhaust nozzles were designed to be compatible with the aspiration system in the main wind tunnel. Also the twin-scoop inlets, flush and diverted, were designed to use the same calibration nozzles. The GUN II tests had shown that the single-scoop inlets did not need bellmouths. Since they were similar in design, it was assumed that the twin-scoop inlets would not need a bellmouth, either. There was some doubt, however, as to whether a static calibration without a bellmouth would be adequate for the annular inlet. To check this question, the annular inlet was tested in the tunnel, both statically and at Mach numbers up to 0.70. There was no discernible shift in  $C_d$  with Mach number. The complete annular inlet calibration test



Note: (1) The removable nozzles had exit areas of 100%, 80%, 60% for GUN II  
 (2) The removable nozzles had exit areas of 75%, 50%, 25% for GUN III

Figure B1. - Instrumentation used for mass flow calibration.

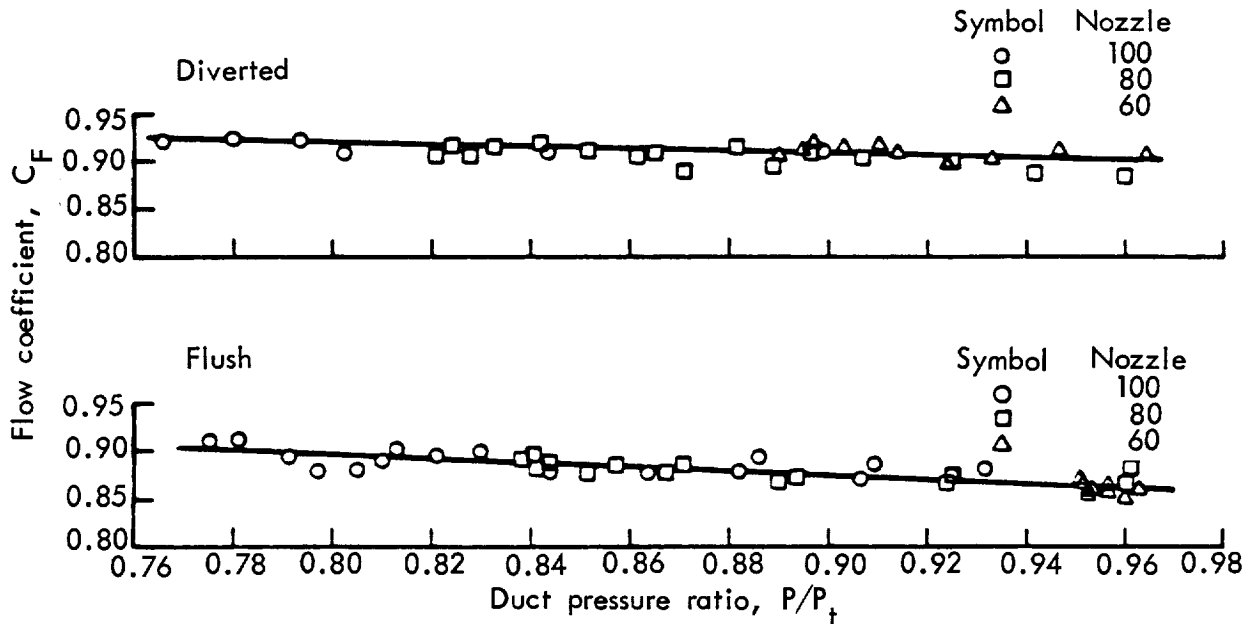


Figure B2. - Nozzle calibrations for single-scoop inlet.

results, along with Mach number effects, are shown plotted in Figure B3.

The nozzles for the annular and twin-scoop inlets were attached to bifurcations and could be individually blocked to segregate each nozzle's discharge flow. These bifurcations were separate ducts designed so that each would be properly sized to pass one-half of the total inlet flow. For some reason, the highest (75 percent) flows did not quite agree when comparing one side with the other. However, the 25 and 50 percent nozzles agreed quite well with each other. After some study of the data taken with the annular inlet installed, the decision was made to utilize the average exit flow coefficients in all cases. Within reasonably narrow limits, if the average flow coefficients for this configuration are compared coincidentally, they collapse into a single Cd curve, as seen in Figure B4.

The calibrations for the twin-scoop inlets are shown in Figure B5. Here we see some differences between the calibration curves for each nozzle, so each twin-scoop configuration required its own set of data for determining tares and inlet mass flow ratio.

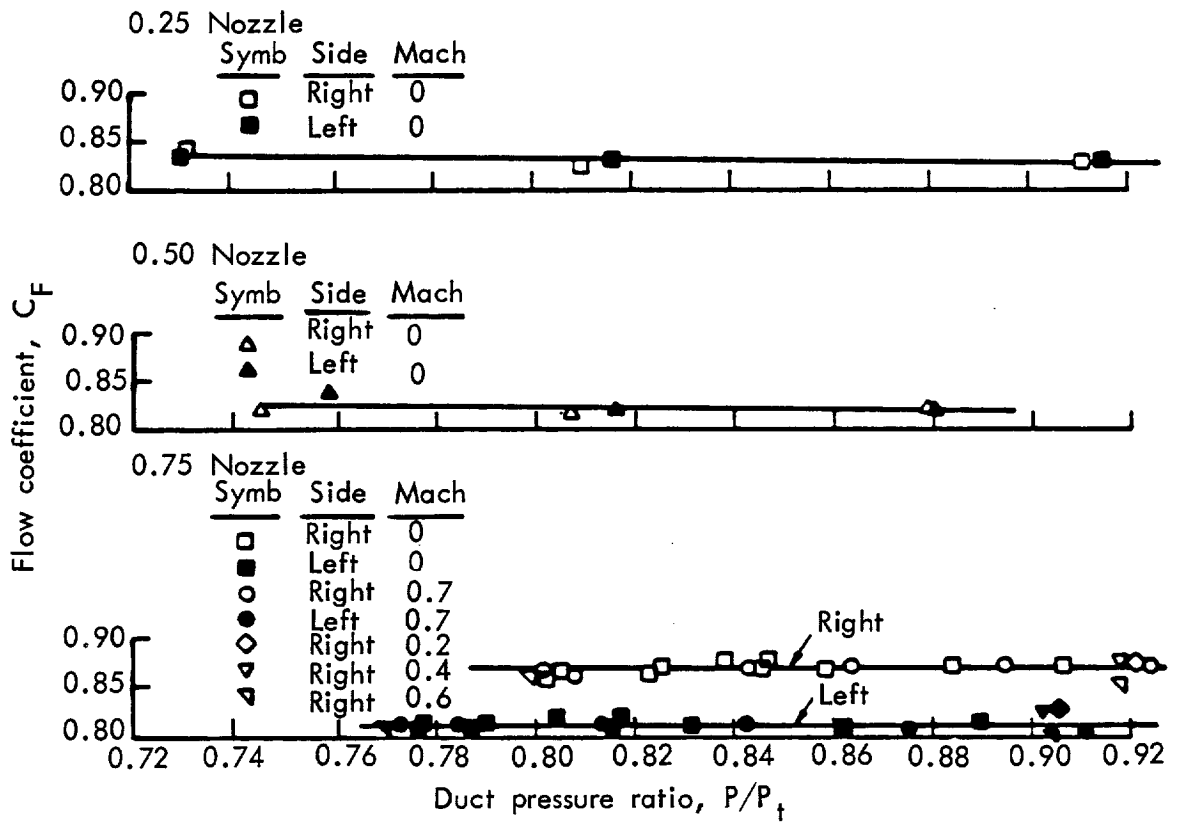


Figure B3. - Nozzle calibrations for annular inlet.



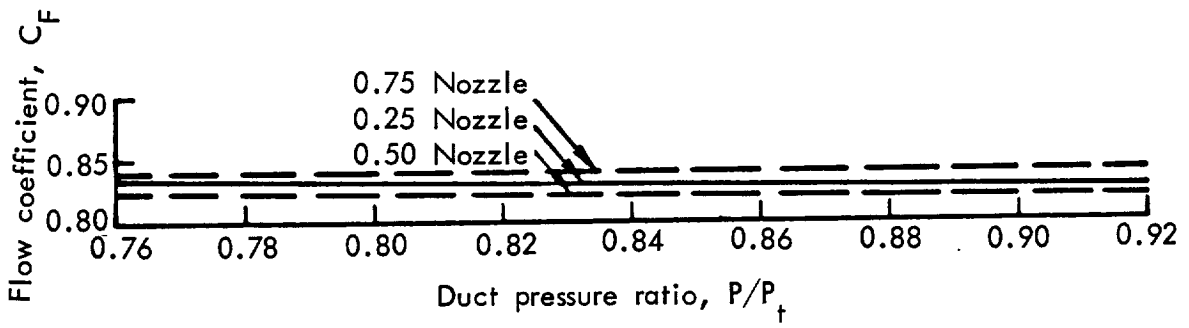


Figure B4. - Nozzle calibrations for annular inlet (average of right and left nozzles).

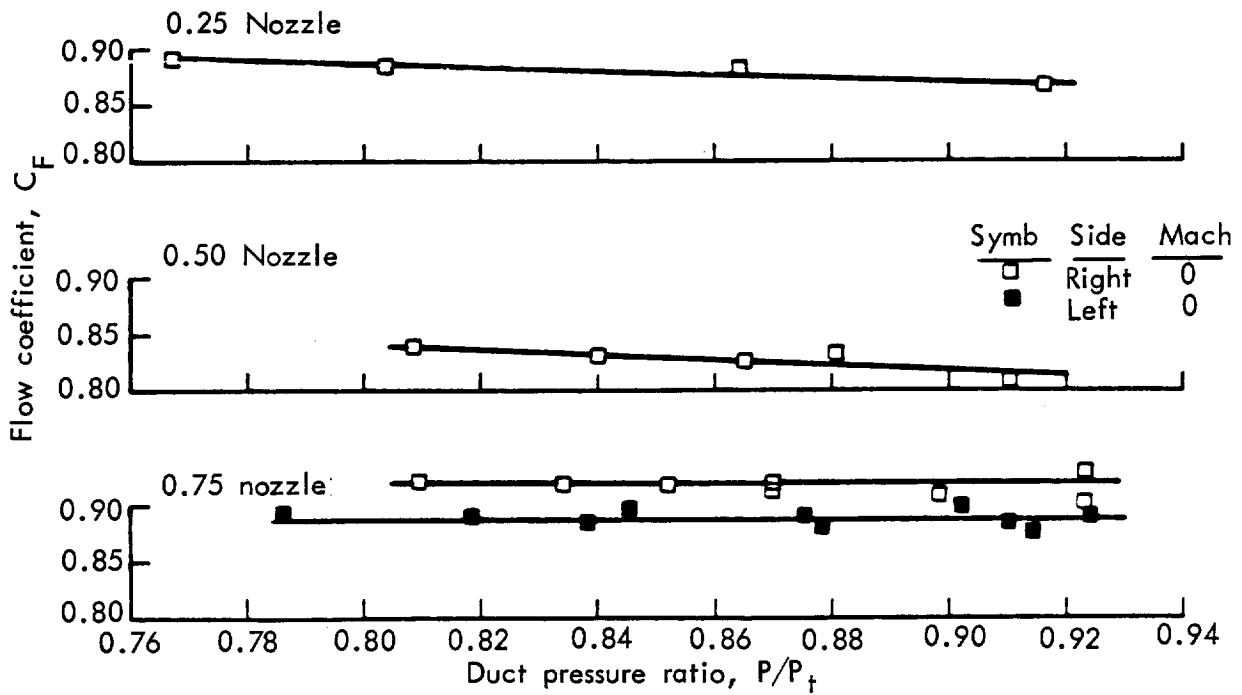


Figure B5. - Nozzle calibrations for twin-scoop inlet.



## Appendix C

### Repeatability Analysis

In the first two test phases, GUN I and GUN II, the efforts were concentrated on close coupled, single-scoop inlets and relative performance trends associated with various amounts of boundary layer diversion and inlet mass flow were established. In the third test phase (GUN III), however, annular, twin-scoop and aft-translated, single-scoop inlet types were also examined for comparison. For this reason, three spinner and nacelle combinations tested in GUN II were tested again in GUN III to check repeatability. These configurations were: bare nacelle without propeller, bare nacelle with propeller, and single-scoop inlet with propeller.

Thrust-minus-drag data for the above-mentioned configurations are presented in Figure C1. The uppermost curves present the isolated nacelle, no prop data indicating that a 1.5 to 2.5 percent discrepancy exists between the GUN II and GUN III data. In the uncertainty analysis (Appendix D), this lack of repeatability is shown to be about the best that one can expect. Basically, this is due to internal pressure tare uncertainty and the fact that a 71 newton (16 lb.) force is being measured with a 2670 newton (600 lb.) balance. As shown in the middle of Figure C1, excellent repeatability is observed at the lower Mach numbers for the isolated nacelle with propeller installed. At Mach 0.80, however, the curves diverge to a 4 percent discrepancy. With the single-scoop inlet installed, the lower part of Figure C1 shows a 2.5 percent bias over a fairly wide range of Mach numbers. All of these are absolute data comparing one tunnel entry to a completely different one which occurred several months later. It should be noted that, in most cases, GUN III data are lower than GUN II, indicating that the bias is consistent for this one model. However, previous to this test series, the repeatability of propeller thrust data has always been quoted as  $\pm 1.0$  percent, or a potential for bias up to a maximum of 2 percent (Reference 2).

The isolated blade performance of Reference 2 is not a direct measurement, but it is the difference between the spinner-nacelle drag without a prop and the spinner-nacelle with a prop. Both parameters were recorded in the same wind tunnel entry. By taking this approach, the considerable potential for some kind of bias developing between entries was eliminated. The actual characteristic value of the "second entry" bias for the isolated blade case is shown in Figure C2, where thrust coefficient is plotted versus Mach number for GUN II and III. The data are shown to fall within a scatter band of  $\pm 1.0$  percent, which is consistent with the experience cited in Reference 2. The experiments could be conducted and yield meaningful data on an incremental basis if the bias stayed consistent throughout the testing. Unfortunately, unlike the isolated nacelle testing, vastly different types of inlets were being installed on the nacelle, and it was uncertain whether the bias level would remain the same. To interpret the data with some degree of confidence, it seemed essential to understand what was causing the shifts.

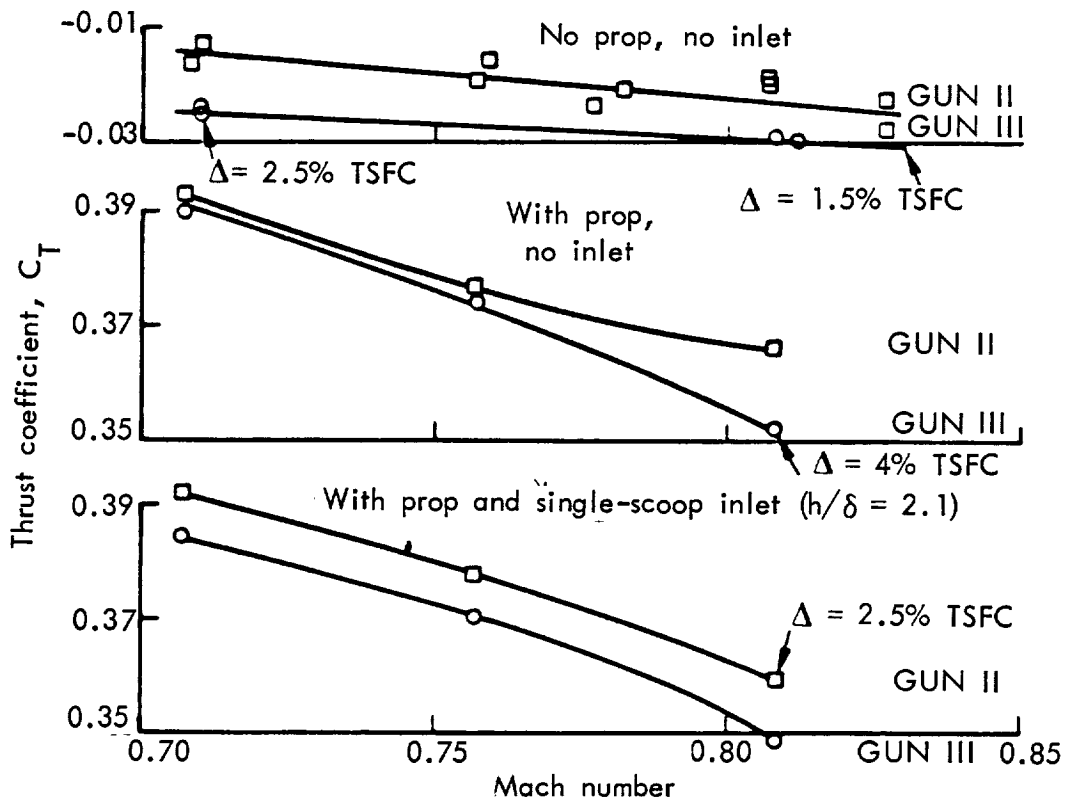


Figure C1. - Comparison of absolute measurements (thrust coefficient) on three configurations.

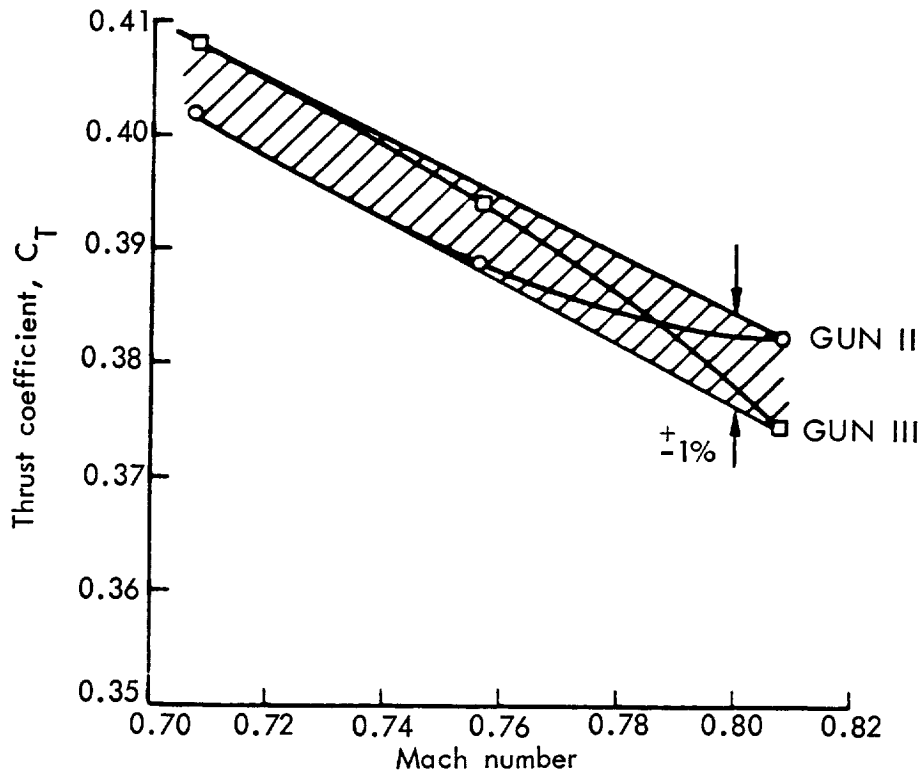


Figure C2. - Propeller isolated blade performance comparison (GUN-II versus GUN-III).

The balance data were reviewed to identify where the bias shift was occurring. The raw balance data implied that GUN III performance should be higher than that measured for GUN II, as shown in Figure C3A. But it was found that the tare corrections drove the GUN III data down to a level below that of GUN II (Figure C3B). Consequently, each individual tare force was isolated and examined.

Three tare forces were used in the data analysis. Comparing two runs at the same advance ratio, it was noted that two of the three tares were quite small and showed reasonable repeatability. These were the base and gap tares, and the internal drag of the inlet. However, the internal (PTR) tare shifted 17 pounds between GUN II and GUN III (Figure C4A). The individual tare was made up of three components and the shifts for each are graphically presented in Figure C4B. One of these, which was called Tab 1, repeated very well. The other two, however, called TFV and TFV3, did not repeat at all. Each of the non-repeatable tares was composed of three pressure readings applied to two large areas, 0.1083 square meter (1.166 sq. ft.) and 0.1301 square meter (1.4 sq. ft.) No problems could be found with the pressure level measurements. However, the levels of the pressure readings were high relative to free stream static pressure and, therefore, probably should have been measured with more pressure taps. Figure C5 shows a comparison of GUN II and GUN III internal tare corrections as made throughout the respective tests and these plots substantiate relatively large, running shifts in tare levels. GUN II experienced tare levels of  $-20.0 \pm 15.6$  newtons ( $-4.5 \pm 3.5$  pounds), while the GUN III data registered levels of  $-80.1 \pm 66.7$  newtons ( $-18.0 \pm 15.0$  pounds). The wide variation about the mean value for the GUN III tare contributed to its lack of credibility relative to GUN II. In conclusion, the tares applied to the internal cavity appeared to be the source of the poor repeatability.

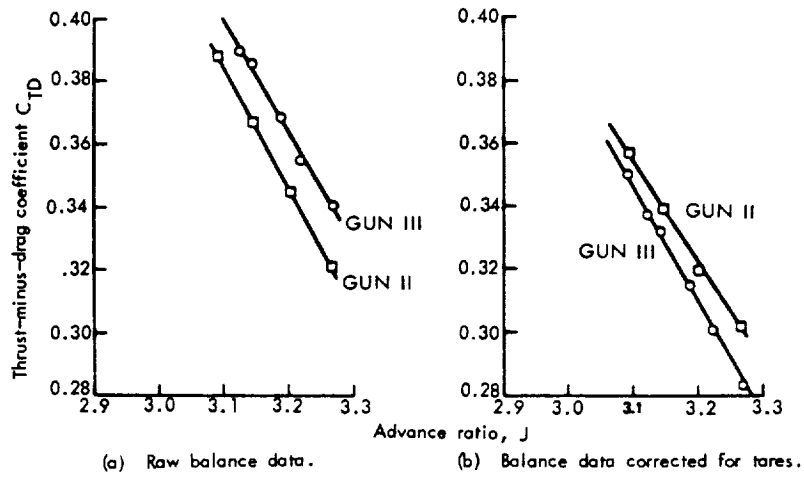


Figure C3. - Application of tares to GUN-III data overcorrects relative to GUN-II.

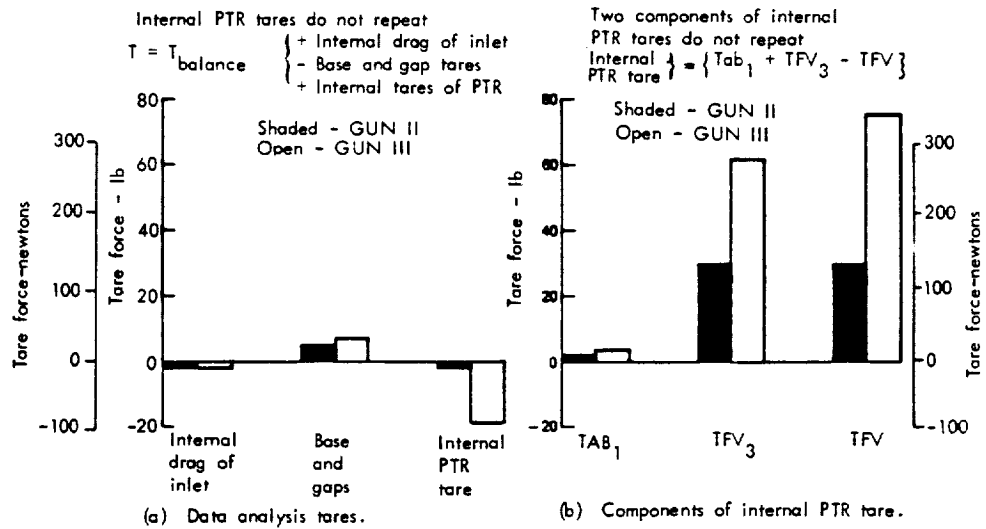


Figure C4. - Contribution of tares to corrected force measurement is significant.

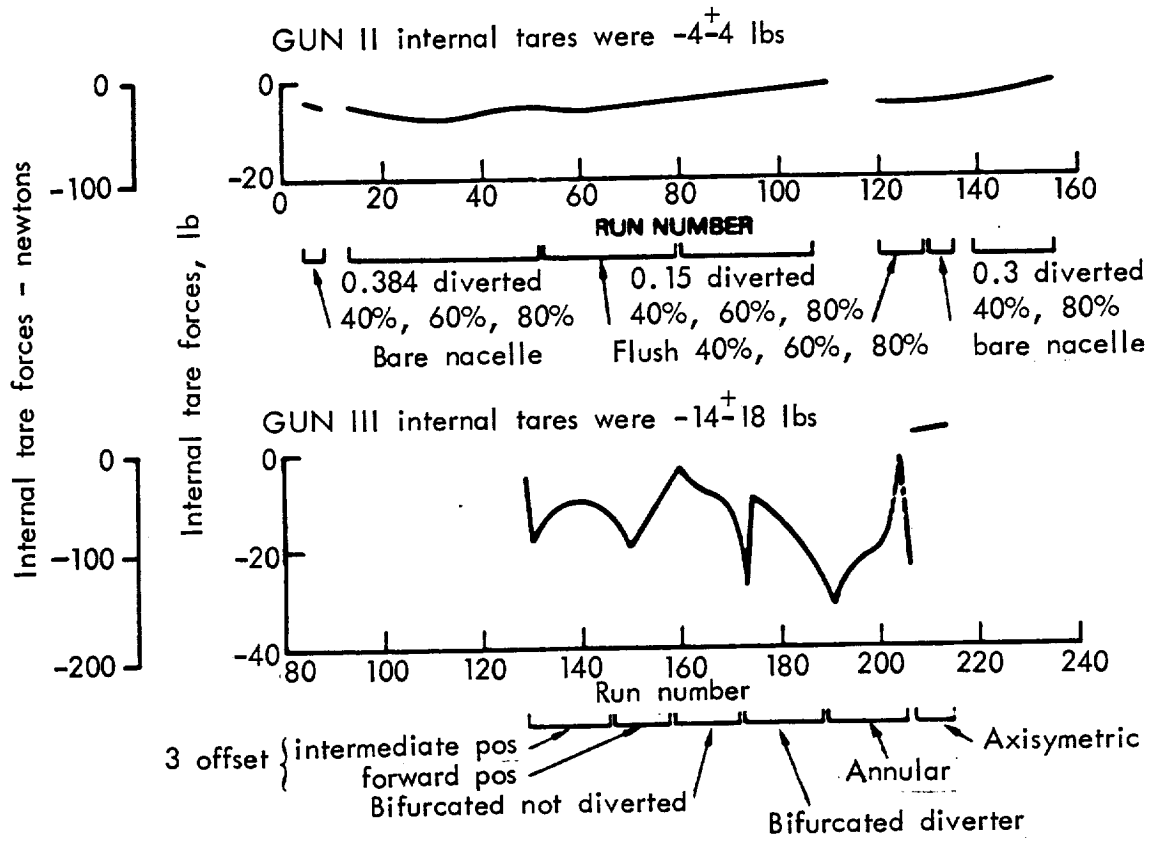


Figure C5. - GUN-III internal tare variations are greater than those of GUN-II.





## Appendix D

### Uncertainty Analysis

The uncertainty of a piece of instrumentation and its contribution to the uncertainty of a system does not necessarily have a direct bearing on repeatability. However, the two are interrelated and uncertainty is a potential threat to repeatability when two different installations in two different tests are involved. For this reason, the uncertainty of the two main pieces of instrumentation, as quoted by United Technologies Research Center personnel, have been included for analysis.

A. Balance  $\sim \pm 1/2$  % of capacity =  $0.005 \times 2670$  (600) =  $\pm 13.3$  newtons (3 lbs.)

B. Pressure  $\sim \pm 68948$  newtons per square meter (10 PSID) transducers were used-- these have 1.0 percent uncertainty.  $0.001 \times 68948$  (10) = 69.0 newtons per square meter (0.010 PSI)

The three internal tare terms discussed in the previous section were as follows:

1. One area was 0.108 square meter (1.17 sq. ft.), thus the uncertainty was 7.6 newtons (1.7 lbs.).
2. Another area was 0.130 square meter (1.4 sq. ft.), thus uncertainty was 8.9 newtons (2.0 lbs.).
3. The other areas were so small that they had a negligible effect.

Determination of the system uncertainty was accomplished by:

$$\begin{aligned}\Delta T &= \text{SQRT} ((\Delta 1)**2 + (\Delta 2)**2) \\ &= \text{SQRT} (13.3(3)**2 + 7.6(1.7)**2 + 8.9(2)**2)\end{aligned}$$

Thus  $\Delta T = 16.9$  newtons (3.8 lbs.)

This is the same magnitude as the 22.2 newton (5 lb.) repeatability problem noted in Appendix C.

#### A. Balance Instrumentation

1. The selected calibration schedule covered a wide range of thrust levels (0 to 2670 newtons (600 lbs.)). The test operating range was from 445 newtons (100 lbs.) to 890 newtons (200 lbs.) with the prop on, and to -156 newtons (-35 lbs.) with the prop off (See Figure D1).
2. Future testing should consider the possibility of acquiring and utilizing an 890 newton (200 lb.) balance.

#### B. Pressure Instrumentation

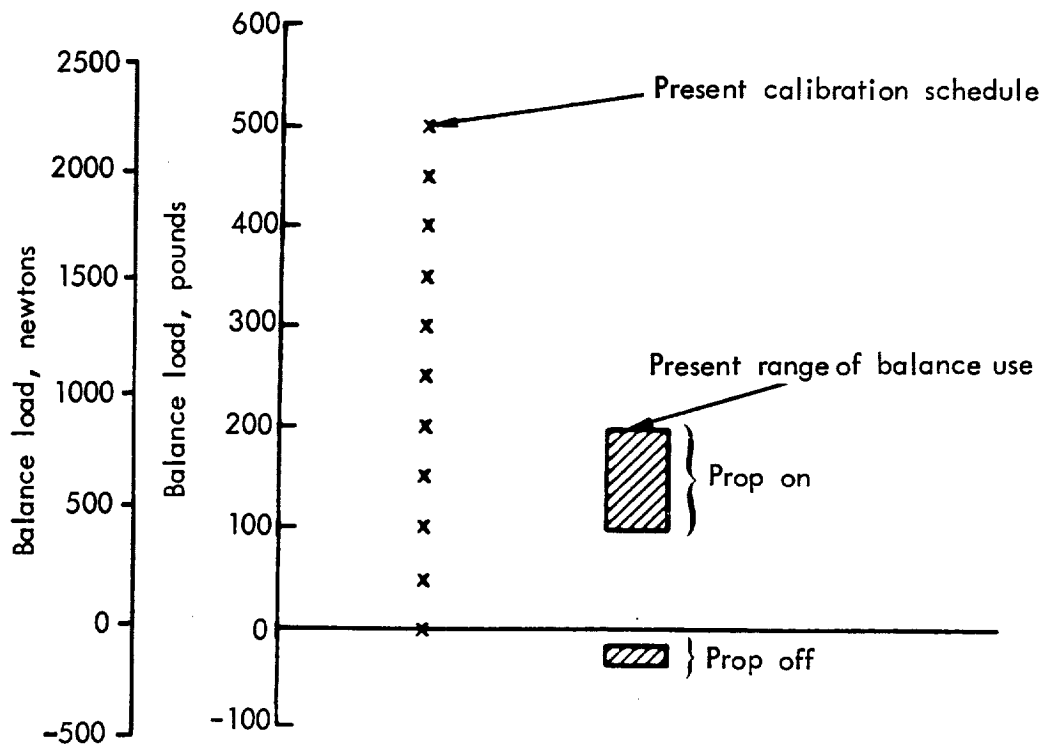


Figure D1. - Balance use and calibration schedule.

1. The selected system measured pressures referenced to Pto. A 68948 newton per square meter (10 PSID) transducer was used. The tare contribution was then computed by means of the relationship,  $(P_i + (P_t - P_o)) * A = \text{tare force}$ .

This could have been improved by measuring the pressure relative to static pressure. This would have required a 689 newton per square meter (0.10 PSID) transducer and the reduction of the 9 newton (2 lb.) uncertainty to 0.9 newton (0.2 lb.). The tare contributions should have then been computed by using the relationship,  $P_i * A_i = \text{tare force}$ .

2. Cavity pressure instrumentation should have been shielded and the instrumentation density should have been increased.



## Appendix E

### Data Reduction Description

The data reduction procedure for this program was modeled after that used by Hamilton Standard. However, the procedure had to be expanded to include the propulsion related terms introduced by the presence of an inlet. The difficulty that compounded the analysis was that the propulsion parameters and competing configurations had to be compared at the same  $C_p$ ,  $J$  point. It was found that the propeller was sensitive and responsive to the inlet and variations in its performance parameters. Therefore, setting the same  $C_p$ ,  $J$  during a test run was not possible. Consequently, the tests had to be performed parametrically and the parameters correlated and interpolated for comparison. The steps that were necessary for establishment of both recovery and  $CT$  were:

1. Collect test at a minimum of 3 blade angles (bracketing the design point of interest) at each Mach number and mass flow.
2. Generate plots of power coefficient ( $CP$ ) versus advance ratio ( $J$ ), as shown in Figure E1a. Experience has shown that since these data are over a limited range, they are nearly linear and can easily be represented by simple expressions.
3. Generate plots of thrust coefficient ( $CT$ ) or pressure recovery versus advance ratio ( $J$ ) (Figure E1b). Again, experience has shown that, over a limited range, a family of linear curves is easily generated.
4. Combine the previous two figures to create families of thrust or pressure curves on the  $C_p$ ,  $J$  coordinate system (Figure E1c).
5. Plot  $CT$  versus  $CP$  at design point value (Figure E1d).
6. Determine the value of  $CT$  or inlet recovery at design point values of  $CP$  and  $J$ .

After analyzing several configurations, it was observed that the lines of constant  $CT$  on a  $CP$ ,  $J$  map were not only nearly linear, but also have virtually the same slope with variable  $y$  intercepts. This resulted in assuming the second order expression:

$$CP = \underbrace{(A) + B (CT)}_{1st\ order\ term} + \underbrace{C (J) + D (J)^2 + E(J)(CT) + F (CT)^2}_{2nd\ order\ term}$$

Combining data and multi-variate curve fit with a regression analysis resulted in the conclusion that the two squared terms in the second order term could be eliminated with negligible consequences. As a result, the preceding equation became:

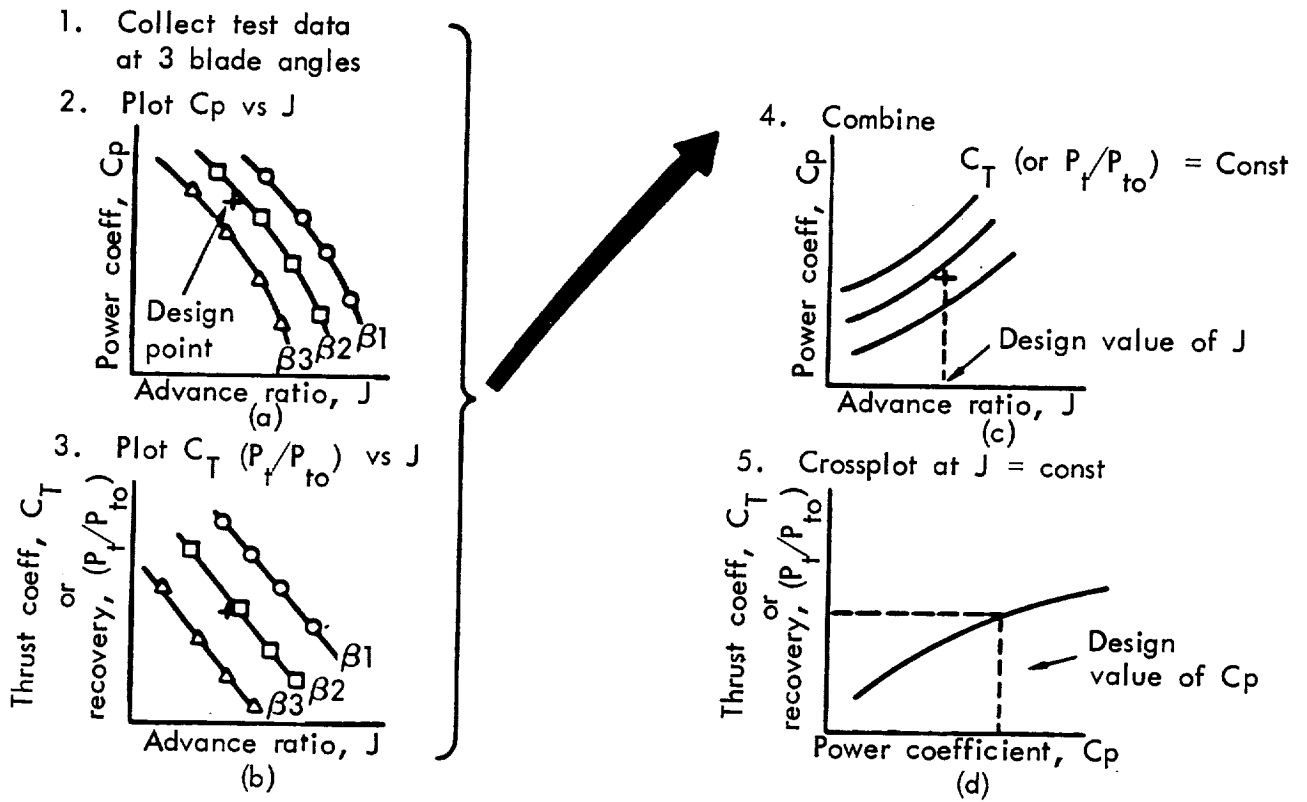


Figure E1. - Description of data reduction process used to determine design point values of thrust coefficient and recovery.

$$CP = \underline{(A) + B (CT) + C (J) + E(J)(CT)}$$

After the constants were evaluated by computer, the desired value of thrust coefficient (CT) was solved for by substituting the desired design point values of power coefficient (CP) and advance ratio (J).





## Appendix F

### List of Symbols

The units used for the physical quantities of this report are given both in SI Units and U. S. Customary Units, except for the tables of Appendix A. These tables contain long lists of dimensional (contour definition) and positional (pressure tap location) data. Substantial additional expense would accrue to the government if it were required that these tables be presented in both sets of units. Measurements and calculations performed during and after the testing were in the U. S. Customary Units.

Aex,AN	Flow-Through Inlet Nozzle Exit Area
Ahl	Inlet Highlight Area
Ao	Cross-Sectional Area of Ingested Freestream Tube
Aref	Nacelle Reference Cross-Sectional Area,
Ath	Inlet Throat Area
B, $\beta$	Propeller Blade Angle @ .75 Radius, Beta - Degrees
Cd	Drag Coefficient, Drag / (qo x Aref)
Cdc	Cowl Drag Coefficient
Cdd	Coefficient for Drag of Boundary Layer Diverter
Cdn	Net Total Drag Coefficient, Cds + Cdc
Cds	Spinner Drag Coefficient, Integral( (Ps-Po) x dA ) / (qo x Aref)
Cde	Installation External Drag Coefficient
Cp	Pressure Coefficient, (Ps - Po) / qo
Ct	Internal Thrust Loss Coefficient
CF	Flow Coefficient, Actual Flow / Ideal Flow
CP	Power Coefficient, Power / ( $\rho_o$ x N**3 x Dp**5)
CT	Thrust Coefficient, Thrust / (qo x Aref)
CTD	Thrust-minus-Drag Coefficient, (F-D) / ( $\rho_o$ x N**2 x D**4)
$\delta$	Calculated Flat-Plate Boundary Layer Height

D	Drag
D <sub>bld</sub>	Drag of Boundary Layer Diverter
D <sub>max</sub>	Diameter of Nacelle at Maximum Cross-section
D <sub>p</sub>	Diameter of Propeller at Tip
$\eta$	Propeller Efficiency
F	Thrust
F <sub>n</sub>	Net Thrust
F <sub>u</sub>	Thrust at 100% Pressure Recovery
g	Gravitational Constant
h, H	Inlet Offset Vertical Distance from Cowl Surface to Inlet Highlight
HP	Horsepower
J	Propeller Advance Ratio, $V_0 / (N \times D_p)$
L	Reference Total Length of Cowl
$\lambda_1$	Thrust-minus-Drag Penalty due to Inlet and and Relative to Isolated Blade, ( (F-D) / (F-D) <sub>ISOL BLADE</sub> ) - 1
$\lambda_2$	Thrust-minus-Drag Penalty due to Inlet and and Relative to Isolated Nacelle, ( (F-D) / (F-D) <sub>ISOL NACELLE</sub> ) - 1
m	Inlet Mass Flow, Freestream Air, $W_a / g$
m <sub>f</sub>	Fuel Mass Flow, $W_f / g$
MFR	Inlet Mass Flow Ratio, $A_0/A_{h1}$
MFRT	Throat Mass Flow Ratio, $A_0/A_{th}$
M <sub>0</sub>	Freestream Mach Number
N	Propeller Rotational Speed
P <sub>0</sub>	Free Stream Static Pressure
P <sub>s</sub>	Static Pressure
P <sub>s1</sub>	Inlet Throat Static Pressure

Pt	Total Pressure
Pt1	Total Pressure at Inlet Throat
Pt2	Total Pressure at Compressor Face
Pto	Freestream Total Pressure
qo	Freestream Dynamic Pressure
$\rho_o$	Freestream Density
R	Radius
Rc	Radius of Curvature
Rp	Radius of Propeller at Tip
$\theta$	Inlet Angular Circumferential Spread
V	Velocity
VE	Exit Velocity of Complete Nacelle
Vo	Freestream Velocity
Wa	Inlet Airflow
Wf	Fuel Flow
X	Axial Distance from Zero Reference Station
Y	Vertical Distance from Zero Reference Line

#### **Nacelle Station Definitions**

0	Freestream at Infinity Forward of the Inlet
1	Inlet Throat
2	Compressor Face
3	Propeller Plane
MAX	Maximum Nacelle Cross-Section
E	Exit

### Abbreviations

BLD	Boundary Layer Diverter
PTR	Propeller Test Rig
SS	Single-scoop
TS	Twin-scoop

## References

1. Final Report for NASA Contract NAS3-22751: Aerodynamic and Mechanical Design of Advanced Turboprop Core Inlets for the NASA-Lewis PTR. Lockheed-Georgia Company LG83ER0136, March 20, 1983.
2. Rohrbach, C., Metzger, F., Black, D., and Ladden, R.: Evaluation of Wind Tunnel Performance Testings of an Advanced 45 Degree Swept Eight Bladed Propeller at Mach Numbers from 0.45 to 0.85. NASA CR 3505, March 1982.
3. Little, B. H., Jr.; and Hinson, B. L.: Inlet Design for High-Speed Propfans. SAE Technical Paper No. 821359, 1982.
4. Little, B. H., Jr., and Trimboli, W. S.: An Experimental Investigation of S-Duct Diffusers for High-Speed Prop-Fans. AIAA 82-1123, 1982.
5. Jameson, A.: Transonic Flow Analysis for Axially Symmetric Inlets with Centerbodies. Antony Jameson and Assoc., Inc., Report 2, 1981.
6. Youngren, H. H., Bouchard, E. E., Coopersmith, R. M., and Miranda, L. R.: Comparison of Panel Method Formulations and its Influence on the Development of QUADPAN, an Advanced Low Order Method. AIAA-83-1827, 1983.
7. Hinson, B. L.: Design and Experimental Evaluation of Propfan Inlets. SAE Technical Paper No. 841477, 1984 SAE Aerospace Congress and Exposition, October 15-18, 1984.
8. Hinson, B. L.: Aerodynamic Design Report. NAS 3-23710. Turboprop Inlet Installation Effort. Lockheed-Georgia Company, March 1984.
9. User's Manual for the Steady State Performance Customer Computer Deck CCD-D 0489-01.0 for the STS589 Study Engine. Report No. PWA Inst. 953, July 8, 1981.
10. Tanner, D.D. and Wynosky, T.A.: Prop-Fan Inlet Data Analysis from GUN Tests. Prepared under Subcontract to Lockheed Georgia Contract CB16909: Prop-Fan Inlet Data Analysis from GUN Tests. Pratt & Whitney, October 31, 1984.
11. Durand, W. F.: Aerodynamic Theory, A General Review of Progress, Volume 4. California Institute of Technology, January 1943.
12. Bansal, Prem N.: Experimental and Analytical Evaluation of the Effects of Simulated Engine Inlets on the Blade Vibratory Stresses of the SR-3 Model Prop-Fan. Hamilton Standard Division, United Technologies Corporation, NASA CR-174959, July 1985.





